| | |
|---|---|
| Title | Construction of Multimolecular Assembled Water Reduction Photocatalyst Nanoparticle for One-directional Electron Transfer |
| Author(s) | 吉村, 修隆 |
| Degree Grantor | 北海道大学 |
| Degree Name | 博士(理学) |
| Dissertation Number | 甲第15408号 |
| Issue Date | 2023-03-23 |
| DOI | https://doi.org/10.14943/doctoral.k15408 |
| Doc URL | https://hdl.handle.net/2115/91532 |
| Type | doctoral thesis |
| File Information | YOSHIMURA_Nobutaka.pdf |

# Construction of Multimolecular Assembled Water Reduction Photocatalyst Nanoparticle for One-directional Electron Transfer

（一方向的な電子移動を志向した分子多層膜担持光水素発生ナノ粒子触媒系の開発）

**Nobutaka Yoshimura**
Graduate School of Chemical Sciences and Engineering
Hokkaido University
2023

# Construction of Multimolecular Assembled Water Reduction Photocatalyst Nanoparticle for One-directional Electron Transfer

（一方向的な電子移動を志向した分子多層膜担持光水素発生ナノ粒子触媒系の開発）

Nobutaka Yoshimura
Graduate School of Chemical Sciences and Engineering
Hokkaido University

Contents

Chapter 1. General Introduction

Chapter 2. A Systematic Study on the Double-layered Photosensitizing Dye Structure on the Surface of Pt-cocatalyst-loaded $TiO_2$ Nanoparticles

Chapter 3. Photosensitizing Ruthenium(II)-Dye Multilayers: Photoinduced Charge Separation and Back Electron Transfer Suppression

Chapter 4. Enhancement of Photocatalytic Activity for Hydrogen Production by Surface Modification of Pt-$TiO_2$ Nanoparticles with a Double Layer of Photosensitizers

Chapter 5. Interfacial Electron Flow Control by Double Nano-architectures for Efficient Ru-dye-sensitized Hydrogen Evolution from Water

Chapter 6. Photocatalyst−mediator Interface Modification by Surface-metal Cations of a Dye-sensitized $H_2$ Evolution Photocatalyst

Chapter 7. The Enhancement of Electron Donation Reaction with Redox Mediators by Surface Modification of Ru(II)-dye-multilayered Pt-cocatalyst-loaded Layered Niobate

Chapter 8. Efficient Hydrogen Production by Photo-redox-cascade Catalyst Composing Dual Photosensitizers and Transparent Electron Mediator

Acknowledgements

# Chapter 1
# General Introduction

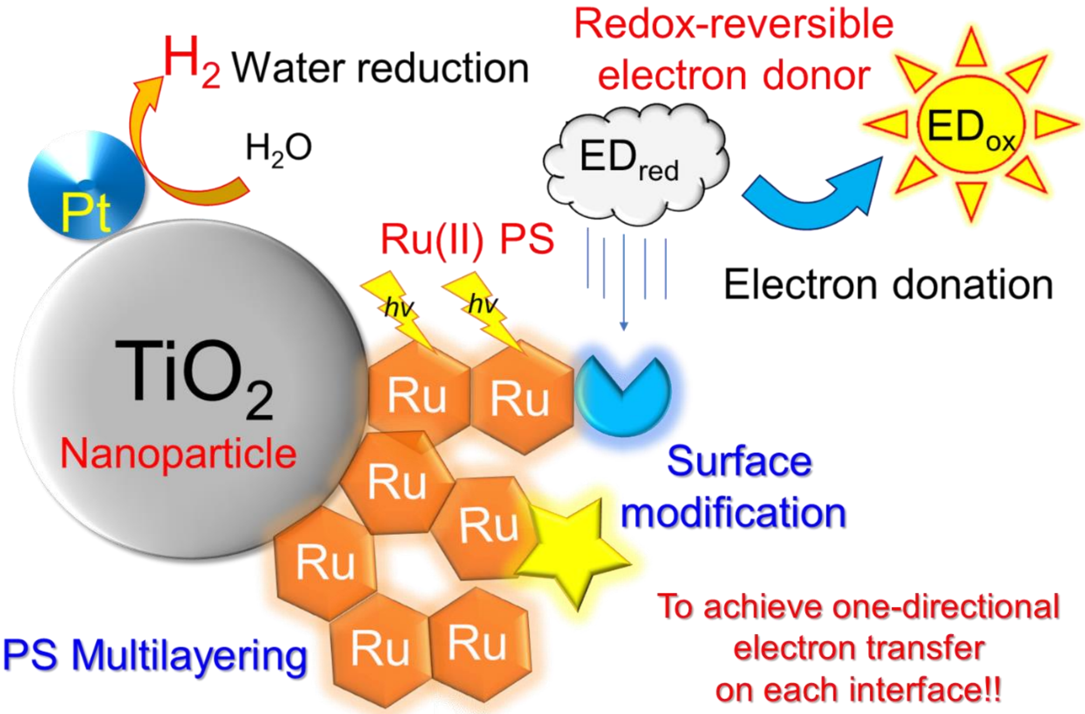

## 1-1 Solar-to-energy conversion

Nowadays, human beings are facing an energy issue by reduce of thermal power generation using fossil fuels to suppress the global warming. To solve this problem, utilization of solar energy is promising because of their almost inexhaustible and permanent nature. For example, total sun energy which irradiates the land part of Japan is $2\times10^{21}$ J/y, which is approximately 100 times more than total annual consumption power in Japan.[1]

$$\begin{aligned}&\text{(Total sun energy)}\\ &= [\text{Solar constant}] \times (1-[\text{geometric albedo of the earth}]) \times \cos([\text{latitude of Tokyo}])\\ &\quad\times 3.15\times10^{7}\ (\text{s/y}) \times 12\ (\text{h})/24\ (\text{h}) \times [\text{land area of Japan}]\\ &= 1.37\times10^{3}\ (\text{W/m}^2) \times (1-0.367) \times \cos 35.7^\circ \times 3.15\times10^{7}\ (\text{s/y}) \times 0.5 \times 3.78\times10^{11}(\text{m}^2)\\ &= 4.2\times10^{21}\ \text{J/y} = 1.3\times10^{14}\ \text{J/s}\end{aligned}$$

Since the sun light irradiation is interrupted by cloud and dust in air, the substantive total sun energy which irradiates the land part of Japan is about the half of "total sun energy".

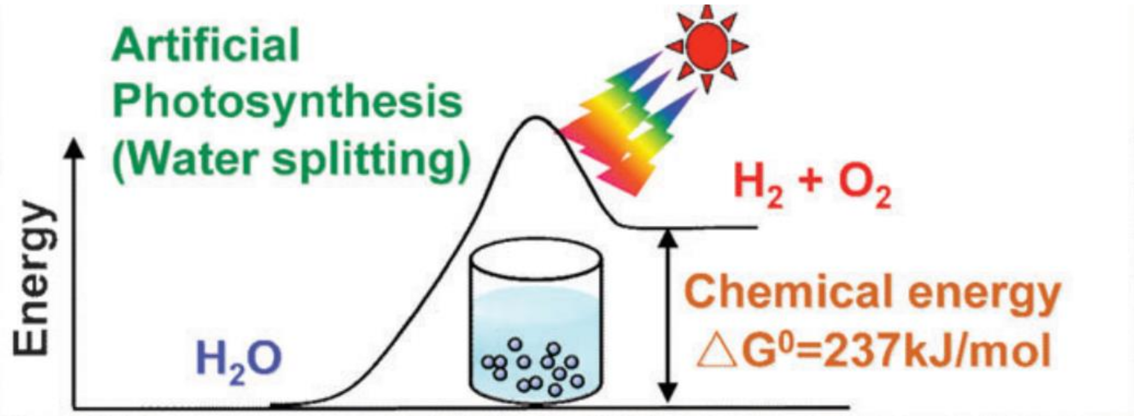

Fig. 1-1-1. Photocatalytic water splitting[2]

For effective utilization of solar energy, photocatalytic water splitting reaction, which converts from sun energy to chemical energy as hydrogen production, has attracted considerable attention because hydrogen emits neither greenhouse gases such as $CO_2$ nor harmful radioactive wastes when used as the energy source. As shown in Figure 1-1-1, water splitting reaction to generate hydrogen needs 237 kJ / mol Gibbs free energy ($\Delta G^0$), thus solar-to-hydrogen efficiency (STH) can be calculated below (Figure 1-1-2).

$$STH = \frac{(hydrogen\ production\ rate) \times \Delta G^0}{(solar\ constant) \times (Surface\ area\ of\ reacter)}$$

For example, if 10% of STH is needed, photocatalyst must absorb up to 700 nm with 40% of apparent quantum yield (AQY).

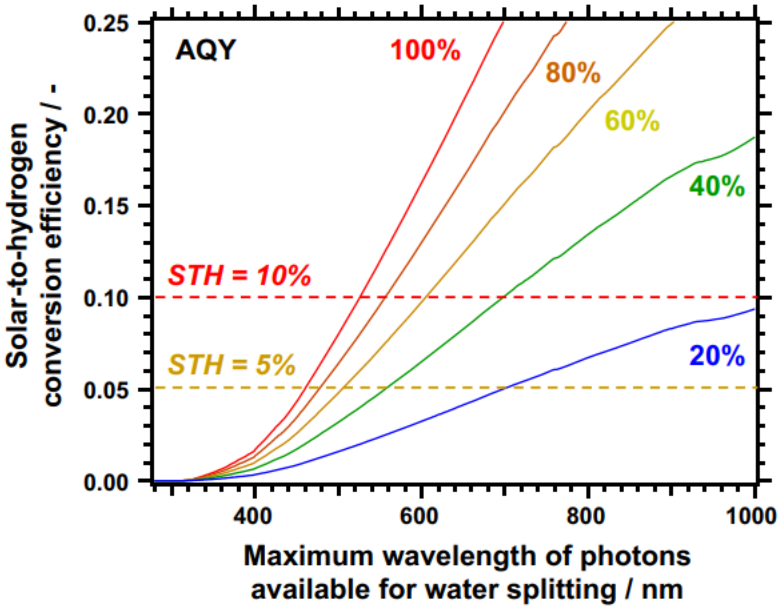

Figure 1-1-2. Relationship between STH and photon wavelengths available at different AQYs.[3]

## 1-2 Honda-Fujishima effect

In 1972, Honda and Fujishima reported water splitting to produce hydrogen when $TiO_2$ was irradiated with UV light.[4] In this system, $TiO_2$ electrode was immersed to aqueous electrolyte and was electrically connected to Pt counter electrode. When $TiO_2$ was irradiated, hydrogen and oxygen were produced on the surfaces of Pt and $TiO_2$ electrodes, respectively, and the electric current from Pt to $TiO_2$ electrode was observed.

The reaction mechanism is as follows (Fig. 1-2-1). Since $TiO_2$ is n-type semiconductor with 3.0 eV bandgap, the photo-excited electron in the conduction band (CB) was transferred to the Pt electrode to reduce water (i.e., $H^+$, proton) to generate hydrogen. The remaining hole on the $TiO_2$ valence band (VB) was used to oxidize a water molecule to generate oxygen. In this reaction, $TiO_2$ plays a role as photocatalyst, which absorbs photon to generate excited electron and hole for water splitting, and then catalyze water oxidation reaction. In the report by K. Honda and A. Fujishima, applied bias was needed for water-splitting reaction, but non-bias water-splitting by $TiO_2$ photocatalyst (NaOH-coated Rh/$TiO_2$ and Pd/$TiO_2$ catalysts) was achieved in 1992, by K. Sayama and H. Arakawa.[5,6]

However, $TiO_2$ can only absorb up to ~400 nm in UV light region. As described in Chap. 1-1, the theorical maximum of STH for water splitting $TiO_2$ photocatalyst is only 2%. Additionally, electron-hole recombination usually occurs in the bulk $TiO_2$ as the deactivation process. In fact, STH of only $TiO_2$ was less than 0.1% until now.[7]

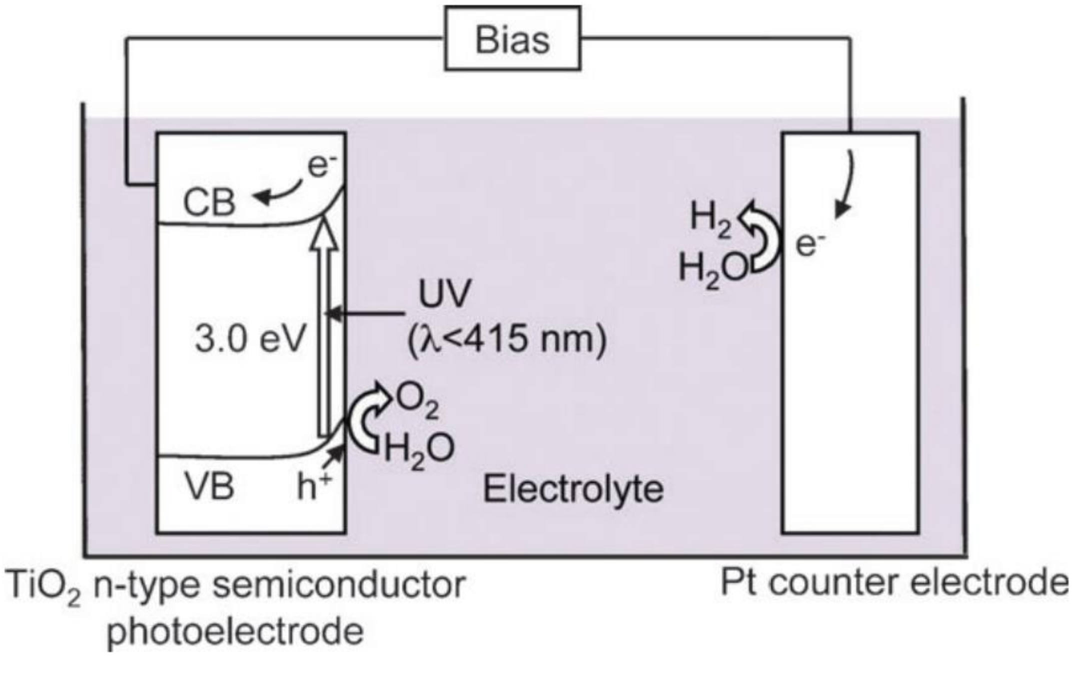

Figure 1-2-1. Schematic diagram of water electrolysis based on the Honda-Fujishima effect.[2]

## 1-3 Z-scheme system

To utilize longer wavelength light in solar light, two-step photoexcitation (Z-scheme) water splitting photocatalyst was suggested in 1990s,[8,9] and stoichiometric water splitting was achieved in 2001, by H. Arakawa and co-workers.[10] This Z-scheme system (Figure 1-3-1) imitated the natural photosystem I and II in chloroplast of plants. In the Z-scheme system, two-step photoexcitation occurs in the oxygen evolution and hydrogen evolution photocatalysts. In this case, one photocatalyst need not have both strong reduction and oxidation potentials compared to one-step excitation photocatalyst. Thus, it is possible to acquire the wide range photo-absorptivity. On the other hand, redox-reversible electron mediator (redox mediator) was generally needed to transport electrons from oxygen evolution photocatalyst to hydrogen evolution photocatalyst in Z-scheme systems.

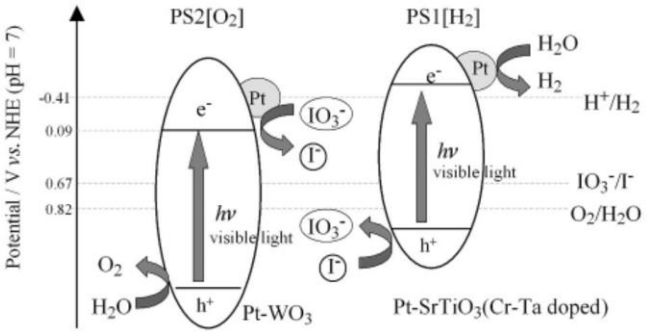

Figure 1-3-1. Schematic energy diagram of initial Z-scheme type water-splitting photocatalysts.[10]

Although the sufficiently high apparent quantum yield (AQY) was reported for the one-step photoexcitation UV-light-driven photocatalyst (95.7% at 350 nm and 91.6% at 365 nm for $SrTiO_3$:Al) by Domen and co-workers,[11] the AQY value of visible-light Z-scheme photocatalysts with redox mediator is still insufficient (e.g. AQY = 6.8% STH = 0.24% for Pt/$BaTaO_2N$ and $WO_3$ in 1 mM NaI aq.).[12] This is probably because back electron transfer reaction with redox mediator easily occurs (Figure 1-3-2). Therefore, new strategies to suppress this back electron transfer process are strongly required to improve the activity of Z-scheme photocatalyst. In the photosynthesis of plants, back electron transfer processes are suppressed by multi-step intermolecular electron transfer processes (Figure 1-3-3).[13]

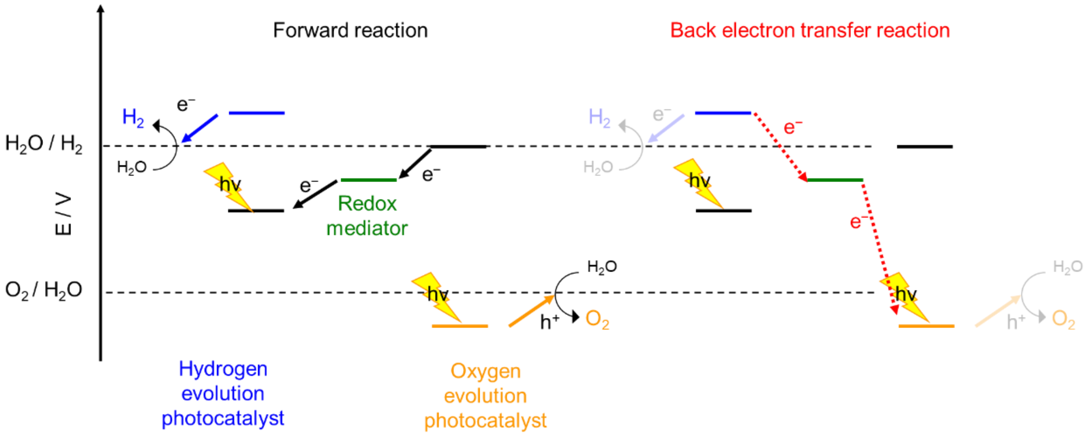

Figure 1-3-2 (Left) forward and (right) back electron transfer reactions with redox mediator.

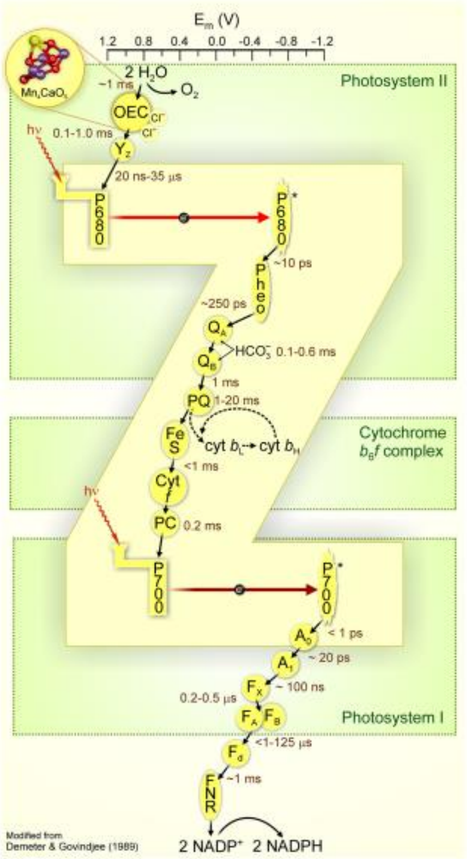

Modified from Demeter & Govindjee (1989)

Figure 1-3-3. Reaction scheme of photosynthesis [13]

## 1-4 Dye-sensitization

To utilize longer wavelength light, the dye-sensitization mechanism has been studied from 1991.[14] In the dye-sensitized system, the dye molecules called photosensitizers (PSs) absorbed visible light and injected electron or hole to semiconductors, leading to water reduction/oxidation reactions.[15] For example, in the case of dye-sensitized photoanode for water reduction reaction or solar cells (Figure 1-4-1(a)), the excited electron generated by light excitation of PS was injected to the CB of semiconductor (Figure 1-4-1(b)). The oxidized PS was regenerated by the electron donation from the redox mediator. In this case, the semiconductor substrate for dye-immobilization plays a role as only electron acceptor to transport electrons to photocathode for $H_2$ evolution, and instead, the surface immobilized PS absorbs irradiation light. Since the redox potentials and light absorption property of PS can be easily controlled by molecular modification, the range of absorption wavelength can be easily controlled from UV to NIR region. Therefore, it can be possible to combine various materials and strategies applicable for highly active water splitting system. Nevertheless, this dye-sensitized system has lower activity than semiconductor photocatalysts due to back electron transfer (charge recombination) process from the electron-injected semiconductor to one-electron-oxidized photosensitizer. At this present, the highest AQY of dye-sensitized photocatalyst reported until 2022 was 4.1 % at 420 nm by Mallouk and Maeda (Figure 1-4-2).[16] In this system, high activity was achieved due to suppression of back electron transfer from both Pt co-catalyst and Ru(II) PS to electron mediator by using poly(styrenesulfonate)-covered Ru(II) PS immobilized Pt/$HCa_2Nb_3O_{10}$. However, there were few dye-sensitized photocatalysts (DSPs) which can work in the presence of redox-reversible electron donor. Further, it is still severe problems not only to suppress the back reaction process between photocatalyst surface and redox mediators but also to accelerate the forward reaction process.

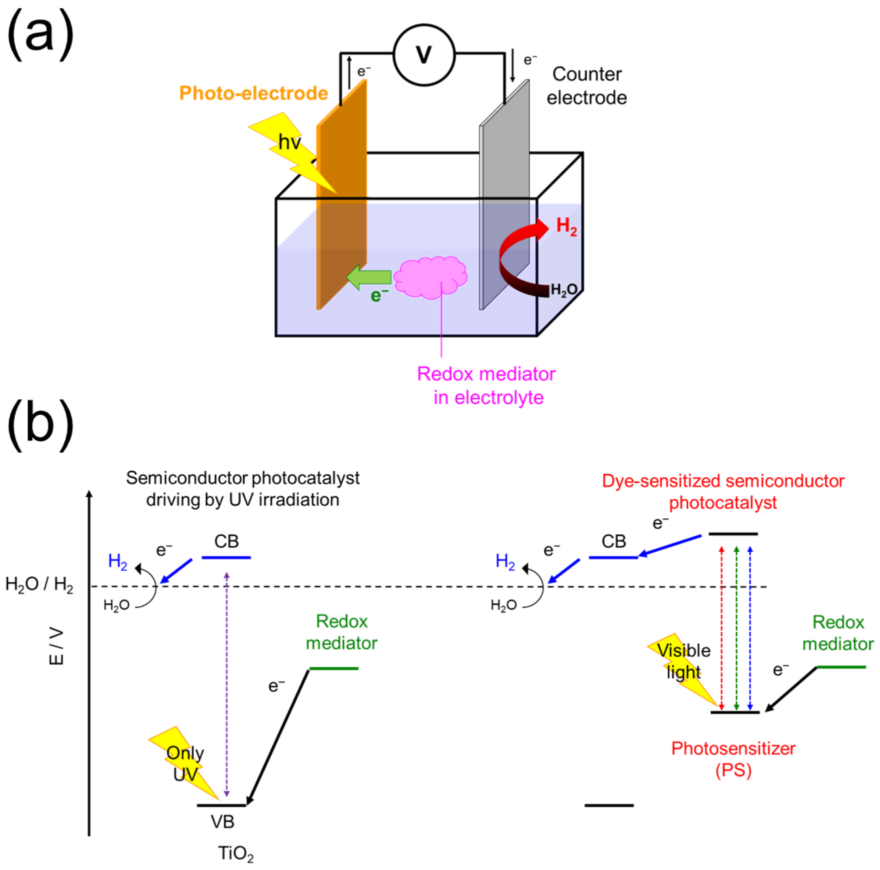

Figure 1-4-1. (a) Schematic image of photoelectrochemical cell for hydrogen production. (b) (Left) semiconductor photocatalyst driving by UV irradiation and (right) dye-sensitized photocatalyst for hydrogen production in the presence of redox mediator.

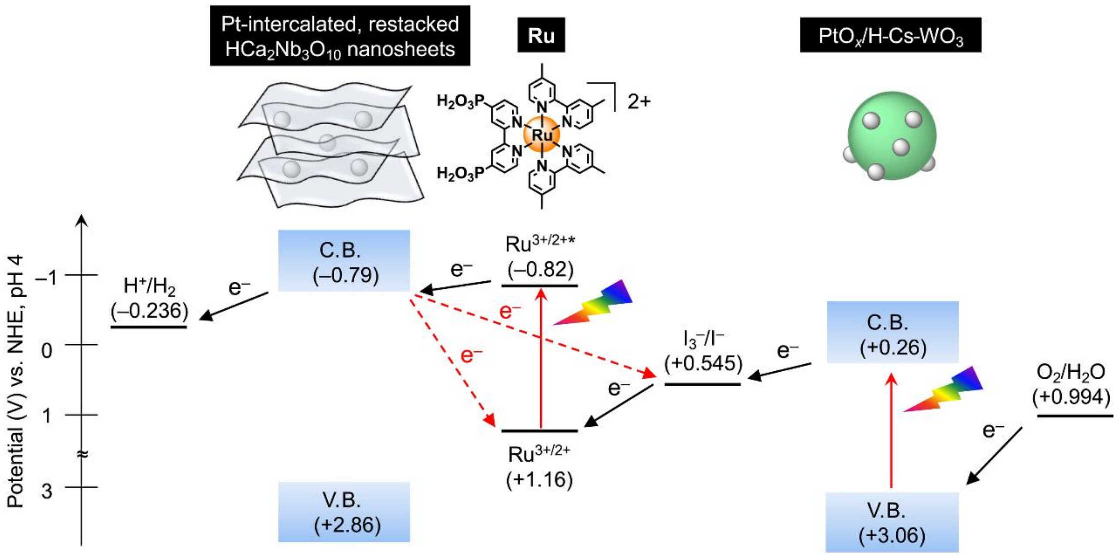

Figure 1-4-2. Schematic energy diagram of the highest dye-sensitized water splitting photocatalyst[16] Red dashed arrows show back electron transfer processes.

## 1-5 Back reactions in dye-sensitized photocatalyst

As mentioned in chapter 1-4, suppression of the back reaction processes is critical issue to design highly active Z-scheme water splitting photocatalyst. In dye-sensitized water reduction system, there are several back reaction processes classified into two phenomena; one is the back electron transfer processes after the charge separation, and another is the deactivation processes in the photoexcited state (Figure 1-5-1). The back electron transfer processes are the reactions to give the excited electron to undesired molecules, as listed below;[17,18] the reaction from electron-injected semiconductor to ① the oxidized PS (i.e. charge recombination) or ②oxidized mediator. ③ the reaction from photo-excited PS to oxidized electron mediator. (Figure 1-5-1(b)). Mallouk and co-workers reported that the charge recombination ① the from conduction band of $TiO_2$ to Ru(II) PS occurred within approximately 0.1~0.4 ms timescale (Figure. 1-5-2).[19] This timescale is faster than electron donation from $IrO_2$ oxygen evolution catalyst to the one-electron oxidized Ru(III) PS (~2 ms), resulting in the low activity. Thus, new strategies to suppress the charge recombination are strongly required to achieve sufficiently high photocatalytic activity.

There are several undesired side reactions such as the re-reduction of oxidized electron donor on hydrogen evolution catalyst and degradation/desorption of PS (Figure 1-5-1(c)). Generally, the layered semiconductor materials have been utilized in the most of DSPs for hydrogen evolution in the presence of redox-reversible electron donor because the re-reduction of oxidized electron donor on the surface of co-catalyst was effectively suppress by the intercalation of co-catalyst into the interlayer space of layered semiconductor materials.[16,20,21] Deactivation processes are mainly wrong pathways of photo-excited PS including both radiative (photoluminescence) and non-radiative deactivations in addition to energy transfer quenching by electron mediator (Figure 1-5-1(d)). To solve these back reaction processes is critical for higher activity of Z-scheme photocatalyst for practical application.

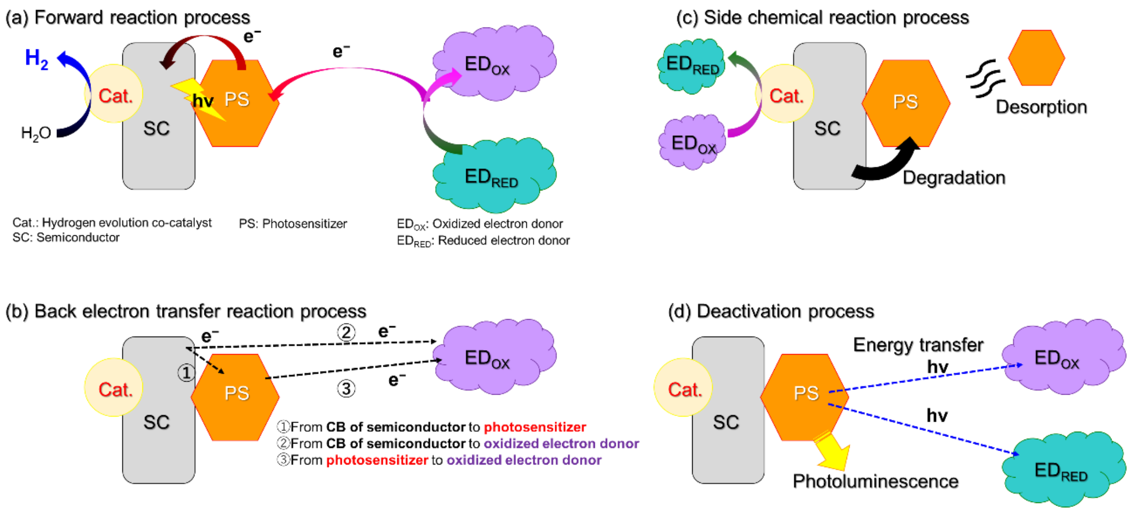

Figure 1-5-1 General scheme of (a) forward reaction process (b) back electron transfer reaction process (c) side chemical reaction process (d) deactivation process

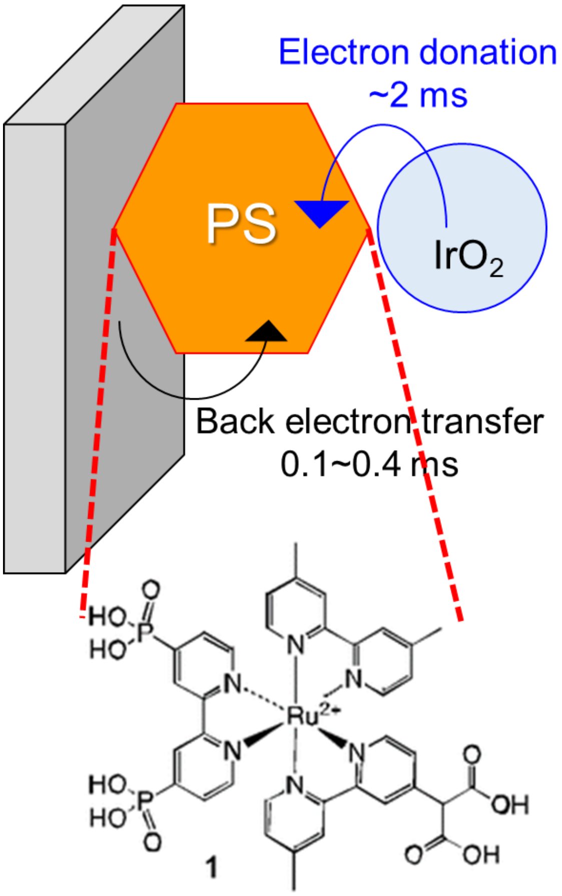

Figure 1-5-2. Schematic image of back electron transfer from semiconductor to dye. [19]

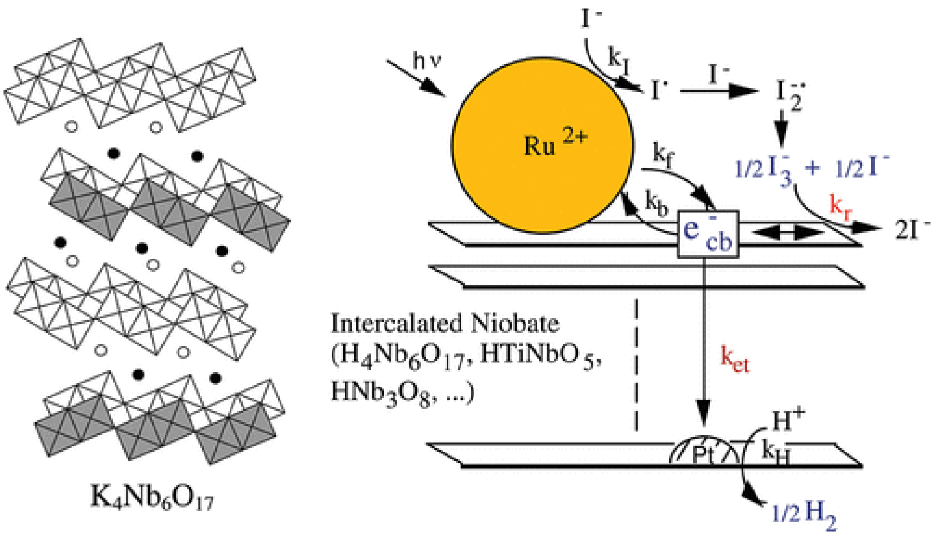

Figure 1-5-3. Schematic images of dye-sensitized Pt-cocatalyst-intercalated niobate photocatalyst for hydrogen evolution from iodide redox-reversible electron donor.[20]

## 1-6 Purpose of this thesis

In this thesis, suppression of the back reaction process and enhancement of the forward reaction were aimed by combining dye multilayering and surface modification techniques. Previous work by Furugori *et. al.* suggested that the double-layering of Ru(II) PS enhanced photocatalytic hydrogen evolution activity in the presence of sacrificial electron donating ascorbic acid probably due to the improvement of charge separation efficiency between injected electron on conduction band of semiconductor and hole migrated to outer PS.[17,18] The suggested mechanism is as follows; at first, when the outer PS was photoexcited, the energy transfer to inner PS should occur when the excitation energy of outer PS was higher than that of inner PS (Fig. 1-6-1-①).[22] Secondly, the electron injection to semiconductor occurs when the potential of photoexcited electron of PS is enough negative to the CB of semiconductor substrate, leaving a hole in the inner PS (Fig. 1-6-1-②). Thirdly, the hole should migrate to the outer PS in the case of the redox potential of inner PS was more positive than that of outer PS, generating the charge-separated state in which the electron and hole were spatially separated in the semiconductor and the outer PS, respectively (Fig. 1-6-1-③). At last, the dye regeneration occurs by the electron donation from electron donor to complete the one-electron photo-redox cycle (Fig. 1-6-1-④). In fact, photocatalytic hydrogen evolution activity was improved by PS double-layering,[18] but it is still unclear how important the energy transfer and electron transfer processes are. To further extend the PS-multilayering strategy, a proton-exchanged niobate oxide ($K_xH_{4-x}Nb_6O_{17}$) was selected as semiconductor substrate for suppression of the side chemical reaction processes on hydrogen evolution co-catalyst.

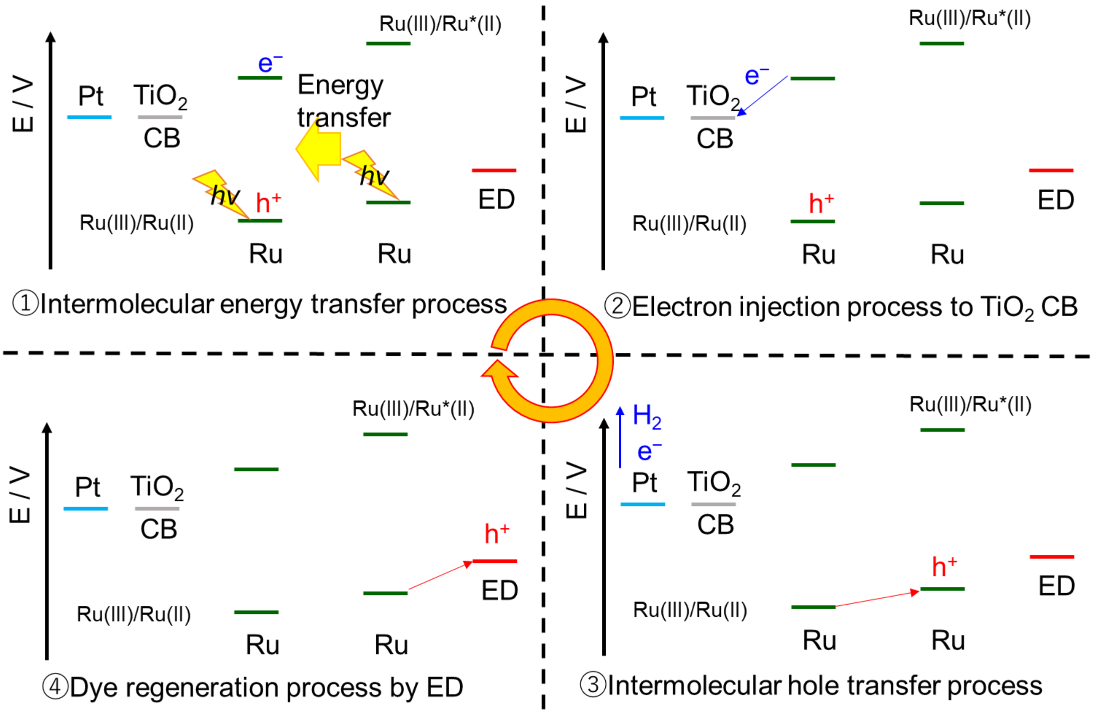

Figure 1-6-1. Suggested reaction scheme of the Ru(II) PS-double-layered Pt-$TiO_2$ hydrogen evolution photocatalyst.[18]

Furthermore, to enhance the reactivity with redox mediator, hole accepter immobilization on photocatalyst surface can improve the charge separation efficiency between photocatalyst surface and electron donor for the first time in DSP. In this thesis, phosphonate, $Zr^{4+}$-phosphonate was modified to make electrostatic interaction with redox reversible electron donors. Additionally, $[M(CN)_6]^{4-}$ complex (M = $Fe^{2+}$ or $Ru^{2+}$) was immobilized to investigate stoichiometric hole accepting effect for one-direction electron transfer cascade. Considering that several research in photochemistry of substrate suggests that long-lived (>ms~s) charge separated state was achieved by this hole accepting effect,[23-27] similar long-lived charge separation state should be expected in DSP.

Therefore, several types of surface-modified Ru(II)-PS-multiple-layered photocatalysts (see Table 1-6 and Figure 1-6-1) were newly synthesized by using the six different phosphonate-functionalized Ru(II) PSs (Figure1-6-2) and their photocatalytic hydrogen evolution activities was investigated.

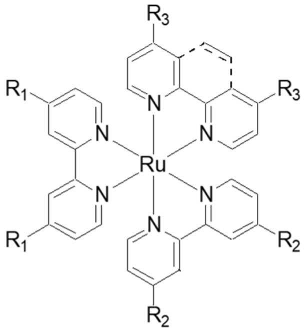

**RuP$^{2}$**: $R_1 = PO_3^{2-}$, $R_2 = R_3 = H$, bpy
**RuP$^{4}$**: $R_1 = R_2 = PO_3^{2-}$, $R_3 = H$, bpy
**RuP$^{6}$**: $R_1 = R_2 = R_3 = PO_3^{2-}$, bpy
**RuCP$^{2}$**: $R_1 = CH_2PO_3^{2-}$, $R_2 = R_3 = H$, bpy
**Ru(phen)CP$^{2}$**: $R_1 = CH_2PO_3^{2-}$, $R_2 = R_3 = H$, phen
**RuCP$^{6}$**: $R_1 = R_2 = R_3 = CH_2PO_3^{2-}$, bpy

Figure 1-6-2. Structure of Ru(II) PSs

Table. 1-6. Components of used photocatalyst

| Chap. | Electron donor | Surface structure | Ru-PS layer | Co-catalyst and semiconductor |
|---|---|---|---|---|
| 2 | Ascorbic acid | - | **Ru(phen)CP$^{2}$-RuP$^{6}$@** | Pt-$TiO_2$ |
| 3 | Iodide | - | **RuCP$^{2}$-RuP$^{4}$-RuP$^{6}$@** | Pt-$TiO_2$ |
| 4 | Iodide | $Zr^{4+}$ cation | Zr-**RuCP$^{6}$-RuP$^{6}$@** | Pt-$TiO_2$ |
| 5 | Iodide | $X^{n+}$ cation | X-**RuCP$^{6}$-RuP$^{6}$@** | Pt-$TiO_2$ |
| 6 | Iodide or $[Co(bpy)_3]^{2+}$ | $Zr^{4+}$ cation or phosphonate | Zr-**RuCP$^{6}$-RuP$^{6}$@** or **RuCP$^{6}$-RuP$^{6}$@** | Pt/$K_xH_{4-x}Nb_6O_{17}$ |
| 7 | $[SiV^{IV}W_{11}O_{40}]^{6-}$ or $[SiW_{11}O_{39}Mn^{II}(H_2O)]^{6-}$ | $Zr^{4+}$ cation or phosphonate | Zr-**RuCP$^{6}$-RuP$^{6}$@** or **RuCP$^{6}$-RuP$^{6}$@** | Pt/$K_xH_{4-x}Nb_6O_{17}$ |
| 8 | $[Co(bpy)_3]^{2+}$ or $[Fe(CN)_6]^{4-}$ | $[M(CN)_6]^{4-}$ | Zr-**RuCP$^{6}$-RuP$^{6}$@** | Pt-$TiO_2$ |

Components labeled by red are the most focused theme of chapter.

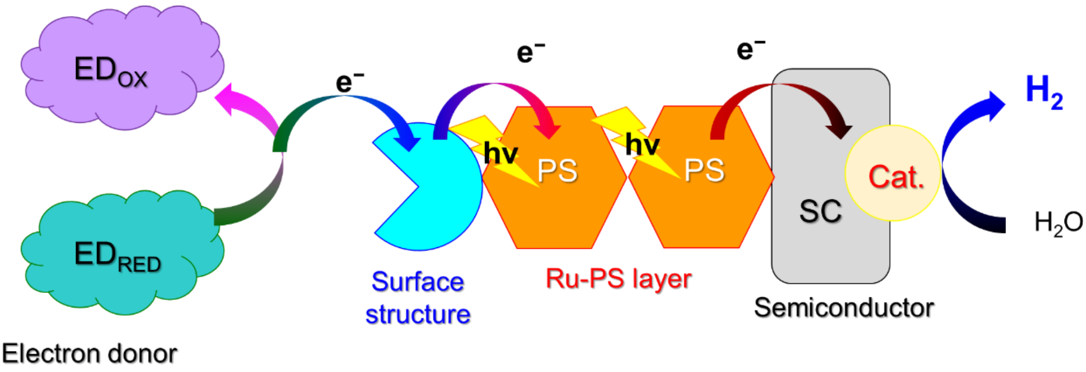

Figure. 1-6-3. Schematic illustration of photocatalytic $H_2$ evolution of Ru(II)-PS-multilayered photocatalyst developed in this thesis.

## 1-7 Outline of this thesis

This thesis consists of 9 chapters, which was briefly described in this session.

In chapter 1, the background and purpose of this research thesis are described with important references (Figure 1-7-1).

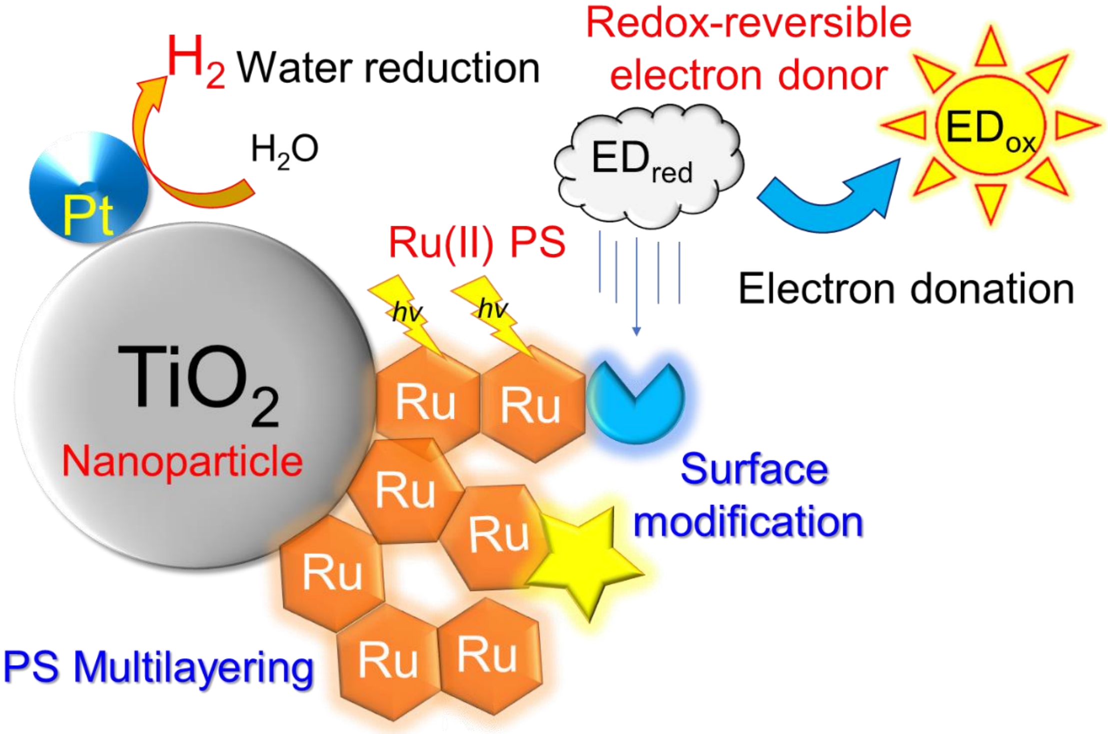

Figure 1-7-1. Overview of this thesis

In chapter 2, a systematic study on the double-layered photosensitizer structure on the surface of Pt-cocatalyst-loaded $TiO_2$ nanoparticles was conducted. The previous work by Furugori et al. suggested that the lower activity of Ru(II)-PS triple layered photocatalyst than that of double-layered one was due to wrong direction of inter PS energy transfer. In this chapter, to verify the effect of energy transfer process between the inner and outer PSs for photocatalytic hydrogen evolution activity, various new photocatalyst nanoparticles: **RuP$^2$**-Zr-**RuP$^6$**@Pt-$TiO_2$, **Ru(phen)CP$^2$**-Zr-**RuP$^6$**@Pt-$TiO_2$ ((**RuCP$^2$** = $[Ru(mpbpy)(bpy)_2]^{2-}$, **RuP$^6$** = $[Ru(pbpy)_3]^{10-}$, and **Ru(phen)CP$^2$** = $[Ru(mpbpy)(phen)_2]^{2-}$, $H_4$mpbpy = 2,2'-bipyridine-4,4'-bis(methane-phosphonic acid), $H_4$pbpy = 2,2'-bipyridine-4,4'-bis(phosphonic acid), bpy = 2,2'-bipyridine, and phen = 1,10'-phenanthroline) were synthesized and photocatalytic hydrogen evolution activity was investigated (Figure 1-7-2). This work revealed that the late-determining step of Ru(II)-PS multilayered photocatalyst was probably in the hole migration step from inner PS to outer PS, and well-structured PS-double-layered photocatalyst could use up lower concentration of ascorbic acid.

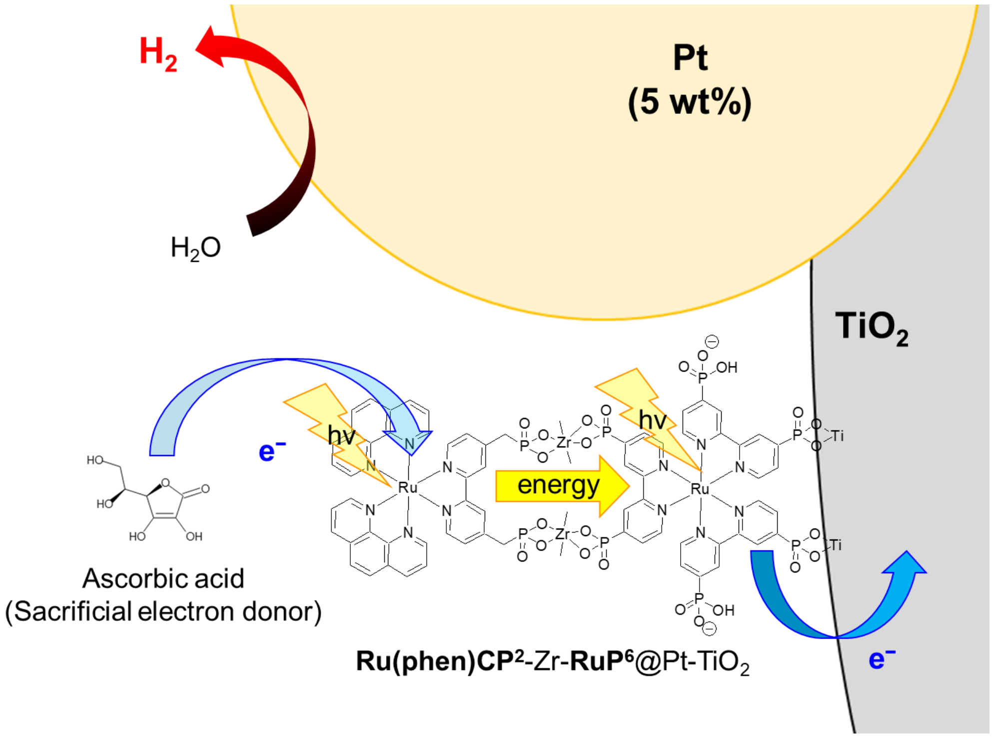

Fig. 1-7-2 Schematic image of photocatalyst discussed in chapter 2.

In chapter 3, photocatalytic hydrogen evolution in the presence of iodide anion as redox-reversible electron donor was evaluated by using Ru(II)-PS double- and Ru(II)-PS triple-layered photocatalyst nanoparticles, **RuCP$^2$-RuP$^6$**@Pt-TiO$_2$, and **RuCP$^2$-RuP$^4$-RuP$^6$**@Pt-TiO$_2$ (**RuP$^4$** = [Ru(pbpy)$_2$(bpy)]$^{6-}$), to aim the connection with water oxidation photocatalysts. Although **RuCP$^2$-RuP$^4$-RuP$^6$**@Pt-TiO$_2$ exhibited lower activity than **RuCP$^2$-RuP$^6$**@Pt-TiO$_2$ in the ascorbic acid aqueous solution as discussed in chapter 2, **RuCP$^2$-RuP$^4$-RuP$^6$**@Pt-TiO$_2$ exhibited higher activity than **RuCP$^2$-RuP$^6$**@Pt-TiO$_2$ in 0.5 M iodide aqueous solution, probably due to the suppression of back reaction from triiodide to iodide on Pt co-catalyst surface by bulkiness of PS triple layering structure (Figure 1-7-3). However, the maximum of AQY was 0.1%, and this AQY was much lower than that in the ascorbic acid condition (AQY = ~7%), the higher reactivity with iodide mediator was required to improve the photocatalytic activity.

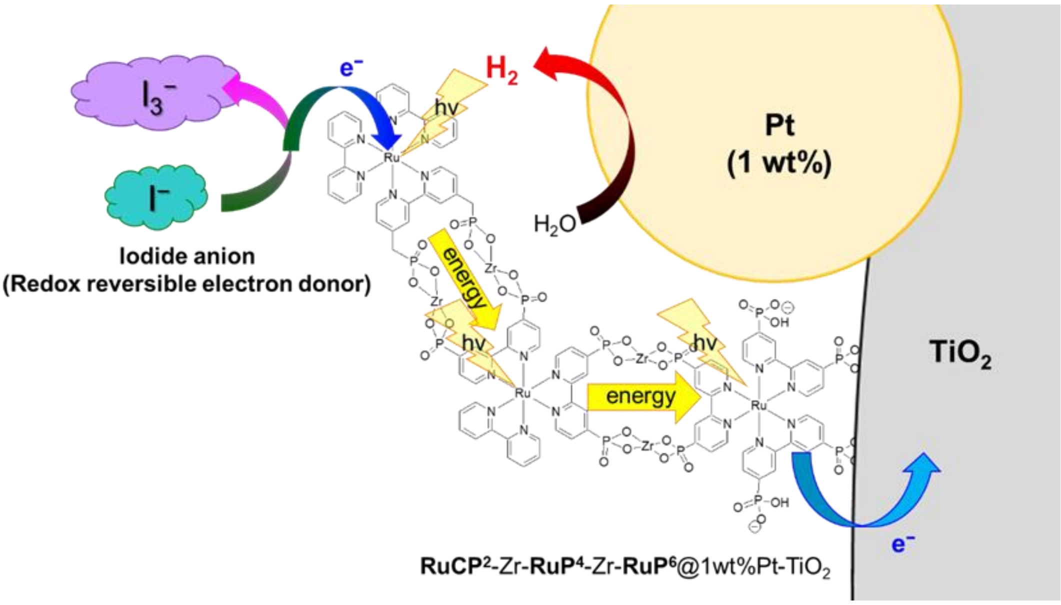

Fig. 1-7-3. Schematic image of photocatalyst discussed in chapter 3.

In chapter 4, enhancement of photocatalytic activity for hydrogen production was aimed by surface modification of Pt-TiO$_2$ nanoparticles with a double layer of PSs. To improve the reactivity with iodide anion, Zr$^{4+}$-phosphonate surface-functionalized Zr-**RuCP$^6$-RuP$^6$**@Pt-TiO$_2$ (**RuCP$^6$** = [Ru(mpbpy)$_3$]$^{10-}$), was newly synthesized and photocatalytic hydrogen evolution activity was investigated. Zr-**RuCP$^6$-RuP$^6$**@Pt-TiO$_2$ exhibited superior activity to phosphonate-exposed **RuCP$^6$-RuP$^6$**@Pt-TiO$_2$ and simple bipyridine-exposed **RuCP$^2$-RuP$^6$**@Pt-TiO$_2$. The initial AQY was reached to 1% (Figure 1-7-4). These results suggest that electrostatic interaction between surface Zr cation and iodide anion was important for attracting iodide anion to the surface of photocatalyst.

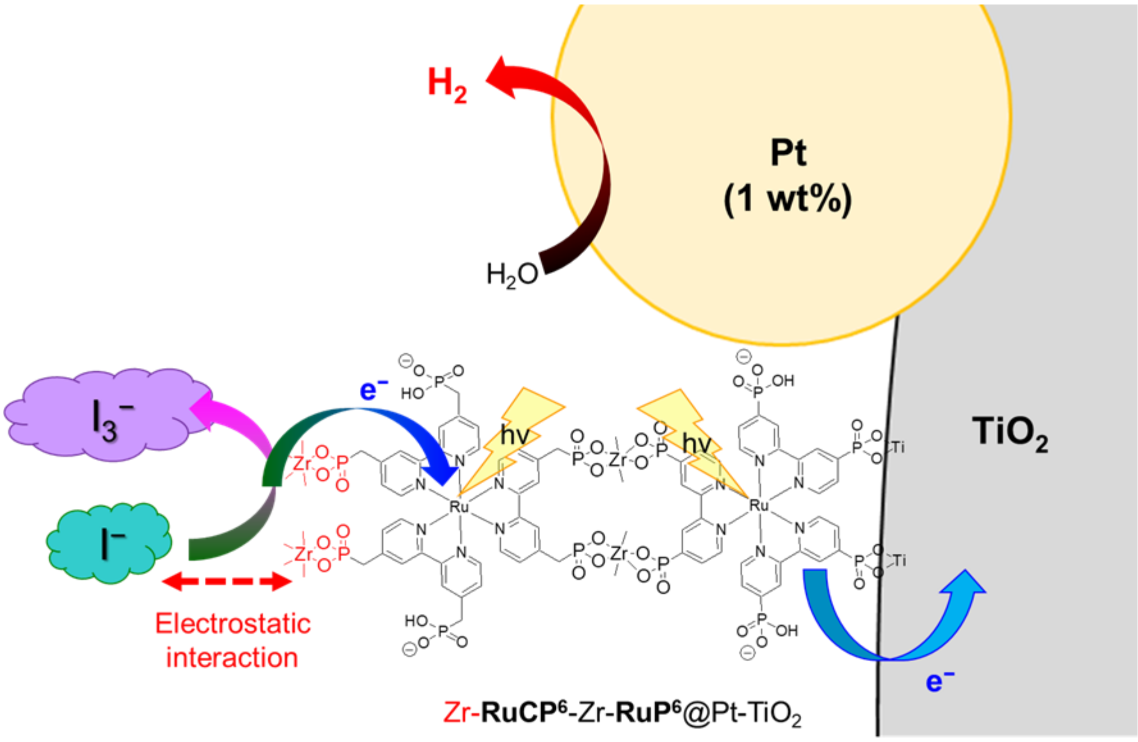

Fig. 1-7-4. Schematic image of photocatalyst discussed in chapter 4.

In chapter 5, photocatalyst–mediator interface modification was investigated by using surface-metal cations of a dye-sensitized hydrogen evolution photocatalyst. As discussed in chapters 3 and 4, the $Zr^{4+}$-phosphonate surface-functionalized photocatalyst system enhanced hydrogen production reaction from iodide anion by electrostatic interaction. Thus, to investigate the effect of surface metal cation for higher reactivity with electron mediator, various metal cations ($Fe^{2+}$, $Y^{3+}$, $Zr^{4+}$, $Hf^{4+}$, and $Bi^{3+}$) were modified on the surface of **RuCP$^6$-RuP$^6$**@Pt-$TiO_2$ nanoparticle (Figure 1-7-5). This work revealed that the redox-inactive and highly charged metal cations tend to improve the electron donation from the iodide electron mediator, probably due to stronger electrostatic force with iodide and more immobilization amount. On the other hand, photocatalyst having heavy metal cations, **$Hf^{4+}$-RuCP$^6$-RuP$^6$**@Pt-$TiO_2$ and **$Bi^{3+}$-RuCP$^6$-RuP$^6$**@Pt-$TiO_2$ exhibited slightly better activity under green light irradiation (λ = 530±15 nm) than **$Zr^{4+}$-RuCP$^6$-RuP$^6$**@Pt-$TiO_2$, implying the contribution of heavy atom effect of the surface-bound metal cation to partially allow the spin-forbidden metal-to-ligand charge-transfer excitation.

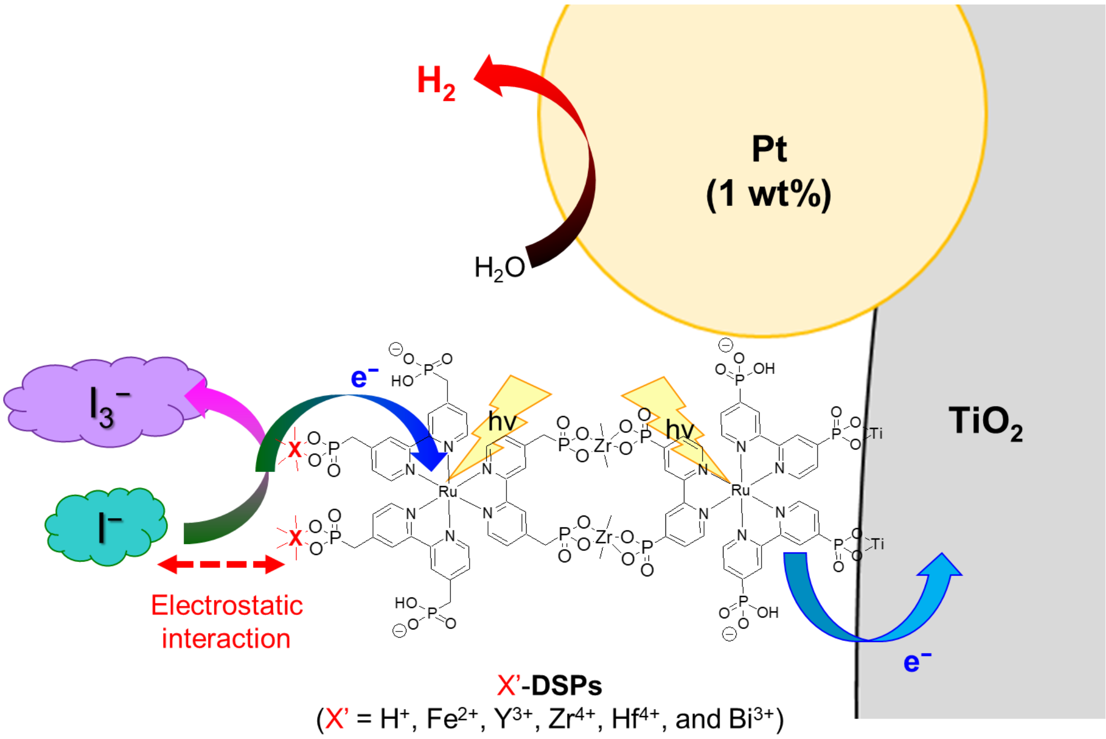

Fig. 1-7-5 Schematic image of photocatalyst discussed in chapter 5.

In chapter 6, one-directional electron transporting was tried to be controlled by Ru(II)-PS-sensitized layered niobate semiconductor. As described in chapters 3 and 4, charge separation efficiency on the interfaces of $TiO_2$-PS and PS-electron donor could be improved by PS multilayering and surface modification, respectively. Thus, to extend PS-multilayering strategy for other semiconductor nanoparticles, the Pt-cocatalyst-intercalated layered niobate, Pt/$K_xH_{4-x}Nb_6O_{17}$ was selected as semiconductor nanoparticle to immobilize Ru(II)-PS double layer for suppression of the back reaction process, the re-reduction of triiodide anion on the Pt co-catalyst (Figure 1-7-6). As a result, Zr cation exposed Zr-**RuCP⁶**-Zr-**RuP⁶**@Pt/$K_xH_{4-x}Nb_6O_{17}$ exhibited the highest photocatalytic activity in the presence of iodide anion donor, whereas phosphate anion exposed **RuCP⁶**-Zr-**RuP⁶**@Pt/$K_xH_{4-x}Nb_6O_{17}$ was the best activity in the $[Co(bpy)_3]^{2+}$ cation donor. In addition, **RuCP⁶**-Zr-**RuP⁶**@Pt/$K_xH_{4-x}Nb_6O_{17}$ could completely consume 1.6 mM of $[Co(bpy)_3]^{2+}$ cation donor with 0.40 % of initial AQY. Therefore, PS-multilayering strategy is also effective not only simple $TiO_2$ but also layered $K_xH_{4-x}Nb_6O_{17}$ nanoparticle, and These hydrogen evolution reaction results indicate that surface modification of dye-sensitized photocatalysts to modify the electrostatic interaction between the photocatalyst surface and redox mediator is a promising approach not only to enhance electron donation but also to suppress back electron transfer to the redox mediator.

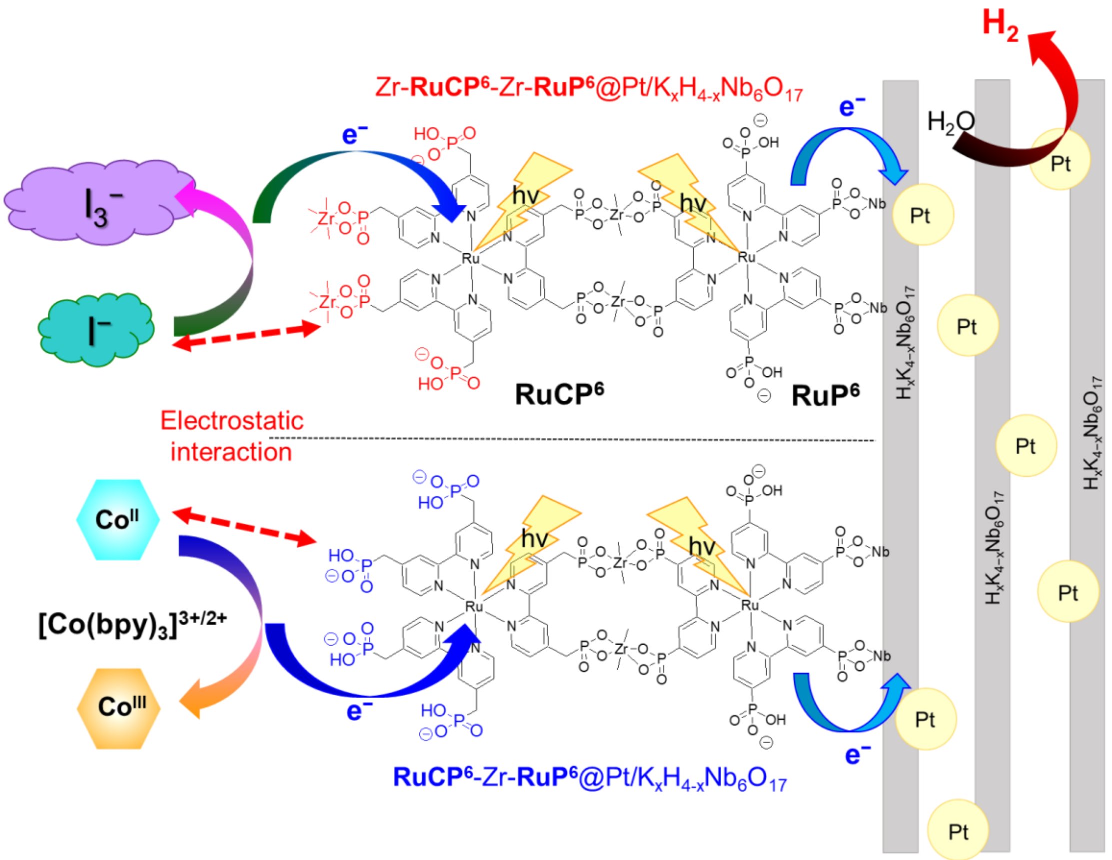

Fig. 1-7-6 Schematic image of photocatalyst discussed in chapter 6.

In chapter 7, to construct stronger electrostatic interaction between photocatalyst surface and electron donor, two hexavalent polyoxometalates, $K_6[SiV^{IV}W_{11}O_{40}]$ (**V$^{IV}$POM**) and $K_6[SiW_{11}O_{39}Mn^{II}(H_2O)]\bullet nH_2O$ (**Mn$^{II}$POM**) were selected as the redox-reversible electron donor for hydrogen production by Zr-**RuCP$^6$**-Zr-**RuP$^6$**@Pt/$K_xH_{4-x}Nb_6O_{17}$ and **RuCP$^6$**-Zr-**RuP$^6$**@Pt/$K_xH_{4-x}Nb_6O_{17}$ (Figure 1-7-7). In HCl aqueous solution, **V$^{IV}$POM** and **Mn$^{II}$POM** were partly immobilized on the surface of Zr-**RuCP$^6$-RuP$^6$**@Pt/$K_xH_{4-x}Nb_6O_{17}$ during the photocatalytic hydrogen evolution reaction, but activity decrease in the presence of visible-light-absorptive **V$^{IV}$POM** was observed probably due to energy transfer quenching from photo-excited Ru-PS to **V$^{IV}$POM**. This hypothesis was supported by the result that photocatalytic activity did not decrease in the visible-light-non-absorptive **Mn$^{II}$POM** condition. These results suggest that the accumulation of visible-light-transparent electron donors to eliminate non-favorable energy transfer quenching on the photocatalyst surface should be a promising method for efficient one-directional electron transfer in the Z-scheme water splitting system.

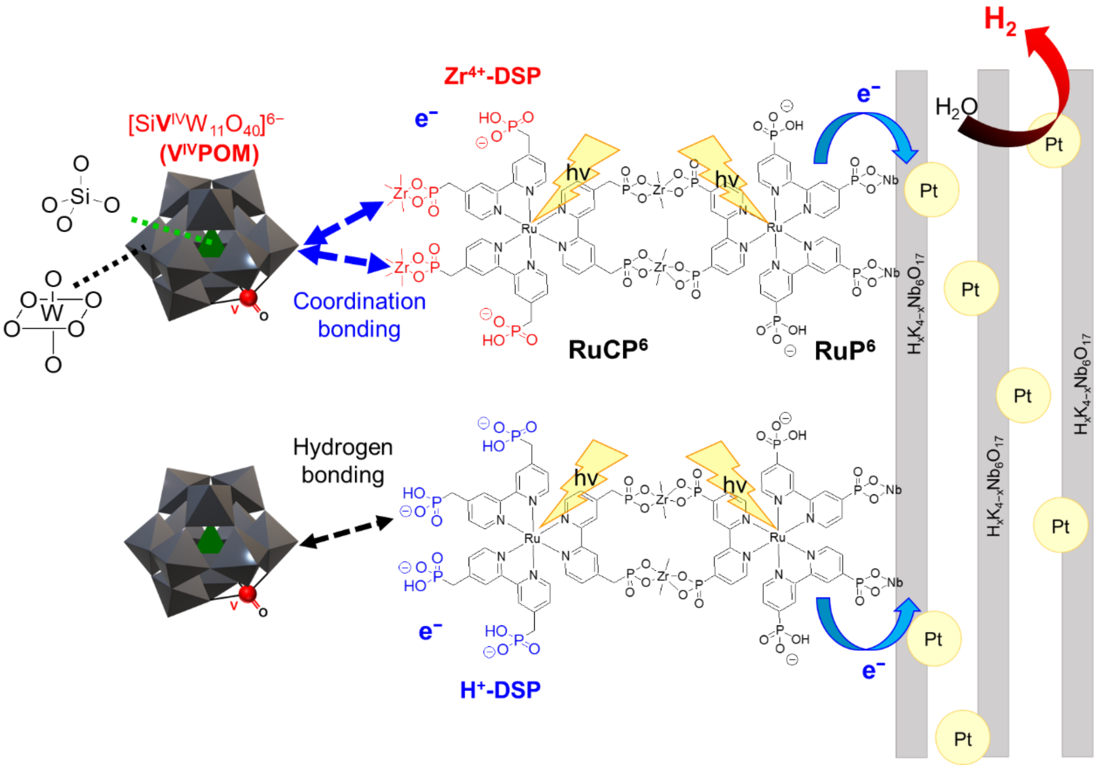

Fig. 1-7-7 Schematic image of photocatalyst discussed in chapter 7.

In chapter 8, hole accepter effect on the photocatalyst surface for higher charge separation efficiency on the PS-electron donor interface was described. As shown in chapter 7, positive effect by immobilization of electron donor on the photocatalyst surface because of the low immobilization amount of sterically bulky **POM**s. Thus, to investigate stoichiometric hole accepting effect for one-direction electron transfer cascade, $[M(CN)_6]^{4-}$ complex ($M = Fe^{2+}$ or $Ru^{2+}$) immobilized Zr-**RuCP$^6$-RuP$^6$**@Pt-$TiO_2$ nanoparticle was newly synthesized and immobilization effect of $[M(CN)_6]^{4-}$ for electron donation from redox-reversible electron donor was investigated (Figure 1-7-8). As a result, $Ru(CN)_6$-Zr-**RuCP$^6$-RuP$^6$**@Pt-$TiO_2$ exhibited the highest initial AQY (2.23%) of the dye-sensitized photocatalysts using $TiO_2$ nanoparticle in the presence of redox-reversible electron donor. These results suggested that construction of redox cascade was important to achieve the one-directional electron transfer in Z-Scheme water splitting cascade.

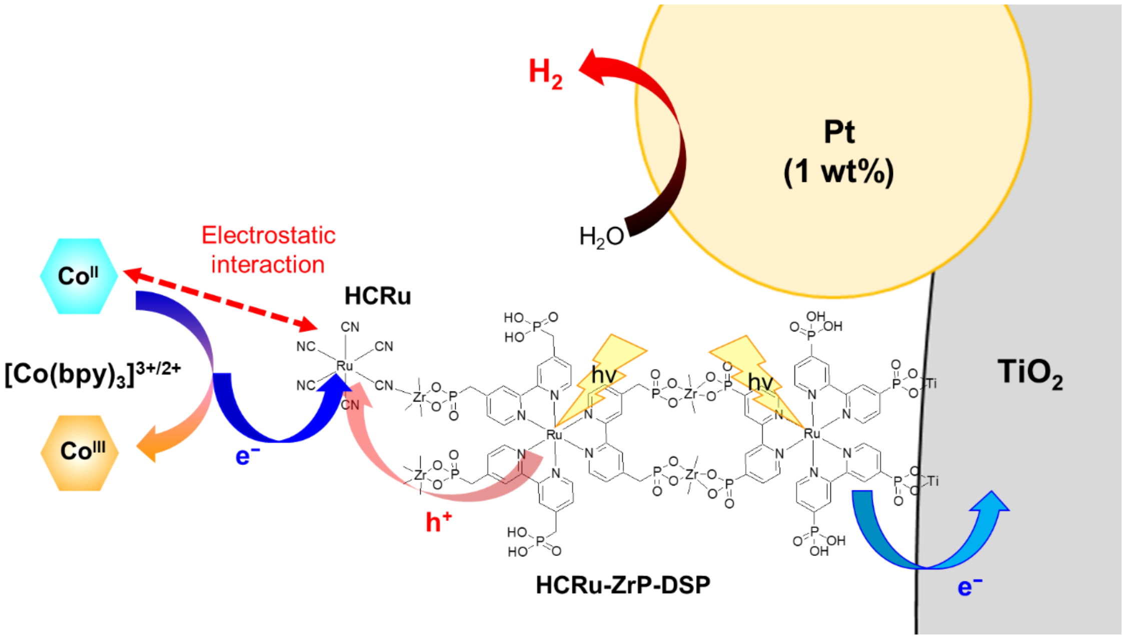

Fig. 1-7-8. Schematic image of photocatalyst discussed in chapter 8.

In chapter 9, the general conclusion and future prospective of this research thesis were summarized.

## 1-8 Reference

1. Website of Agency for Natural Resources and Energy, 『令和２年度(2020 年度)における エネルギー需給実績(確報）』 https://www.enecho.meti.go.jp/statistics/total_energy/pdf/honbun2020fykaku.pdf
2. A. Kudo and Y. Miseki, *Chem. Soc. Rev.*, **2009**, *38*, 253–278.
3. T. Hisatomi, K. Takanabe, K. Domen. *Catal Lett*, **2015**, *145*, 95-108.
4. A. Fujishima, K. Honda. *Nature* **1972**, *238*, 37−38.
5. K. Yamaguchi and S. Sato, *J. Chem. Soc., Faraday Trans.***1985**, *1*, 1237.
6. K. Sayama and H. Arakawa, *J. Chem. Soc., Chem. Commun.*, **1992**, 150.
7. M. Ge, Q. Li, C. Cao, J. Huang, S. Li, S. Zhang, Z. Chen, K. Zhang, S. S. Al-Deyab, and Y. Lai. *Adv. Sci*. **2017**, *4*, 1600152.
8. E. Greenbaum, J. W. Lee, C. V. Tevault, S. L. Blankinship and L. J. Mets. *Nature,* **1995**, *376*, 438–441.
9. J. W. Leec. V. Tevaultt. G. Owensand E. Greenbaum. *Science*, **1996**, *273*, 364-367.
10. K. Sayama, K. Mukasa, R. Abe, Y. Abe, H. Arakawa. *Chem. Comm.*, **2001**, *23*, 2416-2417.
11. T. Takata, J. Jiang, Y. Sakata, M. Nakabayashi, N. Shibata, V. Nandal, K. Seki, T. Hisatomi, K. Domen. *Nature*, **2020**, *581*, 411-414.
12. Z. Wang, Y. Luo, T. Hisatomi, J. J. M. Vequizo, S. Suzuki, S. Chen, M. Nakabayashi, L. Lin, Z. Pan, N. Kariya, *Nat. Commun.* **2021**, *12*, 1005
13. Govindjee, D. Shevela, L. O. Björn. *Photosynth Res*., **2017**, *133*, 5–15.
14. B. O'Regan, M. Grätzel. *Nature* **1991**, *353*, 737-740.
15. K. Kalyanasundaram, M. Grätzel. *Coord. Chem. Rev.*, **1998**, *177*, 347-414.
16. S. Nishioka, K. Hojo, L. Xiao, T. Gao, Y. Miseki, S. Yasuda, T. Yokoi, K. Sayama, T. E. Mallouk, K. Maeda. *Sci. Adv.*, **2022**, *8*, 9115.
17. K. Hanson, M. K. Brennaman, H. Luo, C. R. K. Glasson, J. J. Concepcion, W. Song, T. J. Meyer. *ACS Appl. Mater. Interfaces*, **2012**, *4*, 1462-1469.
18. S. Furugori, A. Kobayashi, A. Watanabe, M. Yoshida, M. Kato. *ACS Omega*, **2017**, *2*, 3901-3912.
19. S. A. Lee, Y. Zhao, E. A. Hernandez-Pagan, L. Blasdel, W. J. Youngblood, T. E. Mallouk. *Faraday Discuss*., **2012**, *155*, 165-176.
20. R. Abe, K. Shinmei, N. Koumura, K. Hara, B. Ohtani. *J. Am. Chem. Soc*., **2013**, *135*, 16872-16884.
21. G. B. Saupe, T. E. Mallouk, W. Kim, R. H. Schmehl. *J. Phys. Chem. B* **1997**, *101*, 2508–2513.
22. 22 Q. He, M. Worku, H. Liu, E. Lochner, A. J. Robb, S. Lteif, J. S. R. V. Winfred, K. Hanson, J. B. Schlenoff, B. J. Kim, B. Ma. *Angew. Chem. Int. Ed*. **2021**, *60*, 2485– 2492.
23. E. Sundina, M, Abrahamsson, *Chem. Commun*., **2018**, *54*, 5289-5298.

24. Y. Hu, S. Tsukiji, S. Shinkai, S. Oishi, I. Hamachi. *J. Am. Chem. Soc*. **2000**, *122*, 241–253.
25. M. E. El-Khouly, Y. Chen, X. Zhuang, S. Fukuzumi. J. Am. Chem. Soc. **2009**, *131*, 6370–6371.
26. M. Borgström, N. Shaikh, O. Johansson, M. F. Anderlund, S. Styring, B. Åkermark, A. Magnuson, L. Hammarström. *J. Am. Chem. Soc*. **2005**, *127*, 17504–17515.
27. A. J. Cowana, J. R. Durrant. *Chem. Soc. Rev*., **2013**, *42*, 2281-2293.

# Chapter 2

# A Systematic Study on the Double-layered Photosensitizing Dye Structure on the Surface of Pt-cocatalyst-loaded $TiO_2$ Nanoparticles

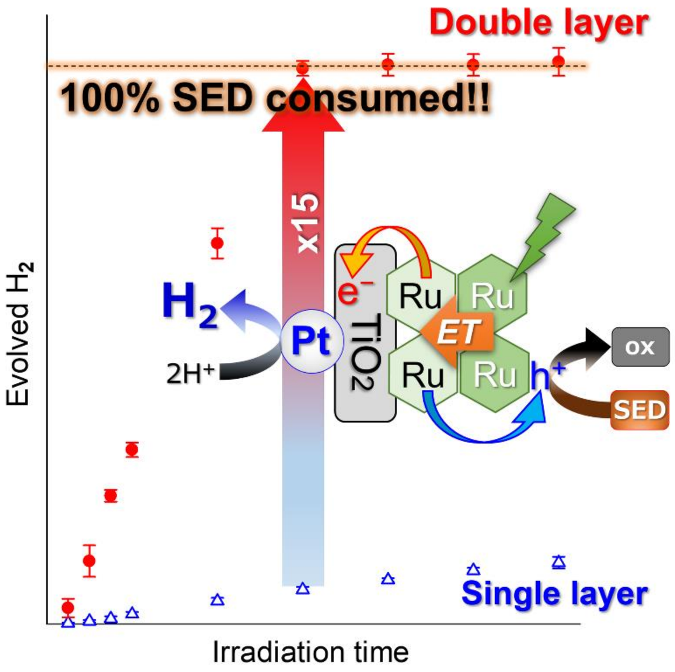

## 2-1 Introduction

Solar fuel production based on sustainable solar energy and water has attracted considerable attention as a solution to global warming and energy issues.[1-5] Since the discovery of the Honda-Fujishima effect,[6] water-splitting using semiconductor photocatalysts has been extensively studied as a promising reaction for the production of $H_2$ as a clean energy resource without generating environmental pollutants such as $CO_2$.[7-11] Since the $H_2$ and $O_2$ evolution reactions involve two- and four- electron transfer processes, respectively, the effective separation of the electron-hole pairs generated by light absorption is crucial. One promising method to achieve such charge separation[12-16] is the dye-sensitization mechanism, in which a light-absorbing dye molecule is immobilized on the surface of a semiconductor electrode.[17-23] For example, this mechanism is utilized in Grätzel dye-sensitized solar cells (DSSCs),[24-26] which exhibit energy conversion efficiencies of over 10%.[27-31] In Grätzel cells, Ru(II)-complex dye molecules are immobilized on a porous $TiO_2$ electrode surface to achieve effective separation of photogenerated electron-hole pairs at the dye-semiconductor interface. Furthermore, this promising dye sensitization mechanism has recently been applied to the water splitting reaction using dye-sensitized photoelectrochemical (DSPEC) cells composed of Ru(II) dyes and various water reduction and oxidation catalysts.[32-36] However, unlike DSSCs, which utilize relatively low-polarity solvents, water-splitting DSPEC cells must operate in a highly polar and coordinating solvent, water. Thus, the desorption and decomposition of the immobilized dye and catalysts are important issues that must be overcome to ensure the long-term durability of DSPEC cells.[37-48]

To inhibit the desorption of the dye from the semiconductor surface, it was recently reported that a new $H_2$-evolving nanoparticle photocatalyst composed of $TiO_2$ nanoparticles loaded with a Pt cocatalyst and two Ru(II) polypyridine-based photosensitizing (PS) dyes with a doubly-layered structure on the nanoparticle surface, **RuCP$^2$**-Zr-**RuP$^6$**@Pt-$TiO_2$ (Chart 2-1(a) and 2-1(b); **RuP$^6$** = $[Ru(pbpy)_3]^{10-}$, **RuCP$^2$** = $[Ru(bpy)_2(mpbpy)]^{2-}$, bpy = 2,2′-bipyridine, $H_4$mpbpy = 2,2′-bipyridine-4,4′-bis(methane phosphonic acid), and $H_4$pbpy = 2,2′-bipyridine-4,4′-bis (phosphonic acid)). The photocatalytic $H_2$ evolution ability of the double-PS-layer particle was higher than that of single-PS-layer **RuCP$^2$**@Pt-$TiO_2$ nanoparticles.[49-50] Although previous work indicated the importance of the doubly-layered PS dye structure for the photocatalytic $H_2$ evolution reaction,[50] the origins of the higher photocatalytic activities of the double-PS-layer photocatalyst compared to the single-PS-layer particle was unclear. Especially, the evaluation of the importance of excited energy and electron transfer processes in the double-layered PS structure is crucial to improve the photo-induced charge-separation efficiency at the dye-semiconductor interface. Therefore, in this study, I aimed to systematically control the electronic state of the double-layered PS structure on the Pt-$TiO_2$ nanoparticle surface using combinations of four different Ru(II) photosensitizers (Chart 2-1), including a newly synthesized

Ru(II) complex, **RuCP$^2$phen** (Chart 2-1(d)). Since the triplet metal-to-ligand charge-transfer ($^3$MLCT) emission energy and Ru(III)/Ru(II) redox potential of the Ru(bpy)$_3$-type dye can be controlled replacing the bpy ligand with a phen ligand (phen = 1,10-phenanthoroline) and by introducing phosphonate functional groups,[51] the energy and electron transfer processes in the double-layered PS structures can be precisely controlled by the combination of these four PS dyes. Herein, the photoelectrochemical property of the Ru(II) PS dye, **RuCP$^2$phen** was newly synthesized, and the photocatalytic $H_2$ evolution performances of Pt-TiO$_2$ nanoparticles with three different double-layered PS structures were investigated. As a result, all three double-PS-layer photocatalysts exhibited higher photocatalytic activity than the single-PS-layer one in the diluted sacrificial electron donor (SED) concentration and the high activities remained until all the SED were consumed.

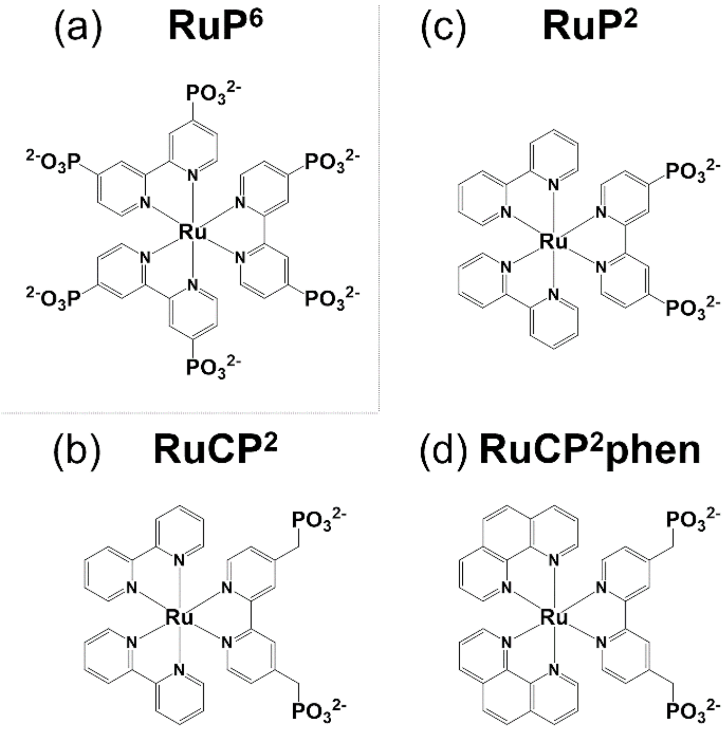

**Chart 2-1.** Molecular structures of Ru(II) photosensitizers used in this chapter.

## 2-2 Experimental

### 2-2-1 Materials and Syntheses

Caution! *Although I did not encounter any difficulties, most of the chemicals used in this study are potentially harmful and should be used in small quantities and handled with care in a fume hood.* All commercially available starting materials were used as received without further purification. The $TiO_2$ nanoparticles (SSP-M, anatase, ~15 nm in diameter) were purchased from Sakai Chemical Industry Co. Ltd. Pt-$TiO_2$ (5.26 wt%) was prepared using a previously reported photodeposition method and characterized using X-ray fluorescence (XRF) spectroscopy.[52] The Ru(II) PS dyes (**RuCP$^2$**, **RuP$^2$**, and **RuP$^6$**) and the starting materials, [Ru(phen)$_2$Cl$_2$] (phen = 1,10-phenanthroline), and CP-bpy (CP-bpy = 4,4′-bis(methyl phosphonic acid)-2,2′-bipyridine) were prepared using previously reported methods from the literatures.[53,54]

### 2-2-2 Synthesis of [Ru(phen)$_2$(H$_4$mpbpy)]Cl$_2$ (RuCP$^2$phen).

A mixture of dmpEtbpy (4,4’-bis(phosphonomethyl)-2,2’-bipyridine, 187.1 mg, 0.402 mmol) and [Ru(phen)$_2$Cl$_2$] (228.7 mg, 0.410 mmol) was dissolved in EtOH (18 mL) and then heated using microwave irradiation (Biotage Initiator$^+$) at 150 °C for 3.5 h. After cooling to room temperature, the EtOH solvent was removed under reduced pressure. The obtained red solid was dissolved in 18% HCl aq. (120 mL) and refluxed overnight. After the reaction, 36% HCl aq. (60 mL) was added to the solution, and all the solvent was removed under reduced pressure. Recrystallization from a MeOH/Et$_2$O mixture afforded pure **RuCP$^2$phen** as an orange powder. Yield: 323.8 mg (0.329 mmol, 82%). $^1$H NMR (Figure 2-2-2, 270 MHz, D$_2$O, δ ppm): 8.62 (d, 2H, $J$ = 8.2 Hz), 8.51 (d, 2H, $J$ = 8.2 Hz), 8.46 (s, 2H), 8.38 (d, 2H, $J$ = 4.9 Hz), 8.20 (m, 4H), 7.94 (d, 2H, $J$ = 5.3 Hz), 7.74 (t, 2H, $J$ = 5.1 Hz, 8.0 Hz), 7.60 (d, 2H, 5.6 Hz), 7.49 (t, 2H, $J$ = 6.0 Hz, 8.1 Hz), 7.14 (d, 2H, $J$ = 4.9 Hz), 3.20 (d, 4H, $J$ = 21.7 Hz). Anal. Calcd. (%) for $C_{36}H_{30}RuN_6O_6P_2Cl_2 \cdot 6H_2O$: C, 43.91; H, 4.30; N, 8.53. Found: C, 43.96; H, 3.83; N, 8.41.

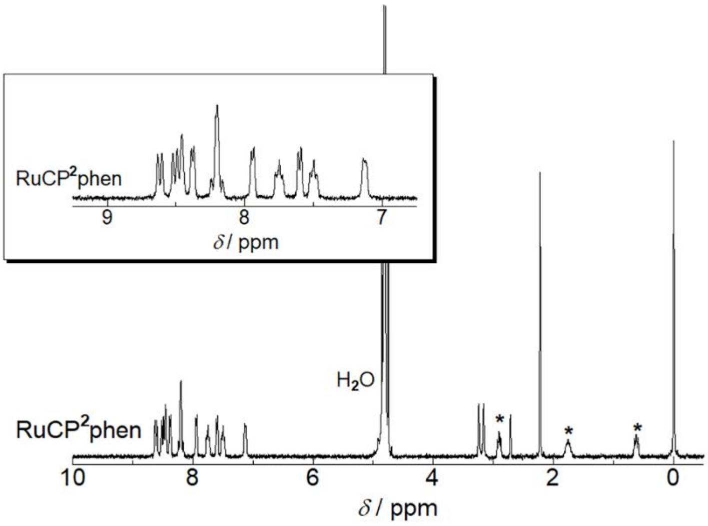

**Figure 2-2-2.** $^1$H NMR spectrum of the **RuCP$^2$phen** in D$_2$O solution. The inset is the magnification of the aromatic region. The peaks marked by asterisk were assigned to the $^1$H signals of the non-deuterated internal standard (DSS = Sodium 2,2-dimethyl-2-silapentane-5-sulfonate).

### 2-2-3 Preparation of Ru(II)-dye-immobilized Pt-$TiO_2$ nanoparticles.

Four kinds of Ru(II)-dye-immobilized Pt-$TiO_2$ nanoparticles (single-PS-layer nanoparticles: **RuCP²**@Pt-$TiO_2$, double-PS-layer nanoparticles: **RuCP²**-Zr-**RuP⁶**@Pt-$TiO_2$, **RuCP²phen**-Zr-**RuP⁶**@Pt-$TiO_2$, and **RuP²**-Zr-**RuP⁶**@Pt-$TiO_2$) were synthesized using the same synthetic procedure as in previous report (Scheme 2-2-3).[50] The amounts of the Ru(II) dyes immobilized on the Pt-$TiO_2$ nanoparticle surface were estimated using X-ray fluorescence spectroscopy and UV-Vis absorption spectroscopy of the supernatant solution (see Figure 2-2-4-2, Table 2-2-4-1, and the "2-2-4 Calculation of the amount of Ru(II) complex immobilized on the Pt-$TiO_2$ nanoparticles" section).

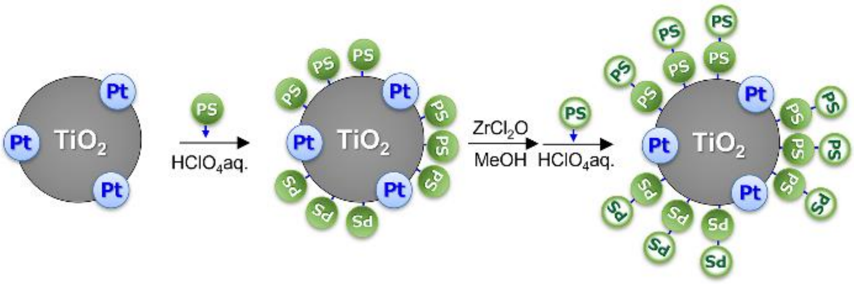

**Scheme 2-2-3.** Layer-by-layer deposition of 1st and 2nd Ru(II) PS dyes on the surface of Pt-$TiO_2$ nanoparticle.

### 2-2-4 Calculation of the amount of Ru(II) complex immobilized on the Pt-$TiO_2$ nanoparticles

To estimate the amount of immobilized Ru(II) complexes on Pt-$TiO_2$ nanoparticle, UV-Vis absorption spectra of each supernatant solution used for the immobilization reaction was measured (see Figure 2-2-4-1 shown below). The Ru(II) complex concentration used for the UV-Vis absorption spectral measurement ($C_A$) is estimated by Equation (1) based on the Lambert-Beer law.

$$A = C_A \cdot l \cdot \varepsilon \quad (Eq.\ 1)$$

$A$ = absorbance, $C_A$ = concentration of the Ru(II) complex,
$l$ = cell path length (1 cm), $\varepsilon$ = molar absorption coefficient

The absorbance at the $^1$MLCT absorption band of each complex (**RuCP$^2$**: 456 nm, **RuP$^2$**: 456 nm, **RuP$^4$**: 462 nm, **RuP$^6$**: 463 nm, **RuCP$^2$phen:** 451 nm, **RuP$^4$phen:** 462 nm) and their corresponding molar absorption coefficients (**RuCP$^2$**: 14,600; **RuP$^2$**: 14,900; **RuP$^4$**: 15,900; **RuP$^6$**: 19,600; **RuCP$^2$phen**: 15,400; **RuP$^4$phen**: 15,300) enable us to estimate the concentration of the Ru(II) complex that was not immobilized in the reaction. Since a 50-fold diluted aqueous solution was used in each measurement, the concentration of the original supernatant solution ($C_B$) is calculated by $C_B = C_A \times 50$. The total volume of the supernatant solution is 6.05 mL (see the Experimental section). Thus, the amount of Ru(II) complexes in the supernatant solution ($M_S$) is estimated by Equation (2).

$$M_s = C_B \times \frac{6.05}{1000}\ (\mathrm{mol}) \quad (Eq.\ 2)$$

Finally, the molar amount of the Ru(II) complex immobilized on the $TiO_2$ surface ($M_i$) can be estimated by Equation (3).

$$M_i = M_o - M_s\ (\mathrm{mol}) \quad (Eq.\ 3)$$

where $M_o$ denotes the molar amount of the Ru(II) complex in the 1.25 mM Ru(II) aqueous solution used for the immobilization reaction. The results are summarized in Table 2-2-4-1.

**Table 2-2-4-1.** Absorbance of each supernatant solution and the calculated $C_B$ and $M_i$ values.

| | **RuCP$^2$**@Pt-TiO$_2$ | **RuP$^6$**@Pt-TiO$_2$ | **RuCP$^2$phen**-Zr-**RuP$^6$**@Pt-TiO$_2$ | |
|---|---|---|---|---|
| | 1st layer (**RuCP$^2$**) | 1st layer (**RuCP$^2$**) | 2nd outer layer (**RuCP$^2$phen**) | 1st inner layer (**RuP$^6$**) |
| $A$ | 0.157 | 0.163 | 0.171 | 0.303 |
| $C_B$ | 0.494 | 0.832 | 0.578 | 0.769 |
| $M_i$ | 4.51 | 2.47 | 4.00 | 2.85 |

| | **RuCP$^2$**-Zr-**RuP$^6$**@Pt-TiO$_2$ | | **RuP$^2$**-Zr-**RuP$^6$**@Pt-TiO$_2$ | |
|---|---|---|---|---|
| | 2nd outer layer (**RuCP$^2$**) | 1st inner layer (**RuP$^6$**) | 2nd outer layer (**RuP$^2$**) | 1st inner layer (**RuP$^6$**) |
| $A$ | 0.166 | 0.341 | 0.115 | 0.341 |
| $C_B$ (mM) | 0.522 | 0.865 | 0.386 | 0.865 |
| $M_i$ | 4.34 | 2.26 | 5.17 | 2.26 |

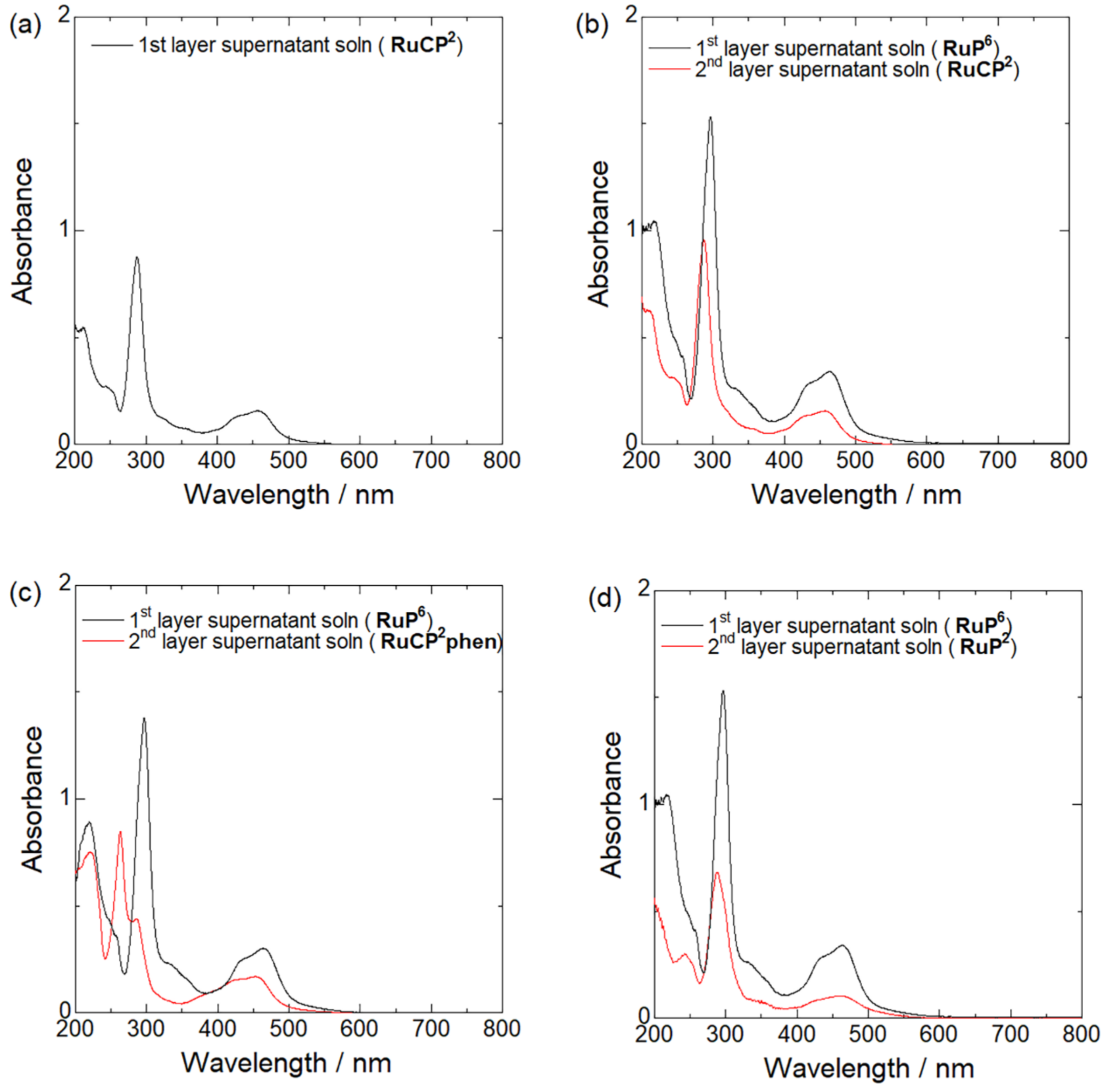

**Figure 2-2-4-2.** UV-vis absorption spectra of the supernatant solutions obtained in the preparation of (a) **RuCP**$^2$@Pt-TiO$_2$, (b) **RuCP**$^2$-Zr-**RuP**$^6$@Pt-TiO$_2$, (c) **RuCP**$^2$**phen**-Zr-**RuP**$^6$@Pt-TiO$_2$, (d) **RuP**$^2$-Zr-**RuP**$^6$@Pt-TiO$_2$ at 298 K. Note that each solution (1 mL) was diluted to 50 mL by the addition of water before the spectral measurement.

### 2-2-5 Calculation of the surface coverage of Ru(II) complexes per unit area of $TiO_2$

Assuming that the $TiO_2$ nanoparticles are spherical, the surface area on the $TiO_2$ nanoparticle ($S_m$) was simply calculated by using Equation (4). In these calculations, the effect of the loaded Pt co-catalyst was omitted.

$$S_m = 4 \cdot \pi \cdot \left(\frac{a}{2} \times 10^{-7}\right)^2 \ (\text{cm}^2 \text{ per one particle}) \quad (Eq. 4)$$

$a$ = Averaged particle diameter of $TiO_2$ nanoparticle (15 nm)

Since the calculated surface area ($S_m$) based on Equation (4) corresponds to only one $TiO_2$ nanoparticle, it is necessary to determine the number of $TiO_2$ nanoparticles ($P_t$) contained in 30 mg to estimate the total surface area of $TiO_2$ ($S_t$) used in the immobilization reaction of the Ru(II) complexes. The total volume of 30 mg of $TiO_2$ nanoparticles ($V_t$) can be calculated using Equation (5) based on the density of $TiO_2$ (anatase $TiO_2$ = 3.90 g/cm$^3$).

$$V_t = \frac{30 \times 10^{-3}\ (\text{g})}{3.90\ (\text{g/cm}^3)} \ (\text{cm}^3) \quad (Eq. 5)$$

The number of $TiO_2$ nanoparticles ($P_t$) in 30 mg is also estimated using Equations (6) and (7) based on the volume of one $TiO_2$ nanoparticle ($V_m$) and the total volume ($V_t$ ).

$$V_m = \frac{4}{3} \cdot \pi \cdot \left(\frac{a}{2} \times 10^{-7}\right)^3 \ (\text{cm}^3 \text{ per one particle}) \quad (Eq. 6)$$

$$P_t = \frac{V_t}{V_m} \quad (Eq. 7)$$

Then, the total surface area of 30 mg of $TiO_2$ ($S_t$) can be estimated by Equation (8).

$$S_t = S_m \times P_t \ (\text{cm}^2) \quad (Eq. 8)$$

The amount of immobilized Ru(II) complexes per unit area of $TiO_2$ (Surface coverage: $N$) is estimated by Equation (9) based on the amount of immobilized Ru(II) complex ($M_i$) and the total surface area of 30 mg of $TiO_2$ ($S_t$). The estimated $N$ and $M_i$ values are summarized in Table 2-2-4-1 and Table2-3-2-1.

$$N = \frac{M_i}{S_t} \ (\text{mol/cm}^2) \quad (Eq.\ 9)$$

### 2-2-6 Measurements

$^1$H and $^{13}$C NMR spectra at room temperature were recorded on JEOL EX-270 and ECZ-400S NMR spectrometers, respectively. UV−vis absorption spectra were recorded using a Shimadzu UV-2400PC spectrophotometer. Luminescence spectra were recorded using a JASCO FP-8600 spectrofluorometer. Each sample solution was deoxygenated by $N_2$ bubbling for 30 min at 298 K. Energy-dispersive XRF spectra were recorded using a Bruker S2 PUMA analyzer. Emission quantum yields ($\Phi_{em}$) were measured using a Hamamatsu C9920-02 absolute photoluminescence quantum yield measurement system equipped with an integrating sphere apparatus and a 150 W continuous-wave xenon light source. Emission lifetimes were measured by using a Quantaurus-Tau C11367 (Hamamatsu Photonics K. K.) excited by a UV LED light source ($\lambda_{ex}$ = 280 nm). Cyclic voltammograms (CV) were recorded using a HOKUTO DENKO HZ-3000 electrochemical measurement system equipped with a Pt wire and Ag/AgCl (in 3 M NaCl aq.) electrode as the counter and reference electrodes, respectively. A glassy carbon electrode ($\varphi$ = 3.0 mm) was used as the working electrode. Powder X-ray diffraction studies were performed using a Rigaku SPD diffractometer at beamline BL-8B of the Photon Factory, KEK, Japan. The wavelength of the synchrotron X-ray was 1.537(1) Å.

### 2-2-7 Photocatalytic water reduction reaction.

Under dark conditions, an aqueous solution of sacrificial electron donor (SED) L-ascorbic acid (0.5 or 0.02 M) and a pH buffer (0.5 M, pH = 2, 4, or 6) solution containing the Ru(II)-dye-immobilized nanoparticles (100 μM of the Ru(II) dye) were placed into a custom-built quartz cell equipped with a Schlenk flask (volume: 265 mL), along with a small magnetic stirring bar. Each sample flask was doubly sealed with rubber septa. The solution was deoxygenated by Ar bubbling for 1 h. The flask was then irradiated from the bottom with a blue LED lamp ($\lambda$ = 470 ± 10 nm; 70 mW; Opto Device Lab. Ltd., OP6-4710HP2). The temperature was controlled at 293 K using a custom-built aluminum water-cooling jacket with a water-circulating temperature controller (EYELA CCA-1111). The gas samples (0.6 mL) for each analysis were collected from the headspace using a gastight syringe (Valco Instruments Co. Inc.). The amount of evolved $H_2$ was determined using gas chromatography (Agilent 490 Micro Gas Chromatograph). The TON and TOF were estimated from the amount of evolved $H_2$; two photoredox cycles of the Ru(II) PS dye are required to produce one $H_2$ molecule. Each photocatalytic $H_2$ evolution reaction was carried out under the same conditions three times, and the average value with standard deviation was reported. The apparent quantum yield (AQY) was calculated using the following equation.

$$AQY = N_e / N_p = 2N_{H2} / N_p$$

Here, $N_e$ stands for the number of reacted electrons, $N_{H2}$ is the number of the evolved $H_2$ molecules, and $N_p$ is the number of incident photons.

## 2-3 Results and Discussion

### 2-3-1 Photophysical and electrochemical properties of Ru(II) dyes.

To investigate the effect of substituting the phen ligand on the photophysical properties of the $[Ru(bpy)_3]^{2+}$-type chromophores, the UV-vis absorption and emission spectra of **RuCP$^2$phen** in aqueous solution were measured. The results are shown in Figure 2-3-1-1 and the photophysical properties are summarized in Table 2-3-1-1 in comparison with those of the other Ru(II) photosensitizers measured in the same condition. All four complexes exhibited the two characteristic absorption bands of the $[Ru(bpy)_3]$-type moiety, a π-π* absorption band at around 300 nm and a singlet metal-to-ligand charge-transfer ($^1$MLCT) absorption band at around 460 nm. In the emission spectra, a broad emission band attributable to triplet MLCT ($^3$MLCT) phosphorescence was also observed in the 615-650 nm region. The feature of the absorption spectrum of **RuCP$^2$phen** below 300 nm was different from those of the complexes without the phen ligand, probably due to the π-π* absorption band of the phen ligand. On the other hand, the shapes of $^1$MLCT absorption band of **RuCP$^2$phen** was almost identical to those of the other complexes. It should be noted that the $^1$MLCT band positions of the **RuCP$^2$** and **RuCP$^2$phen** were clearly blue-shifted by about 7 and 12 nm to that of **RuP$^6$**. These blue shifts can be ascribed to the electron-donating nature of the methylene spacer between the bpy ligand and the phosphonic acid group. The larger blue shift of **RuCP$^2$phen** compared to **RuCP$^2$** was attributed to the stronger π-accepting ability of the phen ligand, which stabilized the $t_{2g}$ orbital of the Ru(II) ion. In fact, the Ru(III)/Ru(II) redox couple of **RuCP$^2$phen** occurred at slightly more positive potentials than that of **RuCP$^2$** (see Figure 2-3-1-2 and Table 2-3-1-2). Similarly, the wavelengths of the $^3$MLCT phosphorescence emission maxima followed the order **RuCP$^2$phen** < **RuCP$^2$** < **RuP$^6$** < **RuP$^2$** (see Table 2-3-1-1). The $^3$MLCT emission energy of **RuCP$^2$phen** was higher than that of **RuCP$^2$** due to the stronger π-accepting ability of the phen ligand, as discussed in an early paper by Crosby et al.[51] on $[Ru(bpy)_{3-n}(phen)_n]^{2+}$ (n = 1-3) complexes.

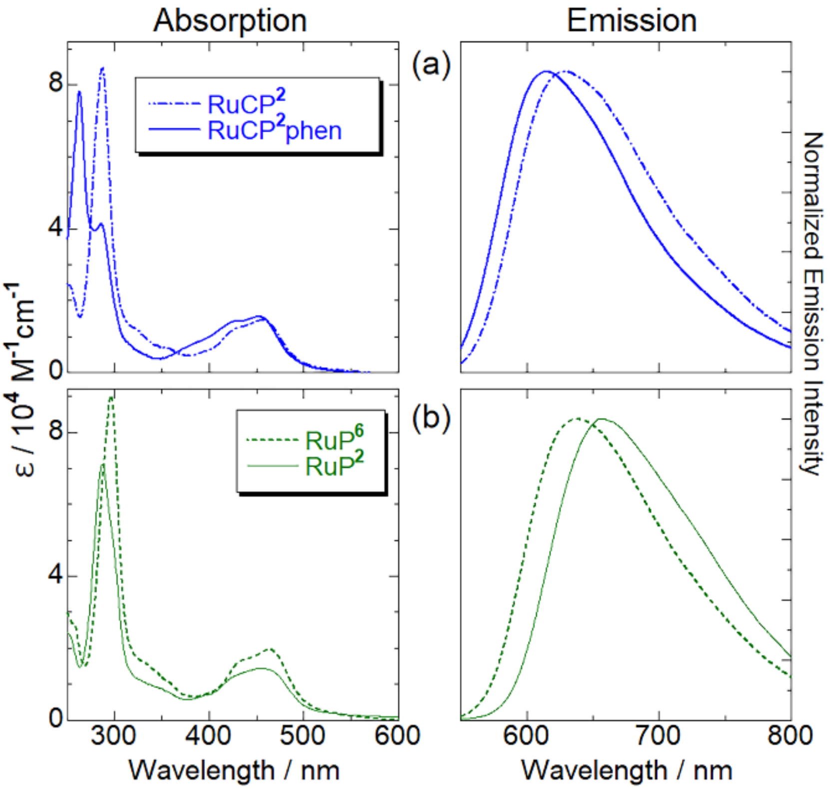

**Figure 2-3-1-1.** (left) UV-Vis absorption and (right) emission spectra ($\lambda_{ex}$ = 470 nm) of the (a) **RuCP$^2$** (blue chain lines), **RuCP$^2$phen** (blue solid lines), (b) **RuP$^6$** (green dotted lines), and **RuP$^2$** (green solid lines) complexes in an aqueous solution of 0.38 M phosphonate buffer (pH = 2.2) at 293 K.

**Table 2-3-1-1.** Photophysical data of Ru(II) complexes.

| Ru(II) PS | $\lambda_{abs}$ (nm) | $\lambda_{em}{}^{a}$ (nm) | $\tau_{em}{}^{b}$ (ns) | $\Phi^{c}$ | $k_r{}^{d}$ ($10^5$s$^{-1}$) | $k_{nr}{}^{e}$ ($10^5$s$^{-1}$) |
|---|---|---|---|---|---|---|
| **RuCP$^2$** | 287, 456 | 629 | 512 | 0.07 | 1.36 | 18.2 |
| **RuCP$^2$phen** | 263, 286, 451 | 614 | 1029 | 0.11 | 1.09 | 8.62 |
| **RuP$^6$** | 297, 463 | 639 | 571 | 0.09 | 1.54 | 16.0 |
| **RuP$^2$** | 286, 456 | 656 | 395 | 0.06 | 1.49 | 23.8 |

[a] Emission maximum; [b] emission lifetime; [c] photoluminescence quantum yield. [d] Radiative rate constants ($k_r$) were estimated using the equation $\Phi/\tau_{em}$. [e] Nonradiative rate constants ($k_{nr}$) were estimated using the equation $k_r(1 - \Phi)/\Phi$.

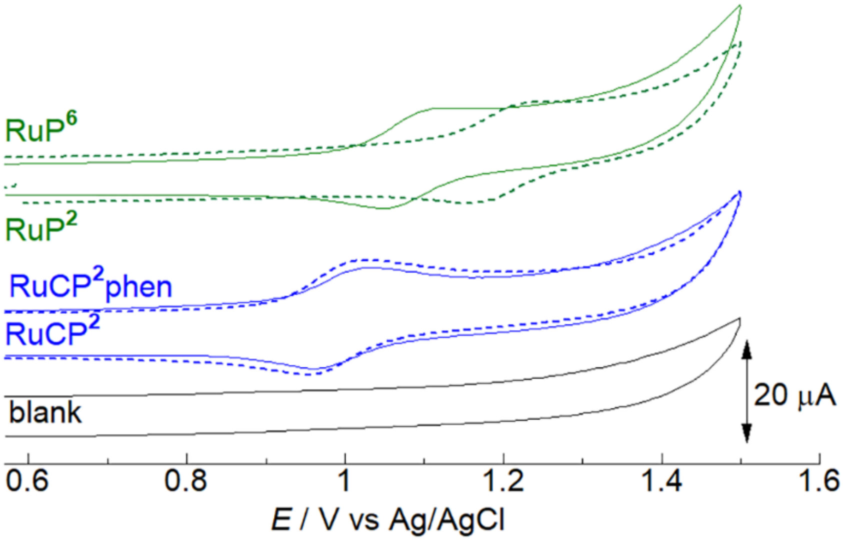

**Figure 2-3-1-2.** Cyclic voltammograms of 1 mM **RuP$^2$** (green solid line), **RuP$^6$** (green broken line), **RuCP$^2$phen** (blue solid line) and **RuCP$^2$** (blue broken line) in 0.5 M $NaClO_4$ electrolyte aqueous solution (pH = 2.2, 0.1 M phosphate buffer). Glassy carbon, Pt wire and Ag/AgCl (in 3 M NaCl aq.) were used as the working, counter and reference electrodes, respectively.

The emission lifetimes ($\tau$) and quantum yields ($\Phi$) of **RuCP$^2$phen** in aqueous solution was evaluated to estimate the effect of substituting the phen ligand for bpy. Figure 2-3-1-3 shows the emission decay curves for each of the Ru complexes, and their photophysical parameters, including radiative and nonradiative rate constants ($k_r$ and $k_{nr}$), are summarized in Table 2-3-1-2. The lifetime and luminescence quantum yield of **RuCP$^2$phen** were longer and higher than those of the bpy-analogue **RuCP$^2$**. Considering the fact that the $k_r$ values of all the four Ru(II) complexes were almost constant at $1\times10^5$ s$^{-1}$, the $k_{nr}$ value of **RuCP$^2$phen** was remarkably smaller than those of the bpy analogue. This was probably because vibrational deactivation from the $^3$MLCT excited state was suppressed by the introduction of the more rigid phen ligand(s).

**Table 2-3-1-2**. Photoelectrochemical properties of Ru(II) dyes used in this work.

| Complex | $\lambda_{abs}$ / nm | $\lambda_{em}$ $^a$ / nm | $\tau_{em}$ $^b$ / ns | $\Phi$ $^c$ | $k_r$ $^d$ / $10^5$ s$^{-1}$ | $k_{nr}$ $^e$ / $10^5$ s$^{-1}$ | $E_{ox}$ $^f$ / V $_{vs\ NHE}$ | $E^*_{ox}$ $^g$ / V $_{vs\ NHE}$ |
|---|---|---|---|---|---|---|---|---|
| **RuCP$^2$** | 287, 456 | 629 | 512 | 0.07 | 1.36 | 18.2 | 1.19 | -0.79 |
| **RuCP$^2$phen** | 263,<br>286, 451 | 614 | 1029 | 0.11 | 1.09 | 8.62 | 1.20 | -0.82 |
| **RuP$^6$** | 297, 463 | 639 | 571 | 0.09 | 1.54 | 16.0 | 1.40 | -0.55 |
| **RuP$^2$** | 286, 456 | 656 | 395 | 0.06 | 1.49 | 23.8 | 1.29 | -0.61 |

$^a$ Emission maximum; $^b$ emission lifetime; $^c$ photoluminescence quantum yield. $^d$ Radiative rate constants ($k_r$) were estimated using the equation $\Phi/\tau_{em}$. $^e$ Nonradiative rate constants ($k_{nr}$) were estimated using the equation $k_r(1-\Phi)/\Phi$. $^f$ Estimated by CV measurement (Figure 2-3-1-2) and the potentials were converted to the value referred to the NHE standard. $^g$ $E^*_{ox}$ was estimated using the following equation: $E^*_{ox} = E_{ox} - E_{00}$, where $E_{00}$ was approximated as $\lambda_{em}$.

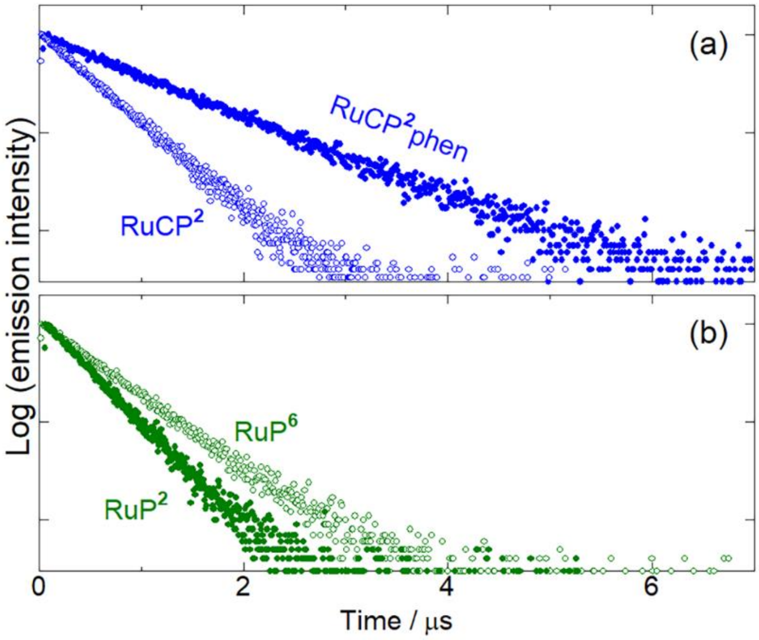

**Figure 2-3-1-3.** Emission decays of (a) **RuCP$^2$** (blue open circles), **RuCP$^2$phen** (blue closed circles), (b) **RuP$^6$** (green open circles) and **RuP$^2$** (green closed circles) complexes in the 0.38 M phosphonate buffer (pH = 2.2) aqueous solution at 298 K ($\lambda_{ex}$ = 280 nm).

### 2-3-2 Characterization of Ru(II)-dye-immobilized Pt-$TiO_2$ nanoparticles

In order to qualitatively estimate the amount of Ru(II) photosensitizer immobilized, the supernatant solutions were separated from the immobilization reactions, and the UV-Vis absorption spectra of the solutions were measured (see Figure 2-3-2-1). The amount of Ru (II) complex immobilized was calculated by subtracting the amount of the Ru(II) complex remaining in the supernatant solution from the initial amount (see "Calculation of the amount of Ru(II) complex immobilized on the Pt-$TiO_2$ nanoparticles" section in the section 2-2-4). Each supernatant solution exhibited almost the identical spectrum to that of the immobilizing PS. For example, two supernatant solutions obtained in the preparation of **RuCP$^2$phen**-Zr-**RuP$^6$**@Pt-$TiO_2$ showed completely different spectra to each other (see, Figure 2-2-4-2(c)), suggesting that the **RuP$^6$** immobilized on the 1st layer hardly desorbed in the next immobilization reaction of the 2nd **RuCP$^2$phen** PS layer. Table 2-3-2-1 shows the amount of Ru(II) photosensitizer immobilized per 1 mg of $TiO_2$ nanoparticles. This analysis clearly indicated that the amount of Ru(II) complex immobilized was increased by the formation of multilayered structures via $Zr^{4+}$ cation binders. The amount of the Ru(II) complex immobilized directly on the surface of the Pt-$TiO_2$ nanoparticles (*i.e.*, the 1st layer) decreased in the order **RuCP$^2$** > **RuP$^6$**, probably based on the molecular size and charge of the Ru(II) photosensitizers. The **RuCP$^2$** has only two phosphonic acid anchors, while **RuP$^6$** has six anchoring groups. The molecular volume of the Ru(II) photosensitizer and the electrostatic repulsion between immobilized Ru(II) photosensitizers should be increased and enhanced with an increasing number of phosphonic acid groups. As a result, the amount of Ru(II) PS immobilized on the surface of the Pt-$TiO_2$ nanoparticles decreased in the order given above. To examine whether the surface of Pt-$TiO_2$ was fully covered by Ru(II) molecules or not, a second immobilization reaction using **RuP$^6$** was carried out under the same conditions as the first reaction (Figure 2-3-2-1). The absorption spectrum of the supernatant solution obtained after the second immobilization reaction was almost identical to the spectrum obtained before the immobilization reaction, indicating that the surface of the Pt-$TiO_2$ nanoparticles was already completely covered with **RuP$^6$** molecules to form the inner Ru(II) PS layer, and that further immobilization without the $Zr^{4+}$ cation binder was negligible.

**Table 2-3-2-1.** Amount of Ru(II) PS immobilized on the Pt-$TiO_2$ nanoparticle surface.

| | Amount of immobilized Ru(II) PS (nmol / 1 mg $TiO_2$) [a] | | |
|---|---|---|---|
| Photocatalyst | $2^{nd}$ outer layer | $1^{st}$ inner layer | Total |
| **RuCP$^2$**@Pt-$TiO_2$ | - | 150 | 150 |
| **RuCP$^2$**-Zr-**RuP$^6$**@Pt-$TiO_2$ | 145 | 75.3 | 220 |
| **RuP$^2$**-Zr-**RuP$^6$**@Pt-$TiO_2$ | 172 | 75.3 | 247 |
| **RuCP$^2$phen**-Zr-**RuP$^6$**@Pt-$TiO_2$ | 133 | 95.0 | 228 |

[a] Estimated based on the absorbance observed in the UV-Vis spectra of each supernatant solution (see Figure 2-2-4-2).

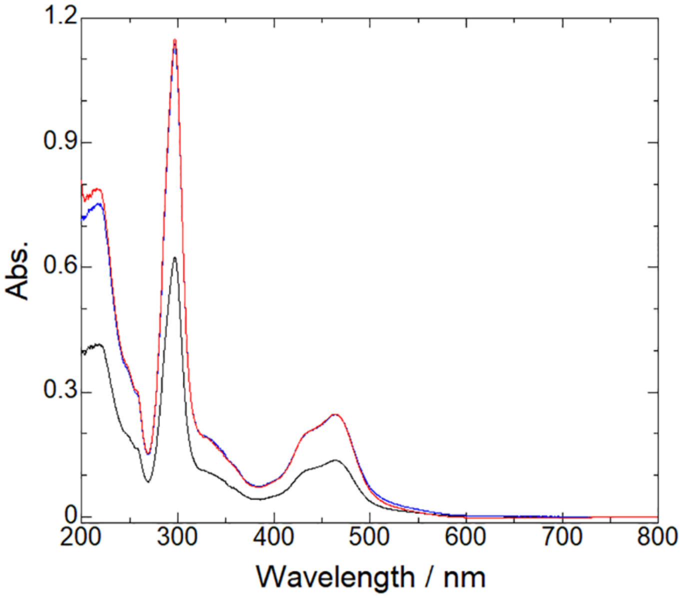

**Figure 2-3-2-1.** UV-Vis absorption spectra of the supernatant solutions obtained from the preparation of **RuP$^6$**@Pt-$TiO_2$ (black line) and **RuP$^6$**(excess)@Pt-$TiO_2$ (red line) at 298 K. Blue line shows the spectrum of the stock **RuP$^6$** solution. The nanoparticle **RuP$^6$**(excess)@Pt-$TiO_2$ was prepared by immersing **RuP$^6$**@Pt-$TiO_2$ again in the 1.25 mM **RuP$^6$** solution (the same concentration to that used in the first immobilization reaction of **RuP$^6$**). Note that each supernatant solution (1 mL) was diluted to 50 mL by the addition of water before the spectral measurement.

Although the immobilized amounts of the Ru(II) PS functionalized with two phosphonates (**RuP$^2$**, **RuCP$^2$**, and **RuCP$^2$phen**) in the 2nd outer layer of double-PS-layer nanoparticles were comparably small, but interesting difference was observed, that is, the amount was increased in the order of **RuCP$^2$phen** < **RuCP$^2$** < **RuP$^2$**. This trend could be also ascribable to the molecular volumes of these Ru(II) PS dyes; the introduction of the methylene spacer and phen ligand to **RuP$^2$** moiety should increase the molecular volume, resulting in the lower immobilized amount. On the other hand, the amount of each Ru(II) complex immobilized in the 2nd outer layer was comparable to that in the 1st PS layer of the single-PS-layer nanoparticle, **RuCP$^2$**@Pt-$TiO_2$, that was immobilized directly on the surface of the Pt-$TiO_2$ nanoparticles. Thus, these results suggest that the $Zr^{4+}$ cation was a suitable binder to build multilayered photosensitizing structures. Note that the sizes of $TiO_2$ nanoparticle and Pt cocatalyst were hardly changed during the PS immobilization reactions as suggested by the PXRD pattern of **RuCP$^2$phen**-Zr- **RuP$^6$**@Pt-$TiO_2$ nanoparticle that was almost identical to that of Pt-$TiO_2$ nanoparticle (Figure 2-3-2-2 and Table 2-3-2-2).

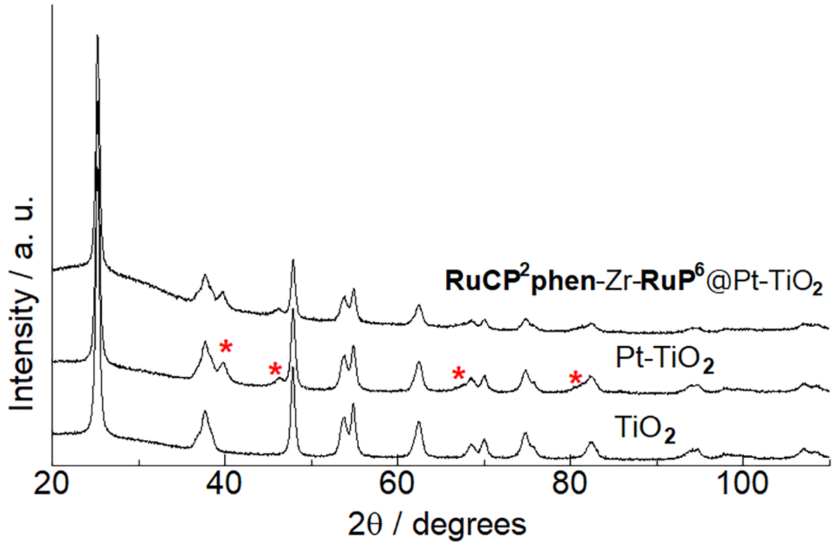

**Figure 2-3-2-2.** PXRD patterns of $TiO_2$, Pt-$TiO_2$, and **RuCP$^2$phen-Zr-RuP$^6$**@ Pt-$TiO_2$, nanoparticles in the solid state. The red asterisks show the diffraction peaks derived from Pt cocatalyst loaded on the surface of $TiO_2$ nanoparticle.

**Table 2-3-2-2**. Estimated particle diameters of $TiO_2$ and Pt cocatalyst.

| Photocatalyst | $TiO_2$ (nm)[a] | Pt (nm)[a] |
|---|---|---|
| $TiO_2$ | 21.28(11) | - |
| Pt-$TiO_2$ | 21.22(12) | 6.7(19) |
| **RuCP$^2$phen**-Zr-**RuP$^6$**@Pt-$TiO_2$ | 21.16(14) | 6.0(12) |

[a] Diameters were estimated based on the diffraction peaks observed at 25.2° for $TiO_2$ and 46.2° for Pt cocatalyst (Figure 2-3-2-2). The peak fitting was done by Pseudo Volgt function.

### 2-3-4 Photocatalytic $H_2$ evolution reaction.

In previous study, the energy and electron transfer processes in the PS multilayers were found to have a strong effect on the photocatalytic $H_2$ evolution activity in high SED concentration.[50] To further investigate the importance of the energy and electron transfer processes in the double-layered PS structure, photocatalytic hydrogen generation experiments were performed using three different double-PS-layer nanoparticles in several different conditions.

At first, the photocatalytic $H_2$ evolution reactions in the presence of a dilute (20 mM) L-ascorbic acid solution were carried out to elucidate the effect of the SED concentration (Figure 2-3-4-1(a)), because the low concentration of the SED should be suitable condition to evaluate the lifetime of photo-induced charge-separated state of the photocatalyst. To remove the influence of the change in the proton concentration, a 0.5 M acetate buffer (pH = 4) was used. The estimated turn over number (TON), turn over frequency (TOF) per one Ru(II) PS and the apparent quantum yield (AQY) are listed in Table 2-3-4-1.

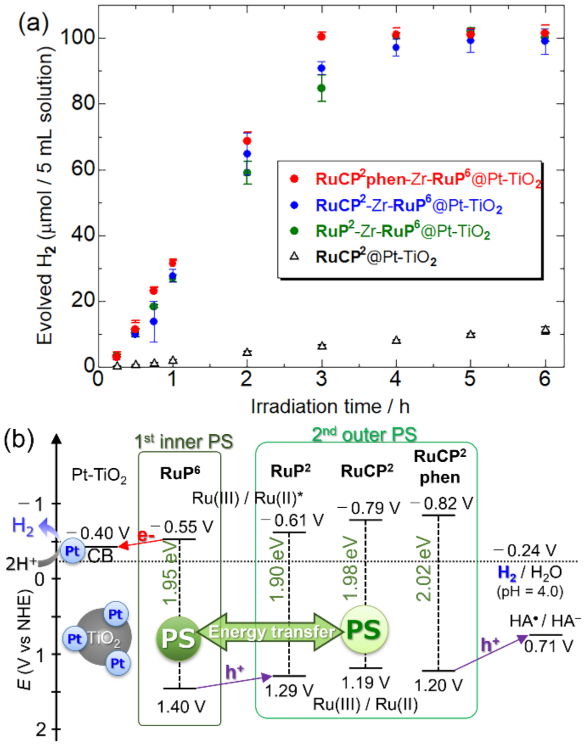

**Figure 2-3-4-1.** (a) Photocatalytic water reduction reaction driven by **RuCP$^2$phen**-Zr-**RuP$^6$**@Pt-TiO$_2$ (red circles), **RuCP$^2$phen-** Zr-**RuP$^6$**@Pt-TiO$_2$ (blue circles), **RuP$^2$**-Zr-**RuP$^6$**@Pt-TiO$_2$ (green circles), and **RuCP$^2$**@Pt-TiO$_2$ (black open triangle) (100 µM of the Ru(II) complex) in a 20 mM L-ascorbic acid sacrificial electron donor aqueous solution (pH = 4, 0.5 M acetate buffer) under an Ar atmosphere (λ = 470 ± 10 nm). (b) Schematic energy diagrams of the double-PS-layer photocatalysts used in these experiments. The values in green are the $^3$MLCT emission energies of the Ru(II) PS dyes. The position of the conduction band minimum of bulk TiO$_2$ was inferred from the literature.[57]

**Table 2-3-4-1.** Results of the photocatalytic H$_2$ evolution reactions in 20 mM L-ascorbic acid solution.

| Photocatalyst | pH | H$_2$ (µmol) | TON$^{a,b}$ | TOF$^b$ | AQY (%)$^a$ |
|---|---|---|---|---|---|
| **RuCP$^2$**@Pt-TiO$_2$ | 4.0 | 6.20 | 24.8 | 9.08 | 0.417 |
| **RuP$^2$**-Zr-**RuP$^6$**@Pt-TiO$_2$ | 4.0 | 84.7 | 339 | 120 | 5.70 |
| **RuCP$^2$**-Zr-**RuP$^6$**@Pt-TiO$_2$ | 4.0 | 92.0 | 366 | 136 | 6.19 |
| **RuCP$^2$**-Zr-**RuP$^6$**@Pt-TiO$_2$ (2$^{nd}$)$^c$ | 4.0 | 66.9 | 226 | 82.4 | 4.50 |
| **RuCP$^2$phen**-Zr-**RuP$^6$**@Pt-TiO$_2$ | 4.0 | 100 | 401 | 143 | 6.73 |
| **RuCP$^2$phen**-Zr-**RuP$^6$**@Pt-TiO$_2$ | 2.0 | 65.0 | 260 | 95.6 | 4.38 |
| **RuCP$^2$phen**-Zr-**RuP$^6$**@Pt-TiO$_2$ | 6.0 | 58.9 | 236 | 91.6 | 3.97 |

[a] After 3 h irradiation. [b] TON and TOF (averaged over 0.25 to 3 hours of irradiation) were calculated based on the Ru(II) photosensitizer. [c] The recycled nanoparticle photocatalyst by ultracentrifugation was used.

Interestingly, the estimated TOF values of all the three double-PS-layer nanoparticles **RuP$^2$**-Zr-**RuP$^6$**@Pt-TiO$_2$, **RuCP$^2$**-Zr-**RuP$^6$**@Pt-TiO$_2$ and **RuCP$^2$phen**-Zr-**RuP$^6$**@Pt-TiO$_2$ exhibited remarkably higher activity by about 13 times than that of the single-PS-layer nanoparticle **RuCP$^2$**@Pt-TiO$_2$ in this condition. It should be noted that these values of double-PS-layer nanoparticles were comparable to the TOF in the 25-times higher SED conditions (0.5 M L-ascorbic acid solution, see Figure 2-3-4-2). In contrast, the activity of single-PS-layer photocatalyst **RuCP$^2$**@Pt-TiO$_2$ was only about 17% of the activity obtained under the 0.5 M SED conditions.[50] The significant decrease in the photocatalytic activity of **RuCP$^2$**@Pt-TiO$_2$ should be due to the slower electron donation from the SED. In the 0.5 M ascorbic acid aqueous solution, the one-electron oxidized **RuCP$^2$(ox)** photosensitizer could quickly be recovered to the original Ru(II) state by electron donation from the L-ascorbic acid. However, in the diluted conditions, the electron donation from L-ascorbic acid could become slow enough to compete with the back-electron transfer from the conduction band of TiO$_2$, resulting in the remarkably lower photocatalytic activity. The double-PS-layer photocatalysts were able to retain comparably high activity even in the low SED conditions due to the spatial charge-separation in their doubly-layered structures, that is, the hole generated by electron injection could migrate from the inner to the outer PS layer via the Ru(III)/Ru(II) redox potential gradient.

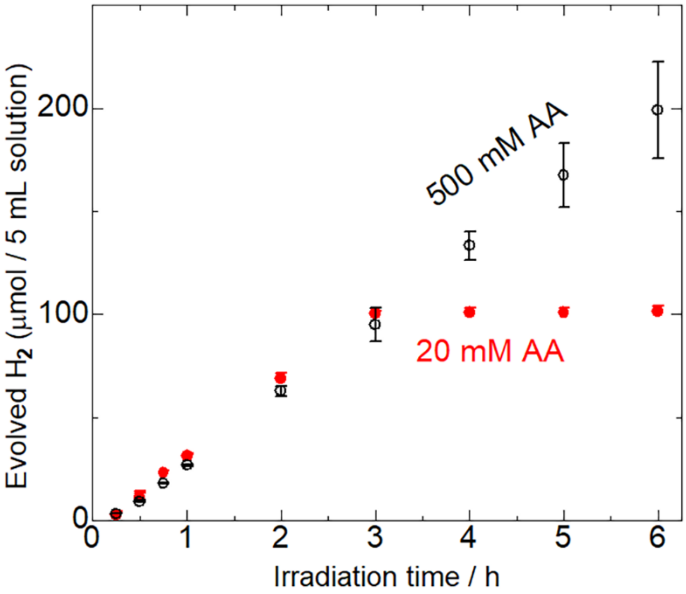

**Figure 2-3-4-2**. SED concentration dependence of the photocatalytic H$_2$ evolution reaction driven by **RuCP$^2$phen**-Zr-**RuP$^6$**@Pt-TiO$_2$ (100 μM of the Ru(II) complex) in 20 mM (red, pH = 4) or 0.5 M (black, pH = 2.2) L-ascorbic acid sacrificial electron donor aqueous solutions (0.5 M acetate buffer) under an Ar atmosphere. A blue LED light (λ = 470 ± 10 nm) was used as the irradiation source.

Although the activity of double-PS-layer nanoparticles were comparable, the activity slightly increased in the order of **RuP$^2$**-Zr-**RuP$^6$**@Pt-TiO$_2$ < **RuCP$^2$**-Zr-**RuP$^6$**@Pt-TiO$_2$ < **RuCP$^2$phen**-Zr-**RuP$^6$**@Pt-TiO$_2$. The slightly lower activity of **RuP$^2$**-Zr-**RuP$^6$**@Pt-TiO$_2$ was probably due to a mechanistic difference in the charge separation of these two photocatalysts. The excitation energy transfer from the inner to outer layer should be thermodynamically favorable in **RuP$^2$**-Zr-**RuP$^6$**@ Pt-TiO$_2$ (Figure 2-3-4-1(b)). In this case, not only the electron transfer (oxidative) quenching of the Pt-TiO$_2$ nanoparticle, but also the reductive quenching by L-ascorbic acid, could possibly contribute to the H$_2$ evolution reaction. Thus, the reductive quenching pathway should be slower in the lower SED concentration, reducing the photocatalytic activity of **RuP$^2$**-Zr-**RuP$^6$**@Pt-TiO$_2$. In contrast, such reductive quenching would be negligible in **RuCP$^2$**-Zr-**RuP$^6$**@Pt-TiO$_2$ and **RuCP$^2$phen**-Zr-**RuP$^6$**@Pt-TiO$_2$, because the energy transfer in the opposite direction, from the outer **RuCP$^2$** or **RuCP$^2$phen** to the inner **RuP$^6$**, should be more thermodynamically favorable (Figure 2-3-4-1(b)). In addition, the smaller difference of Ru(III)/Ru(II) redox potentials between the outer and inner PS dyes of **RuP$^2$**-Zr-**RuP$^6$**@Pt-TiO$_2$ (0.11 V) than the others might make the hole transfer slower. As a result, the TOF observed for **RuP$^2$**-Zr-**RuP$^6$**@Pt-TiO$_2$ was slightly lower than that of the other two double-PS-layer nanoparticles. The activity of **RuCP$^2$phen**-Zr-**RuP$^6$**@Pt-TiO$_2$ was slightly higher than that of **RuCP$^2$**-Zr-**RuP$^6$**@Pt-TiO$_2$, implying that more thermodynamically favourable energy transfer process from outer **RuCP$^2$phen** to the inner **RuP$^6$** might give the positive effect (Table 2-3-4-1 and Figure 2-3-4-1(a)). The photocatalytic H$_2$ evolution reactions driven by the double-PS-layer photocatalysts were completely terminated after 3 or 4 h of light irradiation, as all the SED in the reaction solution (100 μmol) had been consumed as a two-electron reducing reagent to evolve an equimolar amount of H$_2$. The complete consumption of L-ascorbic acid SED to form the two-electron oxidized species, dehydroascorbic acid, was also evidenced by the change of $^{13}$C NMR spectrum (Figure 2-3-4-3). Surprisingly, all the three photocatalysts showed almost constant H$_2$ evolution rates, even in the region where almost all the SED had been consumed. These results clearly indicate that the double-PS-layered structure is an effective and promising method to suppress the back-electron transfer process. The stability of **RuCP$^2$**-Zr-**RuP$^6$**@Pt-TiO$_2$ was further examined by the 2nd photocatalytic H$_2$ evolution reaction in which the same nanoparticle was recycled by ultracentrifugation of the reaction solution used in the 1st reaction (Figure 2-3-4-4(a) and Table 2-3-4-1). The activity in the 2nd cycle decreased to about 60% of the 1st cycle, but the value was still 9 times higher than that of single-PS-layer photocatalyst **RuCP$^2$**@Pt-TiO$_2$. The reason should be due to the partial release of outer **RuCP$^2$** PS from the nanoparticle surface as suggested by the emission spectra of the supernatant solution obtained in the ultracentrifugation (Figure 2-3-4-4(b)). Notably, the emission spectrum was almost identical to that of **RuCP$^2$** but not to **RuP$^6$** immobilized directly on the Pt-TiO$_2$ surface. Thus, the Zr$^{4+}$ cation binding would effectively suppress the desorption of **RuP$^6$** PS in the 1st inner layer.

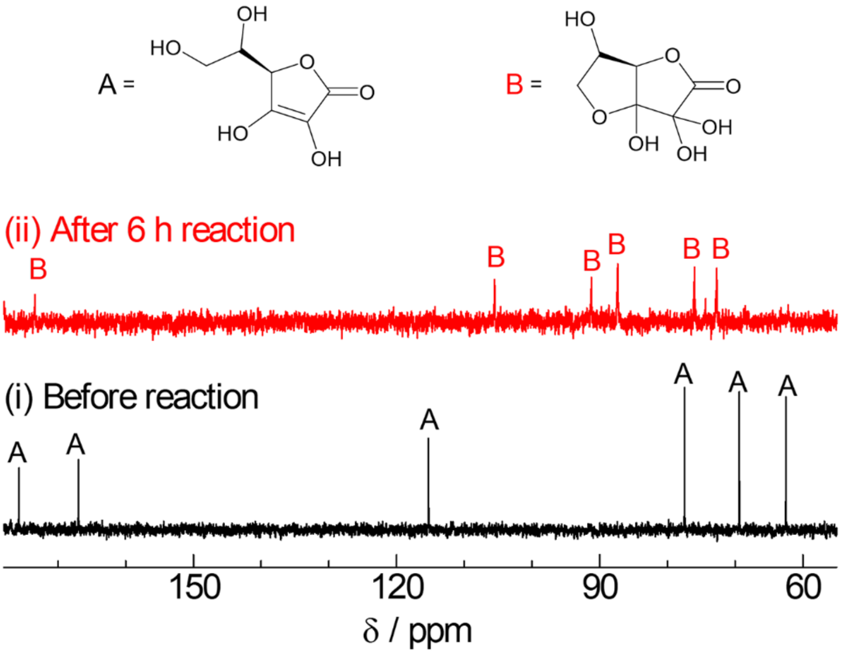

**Figure 2-3-4-3.** $^{13}$C NMR spectral change of the solution containing **RuCP$^2$phen**-Zr-**RuP$^6$**@Pt-TiO$_2$ ([Ru] = 100 μM), and L-ascorbic acid (20 mM) in the 0.5 M acetate buffer aqueous solution (pH = 4) (i) before and (ii) after 6 h light irradiation. A blue LED light (λ = 470 ± 10 nm) was used as the irradiation source. Label for resonances are as follows: (A) ascorbic acid, and (B) hydrate dehydroascorbic acid.

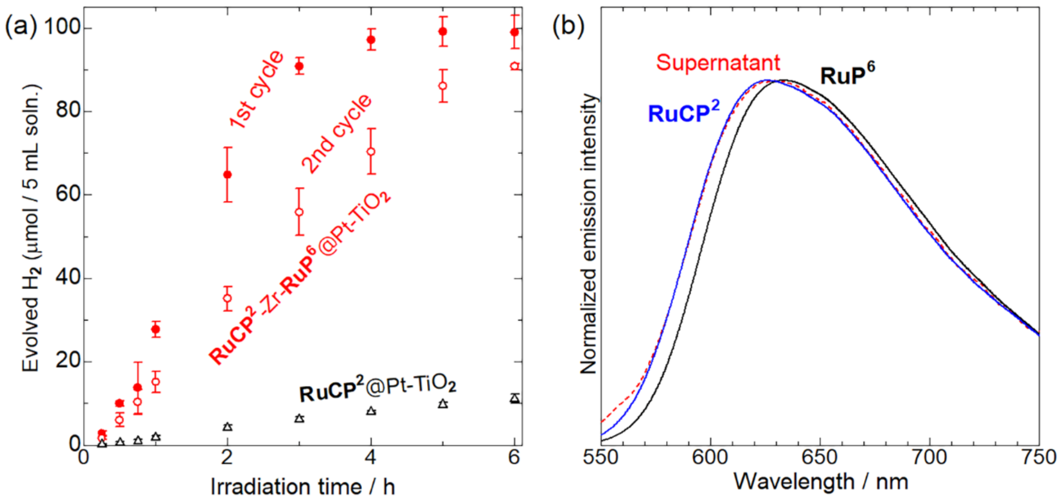

**Figure 2-3-4-4**. (a) Photocatalytic $H_2$ evolution reactions driven by **RuCP$^2$**-Zr-**RuP$^6$**@Pt-TiO$_2$ (red circles) and **RuCP$^2$**@Pt-TiO$_2$ (black triangles) (100 μM of the Ru(II) complex for the 1st cycle) in a 20 mM L-ascorbic acid sacrificial electron donor aqueous solution (pH = 4, 0.5 M acetate buffer) under an Ar atmosphere. The closed and open red circles show the results of photocatalytic $H_2$ evolution reaction of **RuCP$^2$**-Zr-**RuP$^6$**@Pt-TiO$_2$ in 1st and 2nd cycles, respectively. (b) Emission spectrum of the supernatant solution (red dotted line) obtained by the ultracentrifugation of the 1st reaction solution of **RuCP$^2$**-Zr-**RuP$^6$**@Pt-TiO$_2$ after 6 h irradiation. Blue and black solid lines show the spectra of **RuCP$^2$** and **RuP$^6$** in aqueous solutions.

In the photocatalytic $H_2$ evolution reaction, the pH of the aqueous solution is an important factor in the catalytic activity. For example, Natali reported that the photocatalytic activity of a homogeneous system composed of $[Ru(bpy)_3]^{2+}$ as a photosensitizer, $[Co(dmg)_2(py)Cl]$ ($H_2$dmg = dimethylglyoxime) as a $H_2$ evolving catalyst, and L-ascorbic acid as a sacrificial reducing agent strongly depended on the pH, and was the highest at pH = 5.[58] Therefore, the pH dependence of the photocatalytic $H_2$ evolution activity of a nanoparticle photocatalyst with a double-PS-layer structure, **RuCP$^2$phen**-Zr-**RuP$^6$**@Pt-$TiO_2$ was investigated. Figure 2-3-4-5 shows the results of the photocatalytic $H_2$ evolution reaction at pH = 2, 4, and 6; the estimated TON and TOF values are listed in Table 2-3-4-1. The concentration of L-ascorbic acid was set to 20 mM, which was about one-twenty-fifth that of the buffer concentration, to avoid significant pH change during the reaction. **RuCP$^2$phen**-Zr-**RuP$^6$**@Pt-$TiO_2$ exhibited the highest activity at pH 4, consuming all the ascorbic acid within only 3 h of light irradiation. On the other hand, at pH 2 and 6, a TOF decrease of about 35% was observed. As described above, the redox potential of L-ascorbic acid strongly depends on the number of protons in the solution. Its redox potential in the neutral state ($H_2A$) is 1.17 V vs NHE; this potential decreases to 0.71 V in its singly deprotonated state ($HA^-$). Since the first dissociation constant (pKa) of L-ascorbic acid is 4.1, most of the ascorbic acid exists in the neutral $H_2A$ state at pH 2, and about half is converted to the singly deprotonated $HA^-$ state at pH 4. At pH 6, most of the ascorbic acid exists in the $HA^-$ state. Therefore, the reason that the highest TOF was observed at pH 4 was probably because the reducing ability of $HA^-$ is higher than that of $H_2A$ at pH 2, which promotes electron donation to the photosensitizer. On the other hand, at pH 6, most of the ascorbic acid was in the $HA^-$ state, but the proton concentration had decreased to only 1% of that at pH 4. As a result, the photocatalytic activity decreased because of the lower concentration of the reaction substrate ($H^+$).

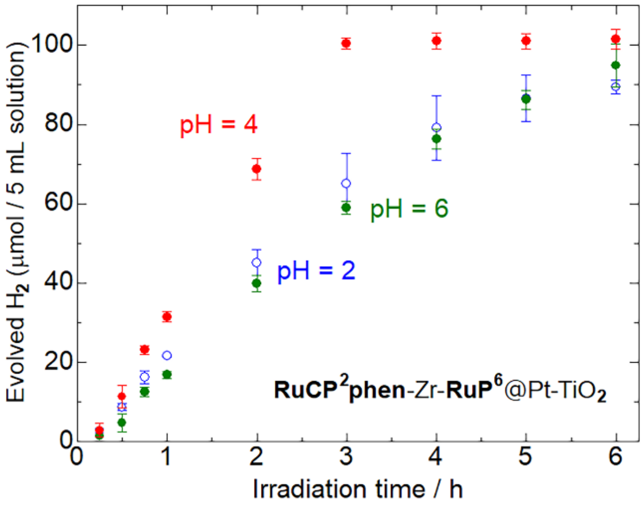

**Figure 2-3-4-5**. pH dependence of the photocatalytic water reduction reaction of the double-PS-layer nanoparticle photocatalyst **RuCP$^2$phen**-Zr-**RuP$^6$**@Pt-$TiO_2$ (100 μM of the Ru(II) complex) in a 20 mM L-ascorbic acid sacrificial electron donor aqueous solution under an Ar atmosphere. The blue open, red closed, and green closed circles show the results obtained in the 0.5 M buffer solution at pH = 2, 4, and 6, respectively (λ = 470 ± 10 nm).

## 2-4 Conclusion

To improve the photo-induced charge separation efficiency at the photosensitizing (PS) dye-semiconductor interface, immobilized three different double layers of phosphonate-functionalized Ru(II) PS dyes were immobilized on the surface of Pt-cocatalyst-loaded $TiO_2$ nanoparticles using $Zr^{4+}$ cation binders. All the double-PS-layer nanoparticles exhibited remarkably higher photocatalytic activity for $H_2$ evolution than the single-PS-layer nanoparticle, and the difference was more enhanced in lower concentration of sacrificial electron donor (20 mM L-ascorbic acid, $H_2A$) aqueous solution. The photocatalytic $H_2$ evolution activity slightly increased in the low SED concentration by changing the 2nd outer PS dye in the order of **$RuP^2$**-Zr-**$RuP^6$**@Pt-$TiO_2$ < **$RuCP^2$**-Zr-**$RuP^6$**@Pt-$TiO_2$ < **$RuCP^2$phen**-Zr-**$RuP^6$**@Pt-$TiO_2$, suggesting that the photoexcitation energy transfer from the outer to inner PS could give a positive effect on the photocatalytic activity. The pH dependence of the photocatalytic activity of **$RuCP^2$phen**-Zr-**$RuP^6$**@Pt-$TiO_2$ was evaluated to be maximum at around pH = 4 because of the moderate $H^+$ concentration and the suitable reducing ability of singly deprotonated $HA^-$ anion. The findings in this work clearly indicate the potential of double-PS-layer structure on the semiconductor surface for effective photo-induced charge separation.

## 2-5 Reference

1. M. Grätzel, *Acc. Chem. Res.* **1981**, *14*, 376−384.
2. T. J. Meyer, *Acc. Chem. Res.* **1989**, *22*, 163−170.
3. M. R. Wasielewski, *Chem. Rev.* **1992**, *92*, 435−461.
4. E. Amouyal, *Sol. Energy Mater. Sol. Cells* **1995**, *38*, 249−276.
5. A. Kudo, Y. Miseki, *Chem. Soc. Rev.* **2009**, *38*, 253−278.
6. A. Fujishima, K. Honda, *Nature* **1972**, *238*, 37–38.
7. C. V. Krishnan, N. Sutin, *J. Am. Chem. Soc.* **1981**, *103*, 2141−2142.
8. C. V. Krishnan, B. S. Brunschwig, C. Creutz, N. Sutin, *J. Am. Chem. Soc.* **1985**, *107*, 2005−2015.
9. K. Maeda, G. Sahara, M. Eguchi, O. Ishitani, *ACS Catal.* **2015**, *5*, 1700−1707.
10. J. Park, P. Ramasamy, S. Kim, Y. K. Kim, V. Ahilan, S. Shanmugam, J. Lee, *Chem. Commun.* **2017**, *53*, 3277−3280.
11. G. P. Mane, S. N. Talapaneni, K. S. Lakhi, H. Ilbeygi, U. Ravon, K. Al-bahily, T. Mori, D. Park, A. Vinu, *Angew. Chem. Int. Ed.* **2017**, *56*, 8184−8185.
12. Y. Tachibana, J. E. Moser, M. Grätzel, D. R. Klug, J. R. Durrant, *J. Phys. Chem.* **1996**, *100*, 20056−20062.
13. M. K. Brennaman, A. O. T. Patrocinio, W. Song, J. W. Jurss,J. J. Concepcion, P. G. Hoertz, M. C. Traub, N. Y. M. Iha, T. J. Meyer, *ChemSusChem* **2011**, *4*, 216−227.
14. S. E. Bettis, D. M. Ryan, M. K. Gish, G. L. Alibabaei, T. J. Meyer, M. L. Waters, J. M. Papanikolas, *J. Phys. Chem. C* **2014**, *118*, 6029−6037.
15. Z. A. Morseth, T. V. Pho, M. V. Sheridan, T. J. Meyer, K. S. Schanze, J. R. Reynolds, J. M. Papanikolas, *ACS Appl. Mater. Interfaces* **2017**, *9*, 16651−16659.
16. R. J. Dillon, L. Alibabaei, T. J. Meyer, J. M. Papanikolas, *ACS Appl. Mater. Interfaces* **2017**, *9*, 26786−26796.
17. X. Chen, S. Shen, L. Guo, S. S. Mao, *Chem. Rev.* **2010**, *110*, 6503−6570.
18. S. Y. Reece, J. A. Hamel, K. Sung, T. D. Jarvi, A. J. Esswein, J. J. H. Pijpers, D. G. Nocera, *Science* **2011**, *334*, 645−648.
19. D. G. Nocera, *Acc. Chem. Res.* **2012**, *45*, 767−776.
20. K. Maeda, *ACS Catal.* **2013**, *3*, 1486−1503.
21. T. Hisatomi, J. Kubota, D. Domen, *Chem. Soc. Rev.* **2014**, *43*, 7520−7535.
22. S. J. A. Moniz, S. A. Shevlin, D. J. Martin, Z. Guo, J. Tang, *Energy Environ. Sci.* **2015**, *8*, 731–759.
23. T. N. Suzuki, A. Iwase, H. Tanaka, S. Sato, A. Kudo, T. Morikawa, *J. Mater. Chem. A* **2015**, *3*, 13283−13290.
24. B. Oregan, M. Grätzel, *Nature* **1991**, *353*, 737−740.

25. A. Key, M. Grätzel, *J. Phys. Chem.* **1993**, *97*, 6272−6277.
26. K. Murakoshi, G. Kano, Y. Wada, S. Yanagida, H. Miyazaki, M. Matsumoto, S. Murasawa, *J. Electroanal. Chem.* **1995**, *396*, 27−34.
27. A. Yella, H. W. Lee, H. N. Tsao, C. Y. Yi, A. K. Chandiran, M. K. Nazeeruddin, E. W. G. Diau, C. Y. Yeh, S. M. Zakeeruddin, M. Grätzel, *Science* **2011**, *334*, 629−634.
28. S. Mathew, A. Yella, P. Gao, R. Humphry-Baker, B. F. E. Curchod, N. Ashari-Astani, I. Tavernelli, U. Rothlisberger, M. K. Nazeeruddin, M. Grätzel, *Nat. Chem.* **2014**, *6*, 242−247.
29. Z. Y. Yao, M. Zhang, R. Z. Li, L. Yang, Y. N. Qiao, P. Wang, *Angew. Chem. Int. Ed.* **2015**, *54*, 5994−5998.
30. M. Freitag. J. Teuscher, Y. Saygili, X. Zhang, F. Giordano, P. Liska, J. Hua, S. M. Zakeeruddin, J. Moser, M. Grätzel, A. Hagfeldt, *Nat. Photonics* **2017**, *11*, 372−379.
31. S. II Seok, M. Grätzel, N. Park, *Small* **2018**, *14*, 1704177.
32. F. P. Rotzinger, S. Munavalli, P. Comte, J. K. Hurst, M. Grätzel, F. J. Pern, A. J. Frank, *J. Am. Chem. Soc.* **1987**, *109*, 6619−6626.
33. M. Yamamoto, L. Wang, T. Fukushima, K. Tanaka, L. Sun, H. Imahori, *Chem. Sci.* **2016**, *7*, 1430-1439.
34. C. E. Creissen, J. Warnan, E. Reisner, *Chem. Sci.* **2018**, *9*, 1439-1447.
35. K. Hanson, M. K. Brennaman, A. Ito, H. Luo, W. Song, K. A. Parker, R. Ghosh, M. R. Norris, C. R. K. Glasson, J. J. Concepcion, R. Lopez, T. J. Meyer, *J. Phys. Chem. C* **2012**, *116*, 14837−14847.
36. O. O. Ogunsolu, I. A. Murphy, J. C. Wang, A. Das, K. Hanson, *ACS Appl. Mater. Interfaces* **2016**, *8*, 28633−28640.
37. H. Park, E. Bae, J. Lee, J. Park, W. Choi, *J. Phys. Chem. B* **2006**, *110*, 8740-8749.
38. W. J. Youngblood, S. A. Lee, K. Maeda, T. E. Mallouk, *Acc. Chem. Res.* **2009**, *42*, 1966-1973.
39. L. Duan, F. Bozoglian, S. Mandel, B. Stewart, T. Privalov, A. Llobet, L. Sun, *Nat. Chem.* **2012**, *4*, 418−423.
40. S. A. Lee, Y. Zhao, E. A. Hernandez-Pagan, L. Blasdel, W. J. Youngblood, T. E. Mallouk, *Faraday Discuss.* **2012**, *155*, 165−176.
41. K. Hanson, M. K. Brennaman, H. Luo, C. R. K. Glasson, J. J. Concepcion, W. Song, T. J. Meyer, *ACS Appl. Mater. Interfaces* **2012**, *4*, 1462−1469.
42. P. G. Giokas, S. A. Miller, K. Hanson, M. R. Norris, C. R. K. Glasson, J. J. Concepcion, S. E. Bettis, T. J. Meyer, A. M. Moran, *J. Phys. Chem. C* **2013**, *117*, 812−824.
43. M. V. Sheridan, B. D. Sherman, Z. F. K. Wee, M. K. Coggins, T. J. Meyer, *ACS Catal.* **2015**, *5*, 4404−4409.
44. N. Song, J. J. Concepcion, R. A. Binstead, J. A. Rudd, A. K. Vannucci, C. J. Dares, M. K. Coggins, T. J. Meyer, *Proc. Natl. Acad. Sci. U. S. A.* **2015**, *112*, 4935−4940.
45. D. L. Ashford, M. K. Gish, A. K. Vannucci, M. K. Brennaman, J. L. Templeton, J. M. Papanikolas,

T. J. Meyer, *Chem. Rev.* **2015**, *115*, 13006−13049.

46. Y. Miseki, S. Fujiyoshi, T. Gunji, K. Sayama, *J. Phys. Chem. C* **2017**, *121*, 9691−9697.
47. B. Shan, B. H. Farnun, K. Wee, T. J. Meyer, *J. Phys. Chem. C* **2017**, *121*, 5882−5890.
48. M. M. Raber, M. D. Brady, L. Troian-Gautier, J. C. Dickenson, S. L. Marquard, J. T. Hyde, S. J. Lopez, G. J. Meyer, T. J. Meyer, D. P. Harrison, *ACS Appl. Mater. Interfaces* **2018**, *10*, 22821−22833.
49. A. Kobayashi, S. Furugori, M. Yoshida, M. Kato, *Chem. Lett.* **2016**, *55*, 1978−1985.
50. S. Furugori, A. Kobayashi, A. Watanabe, M. Yoshida, M. Kato, *ACS Omega* **2017**, *2*, 3901–3912.
51. G. A. Crosby, W. H. Elfting Jr., *J. Phys. Chem*, **1976**, *80*, 2206−2211.
52. H. Park, W. Choi, M. R. Hoffmann, *J. Mater. Chem.* **2008**, *18*, 2379–2385.
53. M. R. Norris, J. J.; Concepcion, C. R. K. Glasson, Z. Fang, A. M. Lapides, D. L. Ashford, J. L. Templeton, T. J. Meyer, *Inorg. Chem.* **2013**, *52*, 12492–12501.
54. L. Zhang, Y. Hou, M. Pan, L. Chen, Y. Zhu, S. Yin, G. Shao, C. Su, *Dalton Trans.* **2015**, *44*, 15212−15219.
55. M. K. Nazeeruddin, F. De Angelis, S. Fantacci, A. Selloni, G. Viscardi, P. Liska, S. Ito, S. Takeru, M. Grätzel, *J. Am. Chem. Soc.* **2005**, *127*, 16835-16847.
56. K. Hanson, D. A. Torelli, A. K. Vannucci, M. K. Brennaman, H. Luo, L. Alibabaei, W. Song, D. L. Ashford, M. R. Norris, C. R. K. Glasson, J. J. Concepcion, T. J. Meyer, *Angew. Chem. Int. Ed.* **2012**, *51*, 12782−12785.
57. G. Rothenberger, D. Fitzmaurice, M. Grätzel, *J. Phys. Chem.* **1992**, *96*, 5983−5986.
58. M. Natali, *ACS Catal.* **2017**, *7*, 1330–1339.

# Chapter 3

# Photosensitizing Ruthenium(II)-Dye Multilayers: Photoinduced Charge Separation and Back Electron Transfer Suppression

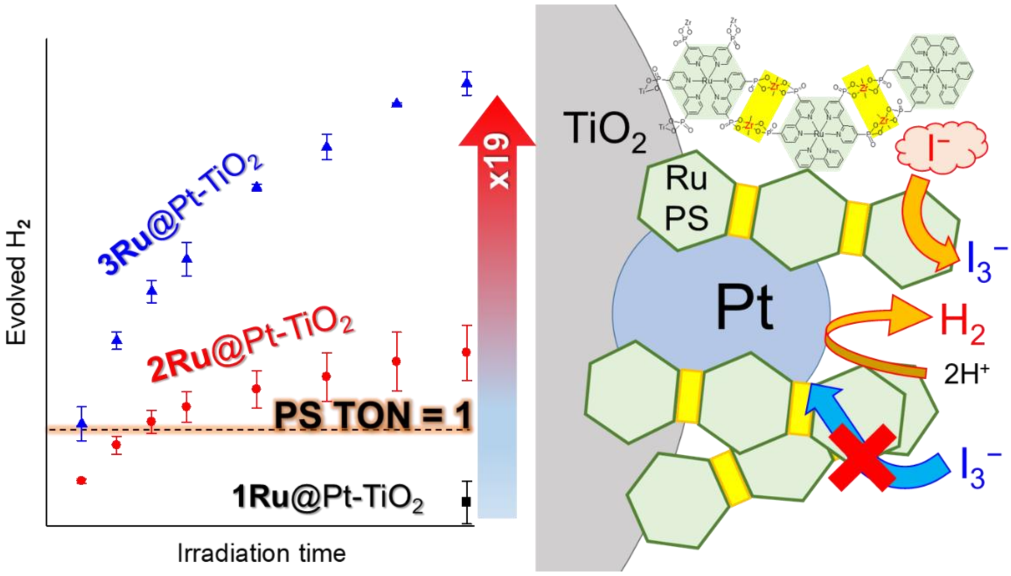

## 3-1 Introduction

Since the discovery of the Honda-Fujishima effect,[1] photocatalytic water splitting has been studied extensively in an effort to produce a clean, environmentally friendly source of $H_2$ from water.[2-6] In particular, the Z-scheme water-splitting system, comprising semiconductor-based water reduction and oxidation photocatalysts coupled with a redox-reversible electron mediator, has attracted considerable attention as a means of water splitting under visible light irradiation.[7-19] The activity of the Z-scheme water splitting photocatalyst relies on efficient electron transfer through the mediator from the $O_2$ to the $H_2$ evolution photocatalysts.[9-14] Although several promising techniques have been developed to suppress back electron transfer at the photocatalyst-mediator interface,[15-19] further improvement of photoinduced charge-separation efficiency is necessary to make solar fuel production feasible.

Immobilization of photosensitizing dye is a favorable approach for achieving high charge-separation efficiency at the dye-semiconductor interface.[20-24] Several dye-sensitized photocatalysts (DSP) and dye-sensitized photoelectrochemical cells (DSPEC) show promise.[25-31] However, back electron transfer at the semiconductor-dye-catalyst interfaces remains an issue.[32-34] Often, water reduction or oxidation at DSPs decreases when a sacrificial reagent is replaced to the electron mediator.[15,35] This trend is more severe for the homogeneous photosensitizers (PSs); photocatalytic water oxidation or reduction in the presence of molecular PS and electron mediator have been hardly achieved because the random diffusion in the solution state easily induces the charge-recombination and back electron transfer reactions.[36-39] Thus, a more sophisticated dye-sensitization mechanism that could not only inject an electron to the semiconductor substrate and but also suppress the charge recombination is desired. Self-assembling photofunctional molecules on a semiconductor surface may satisfy these requirements, as discussed recently in the fields of dye-sensitized solar cells and DSPEC.[26,40-44] Chapter 2 has focused on the multilayering of Ru(II) PSs by the coordination to $Zr^{4+}$ cations on the surface of Pt-cocatalyst-loaded $TiO_2$ nanoparticle to develop a redox-potential cascade for effective charge separation, and found that PS-doubly-layered nanoparticle, **RuCP$^2$**-Zr-**RuP$^6$**@Pt-$TiO_2$ exhibited remarkably higher activity than that of PS-singly-layered one, **RuCP$^2$**@Pt-$TiO_2$ in the presence of sacrificial electron donating L-ascorbic acid, whereas the activity of PS-triply-layered one, **RuCP$^2$**-Zr-**RuP$^4$**-Zr-**RuP$^6$**@Pt-$TiO_2$ was lower than the other two (Scheme 3-1; **RuCP$^2$** = $[Ru(bpy)_2(mpbpy)]^{2-}$, **RuP$^4$** = $[Ru(bpy)(pbpy)_2]^{6-}$, **RuP$^6$** = $[Ru(pbpy)_3]^{10-}$, $H_4$mpbpy = 2,2′-bipyridine-4,4′-bis(methane-phosphonic acid), and $H_4$pbpy = 2,2′-bipyridine-4,4′-bis(phosphonic acid)).[45,46] However, in order to design a Z-scheme water splitting photocatalyst, the electron source for $H_2$ production must be replaced from the L-ascorbic acid to the other redox-reversible electron mediator, because the disproportionation reaction of one-electron-oxidized monodehydroascorbic acid to form the non-oxidized ascorbic acid and the two-electron-oxidized dehydroascorbic acid should suppress the charge-recombination at the dye-solution interface. Thus, in this study, the photocatalytic $H_2$

evolution activity of these three photocatalysts were investigated in the presence of the redox-reversible iodide ($I^-$) electron source that is widely used in the Z-scheme semiconductor water-splitting systems. Herein, for the first time, it was demonstrated that the self-assembled PS-multilayered structure with $Zr^{4+}$ cation binders on the surface of a Pt-$TiO_2$ nanoparticle acts not only as an effective barrier for back electron transfer from the Pt cocatalyst surface to the oxidized iodine species but also as the iodide capturing site to promote the electron donation, resulting in significant enhancement of photocatalytic $H_2$ evolution in the redox-reversible iodide ($I^-$) electron donor aqueous solution.

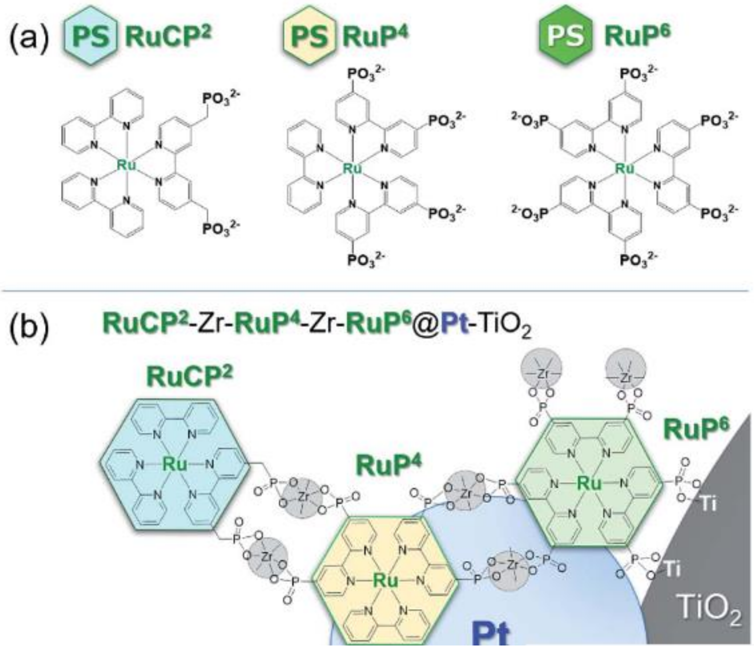

**Scheme 3-1.** (a) Molecular structures of three Ru(II) photosensitizers and (b) schematic representation of PS-triply-layered **RuCP$^2$**-Zr-**RuP$^4$**-Zr-**RuP$^6$**@Pt-$TiO_2$ nanoparticle.

## 3-2 Experimental

### 3-2-1 Synthesis

All Ru(II)-PSs and PS-multilayered photocatalysts were prepared by the same method as described in chapter 2-2.

### 3-2-2 Photocatalytic hydrogen evolution

Under dark conditions, an aqueous solution of KI (0.5 or 0.02 M) and hydrochloride (pH = 2) or phosphate pH buffer (0.5 M, pH = 2) containing Ru(II)-dye-immobilized nanoparticles (100 μM of the Ru(II) dye) was placed into a homemade Schlenk flask-equipped quartz cell (volume: 265 mL) with a small magnetic stirring bar. The other experimental conditions were the same as described in chapter 2.

### 3-2-3 Preparation of Ru(II)-PS-multilayered $TiO_2$-ITO photoelectrodes.

1. Preparation of $TiO_2$-ITO electrode: ITO electrodes (sheet resistance = 10 $\Omega$ $cm^{-1}$) were washed under ultrasound irradiation with acetone, pure water, KG aq, LC-2 aq, ultra-pure water, and isopropyl alcohol (IPA). Then electrodes were dried in 90 °C and further cleaned by UV light irradiation (PL16-110, AsOne) for 15 min. $TiO_2$ paste (PECC-C01-06, Peccell Technologies) were pasted on the cleaned ITO electrodes, dried in R.T. for 15 min, and then sintered at 150 °C for 10 min to obtain $TiO_2$-ITO electrodes.[1]

2a. Fabrication of **RuCP$^2$**@$TiO_2$-ITO: A $TiO_2$-ITO electrode was immersed in the aqueous solution containing 0.2 mM Ru(II) PS (**RuCP$^2$**) and 0.1 M $HClO_4$ for overnight at 293 K and followed by rinsing with pure water and then dried at 100 °C.

2b. Fabrications of **RuCP$^2$**-Zr-**RuP$^6$**@$TiO_2$-ITO and **RuCP$^2$**-Zr-**RuP$^4$**-Zr-**RuP$^6$**@$TiO_2$-ITO electrodes: These Ru(II)PS-multilayered electrodes were prepared by alternating immersion of a $TiO_2$-ITO electrode to Ru(II)PS aqueous solution (0.2 mM Ru(II) PS in 0.1 M $HClO_4$ aq. for overnight) and 5 mM $ZrCl_2O$ MeOH solution (for 60 min) at 293 K. **RuP$^6$, RuP$^4$** and **RuCP$^2$** were used for the 1st, 2nd and 3rd PS layers, respectively, for **RuCP$^2$**-Zr-**RuP$^4$**-Zr-**RuP$^6$**@$TiO_2$-ITO electrodes. **RuP$^6$** and **RuCP$^2$** were used for the 1st and 2nd PS layers for **RuCP$^2$**-Zr- **RuP$^6$**@$TiO_2$-ITO electrodes. Obtained electrodes were washed with MeOH and dried at 100 °C after immersion.

3. Dye-sensitized solar cell fabrication: For preparation of the counter electrode, an aqueous solution of poly(3,4-ethylenedioxythiophene)tetramethacrylate (PEDOT-TMA, Aldrich 649821) was mixed with ethanol in a volume ratio of 4:1. The mixture was spin-coated (3000 rpm for 10 s) on ITO glass and annealed at 50°C for 10 min. This spin-coating process was repeated for three times. The Ru(II)-dye-multilayered $TiO_2$-ITO and PEDOT-TMA electrodes were assembled to fabricate a sandwich-type cell with a 50 μm spacer. The electrolyte consisted of a solution of lithium iodide (LiI, 0.5 M), iodine ($I_2$, 0.05 M) and 0.5 M *t*-butyl pyridine in methoxy-acetonitrile or lithium iodide (LiI, 0.5 M), and iodine ($I_2$, 0.05 M) in water, and it was injected between the electrodes.

## 3-3 Result and discussion

### 3-3-1 Synthesis and characterization.

Three **RuCP$^2$**@Pt-$TiO_2$, **RuCP$^2$**-Zr-**RuP$^6$**@Pt-$TiO_2$, **RuCP$^2$**-Zr-**RuP$^4$**-Zr-**RuP$^6$**@Pt-$TiO_2$ ([Pt] = 1, 5 wt%) were prepared according to the literature using [Ru(bpy)$_3$]-type dyes with two to six phosphonates (**RuCP$^2$**, **RuP$^4$**, and **RuP$^6$**, Scheme 3-1).[45,46] UV-Vis absorption spectroscopy revealed that the amount of immobilized Ru(II) dye on Pt-$TiO_2$ increases with the number of PS layers from 194 to 305 nmol per 1 mg $TiO_2$ (Figure 3-3-1-1, Tables 3-3-1-1, and 3-3-1-2). It should be noteworthy that $^1$H NMR and emission spectra of the supernatant solution obtained from the **RuCP$^2$** immobilization reaction to prepare **RuCP$^2$**-Zr-**RuP$^6$**@Pt-$TiO_2$ were qualitatively agreed to the spectra of **RuCP$^2$**, suggesting that the desorption of **RuP$^6$** immobilized in the 1st inner layer hardly occurred during the reaction (Figure 3-3-1-2). Thus, the migration of Ru(II) PS from the inner to outer layer during the immobilization reactions should be negligible because of the stable $PO_3$-$Zr^{4+}$ coordination bond. The particle diameters of three nanoparticles were estimated by dynamic light scattering (DLS), because the dispersibility to water could be one of the crucial parameters for the $H_2$ evolution activity of nanoparticle photocatalyst. It was found that the dispersibility of three nanoparticles, **RuCP$^2$**@Pt-$TiO_2$, **RuCP$^2$**-Zr-**RuP$^6$**@Pt-$TiO_2$, **RuCP$^2$**-Zr-**RuP$^4$**-Zr-**RuP$^6$**@Pt-$TiO_2$ were comparable probably because the outer surface of each nanoparticle was covered by the same Ru(II) PS, **RuCP$^2$** (Figure 3-3-1-3). Powder X-ray diffractions were measured to estimate the diameter of Pt-cocatalyst on each nanoparticle that may affect the $H_2$ evolution activity. The peak width of Pt(111) diffraction suggested that the average diameter was ca. 6 nm (Figure 3-3-1-4 and Table 3-3-1-3), being consistent to the estimated diameter of Pt cocatalyst from the transmission electron microscopic (TEM) image of **RuCP$^2$**-Zr-**RuP$^4$**-Zr-**RuP$^6$**@Pt-$TiO_2$ (Figure 3-3-1-5 and Table 3-3-1-4).

**Table 3-3-1-1.** Absorbance of each supernatant solution and the calculated $C_B$ and $M_i$ values.

| | **RuCP$^2$** @Pt-$TiO_2$ | **RuCP$^2$**-Zr-**RuP$^6$** @Pt-$TiO_2$ | | **RuCP$^2$**-Zr-**RuP$^4$**-Zr-**RuP$^6$** @Pt-$TiO_2$ | | |
|---|---|---|---|---|---|---|
| | 1st layer (**RuCP$^2$**) | 2nd outer layer (**RuCP$^2$**) | 1st inner layer (**RuP$^6$**) | 3rd outer layer (**RuCP$^2$**) | 2nd middle layer (**RuP$^4$**) | 1st inner layer (**RuP$^6$**) |
| $A$ | 0.098 | 0.120 | 0.328 | 0.264 | 0.154 | 0.328 |
| $C_B$ | 0.335 | 0.411 | 0.837 | 0.904 | 0.485 | 0.837 |
| $M_i$ | 5.47 | 5.01 | 2.44 | 2.03 | 4.57 | 2.44 |

**Table 3-3-1-2**. Amount of Ru(II) photosensitizer immobilized on the Pt-$TiO_2$ nanoparticle surface

| Photocatalyst | Immobilized Ru(II) PS | Amount of immobilized Ru(II) complex (nmol / 1 mg $TiO_2$)[a] | Surface coverage $N$ (nmol / $cm^2$) |
|---|---|---|---|
| **RuCP$^2$**@Pt-$TiO_2$ | **RuCP$^2$** | 182 | 0.177 |
| **RuCP$^2$**-Zr-**RuP$^6$** @Pt-$TiO_2$ | 1st (inner) layer **RuP$^6$** | 81.3 | 0.0792 |
| | 2nd (outer) layer **RuCP$^2$** | 167 | 0.163 |
| | Total Ru(II) PS | 248 | 0.241 |
| **RuCP$^2$**-Zr-**RuP$^4$**-Zr-**RuP$^6$** @Pt-$TiO_2$ | 1st (inner) layer **RuP$^6$** | 81.3 | 0.0792 |
| | 2nd (middle) layer **RuP$^4$** | 152 | 0.148 |
| | 3rd (outer) layer **RuCP$^2$** | 67.7 | 0.0659 |
| | Total Ru(II) PS | 301 | 0.293 |

[a] Estimated based on the absorbance observed in the UV-Vis spectra of each supernatant solution (Figure 3-3-1-1).

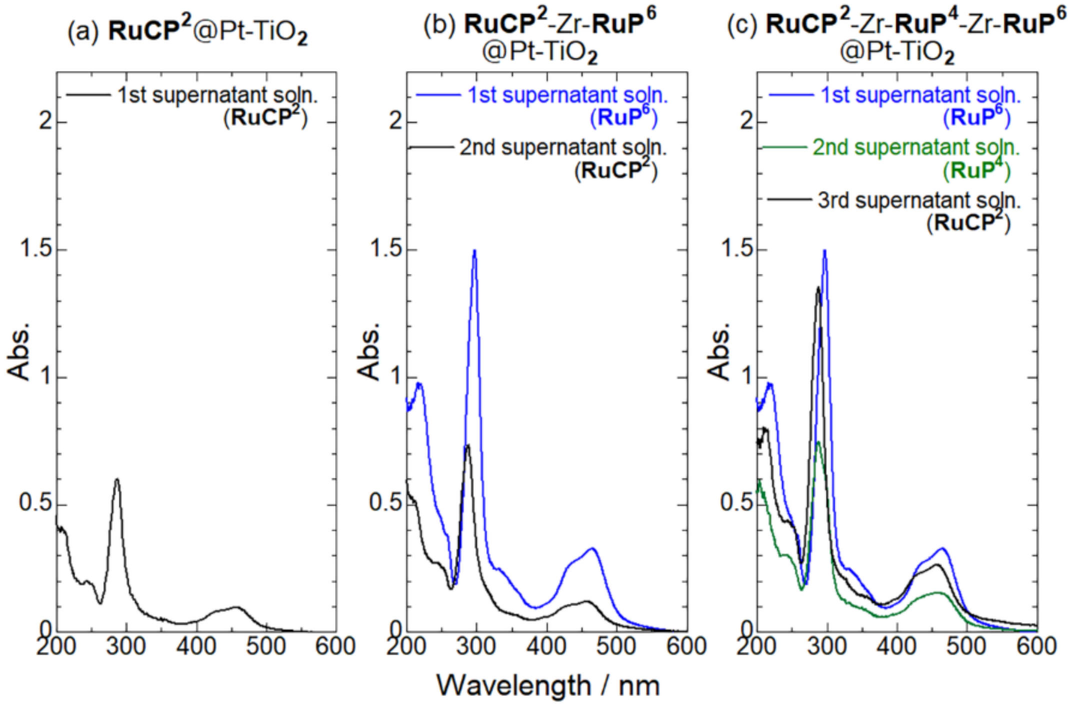

**Figure 3-3-1-1.** UV-Vis absorption spectra of the supernatant solutions at 298 K. (a) **RuCP$^2$**@Pt-$TiO_2$, (b) **RuCP$^2$**-Zr-**RuP$^6$**@Pt-$TiO_2$, and (c) **RuCP$^2$**-Zr-**RuP$^4$**-Zr-**RuP$^6$**@Pt-$TiO_2$. Note that each solution (1 mL) was diluted to 50 mL by the addition of deionized water before the spectral measurement.

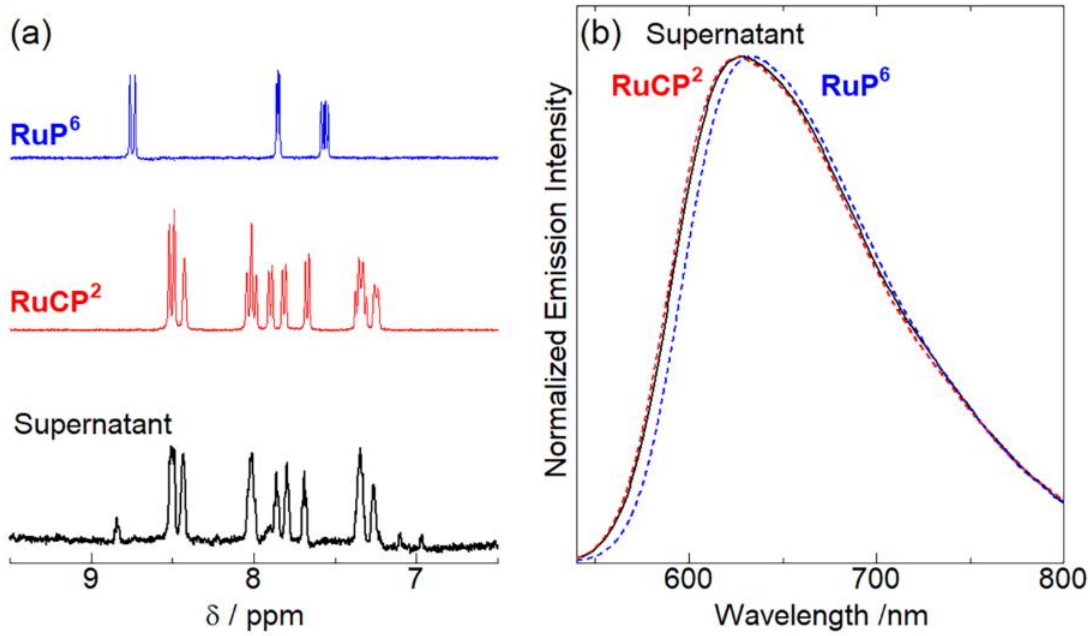

**Figure 3-3-1-2.** (a) $^1$H NMR and (b) emission spectra of the supernatant solution (black lines) obtained from the immobilization reaction of **RuCP$^2$** for the synthesis of **RuCP$^2$**-Zr-**RuP$^6$**@Pt-TiO$_2$ by ultracentrifugation. Blue and red lines are the spectra of **RuP$^6$** and **RuCP$^2$** in the aqueous solution.

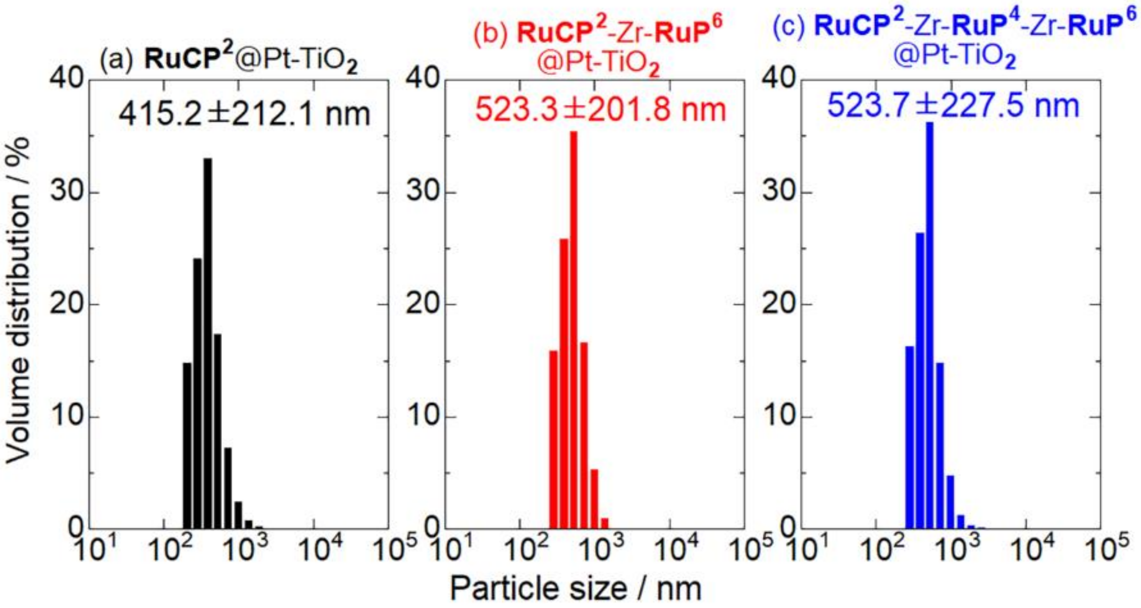

**Figure 3-3-1-3**. Particle diameter distributions estimated by the dynamic light scattering method for (a) **RuCP$^2$**@Pt-TiO$_2$, (b) **RuCP$^2$**-Zr-**RuP$^6$**@Pt-TiO$_2$, and (c) **RuCP$^2$**-Zr-**RuP$^4$**-Zr-**RuP$^6$**@Pt-TiO$_2$ nanoparticles in the diluted HCl aqueous solution (pH = 2).

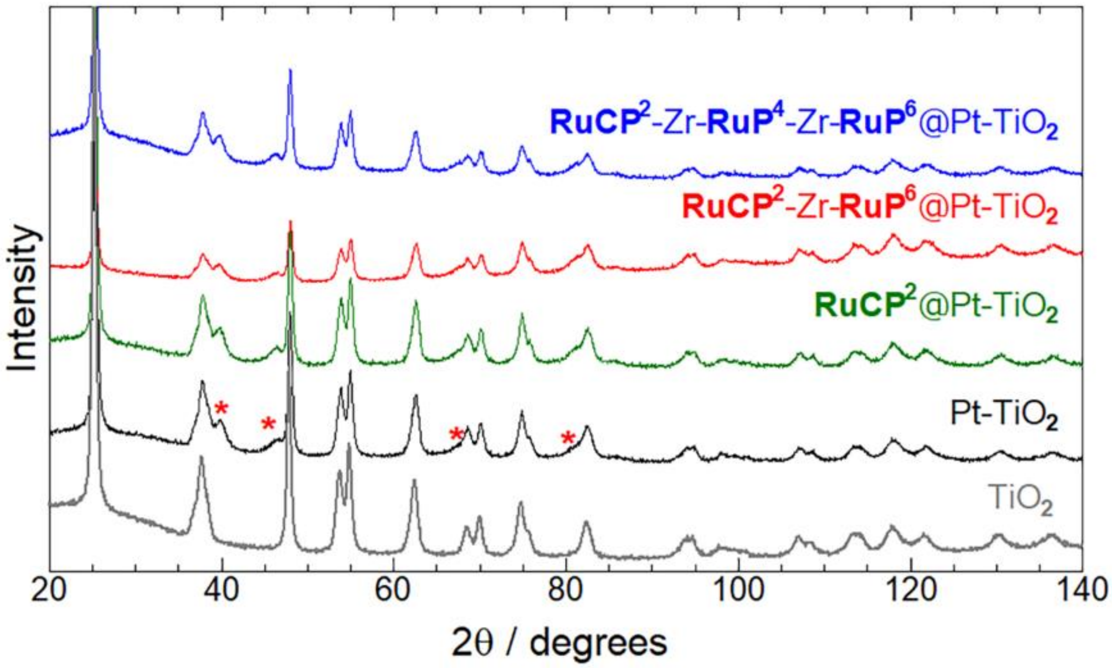

**Figure 3-3-1-4.** Experimental PXRD patterns of $TiO_2$, Pt-$TiO_2$, **RuCP$^2$**@Pt-$TiO_2$, **RuCP$^2$**-Zr-**RuP$^6$**@Pt-$TiO_2$, and **RuCP$^2$**-Zr-**RuP$^4$**-Zr-**RuP$^6$**@Pt-$TiO_2$ nanoparticles (Pt = 5wt%) in the solid state at 293 K. The red asterisks show the diffraction peaks derived from Pt cocatalyst loaded on the surface of $TiO_2$ nanoparticle.

**Table 3-3-1-3**. Estimated particle diameters of $TiO_2$ and Pt cocatalyst.

| Photocatalyst | $TiO_2$ (nm)[a] | Pt (nm)[a] |
|---|---|---|
| $TiO_2$ | 21.3(1) | - |
| Pt-$TiO_2$ | 21.4(2) | 6.0(7) |
| **RuCP$^2$**@Pt-$TiO_2$ | 21.8(1) | 6.2(7) |
| **RuCP$^2$**-Zr-**RuP$^6$**@Pt-$TiO_2$ | 21.3(2) | 6.5(6) |
| **RuCP$^2$**-Zr-**RuP$^4$**-Zr-**RuP$^6$**@Pt-$TiO_2$ | 21.7(2) | 6.3(9) |

[a] Diameters were estimated based on the diffraction peaks observed at 25.2° for $TiO_2$ and 46.2° for Pt cocatalyst (Figure 3-3-1-4). The peak fitting was done by Pseudo Volgt function.

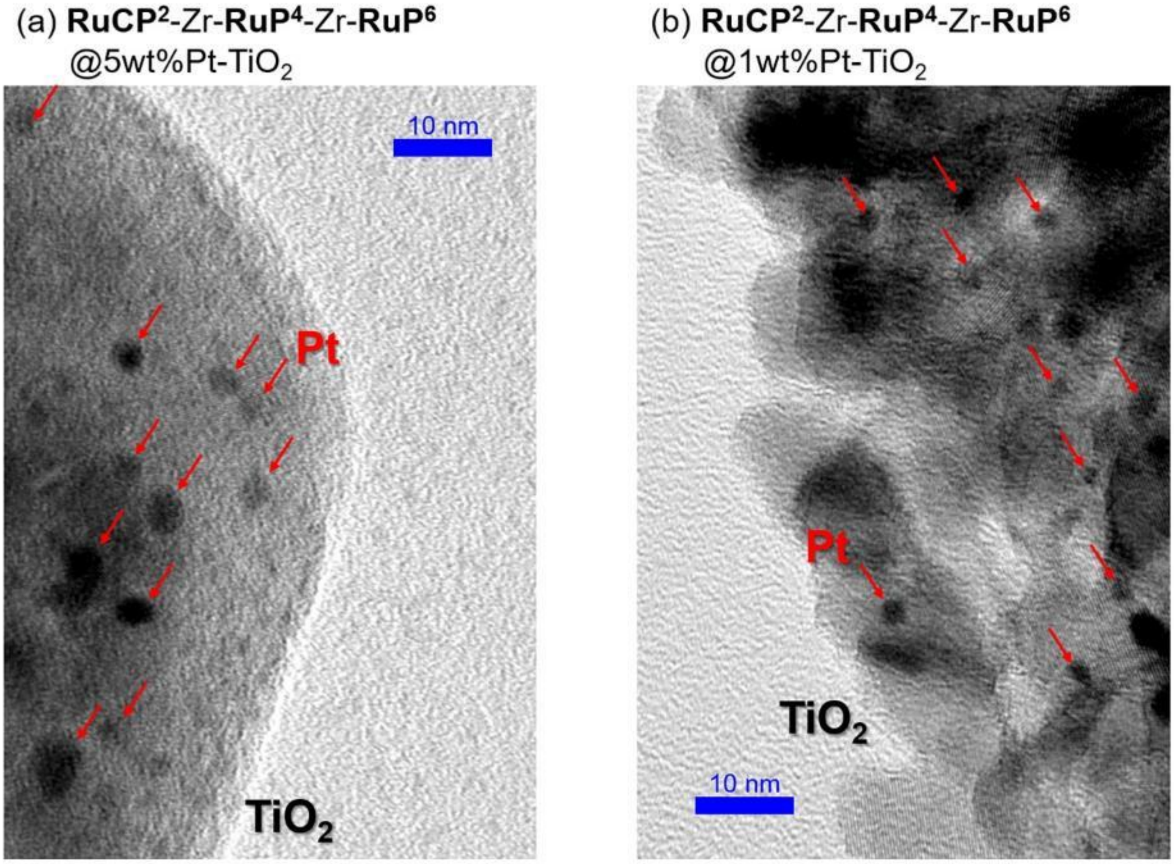

**Figure 3-3-1-5**. Transmission electron microscopic (TEM) images of (a) **RuCP**$^2$-Zr-**RuP**$^4$-Zr-**RuP**$^6$@5wt%Pt-$TiO_2$ and (b) **RuCP**$^2$-Zr-**RuP**$^4$-Zr-**RuP**$^6$@1wt%Pt-$TiO_2$. Red arrows indicate the Pt cocatalysts loaded on the surface of $TiO_2$.

**Table 3-3-1-4** Diameter of Pt colloid estimated from Figure 3-3-1-5

| Photocatalytic nanoparticle | Diameter of Pt colloid (nm) |
|---|---|
| **RuCP**$^2$-Zr-**RuP**$^4$-Zr-**RuP**$^6$@5wt%Pt-$TiO_2$ | 4.99±1.57 |
| **RuCP**$^2$-Zr-**RuP**$^4$-Zr-**RuP**$^6$@1wt%Pt-$TiO_2$ | 2.93±0.45 |

### 3-3-2 Photocatalytic $H_2$ evolution.

Figure 3-3-2-1 illustrates the results of photocatalytic $H_2$ evolution reaction of three nanoparticle photocatalysts, **RuCP$^2$**@Pt-$TiO_2$, **RuCP$^2$**-Zr-**RuP$^6$**@Pt-$TiO_2$, **RuCP$^2$**-Zr-**RuP$^4$**-Zr-**RuP$^6$**@Pt-$TiO_2$ in 0.5 M KI redox-reversible electron source aqueous solution. Although each of the reactions used a total concentration of 100 μM Ru(II) PS, photocatalytic $H_2$ evolution activity in 0.5 M KI aqueous solution was enhanced remarkably by increasing the number of PS layers on the surface of the Pt-$TiO_2$. **RuCP$^2$**@Pt-$TiO_2$ produced a negligible amount of $H_2$ after 6 h light irradiation and the turn-over number per one PS dye (PS TON) was less than 1, while 7- and 19-fold increases in PS TON were observed for **RuCP$^2$**-Zr-**RuP$^6$**@Pt-$TiO_2$ and **RuCP$^2$**-Zr-**RuP$^4$**-Zr-**RuP$^6$**@Pt-$TiO_2$, respectively (Table 3-3-2-1). Similar enhancement was found in the TON per one Pt atom in the cocatalyst (Pt TON; < 0.1 for **RuCP$^2$**@Pt-$TiO_2$, 0.99 for **RuCP$^2$**-Zr-**RuP$^6$**@Pt-$TiO_2$, and 1.91 for **RuCP$^2$**-Zr-**RuP$^4$**-Zr-**RuP$^6$**@Pt-$TiO_2$). Thus, the higher TONs of Pt-$TiO_2$ nanoparticles with the thicker Ru(II)-dye layer compared to that of **RuCP$^2$**@Pt-$TiO_2$ suggests that the photoinduced charge-separation efficiency could be improved by the multilayering of Ru(II) dyes. Further, almost the same $H_2$ evolution activity was retained in the 2nd run of the once-used **RuCP$^2$**-Zr-**RuP$^4$**-Zr-**RuP$^6$**@Pt-$TiO_2$ (Figure 3-3-2-2(a)). In the $^1$H NMR and emission spectra of the supernatant solution obtained from the 1st reaction (Figures 3-3-2-2(b) and 3-3-2-2(c)), no peak was observed in both spectra. Thus, the origin of the decrease in photocatalytic activity with irradiation time should not be due to the desorption of Ru(II) PS from the Pt-$TiO_2$ surface. UV-Vis absorption spectra of the reaction solutions after 6 h irradiation clearly suggest that the amount of triiodide ($I_3^-$) formed by the oxidation of $I^-$ agrees quantitatively with the amount of $H_2$ detected by gas chromatography (Figures 3-3-2-1b, 3-3-2-3 and Table 3-3-2-1). Thus, **RuCP$^2$**-Zr-**RuP$^6$**@Pt-$TiO_2$ and **RuCP$^2$**-Zr-**RuP$^4$**-Zr-**RuP$^6$**@Pt-$TiO_2$ acts as an active photocatalyst to form quantitative amounts of the reduction and oxidation products, $H_2$ and $I_3^-$, in aqueous KI solution. This is also consistent to the results of control experiments with different electron donors (Table 3-3-2-2); negligible $H_2$ was observed in the presence of bromide instead of iodide probably due to the more positive redox potential of $Br^-$ than $I^-$, but the other iodide salts (NaI, CsI, and $[Cu(dmp)_2]I$ (dmp = 2,9-dimethyl-1,10-phenanthroline) acted as the electron donor for $H_2$ evolution (Entries 1-6). $H_2$ hardly evolved in the absence of photocatalyst, iodide, or light (Entries 7-9). In contrast, the **RuCP$^2$** dyes immobilized directly on $TiO_2$ nanoparticle (**RuCP$^2$**@Pt-$TiO_2$) partially desorbed during the 6 h photocatalytic reaction as detected by the UV-Vis absorption and emission spectra (Figures 3-3-2-1(b) and 3-3-2-2(c)). Thus, the dye immobilized by the coordination to $Zr^{4+}$ cation could be more stable than that immobilized directly on the $TiO_2$ surface.

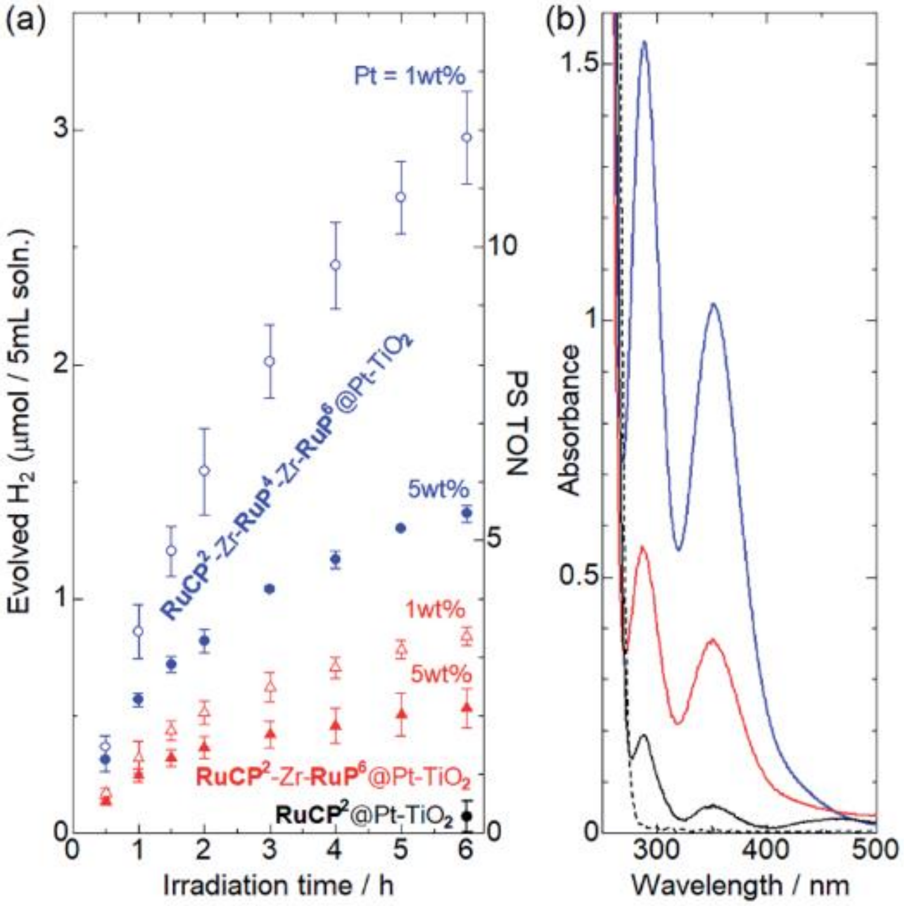

**Figure 3-3-2-1.** (a) Photocatalytic $H_2$ evolution reactions driven by (black) **RuCP²**@Pt-$TiO_2$, (red) **RuCP²**-Zr-**RuP⁶**@Pt-$TiO_2$, and (blue) **RuCP²**-Zr-**RuP⁴**-Zr-**RuP⁶**@Pt-$TiO_2$ (100 μM Ru(II) dye) in the presence of 0.5 M KI as the electron donor (initial pH = 2.0, λ = 470 ± 10 nm). Closed and open symbols represent data for nanoparticles with 5 wt% and 1 wt% Pt, respectively. (b) UV-Vis absorption spectra of the supernatants obtained by centrifugation of the reaction solutions of (black) **RuCP²**@Pt-$TiO_2$, (red) **RuCP²**-Zr-**RuP⁶**@Pt-$TiO_2$, and (blue) **RuCP²**-Zr-**RuP⁴**-Zr-**RuP⁶**@Pt-$TiO_2$ (Pt = 5wt%) after 6 h irradiation. Each supernatant (1 mL) was diluted to 10 mL with deionized water prior to the measurement. The dotted line is the spectrum of the supernatant of **RuCP²**@Pt-$TiO_2$ before irradiation.

**Table 3-3-2-1**. Results of photocatalytic $H_2$ evolution experiments with **nRu**@Pt-TiO$_2$ in aqueous KI.

| Photocatalyst | Loaded Pt (wt%) | KI (M) | Initial $I_3^-$ (mM) | $H_2$ (μmol) | Produced $I_3^-$ (μmol) | PS TON$^a$ | PS TOF$^b$ | Pt TON$^{a,c}$ | AQY$^a$ (%) |
|---|---|---|---|---|---|---|---|---|---|
| **RuCP$^2$**@Pt-TiO$_2$ | 5 | 0.5 | - | 0.07 | < 0.10 | 0.28 | - | < 0.10 | 0.0024 |
| **RuCP$^2$**-Zr-**RuP$^6$**@Pt-TiO$_2$ | 5 | 0.5 | - | 0.53 | 0.54 | 2.1 | 0.99 | 0.99 | 0.018 |
| **RuCP$^2$**-Zr-**RuP$^6$**@Pt-TiO$_2$ | 1 | 0.5 | - | 0.84 | - | 3.4 | 1.3 | 6.4 | 0.028 |
| **RuCP$^2$**-Zr-**RuP$^6$**@Pt-TiO$_2$ | 5 | 0.5 | 0.2 | 0.02 | - | 0.08 | - | < 0.10 | - |
| **RuCP$^2$**-Zr-**RuP$^4$**-Zr-**RuP$^6$**@Pt-TiO$_2$ | 5 | 0.5 | - | 1.36 | 1.70 | 5.44 | 2.28 | 1.91 | 0.0458 |
| **RuCP$^2$**-Zr-**RuP$^4$**-Zr-**RuP$^6$**@Pt-TiO$_2$ | 1 | 0.5 | - | 2.98 | - | 11.9 | 3.45 | 31.8 | 0.100 |
| **RuCP$^2$**-Zr-**RuP$^4$**-Zr-**RuP$^6$**@Pt-TiO$_2$ | 5 | 0.2 | - | 1.00 | - | 4.02 | 2.08 | 1.40 | - |
| **RuCP$^2$**-Zr-**RuP$^4$**-Zr-**RuP$^6$**@Pt-TiO$_2$ | 5 | 0.1 | - | 0.56 | - | 2.5 | 0.96 | 0.79 | - |
| **RuCP$^2$**-Zr-**RuP$^4$**-Zr-**RuP$^6$**@Pt-TiO$_2$ | 5 | 0.5 | 0.1 | 0.37 | - | 1.5 | 0.32 | 0.52 | - |
| **RuCP$^2$**-Zr-**RuP$^4$**-Zr-**RuP$^6$**@Pt-TiO$_2$ | 5 | 0.5 | 0.2 | 0.16 | - | 0.64 | - | 0.22 | - |

$^a$ After 6 h irradiation. $^b$ Initial 1 h irradiation. $^c$$H_2$ (mol) / Pt (mol).

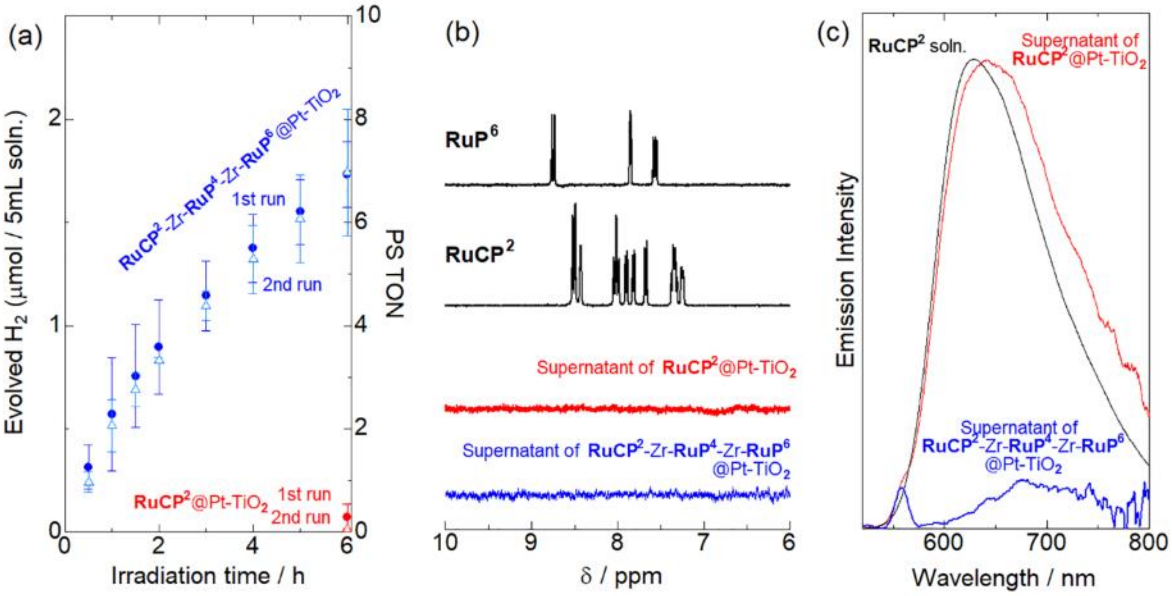

**Figure 3-3-2-2**. (a) Photocatalytic $H_2$ evolution reactions driven by **RuCP$^2$**-Zr-**RuP$^4$**-Zr-**RuP$^6$**@Pt-$TiO_2$ (blue) or **RuCP$^2$**@Pt-$TiO_2$ (red) in the presence of 0.5 M KI as the electron donor (100 μM Ru(II) dye, initial pH = 2.0, λ = 470 ± 10 nm). Closed circles and open triangles show the results of 1st and 2nd runs of the same nanoparticles. After the 1st run, the reaction solution was replaced by freshly prepared 0.5 M KI aqueous solution. (b) $^1H$ NMR (aromatic region) and (c) emission spectra of the supernatant solutions obtained after the 1st reaction of **RuCP$^2$**-Zr-**RuP$^4$**-Zr-**RuP$^6$**@Pt-$TiO_2$ or **RuCP$^2$**@Pt-$TiO_2$ by ultracentrifugation. Black lines in (b) are the spectra of **RuCP$^2$** and **RuP$^6$** in $D_2O$ solvent. Black line in (c) shows the emission spectrum of **RuCP$^2$** solution.

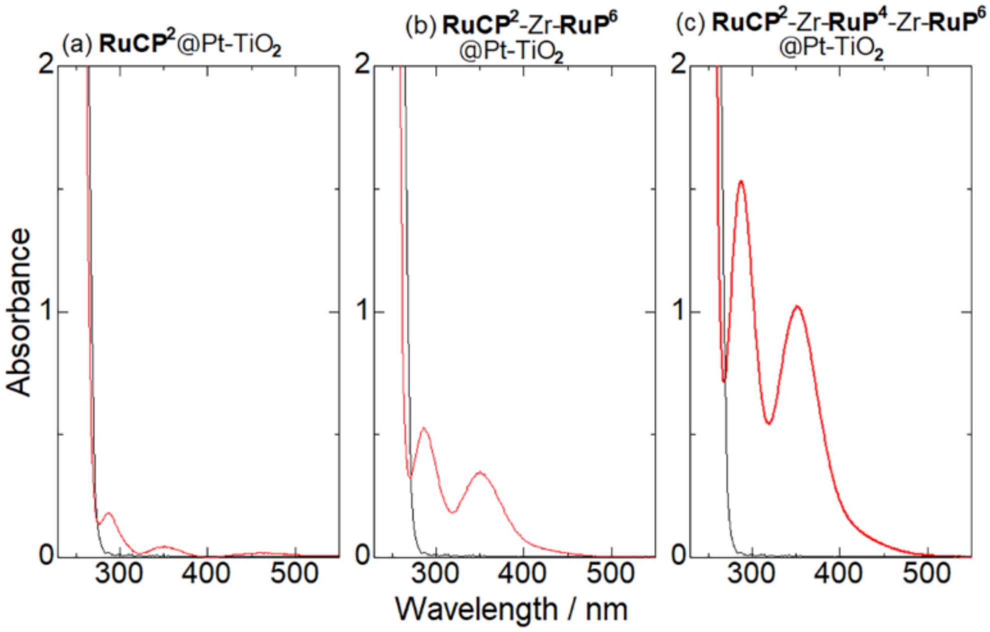

**Figure 3-3-2-3**. UV-Vis absorption spectral changes of the reaction solutions containing (a) **RuCP**$^2$@Pt-TiO$_2$, (b) **RuCP**$^2$-Zr-**RuP**$^6$@Pt-TiO$_2$, or (c) **RuCP**$^2$-Zr-**RuP**$^4$-Zr-**RuP**$^6$@Pt-TiO$_2$ nanoparticles and 0.5 M KI (black) before and (red) after photocatalytic $H_2$ evolution reaction for 6 h. The Ru(II)-PS-multilayered Pt-TiO$_2$ nanoparticles were removed by ultracentrifugation and each supernatant solution (1 mL) was diluted to 10 mL by the addition of water before the spectral measurement.

**Table 3-3-2-2**. Control experiments of photocatalytic hydrogen evolution of **RuCP$^2$**-Zr-**RuP$^6$**@Pt-$TiO_2$.

| Entry [a] | Photocatalyst | Electron Donor (ED) | ED concentration | Light irradiation | Evolved $H_2$ [b] |
|---|---|---|---|---|---|
| 1 | **RuCP$^2$**-Zr-**RuP$^6$**@Pt-$TiO_2$ | KI | 0.5 M | Yes | Yes |
| 2 | **RuCP$^2$**-Zr-**RuP$^6$**@Pt-$TiO_2$ | KBr | 0.5 M | Yes | - |
| 3 | **RuCP$^2$**-Zr-**RuP$^6$**@Pt-$TiO_2$ | NaI | 0.5 M | Yes | Yes |
| 4 | **RuCP$^2$**-Zr-**RuP$^6$**@Pt-$TiO_2$ | CsI | 0.5 M | Yes | Yes |
| 5 | **RuCP$^2$**-Zr-**RuP$^6$**@Pt-$TiO_2$ | $[Cu(dmp)_2]I$ | Saturated | Yes | Yes |
| 6 | **RuCP$^2$**-Zr-**RuP$^6$**@Pt-$TiO_2$ | $[Cu(dmp)_2]Cl$ | Saturated | Yes | - |
| 7 | **RuCP$^2$**-Zr-**RuP$^6$**@Pt-$TiO_2$ | - | - | Yes | - |
| 8[c] | **RuCP$^2$**-Zr-**RuP$^6$**@Pt-$TiO_2$ | $[Cu(dmp)_2]I$ | Saturated | - | - |
| 9[d] | - | $[Cu(dmp)_2]I$ | Saturated | Yes | - |
| 10 | **RuCP$^2$**-Zr-**RuP$^6$**@Pt-$TiO_2$ | $[Co(bpy)_3]Cl_2$ | 3 mM | Yes | - |

[a] Reaction conditions: [Ru] = 100 μM in 20 mM $CH_3COOH$ / $CH_3COONa$ buffer aqueous solution (pH = 5, 5 mL) under blue LED light irradiation ($\lambda = 470 \pm 10$ nm) for 6 h. [b] Gas in the head space was analyzed qualitatively by Gas Chromatography (GC). "Yes" indicates that the evolved amount of $H_2$ was larger than the GC detection limit.

As reported by Mallouk et al.,[35] Pt nanoparticles can catalyse not only $H_2$ evolution but also the reverse reaction, that is, the reduction of oxidized iodine species. The dependence of the photocatalytic activities of **RuCP²**-Zr-**RuP⁶**@Pt-$TiO_2$ and **RuCP²**-Zr-**RuP⁴**-Zr-**RuP⁶**@Pt-$TiO_2$ on Pt-loading amount was estimated to clarify whether the Pt cocatalyst promotes the backward reaction (Figure 3-3-2-1). Activity of **RuCP²**-Zr-**RuP⁴**-Zr-**RuP⁶**@Pt-$TiO_2$ in the initial 30 min was independent of Pt loading amount, suggesting that 1 wt% Pt is sufficient to catalyse the $H_2$ evolution reaction. Notably, the PS TON of **RuCP²**-Zr-**RuP⁴**-Zr-**RuP⁶**@Pt-$TiO_2$ increased twofold by decreasing the loading amount of Pt from 5 to 1 wt%, while a smaller enhancement was observed for **RuCP²**-Zr-**RuP⁶**@Pt-$TiO_2$. Further, the activity of **RuCP²**-Zr-**RuP⁶**@1wt%Pt-$TiO_2$ was only half that of **RuCP²**-Zr-**RuP⁴**-Zr-**RuP⁶**@5wt%Pt-$TiO_2$, even with more Pt present ([Pt] = 0.578 μM and 0.209 μM for **RuCP²**-Zr-**RuP⁶**@1wt%Pt-$TiO_2$ and **RuCP²**-Zr-**RuP⁴**-Zr-**RuP⁶**@5wt%Pt-$TiO_2$, respectively). The TEM images of **RuCP²**-Zr-**RuP⁴**-Zr-**RuP⁶**@Pt-$TiO_2$ nanoparticles with different Pt loading revealed that the diameter of Pt cocatalyst loaded on 1wt%Pt-$TiO_2$ (ca. 3 nm, Figure 3-3-1-5(b)) was smaller than that on 5wt%Pt-$TiO_2$ (ca. 6 nm, Figure 3-3-1-5(a)). Thus, the formation of the third Ru(II)-PS layer should suppresses the back electron transfer from the Pt-$TiO_2$ surface to the oxidized iodine species. This is reasonable because the thickness of the triple-PS-layer estimated from the molecular sizes of the Ru(II) PS and the crosslinking $Zr^{4+}$ cation (ca. 6 nm) is large enough to cover the surface of Pt cocatalyst of 1wt%Pt-$TiO_2$ nanoparticles (Scheme 3-1(b)) that would hamper contact between oxidized iodine species and the Pt cocatalyst. In fact, Pt TON of **RuCP²**-Zr-**RuP⁴**-Zr-**RuP⁶**@1wt%Pt-$TiO_2$ was significantly higher than that of **RuCP²**-Zr-**RuP⁴**-Zr-**RuP⁶**@5wt%Pt-$TiO_2$ (Table 3-3-2-1). The highest apparent quantum yield (AQY) in these system for **RuCP²**-Zr-**RuP⁴**-Zr-**RuP⁶**@1wt%Pt-$TiO_2$ was estimated to be 0.1%, which is comparable to those of DSPs comprising layered niobates with intercalated Pt cocatalyst and coumarin dye (NKX-2677@Pt-$H_4Nb_6O_{17}$, 0.05%)[15] or Ru(II) dye ([Ru(dcbpy)$_3$]@Pt-$K_4Nb_6O_{17}$, $H_2$dcbpy = 4,4′-dicarboxy-2,2′-bipyridine, 0.3%).[35] These similarities suggest that Ru(II)-PS multilayers on the Pt-$TiO_2$ are as effective at suppressing back electron transfer as the intercalated Pt cocatalyst in a layered semiconductor. However, these AQY values of PS-multilayered Pt-$TiO_2$ nanoparticles in the iodide aqueous solution are quite lower than that in the *L*-ascorbic acid sacrificial electron donor solution (e.g. 6.19% for **RuCP²**-Zr-**RuP⁶**@Pt-$TiO_2$)[46], suggesting that the charge-recombination and back electron transfer at the solid-solution interface is still bottle-neck issue.

### 3-3-3 Effect of $I^-$ and $I_3^-$ concentrations.

In order to investigate reactivity with iodide, the dependence of photocatalytic $H_2$ evolution on KI concentration is examined using **RuCP²**-Zr-**RuP⁴**-Zr-**RuP⁶**@Pt-$TiO_2$ (Figure 3-3-3-1(a)). The amount of evolved $H_2$ in the initial 30 min of the reaction was comparable for all KI concentrations (0.1–0.5 M), suggesting that $I^-$ adsorbed on the **RuCP²**-Zr-**RuP⁴**-Zr-**RuP⁶**@Pt-$TiO_2$ surface act as electron donors, driving the initial stage of the hydrogen evolution.[47] In fact, **RuCP²**-Zr-**RuP⁴**-Zr-**RuP⁶**@Pt-$TiO_2$ exhibits a positive zeta potential (+38 mV) in aqueous solution without $I^-$, while it is remarkably shifted to −75 mV in the presence of 0.5 M KI, the same concentration used for the photocatalytic $H_2$ evolution experiment (Table 3-3-3-1). The zeta potential for **RuCP²**-Zr-**RuP⁶**@Pt-$TiO_2$ also shifts to negative, but the shift is about half that of **RuCP²**-Zr-**RuP⁴**-Zr-**RuP⁶**@Pt-$TiO_2$. In contrast, the zeta potential of **RuCP²**@Pt-$TiO_2$ was independent of $I^-$ concentration, suggesting that the driving force for adsorption of $I^-$ on **RuCP²**@Pt-$TiO_2$ is negligible. Recent studies on the photoredox chemistry of hydrogen halides with Ru(II) dyes suggest that electrostatic attraction between $I^-$ and the Ru(II) dye is crucial to regenerate the photooxidized PS dye.[48,49] Thus, the adsorption of $I^-$ on **RuCP²**-Zr-**RuP⁴**-Zr-**RuP⁶**@Pt-$TiO_2$ could be a key to initiate photocatalytic $H_2$ evolution. This hypothesis is consistent with observation that $H_2$ evolution was not detected in the presence of cationic redox-reversible electron donors, $[Co(bpy)_3]Cl_2$ or $[Cu(dmp)_2]Cl$ (bpy = 2,2′-bipyridine, Entries 6 and 10 in Table 3-3-2-2). On the other hand, $H_2$ evolution increased with KI concentration for **RuCP²**-Zr-**RuP⁴**-Zr-**RuP⁶**@Pt-$TiO_2$ when irradiated for more than 1 h. Reduced activity at lower KI concentrations may result from slower desorption of the oxidized iodine species from the nanoparticle surface, because the solubility of $I_2$ in aqueous solution decreases significantly with decreasing $I^-$ anion concentration, thereby inducing charge recombination from the electron-injected Pt-$TiO_2$. This is also consistent with observation that **RuCP²**-Zr-**RuP⁴**-Zr-**RuP⁶**@Pt-$TiO_2$ activity is suppressed by the addition of $I_3^-$ (Figure 3-3-3-1(b)); a negligible difference in PS TOF was observed between the initial 1 h in the presence of 0.2 mM $I_3^-$ (0.3 $h^{-1}$) and the last 1 h (e.g. 5-6 h irradiation, PS TOF =0.25 $h^{-1}$) in the absence of $I_3^-$. Therefore, the decrease in photocatalytic activity with irradiation time likely stems from back electron transfer to the oxidized iodine by-product. In addition, the lower activity in the presence of $I_3^-$ (Figure 3-3-3-1(b)) also suggests that the positively charged **RuCP²**-Zr-**RuP⁴**-Zr-**RuP⁶**@Pt-$TiO_2$ nanoparticle surface would attract not only $I^-$ anions but also the oxidized $I_3^-$ anions. The effect of excitation light absorption by $I_3^-$ is assumed to be negligible because of the lower the molar absorptivity[50] of $I_3^-$ (Figure 3-3-2-1(b), $\varepsilon = 754\ M^{-1}\ cm^{-1}$ at 470 nm) than that of Ru(II) PSs (ca. 15000 $M^{-1}\ cm^{-1}$, Table 3-3-3-2). Further, the activity of **RuCP²**-Zr-**RuP⁶**@Pt-$TiO_2$ completely lost in the presence of 0.2 mM $I_3^-$ solution where **RuCP²**-Zr-**RuP⁴**-Zr-**RuP⁶**@Pt-$TiO_2$ was still active (Figure 3-3-3-1(b) and 3-3-3-2), suggesting that thicker PS-multilayer is more effective for the suppression of the back-electron transfer from the Pt-$TiO_2$ surface to the oxidized iodine species.

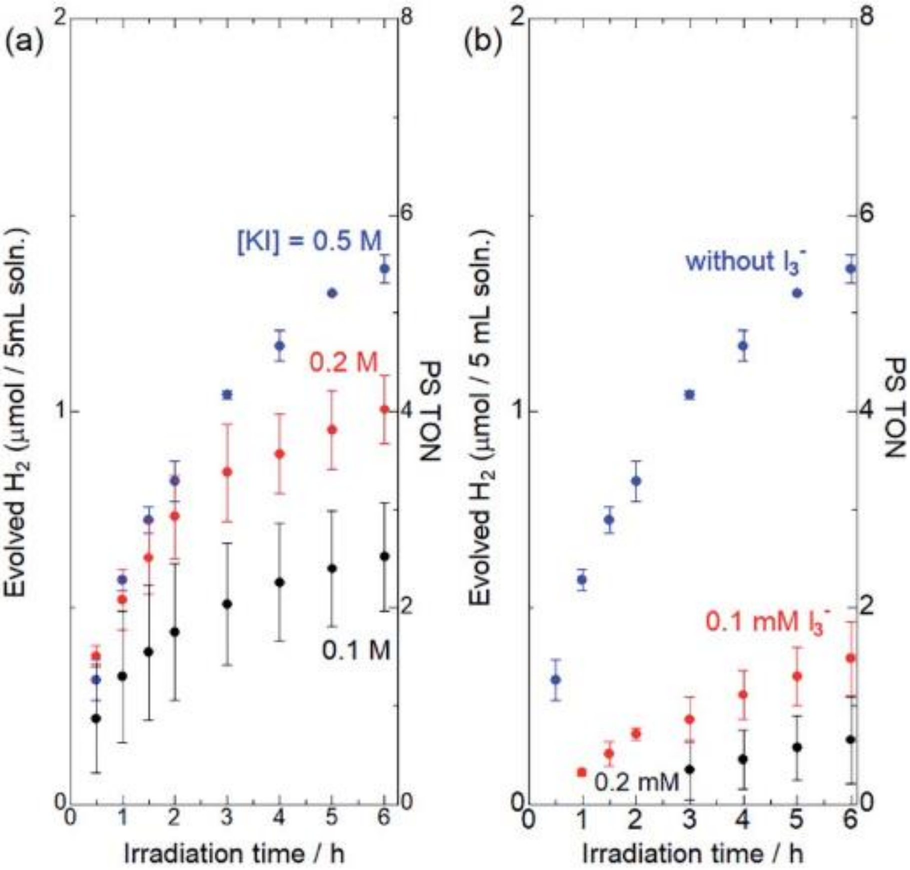

**Figure 3-3-3-1.** (a) KI concentration dependence of photocatalytic $H_2$ evolution reaction with **RuCP$^{2}$**-Zr-**RuP$^{4}$**-Zr-**RuP$^{6}$**@Pt-$TiO_2$ (100 μM Ru(II) dye, 5wt%Pt-$TiO_2$). The black, red, and blue circles represent results in the presence of 0.1, 0.2, and 0.5 M KI, respectively (Initial pH = 2.0, λ = 470 ± 10 nm). (b) Initial $I_3^-$ concentration dependence of photocatalytic $H_2$ evolution reactions driven by **RuCP$^{2}$**-Zr-**RuP$^{4}$**-Zr-**RuP$^{6}$**@Pt-$TiO_2$ (100 μM Ru(II) dye, 5wt%Pt-$TiO_2$) in 0.5 M KI aqueous solution, respectively (Initial pH = 2.0, λ = 470 ± 10 nm). The black, red, and blue circles represent results in the absence and presence of 0.1 and 0.2 mM $I_3^-$, respectively (Initial pH = 2.0, λ = 470 ± 10 nm).

**Table 3-3-3-1**. Zeta-potentials of Ru(II)-PS-immobilized nanoparticles in the absence/presence of 0.5 M KI aqueous solution (pH = 2.0).

| Photocatalyst | without KI (mV) | with 0.5 M KI (mV) | with 0.5 M KBr (mV) |
|---|---|---|---|
| **RuCP$^{2}$**@Pt-$TiO_2$ | −0.36 | +3.6 | - |
| **RuCP$^{2}$**-Zr-**RuP$^{6}$**@Pt-$TiO_2$ | +45 | −1.9 | +4.00 |
| **RuCP$^{2}$**-Zr-**RuP$^{4}$**-Zr-**RuP$^{6}$**@Pt-$TiO_2$ | +38 | −75 | +7.46 |

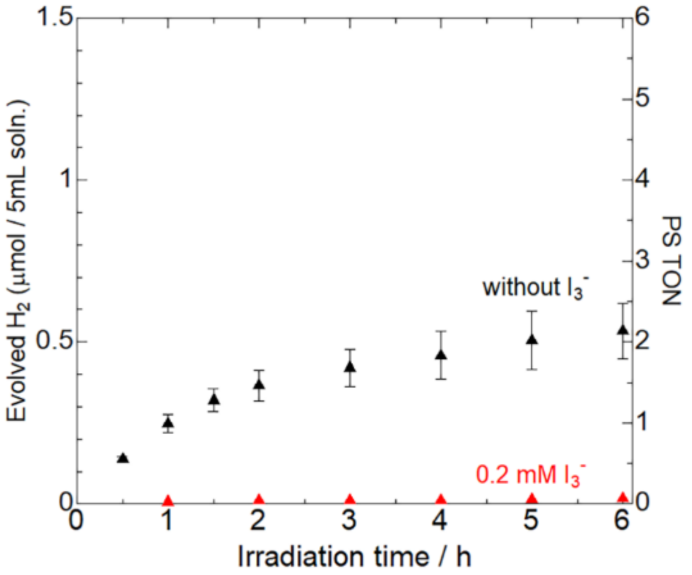

**Figure 3-3-3-2.** Triiodide ion-concentration-dependence of the photocatalytic $H_2$ evolution reaction of **RuCP**$^2$-Zr-**RuP**$^6$@Pt-$TiO_2$ nanoparticles (100 μM of the Ru(II) complex) in 0.5 M KI aqueous solution. Black and red triangles show the results in the absence and presence of 0.2 mM $I_3^-$, respectively. A blue LED light (λ = 470 ± 10 nm) was used as the irradiation source. The initial pH was adjusted to be 2.0 by adding HCl aq.

**Table 3-3-3-2**. Molar absorptivity and the absorbance of Ru(II)-PS-multilayered Pt-$TiO_2$ and triiodide at 470 nm after 6 h reaction solution.

| | Molar absorptivity ($L\cdot cm^{-1}\cdot mol^{-1}$) | | Absorbance after 6 h reaction | |
|---|---|---|---|---|
| Photocatalyst | $I_3^-$ | Ru(II) dye | $I_3^-$ | Ru(II) dye |
| **RuCP**$^2$@Pt-$TiO_2$ | 754 | 14600 | <0.01 | 1.46 |
| **RuCP**$^2$-Zr-**RuP**$^6$@Pt-$TiO_2$ | 754 | 16249 | 0.08 | 1.62 |
| **RuCP**$^2$-Zr-**RuP**$^4$-Zr-**RuP**$^6$@Pt-$TiO_2$ | 754 | 16610 | 0.26 | 1.66 |

## 3-3-4 Photocurrent-voltage characteristics.

To investigate photoinduced electron-injection efficiency, photocurrent-voltage (*J*-*V*) characteristics of three Ru(II)-PS-multilayered $TiO_2$-ITO photoelectrodes (**RuCP$^2$**@$TiO_2$-ITO, **RuCP$^2$**-Zr-**RuP$^6$**@$TiO_2$-ITO, and **RuCP$^2$**-Zr-**RuP$^4$**-Zr-**RuP$^6$**@$TiO_2$-ITO) are investigated in two different electrolyte solutions (Figures 3-3-4-1). These three photoelectrodes were prepared in a similar manner as the Ru(II)-PS-multilayered Pt-$TiO_2$ nanoparticles (section 3-2-2). Scanning electron microscopy images indicate that the mesoporous structure of the $TiO_2$-ITO electrode is retained after the immobilization of Ru(II)-PS-multilayers (Figure 3-3-4-2). Energy dispersive X-ray fluorescence analysis for **RuCP$^2$**-Zr-**RuP$^4$**-Zr-**RuP$^6$**@$TiO_2$-ITO revealed that Ru(II) dyes and $Zr^{4+}$ ions are immobilized uniformly on the surface of the $TiO_2$-ITO electrode (Figure 3-3-4-3). Further, the intensities of Ru K$\alpha$ and Zr K$\alpha$ radiations in X-ray fluorescence spectra increase in the order of **RuCP$^2$**@$TiO_2$-ITO < **RuCP$^2$**-Zr-**RuP$^6$**@$TiO_2$-ITO < **RuCP$^2$**-Zr-**RuP$^4$**-Zr-**RuP$^6$**@$TiO_2$-ITO (Figure 3-3-4-4 and Table 3-3-4-1), suggesting that the Ru(II)-PS-multilayered structure on the $TiO_2$-ITO surface is the same as that on the Pt-$TiO_2$ nanoparticle surface. In the methoxyacetonitrile solution, the **RuCP$^2$**-Zr-**RuP$^4$**-Zr-**RuP$^6$**@$TiO_2$-ITO exhibits less than half the short-circuit current ($J_{SC}$) of **RuCP$^2$**-Zr-**RuP$^6$**@$TiO_2$-ITO (Figure 3-3-4-1(a) and Table 3-3-4-2), whereas the open-circuit voltage ($V_{OC}$) and fill factor (FF) are comparable for both. In contrast, the performance of the PS-single-layered **RuCP$^2$**@$TiO_2$-ITO was considerably lower than the others. The higher $V_{OC}$ of PS-multilayered photoelectrodes than that of **RuCP$^2$**@$TiO_2$-ITO suggests that the back-electron transfer from $TiO_2$ surface to oxidized iodine mediator could be suppressed by thicker Ru(II)-PS-multilayer. Considering the PS-multilayered structure on the $TiO_2$ substrate, the improved $J_{SC}$ by the PS-multilayering is basically due to the effective light absorption by higher loading amount of Ru(II)-PS per unit area of $TiO_2$ surface as suggested by the higher absorbance of the PS-double- and PS-triple-layered photoelectrodes than that of PS-single-layer photoelectrode in UV-Vis diffuse reflectance spectra (Figure 3-3-4-5). In addition, the efficient energy transfer among the Ru(II) PS layers[40] coupled with the rapid interfacial electron transfer from Ru(II)* dye to $TiO_2$ could enhance the photo-induced electron-injection efficiency. As discussed in previous paper,[45] the hole generated by photoinduced interfacial electron transfer from Ru(II)*-PS to $TiO_2$ could can migrate from inner to outer Ru(II)-PS layer because of the favorable Ru(III)/Ru(II) redox potential differences (Scheme 3-3-4). As a result, the injected electron and hole are spatially separated to suppress effectively the charge-recombination process. On the other hand, a plausible origin for lower $J_{SC}$ of **RuCP$^2$**-Zr-**RuP$^4$**-Zr-**RuP$^6$**@$TiO_2$-ITO than **RuCP$^2$**-Zr-**RuP$^6$**@$TiO_2$-ITO is the smaller driving force for hole transfer in multilayered PS structures after photoinduced electron injection to $TiO_2$ (Scheme 3-3-4). Namely, the driving force for the one-step hole transfer process from the inner to outer PS-layer in **RuCP$^2$**-Zr-**RuP$^6$**@$TiO_2$-ITO was about 0.2 V, and about half that in **RuCP$^2$**-Zr-**RuP$^4$**-Zr-**RuP$^6$**@$TiO_2$-ITO (ca. 0.1 V), per step, resulting in slower hole transfer in a multilayered PS structure. This is confirmed by the results of incident photon to current conversion efficiency (IPCE) spectra (Figure 3-3-4-5(a)). Higher IPCE is observed for **RuCP$^{2}$**-Zr-**RuP$^{6}$**@TiO$_2$-ITO than for **RuCP$^{2}$**-Zr-**RuP$^{4}$**-Zr-**RuP$^{6}$**@TiO$_2$-ITO over the entire measured range; the spectral shape qualitatively matches that of the UV-Vis diffuse reflectance spectra of these photoelectrodes (Figure 3-3-4-5(b)). These results are consistent with previously reported results on photocatalytic $H_2$ evolution activity in the sacrificial electron donating L-ascorbic acid solution.[45]

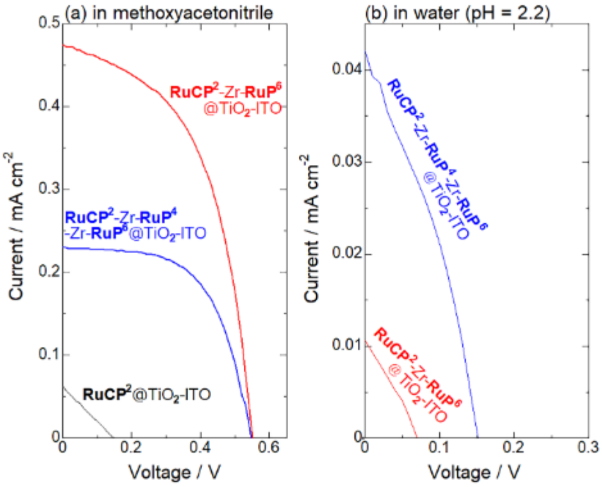

**Figure 3-3-4-1.** Photocurrent-voltage (*J*-*V*) characteristics of (black) **RuCP$^{2}$**@TiO$_2$-ITO, (red) **RuCP$^{2}$**-Zr-**RuP$^{6}$**@TiO$_2$-ITO, or (blue) **RuCP$^{2}$**-Zr-**RuP$^{4}$**-Zr-**RuP$^{6}$**@TiO$_2$-ITO as the photoanode in the presence of (a) 0.1 M LiI, 0.05 M $I_2$, and 0.5 M *t*-butyl-pyridine in methoxyacetonitrile under AM1.5G irradiation or (b) 0.5 M KI, 0.05 M $I_2$ in water (pH = 2.2) under blue light irradiation ($\lambda$ = 470 nm, 800 W/m$^2$). A PEDOT-TMA coated ITO electrode was used as the counter electrode.

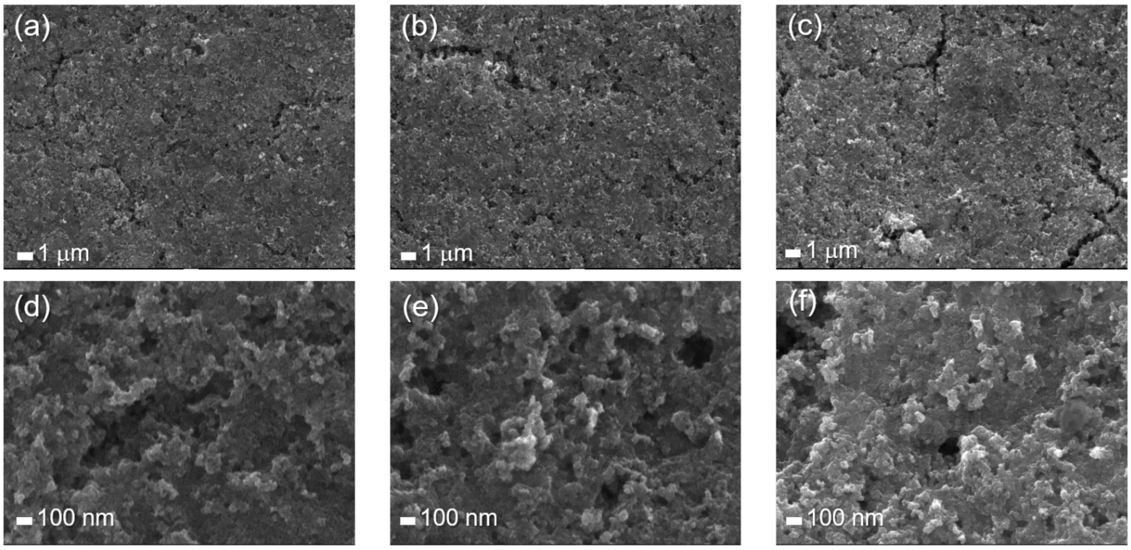

**Figure 3-3-4-2**. SEM images of (a, d) **RuCP**$^2$@TiO$_2$-ITO, (b, e) **RuCP**$^2$-Zr-**RuP**$^6$@TiO$_2$-ITO, (c, f) **RuCP**$^2$-Zr-**RuP**$^4$-Zr-**RuP**$^6$@TiO$_2$-ITO. The scale bar of (a-c) and (d-f) is 1 μm and 100 nm, respectively.

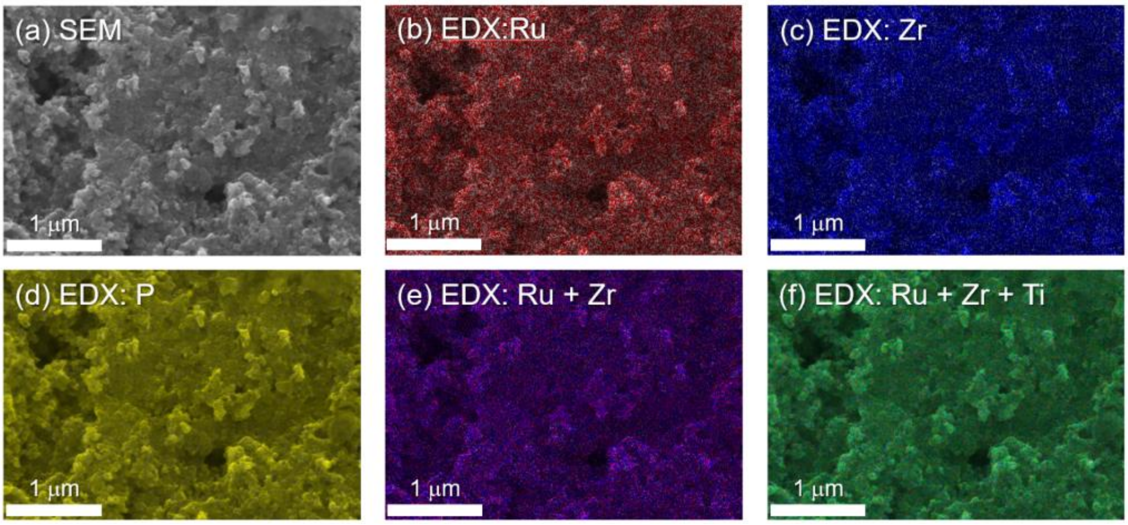

**Figure 3-3-4-3**. (a) SEM and (b-f) EDX images of **RuCP**$^2$-Zr-**RuP**$^4$-Zr-**RuP**$^6$@TiO$_2$-ITO of the elements (b) Ru, (c) Zr, (d) P, (e) Ru and Zr, (f) Ru , Zr, and Ti. Each scale bar is 1 μm.

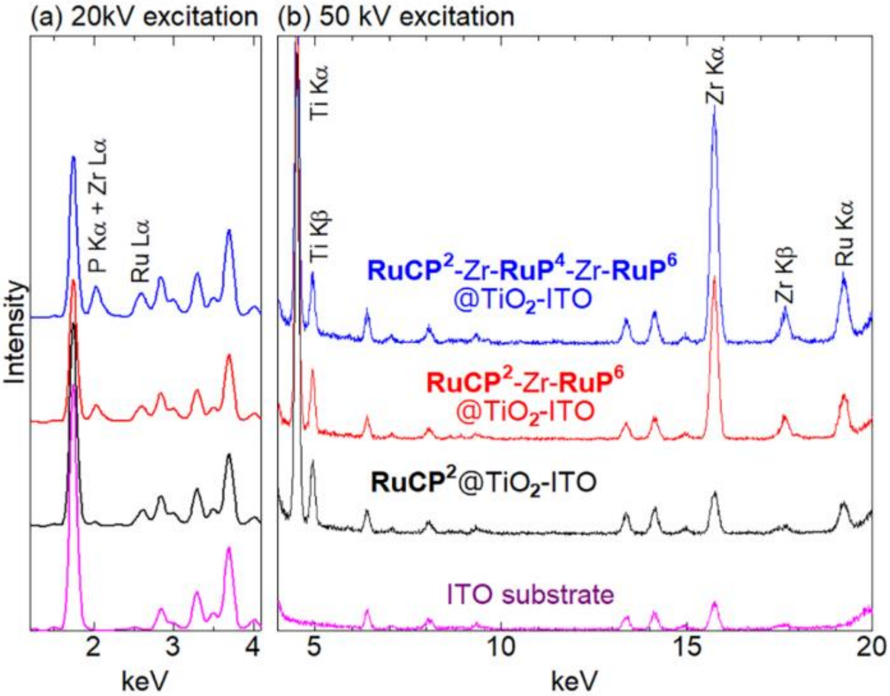

**Figure 3-3-4-4**. XRF spectra of ITO substrate (pink), **RuCP$^2$**@TiO$_2$-ITO (black), **RuCP$^2$**-Zr-**RuP$^6$**@TiO$_2$-ITO (red), **RuCP$^2$**-Zr-**RuP$^4$**-Zr-**RuP$^6$**@TiO$_2$-ITO (blue) in the solid state with (a) 20 kV and (b) 50 kV excitation. All spectra of Ru(II)-PS-multilayered TiO$_2$-ITO electrodes were normalized by using Ti Kβ peak.

**Table 3-3-4-1**. Immobilized amount of Ru(II) photosensitizer on TiO$_2$-ITO photoelectrode.

| | Weight percentage of elements | | | |
|---|---|---|---|---|
| Photoelectrode | Pt | Ti | Zr | Ru |
| **RuCP$^2$**-@TiO$_2$-ITO | 1.75 | 97.99 | -[a] | 0.26 |
| **RuCP$^2$**-Zr-**RuP$^6$**@TiO$_2$-ITO | 7.16 | 91.26 | 1.26 | 0.32 |
| **RuCP$^2$**-Zr-**RuP$^4$**-Zr-**RuP$^6$**@TiO$_2$-ITO | 12.87 | 85.13 | 1.58 | 0.42 |

[a] *Comparable intensity to that of bare ITO electrode was observed.*

**Table 3-3-4-2.** The photovoltaic data of DSSCs based on Ru(II)-PS-multilayered $TiO_2$-ITO photoanodes in methoxyacetonitrile (MAN) and water $I^-/I_3^-$ electrolyte solutions.

| | $J_{SC}$ (mA / cm$^2$) | | $V_{OC}$ (V) | | FF | | PCE (%) | |
|---|---|---|---|---|---|---|---|---|
| Photoelectrode [c] | MAN[a] | Water[b] | MAN[a] | Water[b] | MAN[a] | Water[b] | MAN[a] | Water[b] |
| **RuCP**$^2$@$TiO_2$-ITO | 0.063 | - | 0.148 | - | 0.24 | - | 0.002 | - |
| **RuCP**$^2$-Zr-**RuP**$^6$@$TiO_2$-ITO | 0.475 | 0.011 | 0.552 | 0.070 | 0.52 | 0.28 | 0.136 | $2.7 \times 10^{-4}$ |
| **RuCP**$^2$-Zr-**RuP**$^4$-Zr-**RuP**$^6$ @$TiO_2$-ITO | 0.230 | 0.042 | 0.547 | 0.151 | 0.59 | 0.34 | 0.075 | $2.7 \times 10^{-3}$ |

[a] LiI (0.1 M), $I_2$ (0.05 M), and 0.5 M *t*-butyl-pyridine in methoxy-acetonitrile under AM1.5G irradiation. [b] KI (0.5 M), and $I_2$ (0.05 M), in water (pH = 2) under blue light irradiation ($\lambda_{ex}$ = 470 nm, 800 W/m$^2$). [c] A PEDOT-TMA coated ITO electrode was used as the counter electrode.

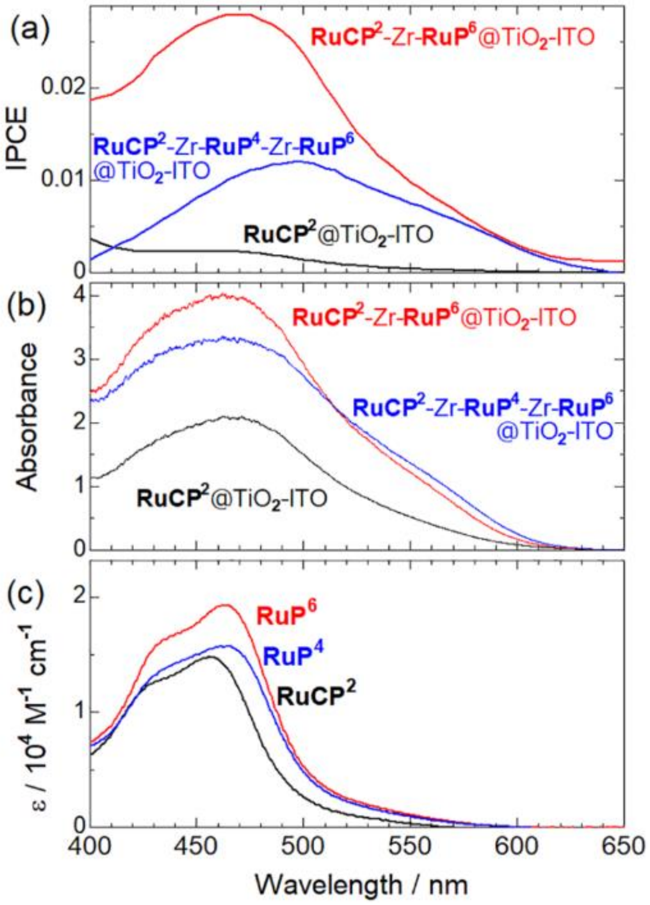

**Figure 3-3-4-5**. (a) IPCE action spectra of (black) **RuCP$^2$**@TiO$_2$-ITO, (red) **RuCP$^2$**-Zr-**RuP$^6$**@TiO$_2$-ITO, or (blue) **RuCP$^2$**-Zr-**RuP$^4$**-Zr-**RuP$^6$**@TiO$_2$-ITO as the photoanode in the presence of LiI (0.1 M), I$_2$ (0.05 M), and 0.5 M *t*-butyl-pyridine in methoxy-acetonitrile under AM1.5G irradiation. A PEDOT-TMA coated ITO electrode was used as the counter electrode. (b) UV-Vis diffuse reflectance spectra of these photoelectrodes in air. (c) UV-Vis absorption spectra of (red) **RuP$^6$**, (blue) **RuP$^4$**, and (black) **RuCP$^2$** dyes in water (pH = 2.2).

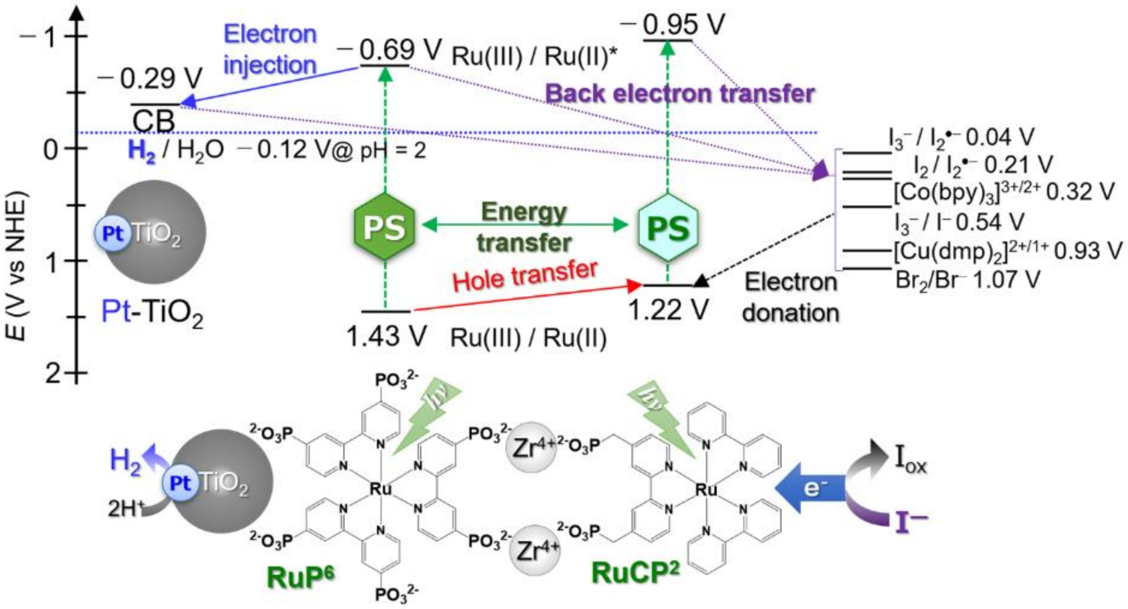

**Scheme 3-3-4**. Schematic diagram showing a plausible energy and electron transfer mechanism of **RuCP$^2$**-Zr- **RuP$^6$**@Pt-TiO$_2$. Redox potentials of bromide, iodide species, [Co(bpy)$_3$]$^{3+/2+}$ and [Cu(dmp)$_2$]$^{2+/1+}$ complexes are interfered from the literatures.[2,3,4]

## 3-4 Conclusion

In summary, nanoparticle photocatalysts with multi-layered PS structure, **RuCP$^2$**@Pt-TiO$_2$, **RuCP$^2$**-Zr-**RuP$^6$**@Pt-TiO$_2$, and **RuCP$^2$**-Zr-**RuP$^4$**-Zr-**RuP$^6$**@Pt-TiO$_2$, were evaluated for photocatalytic H$_2$ evolution activity in a redox-reversible electron-donating iodide aqueous solution. The activity was greatly improved by multilayering Ru(II) PSs with Zr$^{4+}$ cations, as the multilayered Ru(II) PS structure not only allows iodide access to sites to promote electron donation but also prevents the oxidized iodine species from the direct accessing the surface of Pt-TiO$_2$ nanoparticle. The loading amount of Pt-cocatalyst on the TiO$_2$ surface significantly affected on the activity; the smaller Pt-cocatalyst-loaded and the thicker-Ru(II)-dye-layered nanoparticle, **RuCP$^2$**-Zr-**RuP$^4$**-Zr-**RuP$^6$**@1wt%Pt-TiO$_2$ was the best among the photocatalysts used in this work. In addition, the stability of Ru(II) dyes immobilized by the coordination bonds of phosphonate anchors to Zr$^{4+}$ cations was superior than that immobilized directly on the TiO$_2$ surface. The results described herein make a valuable contribution to the design of Z-scheme water-splitting DSP and DSPEC.

## 3-5 References

A. Fujishima, K. Honda, *Nature* **1972**, *238*, 37–38.

M. Grätzel, *Acc. Chem. Res.* **1981**, *14*, 376-384.

A. Kudo, Y. Miseki, *Chem. Soc. Rev.* **2009**, *38*, 253-278.

Y. Ma, X. Wang, Y. Jia, X. Chen, H. Han, C. Li, *Chem. Rev.* **2014**, *114*, 9887-10043.

T. Hisatomi, K. Domen, *Nat. Cat.*, **2019**, *2*, 387-399.

Z. Wang, C. Li, K. Domen, *Chem. Soc. Rev.*, **2019**, *48*, 2109-2125.

K. Maeda, *ACS Catal.* ***2013***, *3*, 1486-1503.

X. Li, J. Yu, J. Low, Y. Fang, J. Xiao X. Chen, *J. Mater. Chem. A* **2015**, *3*, 2485-2534.

D. M. Fabian, S. Hu, N. Singh, F. A. Houle, T. Hisatomi, K. Domen, F. E. Osterloh, S. Ardo, *Energy Environ. Sci.* **2015**, *8*, 2825-2850.

K. Sekizawa, K. Maeda, K. Domen, K. Koike, O. Ishitani. *J. Am. Chem. Soc.*, **2013**, *135*, 4596-4599.

S. Chen, T. Takata, K. Domen, *Nat. Rev. Mater.* **2017**, *2*, 17050-17053.

Y. Wang, H. Suzuki, J. Xie, O. Tomita, D. Martin, M. Higashi, D. Kong, R. Abe, J. Tang. *Chem. Rev.*, **2018**, *118*, 5201-5241.

Y. Iwase, O. Tomita, H. Naito, M. Higashi, R. Abe. *J. Photochem. Photobiol. A: Chem.*, **2018**, *356*, 347-354.

C. D. Windle, H. Kumagai, M. Higashi, R. Brisse, S. Bold, B. Jousselme, M. C.-Kerlidou, K. Maeda, R. Abe, O. Ishitani, V. Artero. *J. Am. Chem. Soc.*, **2019**, *141*, 9593-9602.

R. Abe, K. Shinmei, N. Koumura, K. Hara, B. Ohtani, *J. Am. Chem. Soc.*, **2013**, *135*, 16872-16884.

Q. Wang, T. Hisatomi, Q. Jia, H. Tokudome, M. Zhong, C. Wang, Z. Pan, T. Takata, M. Nakabayashi, N. Shibata, Y. Li, I. D. Sharp, A. Kudo, T. Yamada, K. Domen, *Nat. Mater.* ***2016***, *15*, 611–615.

M. S. Eberhart, L. M. R. Bowers, B. Shan, L. T-Gautier, M. K. Brennaman, J. M. Papanikolas, T. J. Meyer. *J. Am. Chem. Soc.*, **2018**, *140*, 9823-9826.

J. Warnam, J. Willkomm, Y. Farré, Y. Pellegrin, M. Boujtita, F. Odobel, E. Reisner. *Chem. Sci.*, **2019**, *10*, 2758-2766.

D. Wang, R. N. Sampaio, L. T-Gautier, S. L. Marquard, B. H. Farnum, B. D. Sherman, M. V. Sheridan, C. J. Dares, G. J. Meyer, T. J. Meyer. *J. Am. Chem. Soc.*, **2019**, *141*, 7926-7933.

B. O'Regan, M. Grätzel, *Nature* **1991**, *353*, 737-740.

S. Ardo, G. J. Meyer, *Chem. Soc. Rev.* **2009**, *38*, 115-164.

S. Mathew, A. Yella, P. Gao, R. Humphry-Baker, B. F. E. Curchod, N. Ashari-Astani, I. Tavernelli, U. Rothlisberger, M. K. Nazeeruddin, M. Grätzel, *Nat. Chem.* **2014**, *6*, 242-247.

D. F. Zigler, Z. A. Morseth, L. Wang, D. L. Ashford, M. K. Brennaman, E. M. Grumstrup, E. C. Brigham, M. K. Gish, R. J. Dillon, L. Alibabaei, G. J. Meyer, T. J. Meyer, J. M. Papanikolas, *J. Am. Chem. Soc.*, **2016**, *138*, 4426.

P. Xu, T. E. Mallouk. *J. Phys. Chem. C,* **2019**, *123*, 299-305.

L. Hammarström, *Acc. Chem. Res.* **2015**, *48*, 840-850.

D. L. Ashford, M. K. Gish, A. K. Vannucci, M. K. Brennaman, J. L. Templeton, J. M. Papanikolas, T. J. Meyer, *Chem. Rev*. **2015**, *115*, 13006-13049.

J. Willkomm, K. L. Orchard, A. Reynal, E. Pastor, J. R. Durrant, E. Reisner, *Chem. Soc. Rev.* **2016**, *45*, 9-23.

W. Motonari, *Sci. Technol. Adv. Mater.* **2017**, *18*, 705-723.

P. Xu, N. S. McCool, T. E. Mallouk, *Nano Today* ***2017***, *14*, 42-58.

T. J. Meyer, M. V. Sheridan, B. D. Sherman, *Chem. Soc. Rev.* **2017**, *46*, 6148-6169.

M. D. Brady, L. Troian-Gautier, R. N. Sampaio, T. C. Motley, G. J. Meyer, *ACS Appl. Mater. Interfaces* **2018**, *10,* 31312-31323.

W. J. Youngblood, S.-H. A. Lee, K. Maeda, T. E. Mallouk, *Acc. Chem. Res.* **2009**, *42*, 1966-1973.

M. R. Nellist, F. A. L. Laskowski, F. Lin, T. J. Mills, S. W. Boettcher, *Acc. Chem. Res.* **2016**, *49*, 733-740.

H. Suzuki, O. Tomita, M. Higashi, R. Abe. *J. Mater. Chem. A*, **2016**, *4*, 14444-14452.

Y. I. Kim, S. Salim, M. J. Huq, T. E. Mallouk, *J. Am. Chem. Soc.* **1991**, *113*, 9561-9563.

Y. Pellegrin, F. Odobel, *C. R. Chimie*, **2017**, *20*, 283-295.

S. Takizawa, N. Ikuta, F. Zeng, S. Komaru, S. Sebata, S. Murata. *Inorg. Chem.*, **2016**, *55*, 8723-8735.

K. Yamamoto, A. Call, K. Sakai. *Chem. Eur. J.*, **2018**, *24*, 16620-16629.

K. Wu, K. Li, S. Chen, Y. Hou, Y. Lu, J. Wang, M. Wei, M. Pan, C. Su. *Angew. Chem. Int. Ed.*, **2020**, *59*, 2639-2643.

K. Hanson, D. A. Torelli, A. K. Vannucci, M. K. Brennaman, H. Luo, L. Alibabaei, W. Song, D. L. Ashford, M. R. Norris, C. R. K. Glasson, J. J. Concepcion, T. J. Meyer, *Angew. Chem., Int. Ed.* **2012**, *51*, 12782-12785.

O. O. Ogunsolu, I. A. Murphy, J. C. Wang, A. Das, K. Hanson, *ACS Appl. Mater. Interfaces* **2016**, *8*, 28633-28640.

R. E. Bangle, G. J. Meyer. *J. Phys. Chem. C,* **2019**, *123*, 25967−25976.

M. R. Norris, J. J. Concepcion, C. R. K. Glasson, Z. Fang, A. M. Lapides, D. L. Ashford, J. L. Templeton, T. J. Meyer. *Inorg. Chem.*, **2013**, *52*, 21492-12501.

J. C. Wang, S. P. Hill, T. Dilbeck, O. O. Ogunsolu, T. Banerjee, K. Hanson, *Chem. Soc. Rev.* **2018**, *47*, 107-148.

S. Furugori, A. Kobayashi, A. Watanabe, M. Yoshida, M. Kato, *ACS Omega*, **2017**, *2*, 3901-3912.

N. Yoshimura, A. Kobayashi, M. Yoshida, M. Kato, *Bull. Chem. Soc. Jpn.,* **2019**, *92*, 1793-1800.

F.G.L. Parlane, C. Mustoe, C. W. Kellett, S. J. Simon, W. B. Swords, G. J. Meyer, P. Kennepohl, C. P. Berlinguette, *Nat. Commun.* **2017**, *8*, 1761.

A. Marton, C. C. Clark, R. Srinivasan, R. E. Freundlich, A. A. N. Sarjeant, G. J. Meyer, *Inorg. Chem.* **2006**, *45*, 362-369.

L. Troian-Gautier, M. D. Turlington, S. A. M. Wehlin, A. B. Maurer, M. D. Brady, W. B. Swords, G. J. Meyer, *Chem. Rev.*, **2019**, *119*, 4628-4683.

A. D. Awtrey, R. E. Connick, *J. Am. Chem. Soc.,* **1951**, *73*, 1842-1843.

H. Park, W. Choi, H. R. Hoffmann, *J. Mater. Chem.* **2008**, *18*, 2379−2385.

M. R. Norris, J. J. Concepcion, C. R. K. Glasson, Z. Fang, A. M. Lapides, D. L. Ashford, J. L. Templeton, T. J. Meyer, *Inorg. Chem.* **2013**, *52*, 12492−12501.

# Chapter 4

# Enhancement of Photocatalytic Activity for Hydrogen Production by Surface Modification of Pt-TiO₂ Nanoparticles with a Double Layer of Photosensitizers

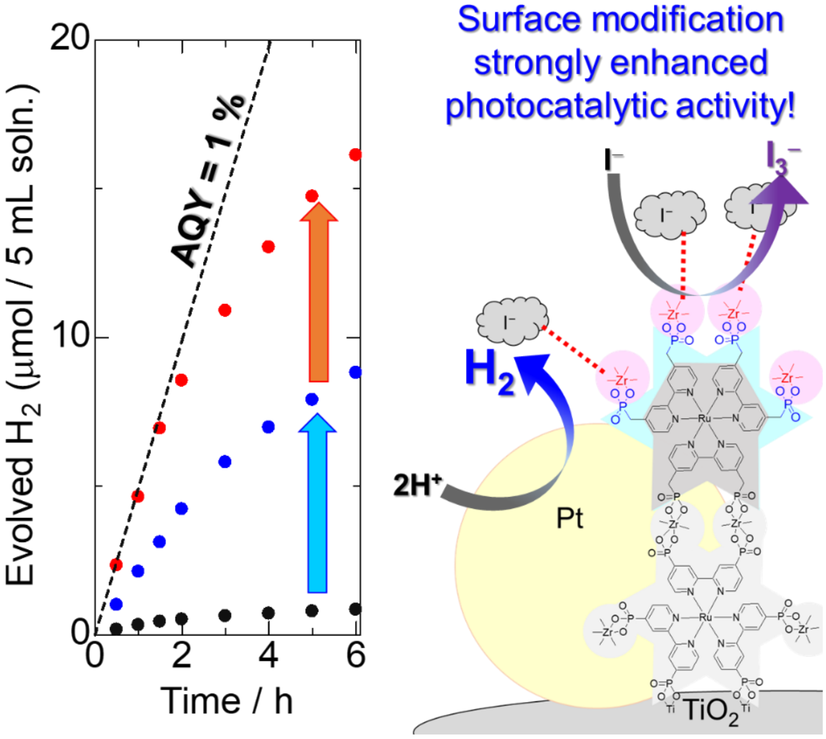

## 4-1 Introduction

"Solar fuel" made using sunlight energy, a sustainable energy source, has attracted considerable attention in recent decades as a promising solution to global warming and the depletion of fossil fuels.[1–5] Photocatalytic water splitting is a simple reaction to produce $H_2$ as a solar fuel, and, since the discovery of the Honda–Fujishima effect,[6] many studies have been conducted using semiconductor materials[7–12] and perovskite-type composites.[13–15] The sensitization of a semiconductor photocatalyst using a dye, yielding a so-called dye-sensitized photocatalyst (DSP), is a useful strategy to improve the light absorption ability in the visible region by exploiting the absorption bands of the surface-immobilized dye.[16–25] This mechanism is also applicable for Z-scheme water-splitting photocatalysis composed of oxygen- and hydrogen-evolution photocatalysts coupled with a suitable redox mediator.[26–29] To construct highly active Z-scheme water splitting photocatalysts, the charge separation efficiency in the DSP must be improved and the selective recognition of oxidized or reduced mediators is important for achieving one-way electron transfer from the oxygen evolution photocatalyst to hydrogen evolution photocatalyst. Although most studies of DSPs have been conducted in the presence of sacrificial electron donators to promote the water-splitting half reaction,[30–35] there have been several reports concerning water reduction or overall water splitting in the presence of redox-reversible electron mediators.[36,37] In 1993, Mallouk and co-workers achieved an apparent quantum yield (AQY) of 0.3% using a Ru(II) photosensitizer (PS) immobilized on the surface of a water reduction catalyst, $Pt/H_xK_{4-x}Nb_6O_{17}$, using iodide as a redox-reversible electron donor.[38] In 2013, Abe *et al.* reported overall water splitting (AQY = 0.05%) using coumarin derivatives (NKX-2677) immobilized on $Pt/H_xK_{4-x}Nb_6O_{17}$ as a water reduction DSP coupled with an $O_2$ evolution photocatalyst comprising $IrO_2$–$Pt/WO_3$ and iodide redox mediator.[39] Recently, Maeda and co-workers reported a high AQY value (2.4%) for a Z-scheme DSP composed of Ru(II) dye-sensitized $Al_2O_3/Pt/HCa_2Nb_3O_{10}$ nanosheets for water reduction and $PtO_x$/H–Cs–$WO_3$ $O_2$ evolution photocatalyst.[40] These remarkable works suggest that the suppression of the back reaction from the $H_2$ evolution Pt cocatalyst to the oxidized redox mediator by immobilization of Pt cocatalyst in the interlayer space of layered niobates is a key strategy for achieving electron donation from the redox mediator. However, this approach does not improve the charge separation efficiency between the surface-immobilized PS and redox mediator.

Thus, as described in chapter 2 and 3, multi-dye-layers on the Pt-cocatalyst-loaded $TiO_2$ (Pt-$TiO_2$) nanoparticle surface has been systematically prepared using phosphonate-functionalized Ru(II)-polypyridyl complexes as photosensitizing dyes with a $Zr^{4+}$ cation binder and found that the photocatalytic $H_2$ evolution activity is remarkably improved by using multiple layers of the Ru(II) PS.[41,42] Recently, the triple-dye-layered nanoparticle photocatalysts, **RuCP$^2$**-Zr-**RuP$^4$**-Zr-**RuP$^6$**@1 wt%Pt-$TiO_2$ (**RuCP$^2$** = $[Ru(bpy)_2(mpbpy)]^{2-}$, **RuP$^4$** = $[Ru(bpy)(pbpy)_2]^{6-}$, **RuP$^6$** =

$[Ru(pbpy)_3]^{10-}$, bpy = 2,2′-bipyridine, $H_4$mpbpy = 2,2′-bipyridine-4,4′-bis(methane-phosphonic acid), and $H_4$pbpy = 2,2′-bipyridine-4,4′-bis(phosphonic acid)) achieved AQYs of 0.1% in the presence of iodide because of the electrostatic interaction between iodide and positively charged nanoparticle surface.[43] This result is remarkable because the $H_2$ evolution proceeded photocatalytically in the presence of the iodide redox mediator, even though the Pt cocatalyst was simply loaded on the $TiO_2$ nanoparticle surface.

In this work, to enhance the electron donation from iodide, it was focused on the surface structure of the nanoparticle photocatalyst. Specifically, two different double-PS-layer Pt-$TiO_2$ nanoparticles with different surface structures were synthesized: **RuCP$^{6}$**-Zr-**RuP$^{6}$**@Pt-$TiO_2$ having phosphate groups on the surface and Zr-**RuCP$^{6}$**-Zr-**RuP$^{6}$**@Pt-$TiO_2$ with $Zr^{4+}$-phosphate groups on the surface (Schemes 4-1), as well as previously developed **RuCP$^{2}$**-Zr-**RuP$^{6}$**@Pt-$TiO_2$ without any surface phosphonates. The Ru(II) PS **RuCP$^{6}$** immobilized on the outer layer exhibited a comparable Ru(III)/Ru(II) redox potential (1.12 V vs. normal hydrogen electrode (NHE)) to that of previously used **RuCP$^{2}$** (1.19 V) even though **RuCP$^{6}$** has four more phosphate groups than **RuCP$^{2}$**. This difference enables us to investigate the effect of the nanoparticle surface on the photocatalytic $H_2$ evolution activity. Herein, it was demonstrated that the activity increases dramatically in the order of **RuCP$^{2}$**-Zr-**RuP$^{6}$**@Pt-$TiO_2$ < **RuCP$^{6}$**-Zr-**RuP$^{6}$**@Pt-$TiO_2$ < Zr-**RuCP$^{6}$**-Zr-**RuP$^{6}$**@Pt-$TiO_2$, and the AQY value of Zr-**RuCP$^{6}$**-Zr-**RuP$^{6}$**@1 wt%Pt-$TiO_2$ in the first hour of reaction was 1%.

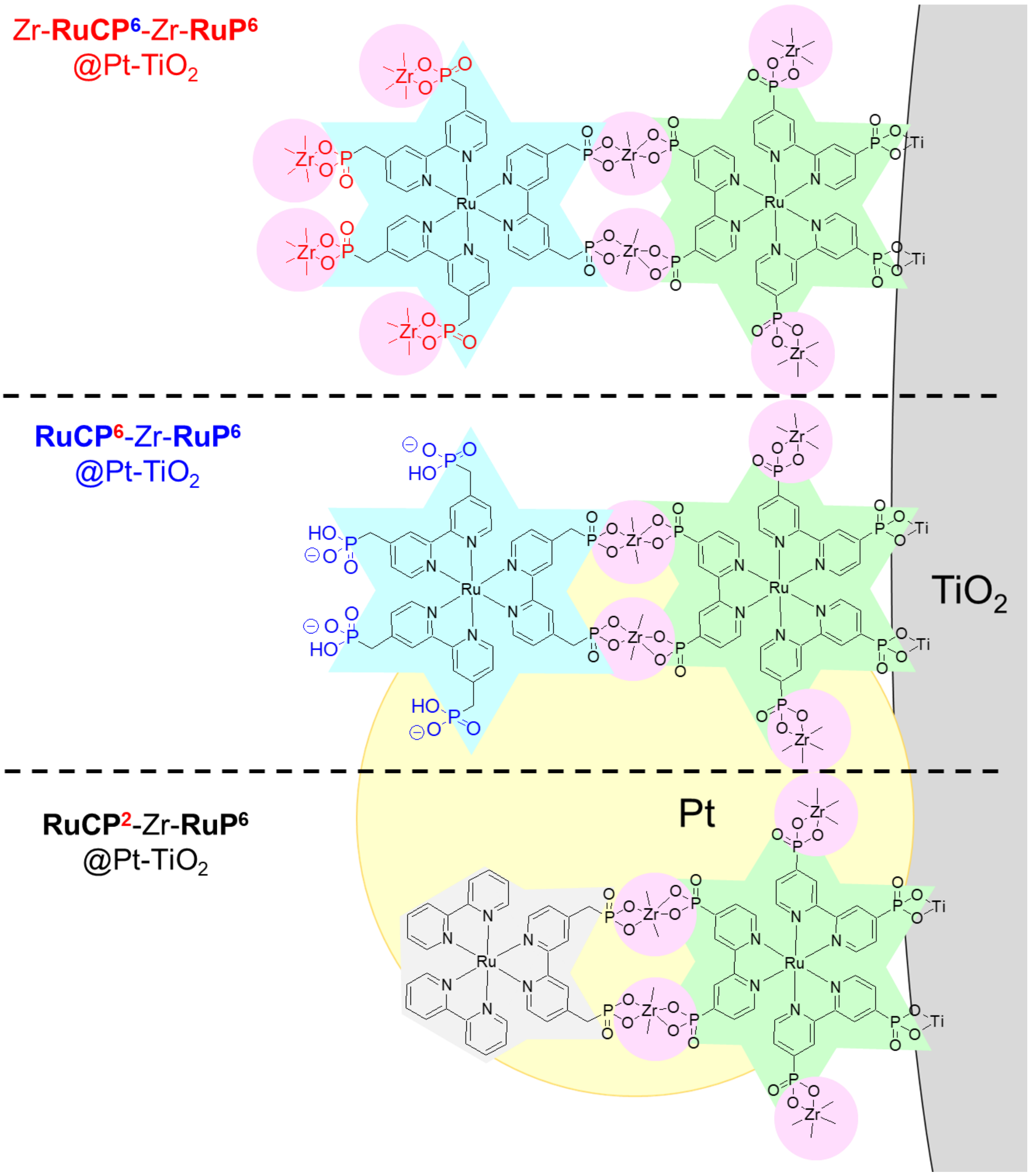

**Scheme 4-1**. Schematic surface structures of three types of PS-double-layered Pt-$TiO_2$ nanoparticles, (a) Zr-**RuCP**$^6$-Zr-**RuP**$^6$@*N*wt%Pt-$TiO_2$, (b) **RuCP**$^6$-Zr-**RuP**$^6$@*N*wt%Pt-$TiO_2$, and (c) **RuCP**$^2$-Zr-**RuP**$^6$@*N*wt%Pt-$TiO_2$ (*N* = 0.2, 1, 5).

## 4-2 Experimental

### 4-2-1 Synthesis

All Ru(II)-PSs were synthesized by previous report.[44] PS-multilayered photocatalysts were prepared by the same method as described in chapter 2-2.

### 4-2-2 Photocatalytic hydrogen evolution

Under dark conditions, an aqueous solution of KI (0.5 or 0.02 M) and hydrochloride (pH = 2) or phosphate pH buffer (0.5 M, pH = 2) containing Ru(II)-dye-immobilized nanoparticles (100 μM of the Ru(II) dye) was placed into a homemade Schlenk flask-equipped quartz cell (volume: 265 mL) with a small magnetic stirring bar. The other experimental conditions were same as Chap. 3-2.

## 4-3 Results and discussion

### 4-3-1 Characterization of Ru(II)-dye-immobilized Pt-TiO$_2$ nanoparticles

Figure 4-3-1-1 shows the amount of Ru(II) PS immobilized on the Pt-TiO$_2$ nanoparticle surface, as estimated from the UV-Vis absorption spectra of the supernatant solutions isolated from the immobilization reaction (see “2-2-4 Calculation of the amount of Ru(II) complex immobilized on the Pt-TiO$_2$ nanoparticles” section, Figure 4-3-1-2 and Table 4-3-1-1). The total amounts of the Ru(II) PS immobilized on the double-PS-layered nanoparticles (**RuY**-Zr-**RuP$^6$**@Pt-TiO$_2$ and Zr-**RuCP$^6$**-Zr-**RuP$^6$**@Pt-TiO$_2$, **Y** = **CP$^2$**, **CP$^6$**) were more than twice those of single-PS-layered nanoparticles (**RuP$^6$**@Pt-TiO$_2$ and Zr-**RuP$^6$**@Pt-TiO$_2$), indicating that the formation of double-PS-layered structures via Zr$^{4+}$ cation binders is an effective approach to increase the amount of immobilized PS per unit surface area, as previously reported.[41–43] The amount in the outer layer of the double-PS-layered nanoparticles strongly depended on the PS, and it decreased on changing **RuCP$^2$** to **RuCP$^6$**. Considering that the amount of the PS (**RuP$^6$**) immobilized directly on the surface in the inner layer of the Pt-TiO$_2$ nanoparticles were comparable for all prepared nanoparticles, this trend is attributed to the difference in occupied area between these two Ru(II) PSs with different numbers of phosphonic acid groups; **RuCP$^2$** has only two phosphonic acids and tends to be electrically neutral by releasing two H$^+$ ions, whereas **RuCP$^6$** is a negatively charged molecule on the release of the six H$^+$ ions from the phosphonic acid groups. As a result, a larger amount of **RuCP$^2$** than **RuCP$^6$** was immobilized on the Pt-TiO$_2$ nanoparticles because of the smaller electrostatic repulsion and molecular size of the former.

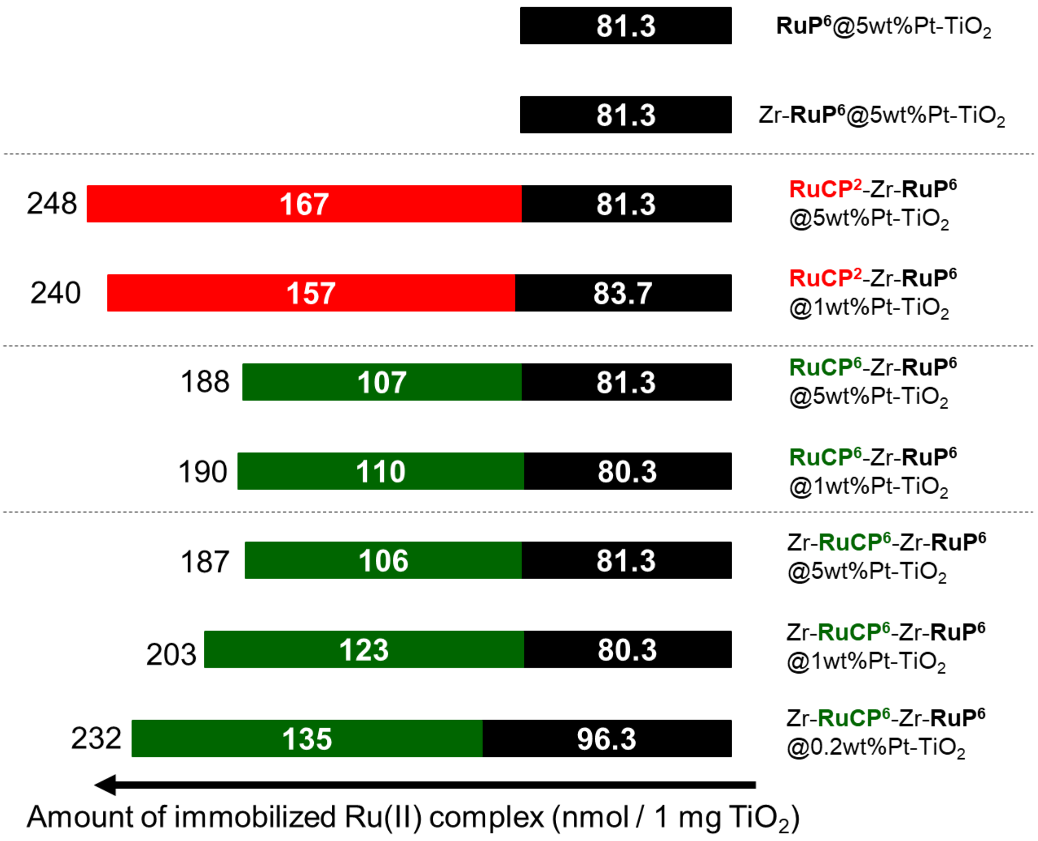

**Figure 4-3-1-1.** Estimated amounts of the Ru(II) PS (red: **RuCP$^2$**, black: **RuP$^6$**, and green: **RuCP$^6$**) immobilized on the Pt-TiO$_2$ nanoparticle surface determined by UV-Vis absorption spectra of the supernatant solutions obtained from the immobilization experiments. Numerical values in each bar show the immobilized amount of Ru(II) PS (nmol /1 mg TiO$_2$). The total amount of Ru(II) PSs of double-PS-layered nanoparticle is given on the left-hand side of each bar.

The influence of the loading amount of the Pt cocatalyst on the amount of Ru(II) PS immobilized was investigated on the Zr-**RuCP**$^{\mathbf{6}}$-Zr-**RuP**$^{\mathbf{6}}$@*N* wt%Pt-$TiO_2$ (*N* = 5, 1, and 0.2) nanoparticles. A negligible difference was observed between the 5 wt% Pt-$TiO_2$ and 1 wt%Pt-$TiO_2$, and the same trend was observed for the other nanoparticles (**RuY**-Zr-**RuP**$^{\mathbf{6}}$@*N* wt% Pt-$TiO_2$; **Y** = **CP**$^{\mathbf{2}}$, **CP**$^{\mathbf{6}}$). On the other hand, the total amount of immobilized Ru(II) PS in Zr-**RuCP**$^{\mathbf{6}}$-Zr-**RuP**$^{\mathbf{6}}$@0.2 wt%Pt-$TiO_2$ was approximately 10% greater than that of the 5 wt%Pt-$TiO_2$ and 1 wt%Pt-$TiO_2$ nanoparticles with the same double-PS-layered structure. Considering that the number of Pt colloidal particles in 0.2 wt%Pt-$TiO_2$ was significantly less than those in 5 wt%Pt-$TiO_2$ and 1 wt%Pt-$TiO_2$ (see "4-4-3 Effect of loaded amount of Pt cocatalyst" section), this trend could be because the surfaces of the $TiO_2$ nanoparticles have a low coverage of colloidal Pt particles. In other words, from the viewpoint of hard-soft acid-base (HSAB) theory, Ru(II) PSs with phosphonates as *hard* bases were preferentially immobilized on the $TiO_2$ surface with relatively *hard* acids rather than the Pt cocatalyst surface as *soft* acids.

The immobilized amounts of inner **RuP**$^{\mathbf{6}}$ were estimated to be 80–96 nmol/1 mg $TiO_2$, and the immobilized amount per unit area of $TiO_2$ nanoparticle surface was estimated to be 0.078–0.094 $nmol{\cdot}cm^{-2}$ (Table 4-3-1-2, see "2-2-4 Calculation of the amount of Ru(II) complex immobilized on the Pt-$TiO_2$ nanoparticles" section). These are consistent with the calculated value (about 0.083 $nmol{\cdot}cm^{-2}$) based on the occupied area of one **RuP**$^{\mathbf{6}}$ molecule (about 2 $nm^2$). Thus, these values indicate that the $TiO_2$ surface should be almost fully covered by **RuP**$^{\mathbf{6}}$.

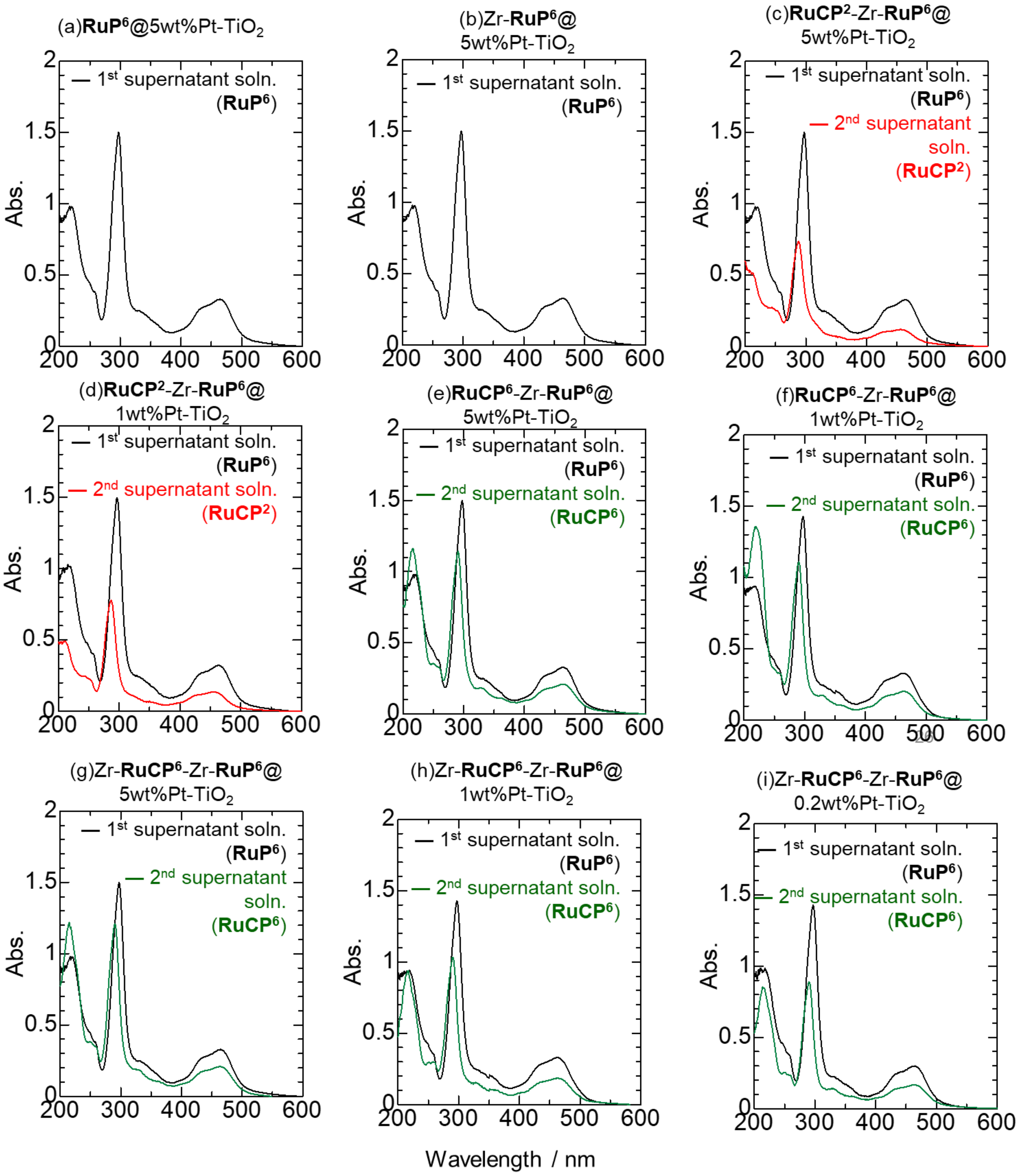

**Figure 4-3-1-2.** UV-Vis absorption spectra of the supernatant solutions at 298 K. (a) **RuP$^6$**@5wt%Pt-TiO$_2$, (b) Zr-**RuP$^6$**@5wt%Pt-TiO$_2$, (c) **RuCP$^2$**-Zr-**RuP$^6$**@5wt%Pt-TiO$_2$, (d) **RuCP$^2$**-Zr-**RuP$^6$**@1wt%Pt-TiO$_2$, (e) **RuCP$^6$**-Zr-**RuP$^6$**@5wt%Pt-TiO$_2$, (f) **RuCP$^6$**-Zr-**RuP$^6$**@1wt%Pt-TiO$_2$, (g) Zr-**RuCP$^6$**-Zr-**RuP$^6$**@5wt%Pt-TiO$_2$, (h) Zr-**RuCP$^6$**-Zr-**RuP$^6$**@1wt%Pt-TiO$_2$, i) Zr-**RuCP$^6$**-Zr-**RuP$^6$**@0.2wt%Pt-TiO$_2$. Note that each solution (1 mL) was diluted to 50 mL by the addition of deionized water before the spectral measurement.

**Table 4-3-1-1.** Absorbance of each supernatant solution and the calculated $C_B$ and $M_i$ values.

| Photocatalyst | Immobilized Ru(II) PS | $A$ ($M^{-1}cm^{-1}$) | $C_B$ (mM) | $M_i$ (μmol) |
|---|---|---|---|---|
| **RuP**$^6$ @5wt%Pt-TiO$_2$ | **RuP**$^6$ | 0.328 | 0.836 | 2.44 |
| Zr-**RuP**$^6$ @5wt%Pt-TiO$_2$ | **RuP**$^6$ | 0.328 | 0.836 | 2.44 |
| **RuCP**$^2$-Zr-**RuP**$^6$ @5wt%Pt-TiO$_2$ | 1st (inner) layer **RuP**$^6$ | 0.328 | 0.836 | 2.44 |
| | 2nd (outer) layer **RuCP**$^2$ | 0.120 | 0.411 | 5.01 |
| **RuCP**$^2$-Zr-**RuP**$^6$ @1wt%Pt-TiO$_2$ | 1st (inner) layer **RuP**$^6$ | 0.323 | 0.824 | 2.51 |
| | 2nd (outer) layer **RuCP**$^2$ | 0.135 | 0.462 | 4.70 |
| **RuCP**$^6$-Zr-**RuP**$^6$ @5wt%Pt-TiO$_2$ | 1st (inner) layer **RuP**$^6$ | 0.328 | 0.836 | 2.44 |
| | 2nd (outer) layer **RuCP**$^6$ | 0.208 | 0.711 | 3.20 |
| **RuCP**$^6$-Zr-**RuP**$^6$ @1wt%Pt-TiO$_2$ | 1st (inner) layer **RuP**$^6$ | 0.330 | 0.842 | 2.41 |
| | 2nd (outer) layer **RuCP**$^6$ | 0.202 | 0.693 | 3.30 |
| Zr-**RuCP**$^6$-Zr-**RuP**$^6$ @5wt%Pt-TiO$_2$ | 1st (inner) layer **RuP**$^6$ | 0.328 | 0.836 | 2.44 |
| | 2nd (outer) layer **RuCP**$^6$ | 0.208 | 0.713 | 3.19 |
| Zr-**RuCP**$^6$-Zr-**RuP**$^6$ @1wt%Pt-TiO$_2$ | 1st (inner) layer **RuP**$^6$ | 0.330 | 0.842 | 2.41 |
| | 2nd (outer) layer **RuCP**$^6$ | 0.184 | 0.630 | 3.69 |
| Zr-**RuCP**$^6$-Zr-**RuP**$^6$ @0.2wt%Pt-TiO$_2$ | 1st (inner) layer **RuP**$^6$ | 0.299 | 0.763 | 2.89 |
| | 2nd (outer) layer **RuCP**$^6$ | 0.166 | 0.568 | 4.06 |

**Table 4-3-1-2.** Amounts of immobilized Ru(II) complexes on the Pt-$TiO_2$ nanoparticle surface.

| Photocatalyst | Immobilized Ru(II) PS | Amount of immobilized Ru(II) complex (nmol/1 mg $TiO_2$)[a] | Surface coverage *N* (nmol / $cm^2$) |
|---|---|---|---|
| **RuP$^6$**@ 5wt%Pt-$TiO_2$ | **RuP$^6$** | 81.3 | 0.0792 |
| Zr-**RuP$^6$**@ 5wt%Pt-$TiO_2$ | **RuP$^6$** | 81.3 | 0.0792 |
| **RuCP$^2$**-Zr-**RuP$^6$**@ 5wt%Pt-$TiO_2$ | inner layer **RuP$^6$** | 81.3 | 0.0792 |
| | outer layer **RuCP$^2$** | 167 | 0.163 |
| | Total Ru(II) PS | 248 | 0.241 |
| **RuCP$^2$**-Zr-**RuP$^6$**@ 1wt%Pt-$TiO_2$ | inner layer **RuP$^6$** | 83.7 | 0.0814 |
| | outer layer **RuCP$^2$** | 157 | 0.153 |
| | Total Ru(II) PS | 240 | 0.233 |
| **RuCP$^6$**-Zr-**RuP$^6$**@ 5wt%Pt-$TiO_2$ | inner layer **RuP$^6$** | 81.3 | 0.0792 |
| | outer layer **RuCP$^6$** | 107 | 0.104 |
| | Total Ru(II) PS | 188 | 0.183 |
| **RuCP$^6$**-Zr-**RuP$^6$**@ 1wt%Pt-$TiO_2$ | inner layer **RuP$^6$** | 80.3 | 0.0781 |
| | outer layer **RuCP$^6$** | 110 | 0.107 |
| | Total Ru(II) PS | 190 | 0.185 |
| Zr-**RuCP$^6$**-Zr-**RuP$^6$**@ 5wt%Pt-$TiO_2$ | inner layer **RuP$^6$** | 81.3 | 0.0792 |
| | outer layer **RuCP$^6$** | 106 | 0.0931 |
| | Total Ru(II) PS | 187 | 0.182 |
| Zr-**RuCP$^6$**-Zr-**RuP$^6$**@ 1wt%Pt-$TiO_2$ | inner layer **RuP$^6$** | 80.3 | 0.0781 |
| | outer layer **RuCP$^6$** | 123 | 0.120 |
| | Total Ru(II) PS | 203 | 0.197 |
| Zr-**RuCP$^6$**-Zr-**RuP$^6$**@ 0.2wt%Pt-$TiO_2$ | inner layer **RuP$^6$** | 96.3 | 0.0937 |
| | outer layer **RuCP$^6$** | 135 | 0.131 |
| | Total Ru(II) PS | 232 | 0.226 |

[a] Estimated based on the absorbance observed in the UV-Vis spectra of each supernatant solution (Figure 4-3-1-2).

In contrast, the total amounts of Ru(II) PS immobilized on double-PS-layered nanoparticles were more than 180 nmol per 1 mg $TiO_2$ and 0.182 nmol·cm$^{-2}$ per unit area. Thus, **RuP$^6$** was almost fully immobilized on the $TiO_2$ surface directly to form the inner PS layer, and the relatively dense outer PS layer was formed by the immobilization of **RuCP$^6$** on the outer surface of the **RuP$^6$** inner layer via Zr$^{4+}$ binders. It was confirmed that the exchange reaction of the inner **RuP$^6$** by the outer **RuCP$^6$** did not occur significantly during the preparation of the double-PS-layered **RuCP$^6$**-Zr-**RuP$^6$**@5 wt% Pt-$TiO_2$ because the supernatant solution obtained from the immobilization reaction of **RuCP$^6$** showed almost identical emission and $^1$H-NMR spectra and emission decay to those of **RuCP$^6$**, and no signals assigned to **RuP$^6$** were observed (Figure 4-3-1-3). In addition, SEM-EDS point analysis suggested that Ru-PSs are immobilized to Pt-$TiO_2$ in a uniformly dispersed state (Figure 4-3-1-4 and Table 4-3-1-3).

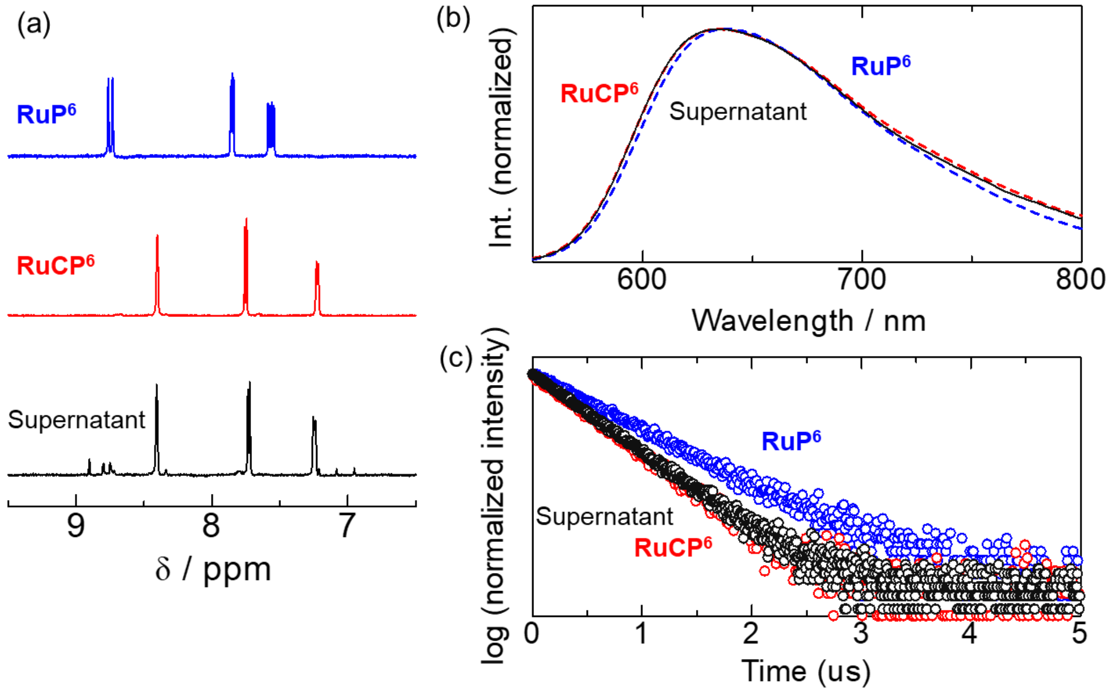

**Figure 4-3-1-3.** (a) $^1$H NMR, (b) emission spectra, and (c) emission decay of the supernatant solution (black lines and circles) obtained from the immobilization reaction of **RuCP$^6$** for the synthesis of **RuCP$^6$**-Zr-**RuP$^6$**@Pt-$TiO_2$ by ultracentrifugation. Blue and red lines and circles are the spectra and decay of **RuP$^6$** and **RuCP$^6$** in the aqueous solution.

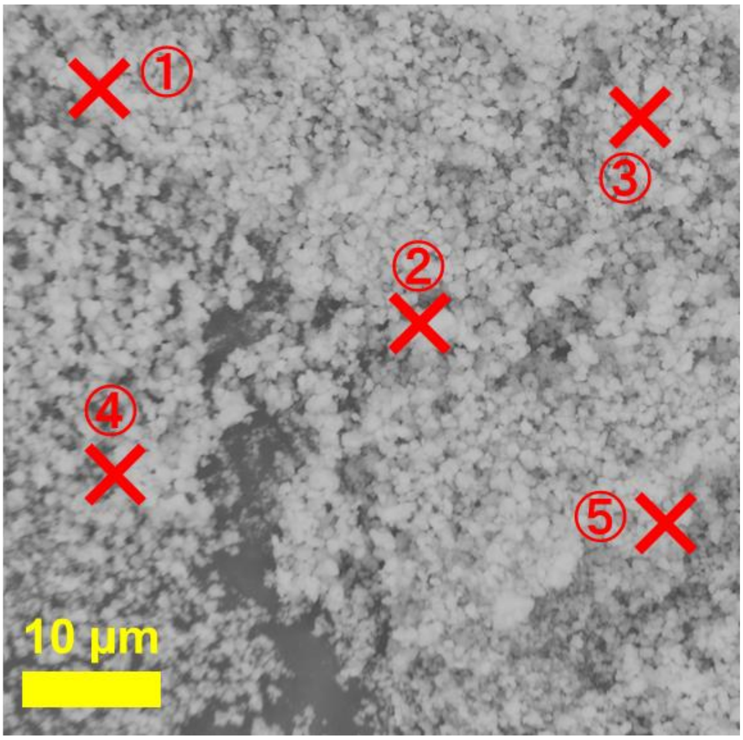

**Figure 4-3-1-4.** SEM images of Zr-**RuCP$^6$**-Zr-**RuP$^6$**@1wt%Pt-$TiO_2$ nanoparticles. Red spot was the point to measure EDS-pointing (see Table 4-3-1-3)

**Table 4-3-1-3**. EDS-pointing of each spot about **Figure S4**.

| Spot [a] | Ti (mol%) | Zr (mol%) [b] | Ru (mol%) |
|---|---|---|---|
| 1 | 82 | 8.2 | 2.5 |
| 2 | 83 | 8.2 | 2.3 |
| 3 | 83 | 6.9 | 2.4 |
| 4 | 83 | 6.9 | 2.1 |
| 5 | 84 | 7.3 | 2.3 |

[a] Pt peak was observed but under quantitative limit.

[b] Zr peak(Zr Lα) and P peak(P Kα) were observed at almost same energy position, so it was impossible to evaluate those peaks completely separated.

X-ray fluorescence (XRF) spectra were recorded to estimate the number of immobilized $Zr^{4+}$ cations (Figure 4-3-1-5). The spectra of all three nanoparticles Zr-**RuCP$^6$**-Zr-**RuP$^6$**@5wt%Pt-$TiO_2$, **RuCP$^6$**-Zr-**RuP$^6$**@5wt%Pt-$TiO_2$, Zr-**RuP$^6$**@5wt%Pt-$TiO_2$, and **RuP$^6$**@5wt%Pt-$TiO_2$ contain peaks corresponding to Ti $K_\alpha$, Ru $K_\alpha$, and Pt $L_\alpha$ derived from the $TiO_2$ nanoparticle, Ru(II) PS, and Pt cocatalyst, respectively. The intensities of the Ru $K_\alpha$ radiation of the double-PS-layered nanoparticles were stronger than those of single-PS-layered nanoparticles, which is consistent with the UV-Vis absorption spectra of the supernatants mentioned above. Zr $K_\alpha$ peaks assigned to the $Zr^{4+}$ cations used as the binder between the inner **RuP$^6$** and outer **RuCP$^6$** PS layers was also observed**,** except for **RuP$^6$**@5wt%Pt-$TiO_2$. Notably, the intensity of the Zr $K_\alpha$ peak of Zr-**RuCP$^6$**-Zr-**RuP$^6$**@5wt%Pt-$TiO_2$ was stronger than that of **RuCP$^6$**-Zr-**RuP$^6$**@5wt%Pt-$TiO_2$ and Zr-**RuP$^6$**@5wt%Pt-$TiO_2$. This result suggests that the number of immobilized $Zr^{4+}$ cations was increased by the second $Zr^{4+}$ immobilization reaction to form Zr-**RuCP$^6$**-Zr-**RuP$^6$**@5wt%Pt-$TiO_2$ and also suggests that the surface structure of Zr-**RuCP$^6$**-Zr-**RuP$^6$**@5wt%Pt-$TiO_2$ is different from that of **RuCP$^6$**-Zr-**RuP$^6$**@5wt%Pt-$TiO_2$. Further differences between these two nanoparticles were observed in the dynamic light scattering (DLS) measurements in aqueous HCl (pH = 2, Figure 4-3-1-6). The average particle size of **RuCP$^6$**-Zr-**RuP$^6$**@5wt%Pt-$TiO_2$ with surface phosphonic acids was estimated to be over 1000 nm, whereas that of Zr-**RuCP$^6$**-Zr-**RuP$^6$**@5wt%Pt-$TiO_2$ with the surface $Zr^{4+}$-phosphate groups was approximately 500 nm. This difference also suggests a difference in the surface structure; the **RuCP$^6$**-Zr-**RuP$^6$**@5wt%Pt-$TiO_2$ nanoparticles were easily aggregated by the hydrogen-bonding interactions of the phosphonic acids, whereas the positively charged $Zr^{4+}$-phosphonate groups on the surface of Zr-**RuCP$^6$**-Zr-**RuP$^6$**@5wt%Pt-$TiO_2$ could suppress nanoparticle aggregation because of electrostatic repulsion.

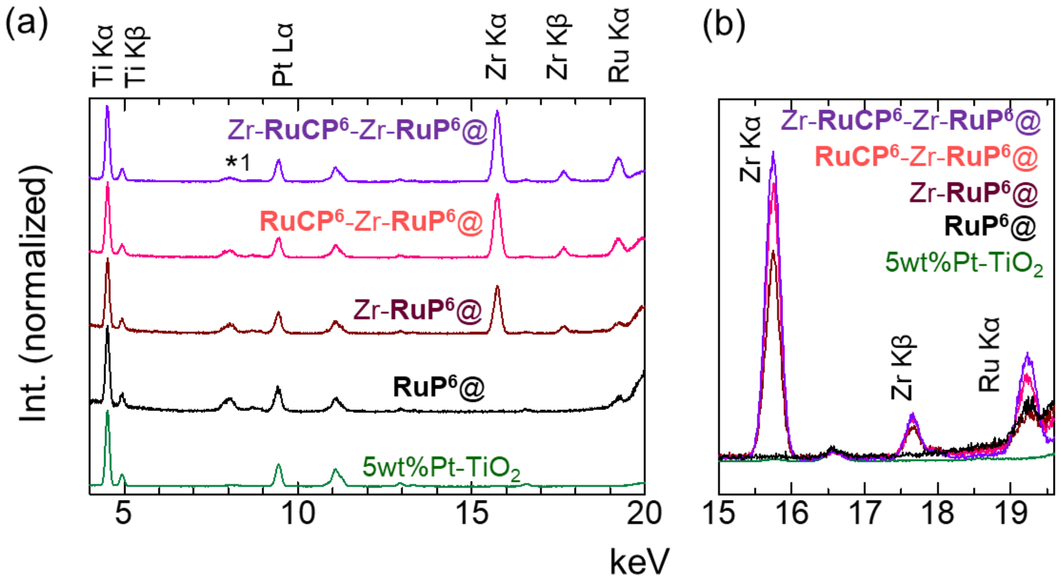

**Figure 4-3-1-5**. (a) XRF spectra of Pt-TiO$_2$(green), **RuP$^6$**@Pt-TiO$_2$ (black), Zr-**RuP$^6$**@Pt-TiO$_2$ (brown), **RuCP$^6$**-Zr-**RuP$^6$**@Pt-TiO$_2$ (pink), Zr-**RuCP$^6$**-Zr-**RuP$^6$**@Pt-TiO$_2$ (purple) using 5wt%Pt in the solid state. All spectra of Ru(II)-PS-multilayered Pt-TiO$_2$ nanoparticles were normalized by using Ti Kα peak. The marked peak (*1) is due to the background of Cu sample holder. (b) Comparison of the XRF spectra of these samples in Zr and Ru Kα regions. All spectra of Ru(II)-PS-multilayered Pt-TiO$_2$ nanoparticles were normalized by using Ti Kα peak.

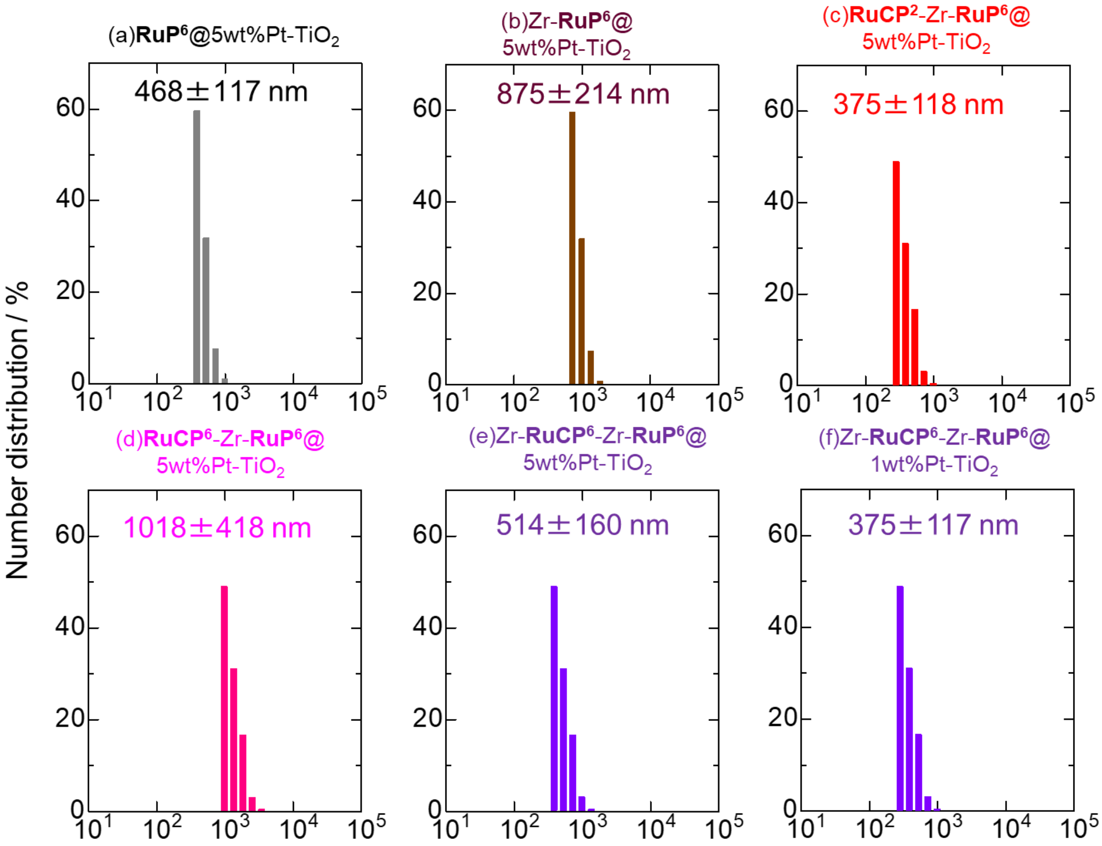

**Figure 4-3-1-6**. Particle diameter distributions estimated by the dynamic light scattering method for (a) **RuP⁶**@5wt%Pt-$TiO_2$, (b) Zr-**RuP⁶**@5wt%Pt-$TiO_2$, (c) **RuCP²**-Zr-**RuP⁶**@5wt%Pt-$TiO_2$, (d) **RuCP⁶**-Zr-**RuP⁶**@5wt%Pt-$TiO_2$, (e) Zr-**RuCP⁶**-Zr-**RuP⁶**@5wt%Pt-$TiO_2$, and (f) Zr-**RuCP⁶**-Zr-**RuP⁶**@1wt%Pt-$TiO_2$ nanoparticles in the diluted HCl aqueous solution (pH = 2).

### 4-3-2 Effect of nanoparticle surface structure for photocatalytic hydrogen evolution

Figure 4-3-2-1 shows the results of photocatalytic $H_2$ evolution reactions in 0.5 M aqueous KI solutions of three kinds of double-PS-layered nanoparticle photocatalysts with different surface structures: Zr-**RuCP$^6$**-Zr-**RuP$^6$**@5wt%Pt-$TiO_2$, **RuCP$^6$**-Zr-**RuP$^6$**@5wt%Pt-$TiO_2$, and **RuCP$^2$**-Zr-**RuP$^6$**@5wt%Pt-$TiO_2$ in comparison with the single-PS-layered nanoparticles **RuP$^6$**@5wt% Pt-$TiO_2$ and Zr-**RuP$^6$**@5wt%Pt-$TiO_2$. The amount of $H_2$ produced after 6 h of light irradiation, the turn-over number per PS dye (PS TON), the turn-over frequency per PS dye (PS TOF), and AQY are listed in Table 4-3-2-1. All reactions were carried out in the presence of the same amount Ru(II) PS (100 µM) to keep the same absorbed light intensity under 470 nm excitation that should not excite $TiO_2$ directly. The amount of $H_2$ produced after 6 h of light irradiation increased in the following order: **RuP$^6$**@5wt%Pt-$TiO_2$ ≅ Zr-**RuP$^6$**@5wt%Pt-$TiO_2$ < **RuCP$^2$**-Zr-**RuP$^6$**@5wt%Pt-$TiO_2$ < **RuCP$^6$**-Zr-**RuP$^6$**@5wt%Pt-$TiO_2$ < Zr-**RuCP$^6$**-Zr-**RuP$^6$**@5wt%Pt-$TiO_2$**.** As previously reported, the photocatalytic $H_2$ evolution activity was enhanced by the double layering of Ru(II) PS by coordination with $Zr^{4+}$ cations. Notably, the activities of the three kinds of double-PS-layered nanoparticles were significantly different. The estimated PS TON after 6 h irradiation of **RuCP$^6$**-Zr-**RuP$^6$**@5wt%Pt-$TiO_2$ having surface phosphate groups was 35% higher than that of **RuCP$^2$**-Zr-**RuP$^6$**@5wt%Pt-$TiO_2$, which lacks surface phosphate groups. This difference is probably due to the reactivity with iodide was improved by the surface phosphate groups of the outer **RuCP$^6$** PS layer. The slightly negative Ru(III)/Ru(II) redox potential of **RuCP$^6$** (1.12 V vs. NHE) compared to that of **RuCP$^2$** (1.19 V vs. NHE) may also contribute to the improvement of the electron transfer between the inner **RuP$^6$** and outer PS layer (Scheme 4-3-2).

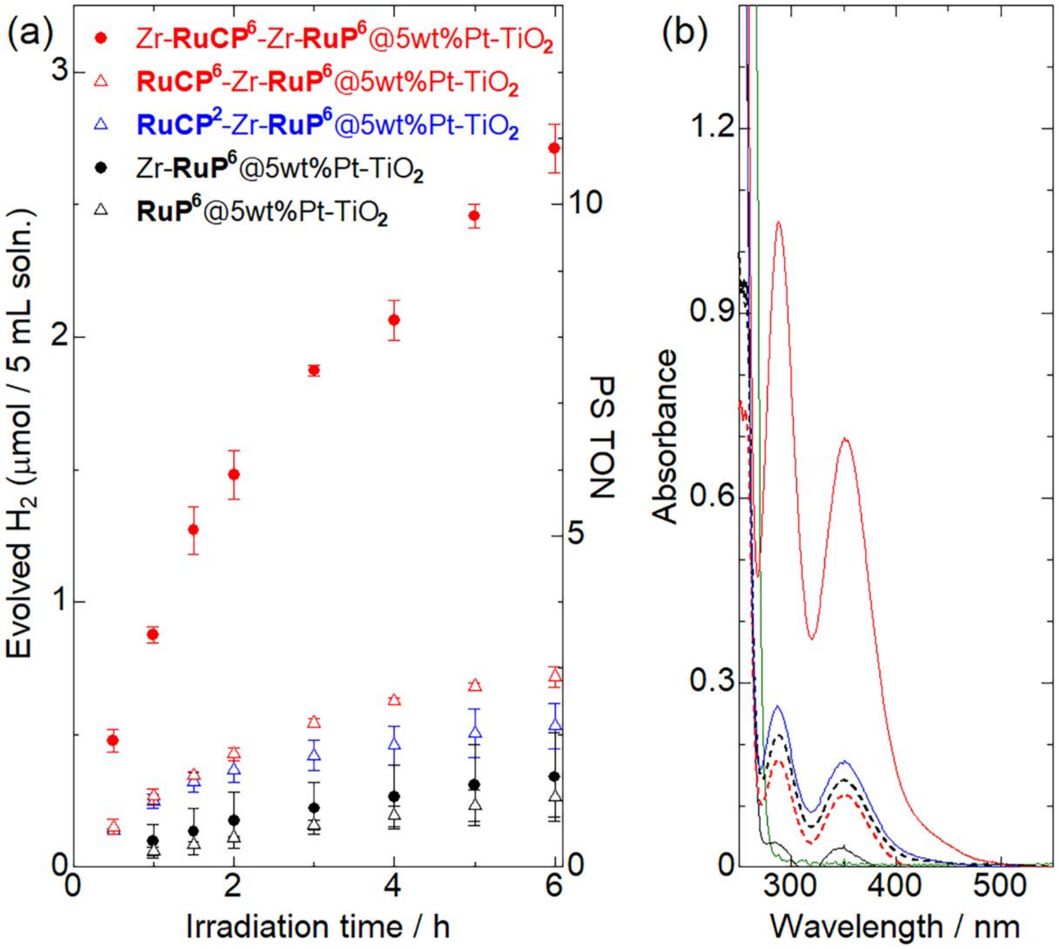

**Figure 4-3-2-1.** (a) Photocatalytic H$_2$ evolution reactions driven by Zr-**RuCP$^{6}$**-Zr-**RuP$^{6}$**@5wt%Pt-TiO$_2$ (red closed circles), **RuCP$^{6}$**-Zr-**RuP$^{6}$**@5wt%Pt-TiO$_2$ (red open triangles), **RuCP$^{2}$**-Zr-**RuP$^{6}$**@5wt%Pt-TiO$_2$ (blue open triangles), Zr-**RuP$^{6}$**@5wt%Pt-TiO$_2$ (black closed circles), and **RuP$^{6}$**@5wt%Pt-TiO$_2$ (black open symbols) in the presence of 100 μM Ru(II) dye and 0.5 M KI as the electron donor (initial pH = 2.0, λ = 470 ± 10 nm). (b) UV-Vis absorption spectra of the supernatants obtained by centrifugation of the reaction solutions after 6 h irradiation of Zr-**RuCP$^{6}$**-Zr-**RuP$^{6}$**@5wt%Pt-TiO$_2$ (red solid line), **RuCP$^{6}$**-Zr-**RuP$^{6}$**@5wt%Pt-TiO$_2$ (red dashed line), **RuCP$^{2}$**-Zr-**RuP$^{6}$**@5wt%Pt-TiO$_2$ (blue solid line), Zr-**RuP$^{6}$**@5wt%Pt-TiO$_2$ (black solid line), and RuP$^{6}$@5wt%Pt-TiO$_2$ (black dashed line). Each supernatant (1 mL) was diluted to 20 mL with deionized water before measurement. The green solid line is the spectrum before irradiation.

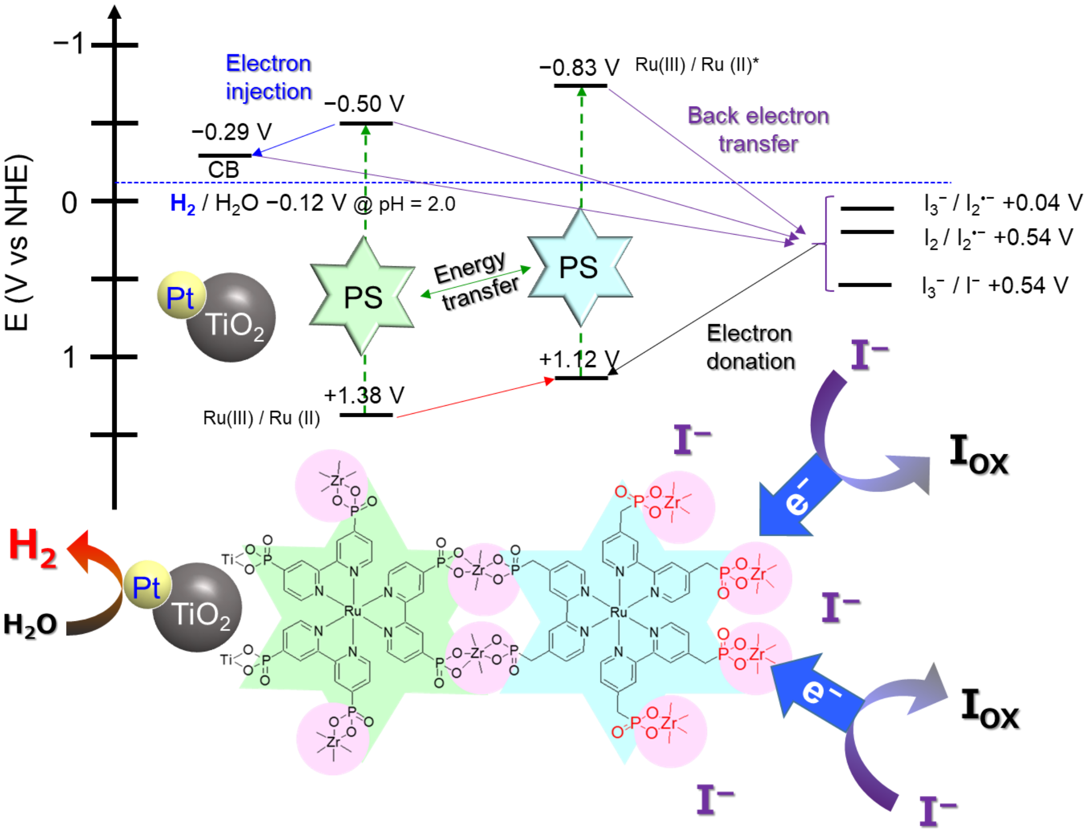

**Scheme 4-3-2**. Schematic diagram showing a plausible energy and electron transfer mechanism of Zr-**RuCP⁶**-Zr-**RuP⁶**@*N*wt%Pt-TiO$_2$. Redox potentials of Ru(II)-PS and iodide species are interfered from the literatures.[44,46]

**Table 4-3-2-1.** Results of photocatalytic H$_2$ evolution experiments in aqueous KI.

| Photocatalyst | KI (M) | Evolved H$_2$ (μmol) | Produced I$_3^-$ (μmol) | PS TON[a] | PS initial TOF[b] | PS final TOF[c] | AQY (%)[a] |
|---|---|---|---|---|---|---|---|
| **RuP$^6$**@5 wt%Pt-TiO$_2$ | 0.5 | 0.27 | 0.37 | 1.1 | 0.24 | - | <0.01 |
| Zr-**RuP$^6$**@5 wt%Pt-TiO$_2$ | 0.5 | 0.34 | < 0.10 | 1.4 | 0.39 | 0.13 | 0.011 |
| **RuCP$^2$**-Zr-**RuP$^6$**@5 wt%Pt-TiO$_2$ | 0.5 | 0.53 | 0.54 | 2.1 | 0.99 | - | 0.018 |
| **RuCP$^2$**-Zr-**RuP$^6$**@1 wt%Pt-TiO$_2$ | 0.5 | 0.84 | - | 3.4 | 1.3 | 0.22 | 0.028 |
| **RuCP$^6$**-Zr-**RuP$^6$**@5 wt%Pt-TiO$_2$ | 0.5 | 0.72 | 0.20 | 2.9 | 1.1 | 0.15 | 0.024 |
| **RuCP$^6$**-Zr-**RuP$^6$**@1 wt%Pt-TiO$_2$ | 0.5 | 8.8 | 6.2 | 33.2 | 8.5 | 3.6 | 0.30 |
| **RuCP$^6$**-Zr-**RuP$^6$**@1 wt%Pt-TiO$_2$ | 0.02 | 3.9 | - | 15.7 | 3.4 | 1.8 | 0.13 |
| **RuCP$^6$**-Zr-**RuP$^6$**@1 wt%Pt-TiO$_2$ | 0.02[d] | 2.12 | - | 8.47 | 0.93 | 1.3 | 0.071 |
| Zr-**RuCP$^6$**-Zr-**RuP$^6$**@5 wt%Pt-TiO$_2$ | 0.5 | 2.71 | 2.4 | 10.8 | 3.5 | 1.0 | 0.18 |
| Zr-**RuCP$^6$**-Zr-**RuP$^6$**@1 wt%Pt-TiO$_2$ | 0.5 | 16.1 | 9.9 | 64.5 | 18.5 | 5.6 | 0.54 |
| Zr-**RuCP$^6$**-Zr-**RuP$^6$**@0.2 wt%Pt-TiO$_2$ | 0.5 | 6.80 | 6.0 | 27.2 | 8.0 | 2.2 | 0.23 |
| Zr-**RuCP$^6$**-Zr-**RuP$^6$**@1 wt%Pt-TiO$_2$ | 0.02 | 5.44 | 1.6 | 21.8 | 5.8 | 2.1 | 0.18 |
| Zr-**RuCP$^6$**-Zr-**RuP$^6$**@1 wt%Pt-TiO$_2$ | 0.02[d] | 2.24 | 1.1 | 8.98 | 1.1 | - | 0.075 |

[a] After 6-h irradiation. [b] First hour of irradiation. [c] Last hour of irradiation. [d] In 0.5 M phosphate buffer (pH = 2.0) aqueous solution.

More interestingly, the estimated PS TON for Zr-**RuCP$^6$**-Zr-**RuP$^6$**@5wt%Pt-$TiO_2$ having surface $Zr^{4+}$-phosphate groups was 3.7-times higher than that of **RuCP$^2$**-Zr-**RuP$^6$**@5wt%Pt-$TiO_2$. According to the report of Meyer *et al.*,[44] the Ru(III)/Ru(II) redox potential of Ru(II) PS with phosphonic acid groups is shifted positively to less than 0.1 V by immobilization to the $TiO_2$ surface or by coordination bond formation with $Zr^{4+}$ cations, suggesting that the binding of $Zr^{4+}$ to the phosphonic acid groups of **RuCP$^6$** PS has little effect on the driving force of the electron donation reaction from the iodide ($I_3^-/I^-$ 0.54 V vs. NHE). Because this slight shift should be too small to enhance the photocatalytic activity more than three-fold, the zeta potentials **of Zr-RuCP$^6$**-Zr-**RuP$^6$**@5wt%Pt-$TiO_2$ and **RuCP$^6$**-Zr-**RuP$^6$**@5wt%Pt-$TiO_2$ in HCl aqueous solution (pH = 2) were measured to verify the effect of $Zr^{4+}$ binding on the surface (Table 4-3-2-2). The zeta potential of Zr-**RuCP$^6$**-Zr-**RuP$^6$**@5wt%Pt-$TiO_2$ was estimated to be +7 mV without KI, and it negatively shifted to −6 mV in the presence of 0.5 M KI. On the other hand, **RuCP$^6$**-Zr-**RuP$^6$**@5wt%Pt-$TiO_2$, which lacks surface $Zr^{4+}$ cations showed a negative value (−7 mV), even without KI, and it negatively shifted to −12 mV upon the addition of 0.5 M KI. The observed zeta potentials without KI suggest that the structure of the nanoparticle surface was different, probably because of $Zr^{4+}$ binding. The negative shifts in the 0.5 M KI aqueous solution could be ascribed to the attraction of iodide anions to the nanoparticle surface by electrostatic interactions with the surface $Zr^{4+}$ cations in the case of Zr-**RuCP$^6$**-Zr-**RuP$^6$**@5wt%Pt-$TiO_2$, and by hydrogen-bonding interactions with the surface phosphonic acids for **RuCP$^6$**-Zr-**RuP$^6$**@5wt%Pt-$TiO_2$. The larger negative shift in the zeta potential by KI addition implies that Zr-**RuCP$^6$**-Zr-**RuP$^6$**@5wt%Pt-$TiO_2$ nanoparticles attract iodide anions more effectively than **RuCP$^6$**-Zr-**RuP$^6$**@5wt%Pt-$TiO_2$. UV-Vis absorption spectra of the supernatant solutions after 6-h reaction were measured to verify whether iodide acted as the electron donor for photocatalytic hydrogen production (Figure 4-3-2-1(b), and Figure 4-3-2-2). The two absorption bands (288 and 352 nm) of triiodide ($I_3^-$) were observed, and the absorbance qualitatively agreed with the amount of evolved hydrogen. No hydrogen evolution was observed without KI or in the dark (Table 4-3-2-3). Thus, in these photocatalytic hydrogen evolution reactions, iodide acted as an electron donor, as previously reported. No singlet metal–ligand charge transfer ($^1$MLCT) absorption band of Ru(II) PS was observed for any of the supernatant solutions (Figure 4-3-2-2). Also, no emission band from fluorescence measurement and no aromatic peaks from $^1$H NMR measurement were observed from supernatant solutions (Figure 4-3-2-3). These results were suggesting that the release of the Ru(II) PS from the Pt-$TiO_2$ nanoparticle surface did not occur sufficiently during the reaction.

**Table 4-3-2-2**. Estimated particle diameters and zeta(ζ)-potentials of Ru(II)-PS-immobilized nanoparticles in the HCl aqueous solution, 0.5 M KI aqueous solution, 0.02 M KI aqueous solution, or 0.02 M KI and 0.5 M phosphate buffer aqueous solution. All measurements were done in pH = 2.0 aq.

| Photocatalyst | Particle diameter (nm) in HCl aq. | ζ potential (mV) | | | |
|---|---|---|---|---|---|
| | | HCl aq. | 0.5 M KI aq. | 0.02 M KI aq. | 0.02 M KI + phosphate buffer aq. |
| **RuCP**$^2$-Zr-**RuP**$^6$ @5wt%Pt-$TiO_2$ | 375±118 | +45 | −1.9 | - | - |
| **RuCP**$^6$-Zr-**RuP**$^6$ @5wt%Pt-$TiO_2$ | 1018±418 | −7.5 | −12 | - | - |
| **RuCP**$^6$-Zr-**RuP**$^6$ @1wt%Pt-$TiO_2$ | 513±158 | −1.7 | −11 | −7.4 | −25 |
| Zr-**RuCP**$^6$-Zr-**RuP**$^6$ @5wt%Pt-$TiO_2$ | 514±160 | +7.3 | −6.1 | - | - |
| Zr-**RuCP**$^6$-Zr-**RuP**$^6$ @1wt%Pt-$TiO_2$ | 375±117 | −0.3 | −7.6 | −1.0 | −24 |

**Table 4-3-2-3**. Control experiments of photocatalytic hydrogen evolution of Zr-**RuCP**$^6$-Zr-**RuP**$^6$@Pt-$TiO_2$.

| Entry [a] | Photocatalyst | Electron Donor (ED) | Light irradiation | Evolved $H_2$ [b] |
|---|---|---|---|---|
| 1 | Zr-**RuCP**$^6$-Zr-**RuP**$^6$@Pt-$TiO_2$ | 0.5 M KI | On | Yes |
| 2 | Zr-**RuCP**$^6$-Zr-**RuP**$^6$@Pt-$TiO_2$ | 0.5 M KI | Off | - |
| 3 | Zr-**RuCP**$^6$-Zr-**RuP**$^6$@Pt-$TiO_2$ | without KI | On | - |
| 4 | without photocatalyst | 0.5 M KI | On | - |

[a] Reaction conditions: [Ru] = 100 μM in HCl aqueous solution (pH = 2, 5 mL) under blue LED light irradiation (λ = 470 ± 10 nm) for 6 h. [b] Gas in the head space was analyzed qualitatively by Gas Chromatography (GC). “Yes” indicates that the evolved amount of $H_2$ was larger than the GC detection limit.

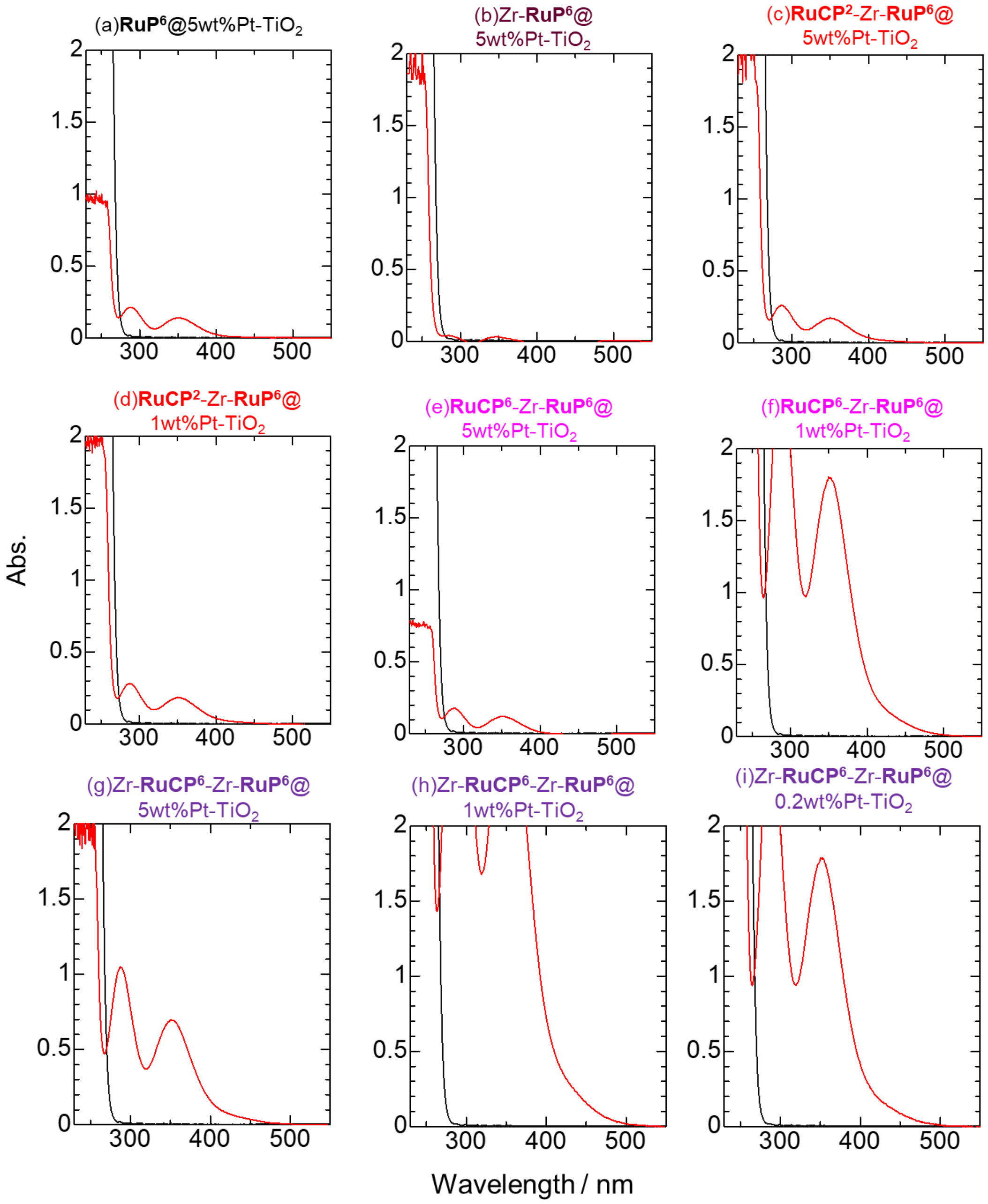

**Figure 4-3-2-2**. UV-Vis absorption spectral changes of the reaction solutions containing (a) **RuP$^6$**@5wt%Pt-TiO$_2$, (b) Zr-**RuP$^6$**@5wt%Pt-TiO$_2$, (c) **RuCP$^2$**-Zr-**RuP$^6$**@5wt%Pt-TiO$_2$, (d) **RuCP$^2$**-Zr-**RuP$^6$**@1wt%Pt-TiO$_2$, (e) **RuCP$^6$**-Zr-**RuP$^6$**@5wt%Pt-TiO$_2$, and (f) **RuCP$^6$**-Zr-**RuP$^6$**@1wt%Pt-TiO$_2$ nanoparticles (g)Zr-**RuCP$^6$**-Zr-**RuP$^6$**@5wt%Pt-TiO$_2$ nanoparticles, (h)Zr-**RuCP$^6$**-Zr-**RuP$^6$**@1wt%Pt-TiO$_2$ nanoparticles, and (i)Zr-**RuCP$^6$**-Zr-**RuP$^6$**@0.2wt%Pt-TiO$_2$ nanoparticles. 0.5 M KI (black) before and (red) after photocatalytic $H_2$ evolution reaction for 6 h. The Ru(II)-PS-multilayered Pt-TiO$_2$ nanoparticles were removed by ultracentrifugation and each supernatant solution (1 mL) was diluted to 20 mL by the addition of water before the spectral measurement.

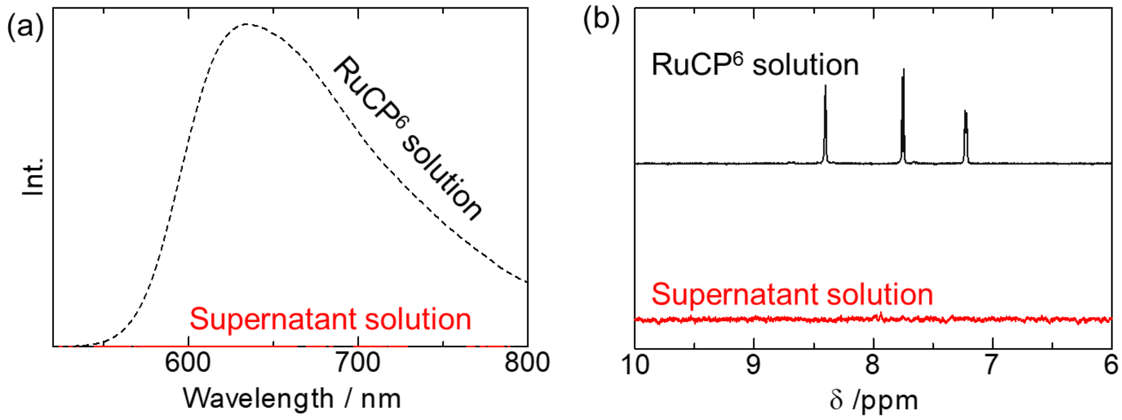

**Figure 4-3-2-3**. (a) Emission spectra and (b) $^1$H NMR spectra of supernatant aqueous solutions after Photocatalytic hydrogen evolution reaction using Zr-**RuCP$^6$**-Zr-**RuP$^6$**@1wt%Pt-TiO$_2$ nanoparticles at 298 K. Black lines show the spectra of outer **RuCP$^6$** PS.

### 4-3-3 Effect of amount of loaded Pt cocatalyst

To reveal the effect of the loading amount of Pt cocatalyst on the double-PS-layered Pt-$TiO_2$ nanoparticles with different surface structures, three types of double-PS-layered nanoparticles, Zr-**RuCP**$^{6}$-Zr-**RuP**$^{6}$@*N* wt%Pt-$TiO_2$, **RuCP**$^{6}$-Zr-**RuP**$^{6}$@*N* wt%Pt-$TiO_2$, and **RuCP**$^{2}$-Zr-**RuP**$^{6}$@*N* wt%Pt-$TiO_2$, with different Pt loadings (*N* = 0.2, 1, and 5) were prepared and their photocatalytic activities were evaluated. This is important because the Pt cocatalyst loaded on the $TiO_2$ surface is well known to catalyze not only the proton reduction to form $H_2$ but also the re-reduction of triiodide by $H_2$.[39] The results are shown in Figure 4-3-3-1 and Table 4-3-2-1. In all three cases, the amount of $H_2$ evolved after 6 h of irradiation increased on decreasing the amount of loaded Pt cocatalyst from 5 to 1 wt%, and the trend was remarkable for **RuCP**$^{6}$-Zr-**RuP**$^{6}$@Pt-$TiO_2$ and Zr-**RuCP**$^{6}$-Zr-**RuP**$^{6}$@Pt-$TiO_2$. Zr-**RuCP**$^{6}$-Zr-**RuP**$^{6}$@1wt%Pt-$TiO_2$ exhibited high activity, and the TOF after the first hour and TON after 6 h irradiation were 18.5 and 64.5, respectively. Notably, the AQY in the first hour of reaction was approximately 1%. Although it gradually decreased after 1.5 h light irradiation, the average AQY for 6 h was 0.54%, which is high compared to those of the recent state-of-the-art dye-sensitized photocatalysts.[29] The average AQY value was 1.8- and 19-times higher than that of **RuCP**$^{6}$-Zr-**RuP**$^{6}$@1wt%Pt-$TiO_2$ having phosphate groups and that of **RuCP**$^{2}$-Zr-**RuP**$^{6}$@1wt%Pt-$TiO_2$ without any surface phosphate groups, respectively. In contrast, the photoactivity of Zr-**RuCP**$^{6}$-Zr-**RuP**$^{6}$@0.2wt%Pt-$TiO_2$ was only 40% that of Zr-**RuCP**$^{6}$-Zr-**RuP**$^{6}$@1wt%Pt-$TiO_2$.

To reveal the origin of this remarkable difference observed with respect the loaded amount of Pt, transmission electron microscopy (TEM) analysis of *N* wt%Pt-$TiO_2$ nanoparticles was performed (Figures 4-3-3-1(d–f) and Figure 4-3-3-2). These images clearly indicate that the size of the Pt colloidal particles on the $TiO_2$ surface were reduced from approximately 5.0 nm for 5wt%Pt-$TiO_2$ to about 2.9 nm for 1 wt%Pt-$TiO_2$. On the other hand, the size of the Pt colloidal particles on 0.2 wt%Pt-$TiO_2$ was almost comparable (approximately 2.6 nm) to that of 1 wt%Pt-$TiO_2$, but the number of Pt colloidal particles per unit area was significantly smaller than that of 1 wt%Pt-$TiO_2$. Considering that Pt colloidal particles catalyze not only the $H_2$ evolution reaction but also the back reaction, that is, re-reduction of triiodide by $H_2$, the reason why the 1 wt%Pt-$TiO_2$ nanoparticles showed higher photoactivity than the 5 wt%Pt-$TiO_2$ nanoparticles could be that triiodide could not approach the surface of the Pt colloidal particles because of the steric bulk of the double-PS-layered structure. The thickness of the single-PS-layer structure on the $TiO_2$ surface was evaluated to be approximately 1.5.2 nm based on the molecular size of Ru(II) PS, and the thickness of the double-PS-layer structure including the $Zr^{4+}$-phosphonate layer should be roughly double (about 3–4 nm) that of the Pt colloid having 1 wt% Pt-$TiO_2$ (2.9 nm). As a result, the sterically bulky triiodide anion hardly approaches the Pt surface. Further, the thickness of the double-PS-layer structure should increase in order: **RuCP**$^{2}$-

Zr-**RuP**$^{6}$@1 wt%Pt-TiO$_2$ < **RuCP**$^{6}$-Zr-**RuP**$^{6}$@1 wt%Pt-TiO$_2$ < Zr-**RuCP**$^{6}$-Zr-**RuP**$^{6}$@1 wt%Pt-TiO$_2$ because of the bulkiness of the surface functional groups (phosphonic acids for **RuCP**$^{6}$-Zr-**RuP**$^{6}$@1 wt%Pt-TiO$_2$ and Zr$^{4+}$-phosphonate for Zr-**RuCP**$^{6}$-Zr-**RuP**$^{6}$@1 wt%Pt-TiO$_2$). This order is consistent with the order of the amount of evolved H$_2$ for the 1 wt% Pt-TiO$_2$ nanoparticles. In contrast, the lower activity of Zr-**RuCP**$^{6}$-Zr-**RuP**$^{6}$@0.2 wt%Pt-TiO$_2$ than Zr-**RuCP**$^{6}$-Zr-**RuP**$^{6}$@1 wt%Pt-TiO$_2$ could be because the number of Pt colloidal particles on 0.2 wt%Pt-TiO$_2$ was too low to accept the excited electrons from the conduction band of TiO$_2$ nanoparticles. The UV-Vis absorption spectra of the supernatant solutions after 6 h irradiation clearly indicate the production of triiodide as the oxidation product of the H$_2$ evolution reaction (Figure 4-3-2-2), and the produced amount of triiodide qualitatively agreed with that of H$_2$ evolved (Table 4-3-2-1).

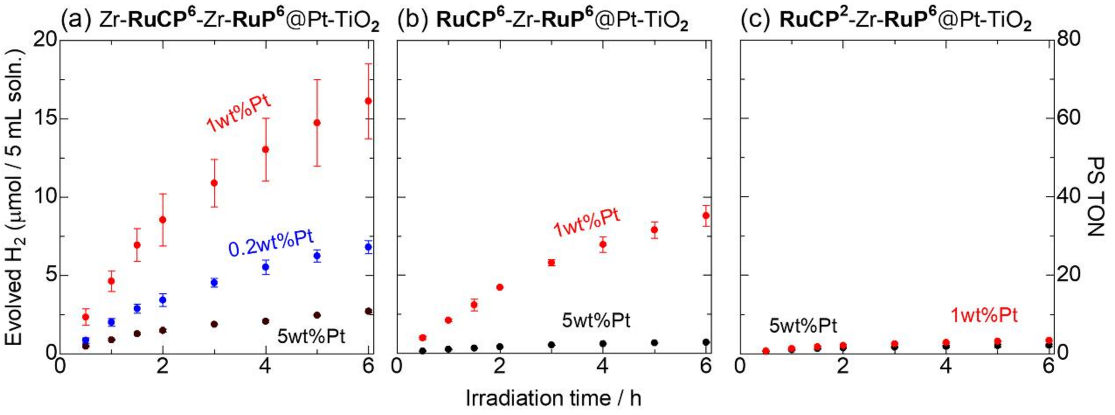

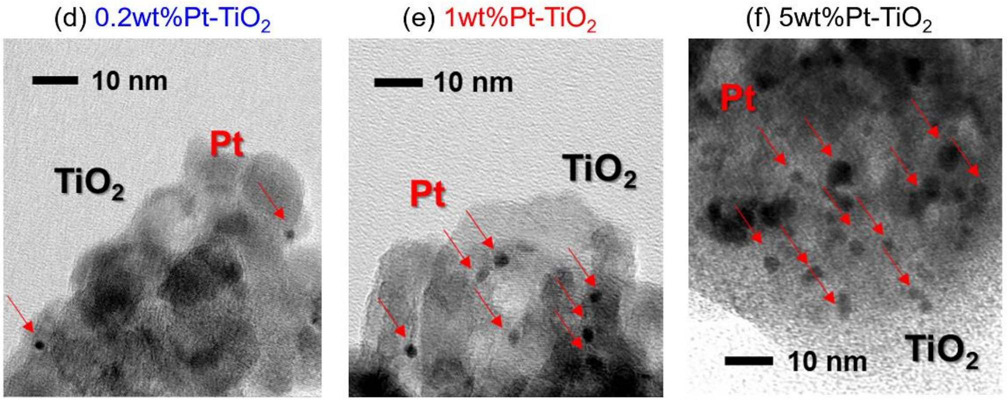
(d) 0.2wt%Pt-TiO$_2$ (e) 1wt%Pt-TiO$_2$ (f) 5wt%Pt-TiO$_2$

**Figure 4-3-3-1**. Dependence on the amount of loaded Pt of the photocatalytic H$_2$ evolution reactions of (a) Zr-**RuCP**$^{6}$-Zr-**RuP**$^{6}$@Pt-TiO$_2$, (b) **RuCP**$^{6}$-Zr-**RuP**$^{6}$@Pt-TiO$_2$, and (c) **RuCP**$^{2}$-Zr-**RuP**$^{6}$@Pt-TiO$_2$ (100 μM Ru(II) dye) in the presence of 0.5 M KI as the electron donor (initial pH = 2.0, λ = 470 ± 10 nm). Black, red, and blue dots represent data for nanoparticles having 5, 1, and 0.2 wt% Pt, respectively. Transmission electron microscopy (TEM) images of (d) 0.2 wt%Pt-TiO$_2$, (e) 1 wt%Pt-TiO$_2$, and (f) 5 wt%Pt-TiO$_2$. Red arrows indicate the Pt cocatalysts loaded on the surface of TiO$_2$.

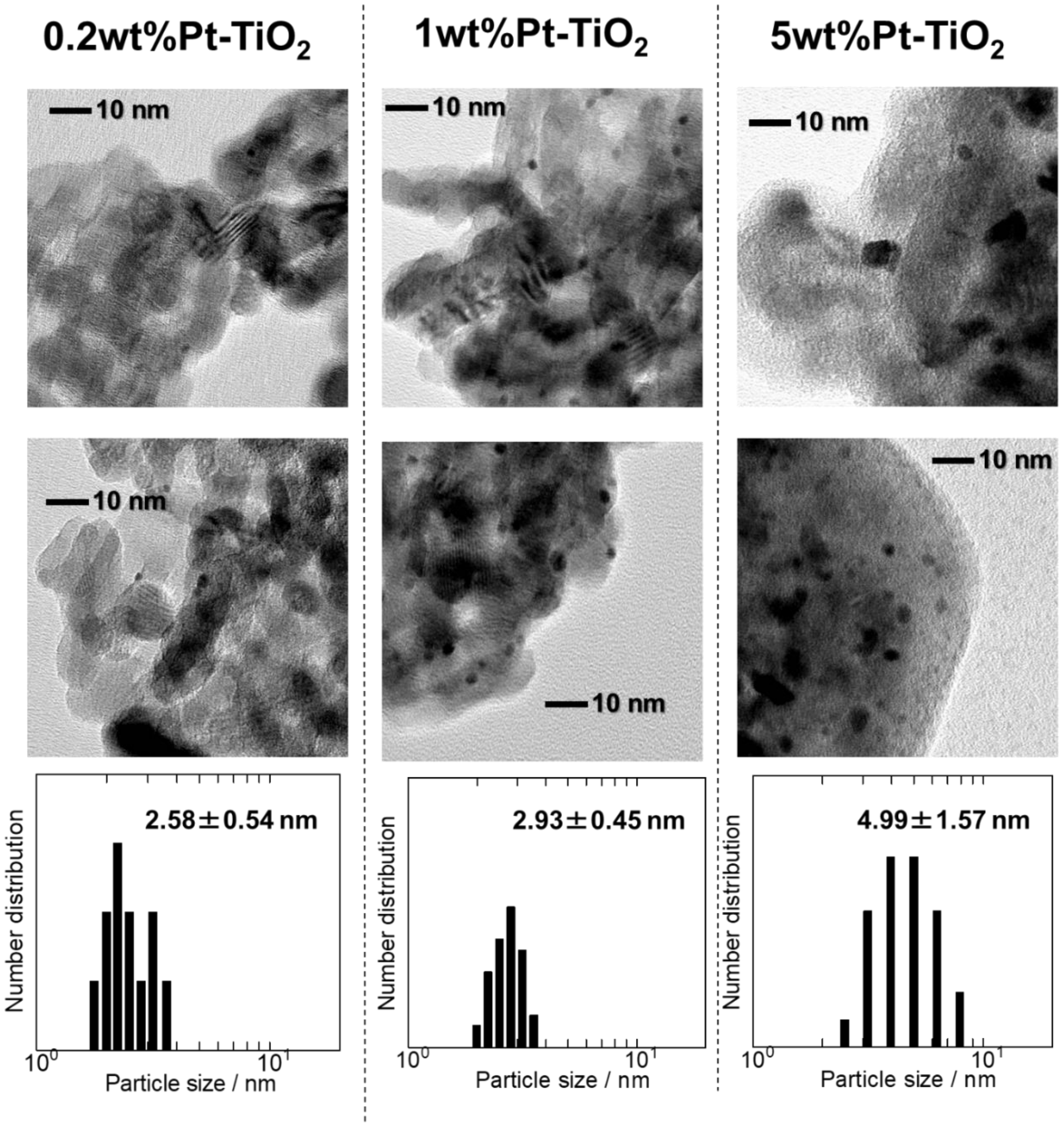

**Figure 4-3-3-2**. TEM images of *N* wtPt-TiO$_2$ (*N* = 0.2, 1, and 5) and number distribution histogram of each Pt colloids. Only representative images were shown due to space limitations.

### 4-3-4 Effects of iodide concentration and phosphate pH buffer

To gain further insight into the role of the $Zr^{4+}$-phosphonate groups of Zr-**RuCP⁶**-Zr-**RuP⁶**@1 wt%Pt-$TiO_2$ nanoparticles, the photocatalytic $H_2$ evolution reaction in the presence of Zr-**RuCP⁶**-Zr-**RuP⁶**@1 wt%Pt-$TiO_2$ or **RuCP⁶**-Zr-**RuP⁶**@1 wt%Pt-$TiO_2$ was carried out in aqueous phosphate buffer (0.5 M, pH = 2) solution. Because phosphate anions can be expected to coordinate to the surface $Zr^{4+}$ cations of Zr-**RuCP⁶**-Zr-**RuP⁶**@1 wt%Pt-$TiO_2$ in a manner similar to that of the phosphonates functionalized on the Ru(II) PS, the coordinated phosphonate anions could change the nanoparticle surface structure considerably. To maintain a constant pH, the concentration of the KI electron donor was reduced from 0.5 M to 20 mM (Figure 4-3-4-1). First, the effect of the KI concentration without phosphate buffer (initial pH = 2) was investigated. The TOF of the initial 1 h irradiation decreased to approximately one-third in both Zr-**RuCP⁶**-Zr-**RuP⁶**@1 wt%Pt-$TiO_2$ and **RuCP⁶**-Zr-**RuP⁶**@1 wt%Pt-$TiO_2$ (TOF = 5.8 and 3.4). These lower activities compared to those in 0.5 M KI are reasonable because triiodide formation should be suppressed at lower iodide concentrations. However, Zr-**RuCP⁶**-Zr-**RuP⁶**@1 wt%Pt-$TiO_2$ still showed a higher activity than **RuCP⁶**-Zr-**RuP⁶**@1 wt%Pt-$TiO_2$ even at low KI concentrations, suggesting the superior attraction of the surface $Zr^{4+}$ cations for the iodide electron donor. On the other hand, in the presence of phosphate buffer (0.5 M, pH = 2), the photocatalytic activity decreased further than that without phosphate buffer, and the TOF values of these two nanoparticles were estimated to be almost comparable (TOF = 1.1 and 0.93 for Zr-**RuCP⁶**-Zr-**RuP⁶**@1 wt%Pt-$TiO_2$ and **RuCP⁶**-Zr-**RuP⁶**@1 wt%Pt-$TiO_2$, respectively). The zeta potentials of both Zr-**RuCP⁶**-Zr-**RuP⁶**@1 wt%Pt-$TiO_2$ and **RuCP⁶**-Zr-**RuP⁶**@1 wt%Pt-$TiO_2$ in the phosphate buffer aqueous solution were negatively shifted to about −25 mV (Table 4-3-2-2), indicating that the nanoparticle surface was effectively surrounded by phosphate anions. Thus, the decrease in the photocatalytic activity of Zr-**RuCP⁶**-Zr-**RuP⁶**@1 wt%Pt-$TiO_2$ in the phosphate buffer condition could be due to the surface covering by electrostatically attracted phosphonate anions that suppress the electron donation from iodide. Meyer *et al.* suggested that, in addition to the iodide that injects an electron to Ru PS, another iodide anion should be close to stabilize the iodine radical generated in the electron injection; they also demonstrated that hydrogen-bonding interactions with iodide by amide and amino functional groups is effective in improving electron injection.[45-47] In Zr-**RuCP⁶**-Zr-**RuP⁶**@1 wt%Pt-$TiO_2$ nanoparticles of chapter 4, the surface $Zr^{4+}$-phosphate groups could attract iodide anions near the surface, probably by electrostatic interactions, leading to enhanced $H_2$ evolution photocatalytic activity.

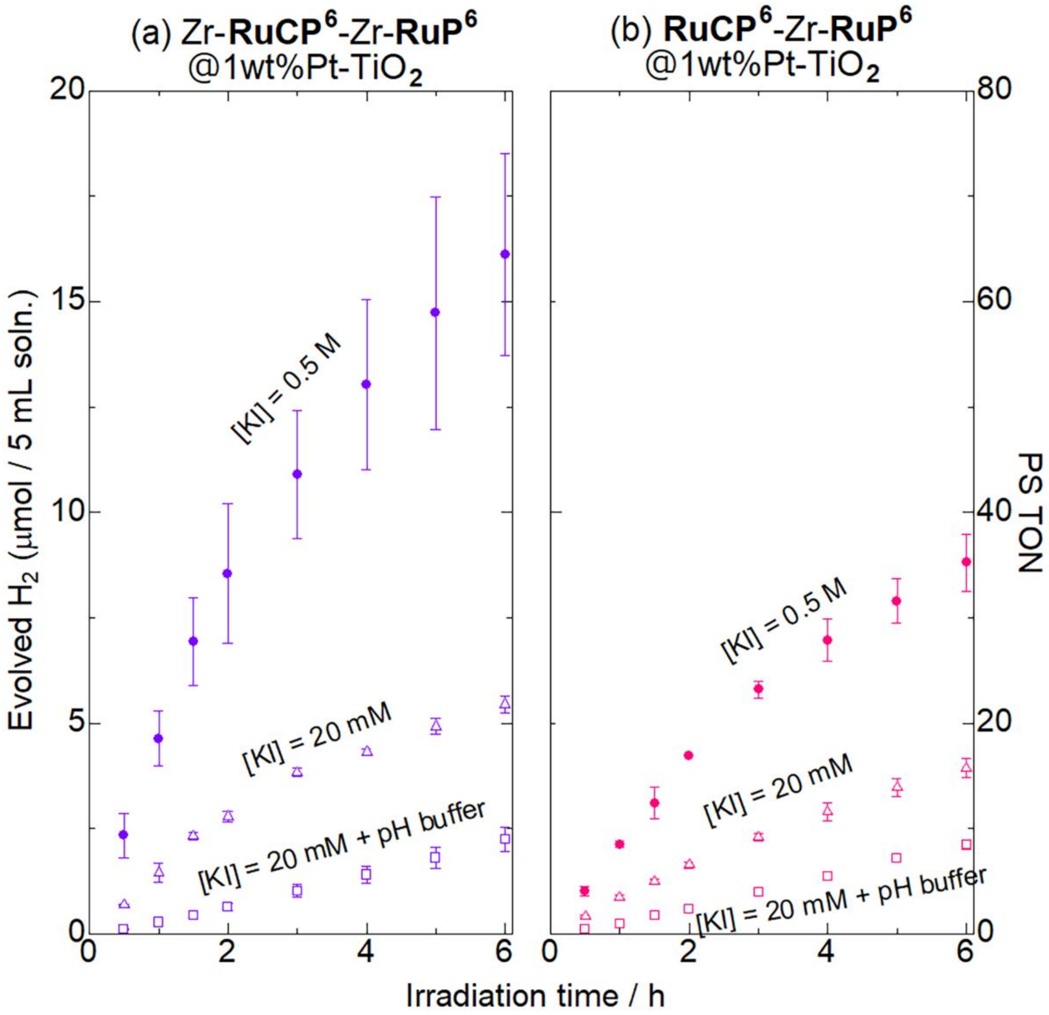

Figure 4-3-4-1. The effects of initial KI concentration and phosphate buffer on the photocatalytic $H_2$ evolution reaction driven by (a) Zr-**RuCP⁶**-Zr-**RuP⁶**@1 wt%Pt-$TiO_2$ and (b) **RuCP⁶**-Zr-**RuP⁶**@1 wt%Pt-$TiO_2$ (100 µM Ru(II) dye). Closed circles show the results in 0.5 M KI without pH buffer (the initial pH = 2.0, the same data shown in Figures 4-3-2-1(a) and 4-3-2-1(b)), and open triangles and squares are the results obtained in the 0.02 M KI without and with phosphate pH buffer, respectively (pH = 2.0, λ = 470 ± 10 nm).

## 4-4 Conclusion

To promote electron injection from the redox mediator to the photosensitizer (PS), three types of Pt-cocatalyst-loaded $TiO_2$ nanoparticles (*N* wt% Pt-$TiO_2$, *N* = 0.2, 1, and 5) photocatalysts with double-layered Ru(II) PSs were prepared: $Zr^{4+}$- phosphonate-exposed type nanoparticles (Zr-**RuCP$^6$**-Zr-**RuP$^6$**@*N* wt%Pt-$TiO_2$), phosphonic acid-exposed type nanoparticles (**RuCP$^6$**-Zr-**RuP$^6$**@*N* wt%Pt-$TiO_2$), and bipyridine-exposed nanoparticles (**RuCP$^2$**-Zr-**RuP$^6$**@*N* wt%Pt-$TiO_2$). In aqueous solutions of potassium iodide, which was used as a redox-reversible electron donor, the amount of evolved $H_2$ increased in order **RuCP$^2$**-Zr-**RuP$^6$**@*N* wt%Pt-$TiO_2$< **RuCP$^6$**-Zr-**RuP$^6$**@*N* wt%Pt-$TiO_2$ < Zr-**RuCP$^6$**-Zr-**RuP$^6$**@*N* wt%Pt-$TiO_2$ (*N* = 1, 5), despite the fact that the driving force for electron injection from $I^-$ to the photooxidized Ru(III) PS is comparable between the three nanoparticles. The highest performance was observed for Zr-**RuCP$^6$**-Zr-**RuP$^6$**@*N* wt%Pt-$TiO_2$, which showed an apparent quantum yield of 1% in the first hour of the reaction. TEM analysis revealed that a comparable number of Pt colloidal particles were loaded on both 1 and 5 wt% Pt-$TiO_2$, but the size of the Pt colloidal particles of 1 wt% Pt-$TiO_2$ (ca. 2.9 nm) was remarkably smaller than that of 5 wt% Pt-$TiO_2$ (ca. 5.0 nm), and it was also smaller than the thickness of the double-PS-layered **RuCP$^6$**-Zr-**RuP$^6$** structure (ca. 4 nm). Thus, the higher activity observed for double-PS-layered 1 wt% Pt-$TiO_2$ could be due to the suppression of back electron transfer from the Pt cocatalyst to triiodide ($I_3^-$) by the steric hindrance of the double-PS-layer, as well as the higher activity of the smaller Pt colloidal particles for $H_2$ evolution. The negative shift in the zeta potential in the iodide aqueous solution suggests that $Zr^{4+}$ ions and phosphonic acid attracted iodide anions to the nanoparticle surface, promoting electron donation to the photooxidized Ru(III) PSs. These results clearly indicate that the surface structure of dye-sensitized nanoparticles has a great influence on the reactivity with the redox mediator, and the reactivity could be modified by changing the functional group of the photosensitizers immobilized on the outer surface. Further studies focusing on the surface structure to regulate the reactivity with various redox mediators is now in progress.

## 4-5 Reference

1. M. Grätzel, *Acc. Chem. Res*. **1981**, *14*, 376-384.
2. A. Kudo, Y. Miseki, *Chem. Soc. Rev.* **2009**, *38*, 253-278.
3. Y. Ma, X. Wang, Y. Jia, X. Chen, H. Han, C. Li, *Chem. Rev.* **2014**, *114*, 9887-10043.
4. T. Hisatomi, K. Domen, *Nat. Cat.* **2019**, *2*, 387-399.
5. X. Fang, S. Kalathil, E. Reisner, *Chem. Soc. Rev*. **2020**, *49*, 4926-4952.
6. A. Fujishima, K. Honda, *Nature* **1972**, *238*, 37-38.
7. R. Abe, M. Higashi, K. Domen, *ChemSusChem* **2011**, *4*, 228-237.
8. T. Takata, J. Jiang, Y. Sakata, M. Nakabayashi, N. Shibata, V. Nandal, K. Seki, T. Hisatomi, K. Domen, *Nature*, **2020**, *581*, 411-414.
9. Z. Song, T. Hisatomi, S. Chen, Q. Wang, G. Ma, S. Li, X. Zhu, S. Sun, K. Domen, *ChemSusChem* **2019**, *12*, 1906-1910.
10. H. Lyu, T. Hisatomi, Y. Goto, M. Yoshida, T. Higashi, M. Katayama, T. Takata, T. Minegishi, H. Nishiyama, T. Yamada, Y. Sakata, K. Asakura, K. Domen, *Chem. Sci*. **2019**, *10*, 3196-3201.
11. D. Xu, P. Xu, Y. Zhu, W. Peng, Y. Li, G. Zhang, F. Zhang, T. E. Mallouk, X. Fan, *ACS Appl. Mater. Interfaces* **2018**, *10*, 2810-2818.
12. A. Vijeta, E. Reisner, *Chem. Comm.* **2019**, *55*, 14007-14010.
13. L. Yao, A. Rahmanudin, N. Guijarro, K. Sivula, *Adv. Energy Mater*. **2018**, 8, 1802585-1802602.
14. F. Zhang, Z. Yao, Y. Guo, Y. Li, J. Bergstrand, C. J. Brett, B. Cai, A. Hajian, Y. Guo, X. Yang, J. M. Gardner, J. Widengren, S. V. Roth, L. Kloo, L. Sun, *J. Am. Chem. Soc*. **2019**, *141*, 19700-19707.
15. Gurudayal, D. Sabba, M. H. Kumar, L. H. Wong, J. Barber, M. Grätzel, N. Mathews, *Nano Lett.* **2015**, *15*, 3833-3839.
16. K. Maeda, G. Sahara, M. Eguchi, O. Ishitani, *ACS Catal.* **2015**, *5*, 1700-1707.
17. K. Morita, K. Sakai, H. Ozawa, *ACS Appl. Energy Mater.* **2019**, *2*, 987-992.
18. B. N. DiMarco, R. N. Sampaio, E. M. James, T. J. Barr, M. Bennett, G. J. Meyer, *ACS Appl. Mater. Interfaces* **2020**, *12*, 23923-23930.
19. D. Wang, J. Hu, B. D. Sherman, M. V. Sheridan, L. Yan, C. J. Dares, Y. Zhu, F. Li, Q. Huang, W. You, T. J. Meyer, *Proc. Natl. Acad. Sci. U.S.A.* **2020**, *117*, 13256-13260.
20. P. Xu, T. E. Mallouk, *J. Phys. Chem. C* **2019**, *123*, 299-305.
21. J. Nomrowski, X. Guo, O. S. Wenger, *Chem. Eur. J.* **2018**, *24*, 14084-14087.
22. Y. B. M'Barek, T. Rosser, J. Sum, S. Blanchard, F. Volatron, G. Izzet, R. Salles, J. Fize, M. Koepf, M. C.-Kerlidou, V. Artero, A. Proust, *Appl. Energy Mater.* **2020**, *3*, 163-169.
23. S. Lyu, J. Massin, M. Pavone, A. B. M.-García, C. Labrugère, T. Toupance, M. C.-Kerlidou, V. Artero, C. Olivier, *ACS Appl. Energy Mater*. **2019**, *2*, 4971-4980.

24. L. Tian, J. Föhlinger, Z. Zhang, P. B. Pati, J. Lin, T. Kubart, Y. Hua, J. Sun, L. Kloo, G. Boschloo, L. Hammarström, H. Tian, *Chem. Comm.* **2018**, *30*, 3739-3742.
25. B. P. Rimgard, J. Föhlinger, J. Peterson, M. Lundberg, B. Zietz, A. M. Woys, S. A. Miller, M. R. Wasielewski, L. Hammarström, *Chem. Sci.* **2018**, *41*, 7958-7967.
26. D. M. Fabian, S. Hu, N. Singh, F. A. Houle, T. Hisatomi, K. Domen, F. E. Osterloh, S. Ardo, *Energy Environ. Sci.* **2015**, *8*, 2825-2850.
27. S. Chen, T. Takata, K. Domen, *Nat. Rev. Mater.* **2017**, *2*, 17050.
28. R. Abe, K. Shinmei, N. Koumura, K. Hara, B. Ohtani, *J. Am. Chem. Soc*. **2013**, *135*, 16872-16884.
29. C. Windle, H. Kumagai, M. Higashi, R. Brisse, S. Bold, B. Jousselme, M. Chavarot-Kerlidou, K. Maeda, R. Abe, O. Ishitani, V. Artero, *J. Am. Chem. Soc*. **2019**, *141*, 9593-9602.
30. K. Koshiba, K. Yamauchi, K. Sakai, *ChemElectroChem*, **2019**, *6*, 2273-2281.
31. K. Yamamoto, A. Call, K. Sakai, *Chem. Eur. J.* **2018**, *24*, 16620-16629.
32. S. Sebata, S. Takizawa, N. Ikuta, S. Murata, *Dalton Trans*. **2019**, *48*, 14914-14925.
33. L. M. Antill, S. Takizawa, S. Murata, J. R. Woodward, *Mol. Phys*. **2019**, *117*, 2594-2603.
34. S. Takizawa, N. Ikuta, F. Zeng, S. Komaru, S. Sebata, S. Murata, *Inorg. Chem*. **2016**, *55*, 8723-8735.
35. H. Yang, X. Li, R. S. Sprick, A. I. Cooper, *Chem. Comm.* **2020**, *56*, 6790-6793.
36. A. Nakada, T. Uchiyama, N. Kawakami, S. Nishioka, R. Kamata, H. Kumagai, O. Ishitani, Y. Uchimoto, K. Maeda, *ChemPhotoChem* **2019**, *3*, 37-45.
37. M. V. Sheridan, Y. Wang, D. Wang, L. T.-Gautier, C. J. Dares, B. D. Sherman, T. J. Meyer, *Angew. Chem., Int. Ed.* **2018**, *57*, 3449-3453.
38. Y. I. Kim, S. J. Atherton, E. S. Brigham, T. E. Mallouk, *J. Phys. Chem.* **1993**, *97*, 11802-11810.
39. R. Abe, K. Shinmei, N. Koumura, K. Hara, B. Ohtani, *J. Am. Chem. Soc*. **2013**, *135*, 16872-16884.
40. T. Oshima, S. Nishioka, Y. Kikuchi, S. Hirai, K. Yanagisawa, M. Eguchi, Y. Miseki, T. Yokoi, T. Yui, K. Kimoto, K. Sayama, O. Ishitani, T. E. Mallouk, K. Maeda. *J. Am. Chem. Soc.* **2020**, *142*, 8412-8420.
41. S. Furugori, A. Kobayashi, A. Watanabe, M. Yoshida, M. Kato, *ACS Omega*, **2017**, *2*, 3901-3912.
42. N. Yoshimura, A. Kobayashi, M. Yoshida, M. Kato, *Bull. Chem. Soc. Jpn.* **2019**, *92*, 1793-1800.
43. N. Yoshimura, A. Kobayashi, W. Genno, T. Okubo, M. Yoshida, M. Kato, *Sustain. Energy Fuels* **2020**, *4*, 3450-3457.
44. K. Hanson, M. K. Brennaman, A. Ito, H. Luo, W. Song, K. A. Parker, R. Ghosh, M. R. Norris, C. R. K. Glasson, J. J. Concepcion, R. Lopez, T. J. Meyer, *J. Phys. Chem. C* **2012**, *116*, 14837-14847.
45. L.T. Gautier, M. D. Turlington, S. A. M. Wehlin, A. B. Maurer, M. D. Brady, W. B. Swords, G. J. Meyer, *Chem. Rev*. **2019**, *119*, 4628-4683.
46. L.T. Gautier, W. B. Swords, G. J. Meyer, *Acc. Chem. Res*. **2019**, *52*, 170-179.

47. K. Hu, R. N. Sampaio, J. Schneider, L. Troian-Gautier, G. J. Meyer, *J. Am. Chem. Soc.* **2020**, Accepted. DOI: 10.1021/jacs.0c04886
48. H. Park, W Choi, M. R. Hoffman, *J. Mater. Chem*. **2008**, *18*, 2379-2385.
49. M. R. Norris, J. J. Conception, C. R. K. Glasson, Z. Fang, A. M. Lapides, D. L. Ashford, J. L. Templeton, T. J. Meyer, *Inorg. Chem.* **2013**, *52*, 12492-12501.

# Chapter 5

# Enhancement of Photocatalytic Activity for Hydrogen Production by Surface Modification of Pt-$TiO_2$ Nanoparticles with a Double Layer of Photosensitizers

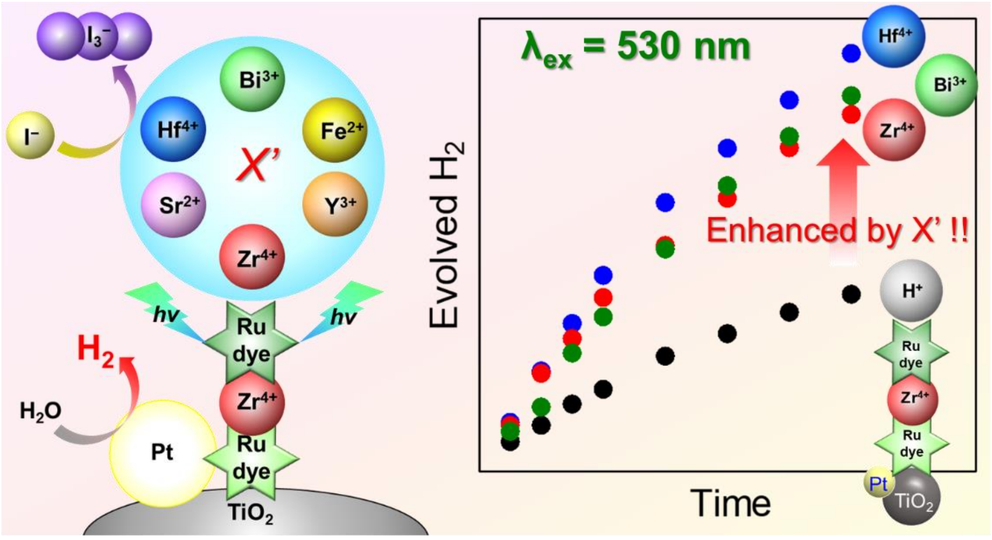

## 5-1 Introduction

Photocatalytic solar water splitting is a desirable reaction for solving global energy and environmental issues.[1-5] Since the discovery of the Honda-Fujishima effect,[6] many semiconductor photocatalysts have been developed. In particular, the construction of a Z-scheme system by combining $H_2$ and $O_2$ evolving photocatalysts (OEP and HEP) has attracted considerable attention as a useful strategy to utilize visible light and ensure a sufficiently large driving force for water splitting and electron transfer reactions.[7-10] For example, in 2016, Domen *et al.* reported a Z-scheme photocatalyst composed of La- and Rh-codoped $SrTiO_3$ and Mo-doped $BiVO_4$—as the $H_2$ and $O_2$ evolving photocatalysts, respectively—on a gold layer, which exhibited 1.1% solar-to-hydrogen (STH) energy conversion efficiency and over 30% apparent quantum efficiency (AQY) at 419 nm.[11] However, further improvement of both the STH and AQY is still necessary for practical application. To achieve this, two targets must be reached: The first is to utilize the longer wavelength range to improve the STH energy conversion efficiency[4,12-13] and the second is to achieve one-way electron transfer from the OEP to HEP *via* an electron mediator.[14-16]

Dye-sensitization is a well-known and extensively studied technique to overcome the weak visible light absorption of a semiconductor substrates.[17-29] Abe *et al.* reported on a Z-scheme water-splitting photocatalyst composed of coumarin-dye-sensitized Pt/$H_4Nb_6O_{17}$ as the HEP and $IrO_2$-Pt/$WO_3$ as the OEP.[30] A remarkably high AQY (2.4% at 420 nm) was achieved by a recently developed Z-scheme system consisting of a Ru(II)-dye-sensitized $Al_2O_3$ cluster-deposited/Pt/$HCa_2Nb_3O_{10}$ as the HEP.[31] Although the AQY and STH values of dye-sensitized photocatalysts (DSPs) are still lower than those of their metal-oxide-based counterparts, the dye-sensitization technique offers a unique advantage. Indeed, further modification at the dye-semiconductor interface is possible by co-absorption and/or multilayering of functional molecules, as evidenced by recent studies in dye-sensitized solar (DSSCs) and electrochemical (DSPEC) cells.[32-35] Meyer *et al.* demonstrated one-directional energy transfer in a bilayer film composed of two different Ru(II) dyes.[35-40] Hanson *et al.* reported that the lifetime of the charge-separated state can be controlled by introducing an organic spacer molecule into the dye–semiconductor interface with various metal cation linkages.[41-44] Further, several research groups have reported that the host–guest interaction is useful for softly immobilizing dyes and catalyst molecules on the semiconductor surface.[45-49] However, literature on the further modification of the dye–semiconductor interface in the field of DSP for water splitting remains limited. Such dye-layer modification is expected to affect the charge-separation behavior of DSP more significantly than that of DSPEC/DSSC because of the dispersive nature of DSP particles in aqueous solution.

In this context, a DSP nanoparticle consisting of a Pt-cocatalyst-loaded $TiO_2$ nanoparticle covered by a bilayer film formed from two Ru(II) dyes with $Zr^{4+}$ cations was reported—Zr-**$RuCP^6$**-Zr-**$RuP^6$**@Pt-$TiO_2$ (**$Zr^{4+}$-DSP**, **$RuCP^6$** = $[Ru(mpbpy)_3]^{10-}$, where **$RuP^6$** = $[Ru(pbpy)_3]^{10-}$, $H_4$mpbpy =

2,2′-bipyridine-4,4′-bis(methane-phosphonic acid), and $H_4$pbpy = 2,2′-bipyridine-4,4′-bis(phosphonic acid)}. It was discovered that the $Zr^{4+}$ cations bound by the outer-surface phosphonate groups of the **RuCP$^6$** dye played a key role in the dye regeneration by the iodide redox-reversible electron donor as in the case of DSSCs,[43] leading to superior photocatalytic $H_2$ evolution activity compared to that observed in the absence of the surface $Zr^{4+}$ cation.[50-54] These results motivated us to improve the outer surface structure by changing the surface $Zr^{4+}$ cations to other metal cations. Such an approach should be valuable not only to enhance the photocatalytic activity, but also to clarify the versatility of this surface-metal cation modification method for one-directional electron transfer at the photocatalyst–mediator interface. Herein, the preparation, characterization, and photocatalytic $H_2$ evolution reactions of surface-metal-replaced DSP nanoparticles—X’-**RuCP$^{6-}$**Zr-**RuP$^6$**@Pt-$TiO_2$ (**X’-DSP**; Scheme 5-1; X’ = $H^+$, $Sr^{2+}$, $Fe^{2+}$, $Y^{3+}$, $Zr^{4+}$, $Hf^{4+}$, and $Bi^{3+}$) are reported. The replacing surface-metal cation from $Zr^{4+}$ to $Sr^{2+}$ or $Y^{3+}$ having the same closed [Kr] electronic configuration should reveal the importance of ionic radius and formal charge. $Hf^{4+}$ exhibiting similar chemical bonding nature to $Zr^{4+}$ was selected to reveal the effect of heavy atom effect on the charge-separation process at the $TiO^{2+}$-dye-mediator interfaces. Further, the redox active metal cations $Fe^{2+}$ and $Bi^{3+}$ were also introduced to evaluate the importance of redox behavior of the surface metal cations that may promote the charge-separation. It was demonstrated that five of the as-synthesized DSPs (X’ = $Fe^{2+}$, $Y^{3+}$, $Hf^{4+}$, $Bi^{3+}$, and the previously synthesized $Zr^{4+}$) showed 1.5- to 2-fold higher photocatalytic activity than that of **$H^+$-DSP** without surface metal ions. This was attributed to the electrostatic interaction between the metal cation and iodide electron donor. Furthermore, the **X’-DSP**s comprising heavy metal cations (X’ = $Zr^{4+}$, $Hf^{4+}$, and $Bi^{3+}$) maintained relatively high activities under green light irradiation ($\lambda$ = 530±15 nm, 0.2~0.3% AQY), which only excited the lower band edge of the metal-to-ligand charge-transfer ($^1$MLCT) transition of the Ru dyes. These results suggest that dye multilayering and surface modification by metal cations are useful approaches for improving the reactivity with anionic electron donors and enhancing the photocatalytic activity under light irradiation at the absorption band edge region.

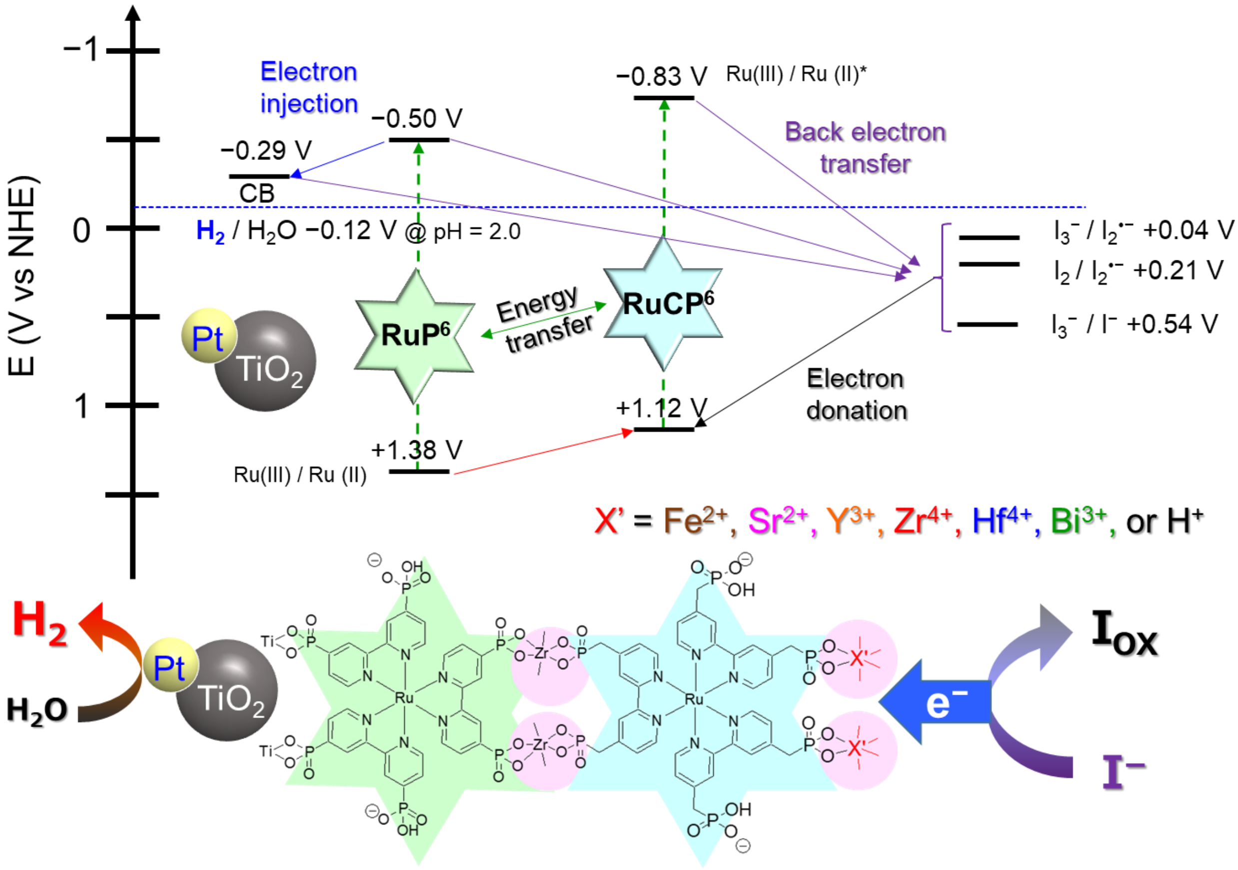

**Scheme 5-1**. Schematic diagram showing a plausible energy and electron transfer mechanism of X'-**RuCP**$^6$-Zr-**RuP**$^6$@Pt-$TiO_2$ (**X'-DSP**). Redox potentials of Ru(II)-PS and iodide species are interfered from the literatures.[37,57]

## 5-2-1 Experimental

### 5-2-1 Preparation of Ru(II)-dye-immobilized Pt-TiO$_2$ nanoparticles (X'-DSPs)

**RuCP**$^{6-}$Zr-**RuP**$^6$@Pt-TiO$_2$ (**H$^+$-DSP**) nanoparticles were synthesized with reference to previous reports (Figure 5-2-1 and Table 5-2-1).[50,53] Immobilization of the outer metal ions was performed by the same synthetic method as that of Zr$^{4+}$-**RuCP**$^{6-}$Zr-**RuP**$^6$@Pt-TiO$_2$ (**Zr$^{4+}$-DSP**), except for the use of other metal salts instead of $ZrCl_2O\cdot8H_2O$ as follows. 30 mg of **H$^+$-DSP** was added to 25 mM of $FeCl_2\cdot4H_2O$, $SrCl_2\cdot6H_2O$, $YCl_3\cdot6H_2O$, $ZrCl_2O\cdot8H_2O$, $HfCl_2O\cdot8H_2O$, or $BiCl_3$ MeOH solution (6 mL, about 50 eq. to the surface immobilized Ru(II) dye) and this suspension was stirred for 1 h at 298 K under dark. Then, the orange suspension was ultra-centrifugated (50,000 rpm, 20 min) and washed twice with small portions of MeOH. The precipitation was dried for a few days at 298~328 K to afford **X'-DSP**.

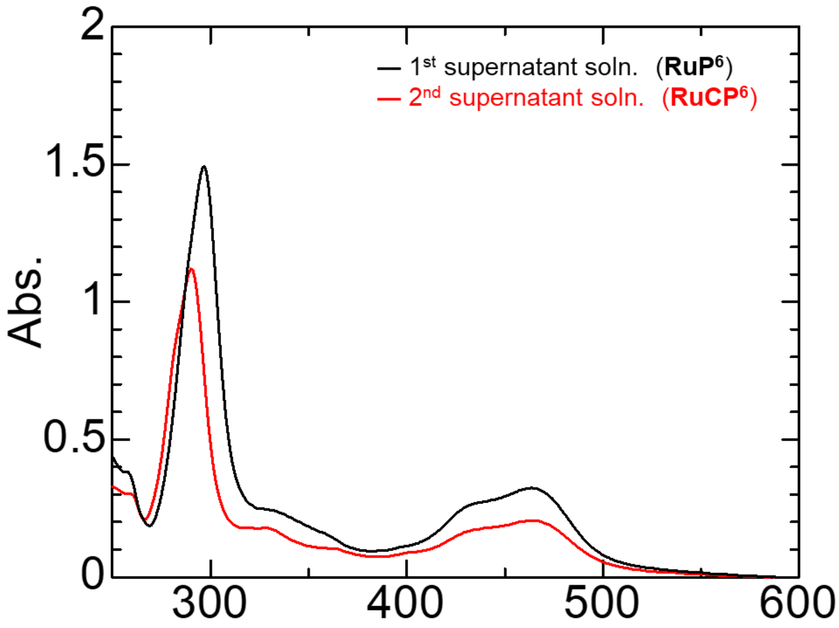

**Figure 5-2-1.** UV-Vis absorption spectra of the supernatant solutions at 298 K.

**Table 5-2-1.** Absorbance of each supernatant solution and the calculated $C_B$ and $M_i$ values about **X'-DSP**

| Photo-catalyst | Immobilized Ru(II) PS | $A$ | $C_B$ (mM) | $M_i$ (μmol) | Surface coverage $N$ (nmol / cm$^2$) |
|---|---|---|---|---|---|
| This work | 1st (inner) layer<br>**RuP$^6$** | 0.324 | 0.826 | 2.50 | 0.0810 |
| | 2nd (outer) layer<br>**RuCP$^6$** | 0.206 | 0.705 | 3.23 | 0.101 |
| Previous work (Chap.4) | 1st (inner) layer<br>**RuP$^6$** | 0.330 | 0.842 | 2.41 | 0.0781 |
| | 2nd (outer) layer<br>**RuCP$^6$** | 0.184 | 0.630 | 3.69 | 0.120 |

### 5-2-2 Measurements

UV−vis absorption spectra were recorded on a Shimadzu UV-2400PC spectrophotometer and Hitachi U-3000 UV-vis spectrometer. The other measurements were performed by using same equipment as chapter 5.

### 5-2-3 Photocatalytic water reduction reaction

The flask-type reactor was irradiated from the bottom using a blue {λ = 460 ± 15 nm; 70 mW; Opto Device Lab. Ltd., (Kumagaya, Saitama, Japan) OP5-4710HP2} or green (λ = 530 ± 15 nm; 40 mW; Opto Device Lab. Ltd., OP5-5310HP2) LED lamp (Figure 5-2-3 and Table 5-2-3-1) as peak top and edge of $^1$MLCT absorption band of Ru(II) dye (Table 5-2-3-2). The other conditions were the same as chapter 4-2.

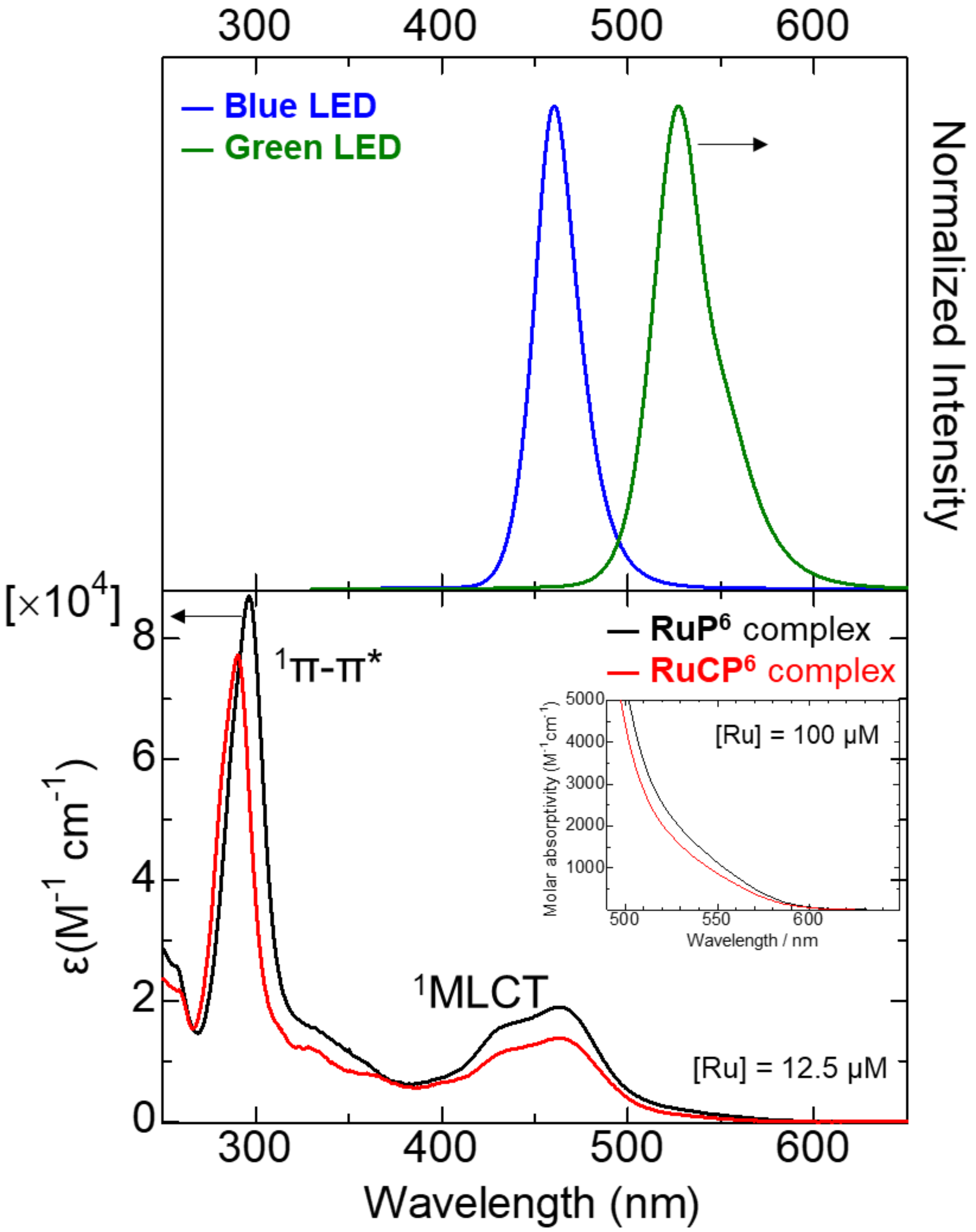

**Figure 5-2-3.** (Top) Emission spectra of (blue) blue LED lamp (Opto Device Lab. Ltd., OP5-4710HP2) and (green) green LED lamp (OP5-5310HP2) recorded on a JASCO FP-6600 spectrofluorometer at 298 K. (bottom) UV-vis absorption spectra of (black) **RuP$^6$** and (red) **RuCP$^6$** complexes in aqueous solution (pH = 2) at 298 K.

**Table 5-2-3-1.** Emission properties of LED lamps used in this study.

| | Peak top[a] (nm) | FWHM[a] (nm) | Shorter wavelength edge[a] (nm) | Longer wavelength edge[a] (nm) |
|---|---|---|---|---|
| blue LED lamp | 460 | 15 | 415 | 535 |
| green LED lamp | 530 | 15 | 460 | 630 |

[a] Statistical error from the emission spectrometer is ±3 nm.

**Table 5-2-3-2.** Molar absorptivity properties of **RuP$^6$** and **RuCP$^6$** complexes.

| | Molar absorptivity ($M^{-1}$ $cm^{-1}$) in aqueous solution (pH = 2) at 298 K | | | | | |
|---|---|---|---|---|---|---|
| | 445 nm[a,b] | 460 nm[a,b] | 475 nm[a,b] | 515 nm[a,c] | 530 nm[a,c] | 545 nm[a,c] |
| **RuP$^6$** | 16800 | 18800 | 16300 | 2960 | 1950 | 1310 |
| **RuCP$^6$** | 12400 | 13700 | 12000 | 2380 | 1540 | 1020 |

[a] Statistical error from the UV-vis absorption spectrometer is ±2 nm.

[b] Estimated by the spectrum with the concentration [Ru] = 12.5 μM.

[c] Estimated by the spectrum with the concentration [Ru] = 100 μM.

## 5-3 Result and discussion

### 5-3-1 Characterization of the Ru(II)-dye-immobilized Pt-$TiO_2$ nanoparticle

Figure 5-3-1-1 shows the XRF spectra of the Ru(II)-dye-immobilized Pt-$TiO_2$ nanoparticles in the solid state at 298 K. As previously reported,[50] Zr Kα and Ru Kα radiation originating from the bridging $Zr^{4+}$ cations and Ru(II) dyes (**RuCP$^6$** and **RuP$^6$**) were clearly observed at the 15.7 and 19.2 keV regions, respectively, in addition to the Pt L and Ti K radiation originating from the Pt-$TiO_2$ nanoparticles. The Zr/Ru molecular ratio for **$Zr^{4+}$-DSP** was estimated from the radiation intensity ratio to be 2.2(1), which is approximately twice the estimated value for **$H^+$-DSP** (1.3(1), Table 5-3-1-1). This result suggests that the **$Zr^{4+}$-DSP** nanoparticle was formed by binding of the $Zr^{4+}$ ion with the phosphonate groups on the outer surface of **$H^+$-DSP**. For the **X'-DSPs** comprising the other metal cations (X' = $Sr^{2+}$, $Fe^{2+}$, $Y^{3+}$, $Hf^{4+}$, and $Bi^{3+}$) at the outer surface of **$H^+$-DSP**, the characteristic X-ray radiation assignable to the metal ions (Fe Kα; Sr Kα; Y Kα; Hf Lα and Lβ; and Bi Lα, Lβ, and Lγ) was observed. The peak intensities of the Zr Kα and Ru Kα radiation for all five **X'-DSPs** were almost comparable to those of **$H^+$-DSP**. Thus, it was supposed that the metal ions were immobilized on the outer phosphonate groups of **RuCP$^6$** without substitution of the inner $Zr^{4+}$ ions or desorption of the **RuCP$^6$** dye. In fact, the characteristic $^1$MLCT absorption of **RuCP$^6$** dye was hardly observed in the UV-vis absorption spectrum of the 2nd $Zr^{4+}$ loading solution (Figure 5-3-1-2). The X'/Ru molecular ratio was estimated based on the intensity of the Kα or Lα radiation of the outer metal cation (Table 5-3-1-1) and decreased in the order **$Zr^{4+}$-DSP** (X'/Ru = 0.9(1)) = **$Hf^{4+}$-DSP** (X'/ Ru = 0.9(1)) ≥ **$Bi^{3+}$-DSP** (X'/Ru = 0.7(1)) ≥ **$Fe^{2+}$-DSP** (X'/Ru = 0.5(1)) > **$Y^{3+}$-DSP** (X'/Ru = 0.1(1)) > **$Sr^{2+}$-DSP** (X'/Ru < 0.1). The estimated X'/Ru ratio tends to decrease with decreasing formal charge ($V_{X'}$) and absolute value of the hydration enthalpy ($\Delta H_{hyd}$) of the outer metal cation (Table 5-3-1-1, Table 5-3-1-2). Although additional experiments are necessary to make the conclusion about this trend, it may occur because the smaller $V_{X'}$ weakens the ionic bond between X' and the phosphonate, and the smaller $\Delta H_{hyd}$ causes rapid ligand exchange reaction of the X' cation. In fact, the $Sr^{2+}$ ions with the smallest $V_{X'}$ and $\Delta H_{hyd}$ values examined in this work were easily desorbed from the nanoparticle surface of **$Sr^{2+}$-DSP** by immersion into a 0.5 M KCl aqueous solution for 1 h at 298 K (Figure 5-3-1-3). Specifically, metal ions with larger $V_{X'}$ and $\Delta H_{hyd}$ values, such as $Hf^{4+}$, can be tightly bound by the surface phosphonates even in highly polar aqueous solutions, and are suitable for the surface functionalization of nanoparticle photocatalysts. In addition, it was also found that the loading amount of $Zr^{4+}$ cation of **$Zr^{4+}$-DSP** hardly increased by twice repeating the immobilization reaction of $Zr^{4+}$ in MeOH solution (Figure 5-3-1-4), suggesting that most of the surface phosphonate groups were bound to $Zr^{4+}$.

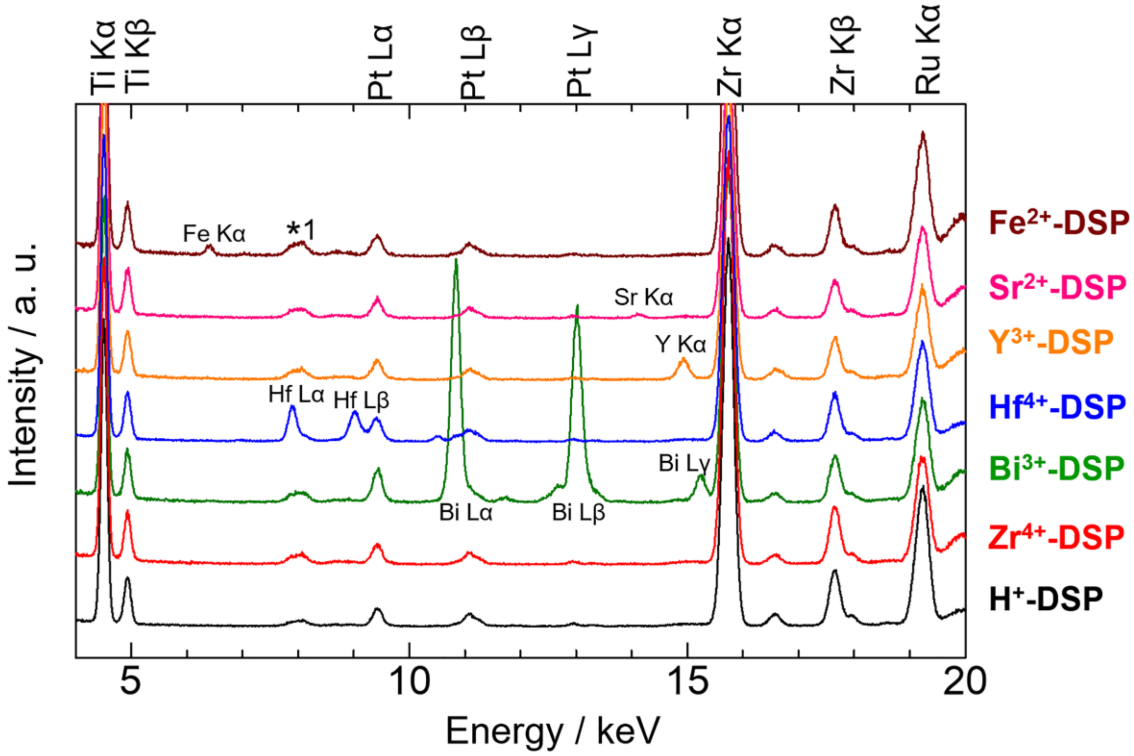

**Figure 5-3-1-1**. X-ray fluorescence (XRF) spectra of **X’-DSPs** in the solid state. All spectra were normalized using the Ti Kα peak. The peak marked as *1 is the background of the Cu sample holder.

**Table 5-3-1-1.** Estimated metal ion rate per Ru of Ru(II)-PS-multilayered Pt-$TiO_2$ nanoparticles by XRF spectra

| Photocatalyst<br>**X’-DSP** | Inner metal ion rate per Ru | Outer (surface) metal ion rate per Ru |
|---|---|---|
| | Zr/Ru | M’/Ru |
| **H$^{+}$-DSP** | 1.3(1) | - |
| **Zr$^{4+}$-DSP** | 1.3(1) | 0.9(1) |
| **Hf$^{4+}$-DSP** | 1.3(1) | 0.9(1) |
| **Bi$^{3+}$-DSP** | 1.3(1) | 0.7(1) |
| **Fe$^{2+}$-DSP** | 1.3(1) | 0.5(1) |
| **Sr$^{2+}$-DSP** | 1.3(1) | <0.1 |
| **Y$^{3+}$-DSP** | 1.3(1) | 0.1(1) |

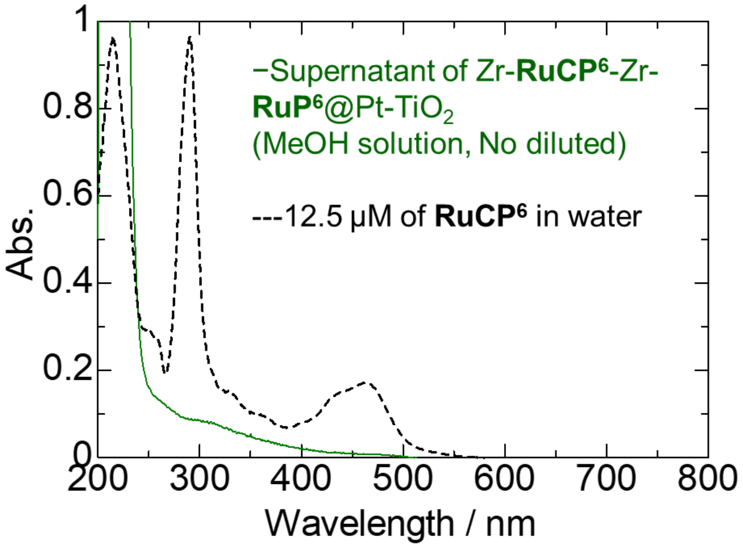

**Figure 5-3-1-2**. UV-vis absorption spectra of the supernatant solution obtained by ultracentrifugation of 2nd $Zr^{4+}$ loading solution to prepare Zr-**RuCP$^{6}$**-Zr-**RuP$^{6}$**@Pt-$TiO_2$ (**$Zr^{4+}$-DSP**). Dashed line shows the absorption spectra of **RuCP$^{6}$** dye in water.

**Table 5-3-1-2**. Ion radius and hydration enthalpy of metal cations.

| Outer metal cations of **X'-DSP** | AQY of photocatalytic $H_2$ evolution reaction (%, 0-1 h) | Ion radius of metal cations on 8 coordinate state [a] (pm) | Hydration enthalpy of metal cations [b] (kJ/mol) |
|---|---|---|---|
| $Zr^{4+}$ | 0.936 | 98 | −7000 |
| $Hf^{4+}$ | 1.06 | 97 | −7200 |
| $Bi^{3+}$ | 0.787 | 131 | −3600 |
| $Fe^{2+}$ | 0.785 | 106 | −2900 |
| $Sr^{2+}$ | - | 140 | −1500 |
| $Y^{3+}$ | 1.09 | 116 | −3600 |

[a] These values are interfered from literature[59]. [b] These values are interfered from literature[60].

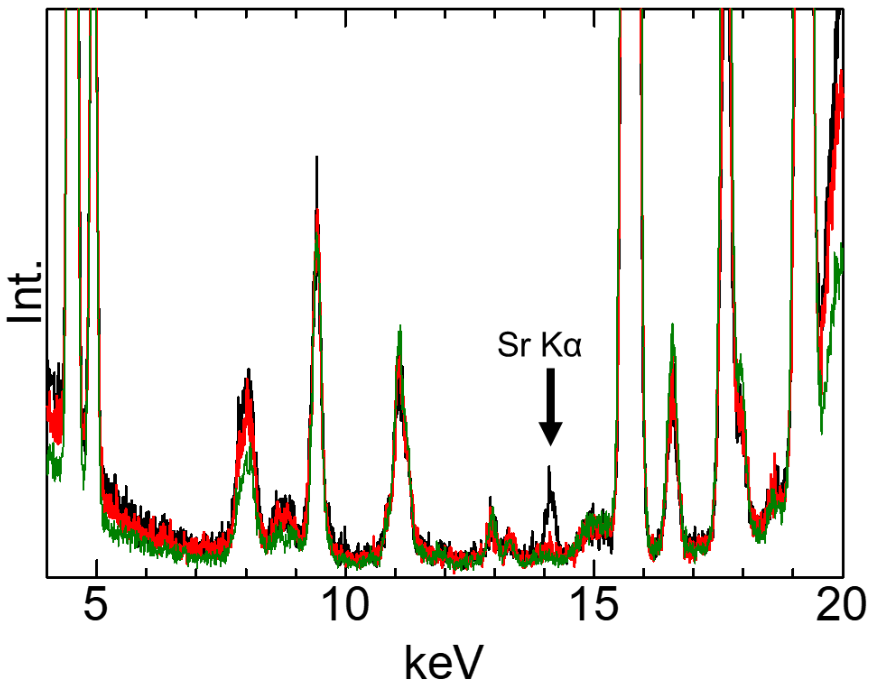

**Figure 5-3-1-3**. XRF spectra of **$Sr^{2+}$-DSP** (black) before and (red) after immersion to 0.5 M KCl aqueous solution for 1 h at 293 K. Green line shows the spectrum of **$H^{+}$-DSP**. All spectra were normalized based on the intensity of Ti Kα radiation. All spectra were measured in the solid state at 293 K.

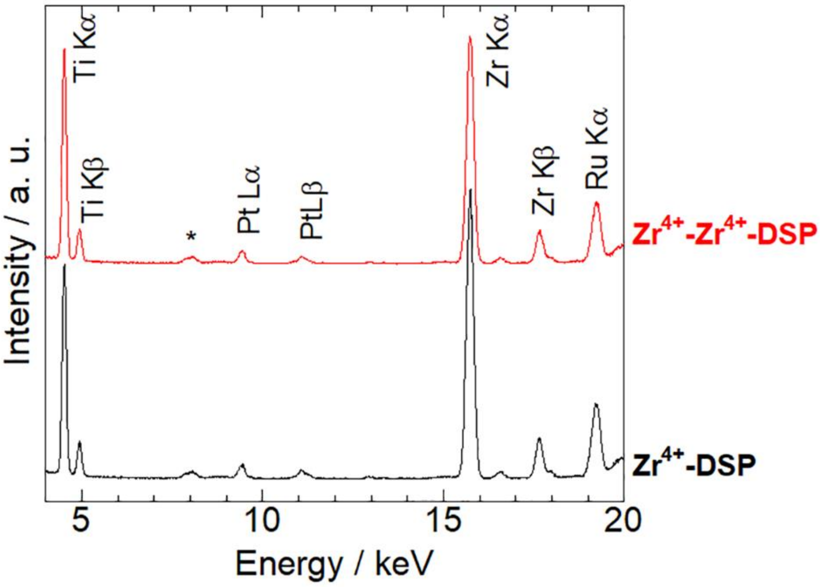

**Figure 5-3-1-4**. XRF spectra of **Zr$^{4+}$-DSP** and **Zr$^{4+}$-Zr$^{4+}$-DSP** that was prepared by twice repeating the Zr$^{4+}$ cation immobilization reaction for **H$^{+}$-DSP**. The peak marked by an asterisk (*) is due to the Cu sample holder.

### 5-3-2 Surface metal ion dependence for water reduction reaction from iodide

Figure 5-3-2-1 shows the results of the photocatalytic $H_2$ evolution reactions using **X'-DSPs** (X' = $H^+$, $Fe^{2+}$, $Y^{3+}$, $Zr^{4+}$ $Hf^{4+}$, $Bi^{3+}$) nanoparticles in 0.5 M KI aqueous solution as the photocatalyst. The turn over number of photosensitizer (PS TON), turn over frequency of PS (PS TOF), and apparent quantum yield (AQY) are listed in Table 5-3-2-1. Note that the total amount of Ru(II) dye in each solution was constant (100 μM) and no hydrogen evolution was observed in the absence of Ru(II) dye, light, or electron donor (Table 5-3-2-2). The characteristic absorption bands of triiodide anion ($I_3^-$) was clearly observed in the UV-vis absorption spectra of the reaction solution after 6 h irradiation (Figure 5-3-2-2). The amount of $I_3^-$ was estimated based on the molar absorption coefficient at 350 nm (about 14 μmol) to be comparable to that of $H_2$, indicating that the electron source of $H_2$ evolution is the iodide anions in the reaction solution. In addition, observed pH change from 2.0 to 2.4 in the reaction driven by **$Zr^{4+}$-DSP** suggest that the protons in the reaction solution were reduced photocatalytically to $H_2$. All metal-cation-immobilized **X'-DSPs** evolved at least 1.5 times more $H_2$ than did the **$H^+$-DSP**, suggesting a positive effect of metal ion coordination to the surface of the phosphonate groups on the photocatalytic $H_2$ evolution reaction. This result qualitatively agrees with the Hanson's works on the Ru(II)-dye-sensitized solar cells in which the open circuit voltage was improved by the surface-metal cation modification.[39] Although all metal-cation-immobilized **X'-DSPs** nanoparticles evolved comparable amounts of $H_2$, notable trends were observed, whereby the amounts of evolved $H_2$ with **$Bi^{3+}$-DSP** and **$Fe^{2+}$-DSP** were 20% less than those with **X'-DSPs** (X' = $Zr^{4+}$, $Hf^{4+}$, and $Y^{3+}$). The plausible reason may be the redox-active nature of these metal cations, wherein $Bi^{3+}$ and $Fe^{2+}$ have more positive reduction potentials than the oxidation potential of the photoexcited Ru(II)* dyes ($E(Bi^{3+}/Bi^{+})$ = +0.20 V vs. NHE, $E(Fe^{3+}/Fe^{2+})$ = +0.77 V vs. NHE, Table 5-3-2-3) in addition to the energy transfer quenching by paramagnetic $Fe^{2+}$ cation as reported in the literature.[39] These may induce the opposite electron/energy transfers from the outer **$RuCP^{6}$*** dye to the surface X' cation, leading to the lower photocatalytic activity. It is interesting to note that **$Y^{3+}$-DSP**, which has the largest X' ionic radius ($Y^{3+}$: 116 pm, $Zr^{4+}$: 98 pm, $Hf^{4+}$: 97 pm) with 10-times diluted X' cations on the surface than **$Zr^{4+}$-DSP**, exhibited near-identical activity as that of **$Zr^{4+}$-DSP**. This suggests that the ion radius of the outer X' ion hardly affected the reactivity with the electron mediator.

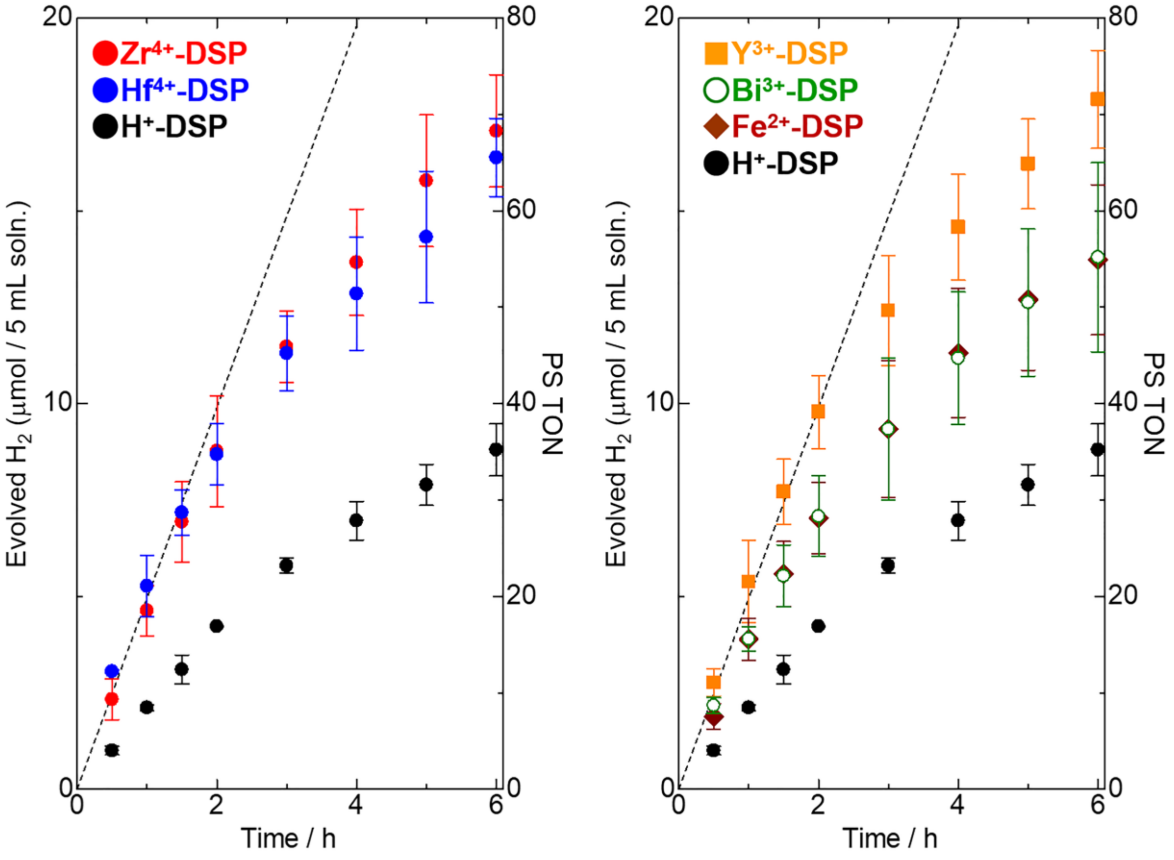

**Figure 5-3-2-1**. Photocatalytic $H_2$ evolution reactions driven by **X'-DSPs** in the presence of 100 μM Ru(II) dye and 0.5 M KI as the electron donor (initial pH = 2.0, λ = 460 ± 15 nm, 70 mW in total). Dashed line in each panel indicates AQY = 1%.

**Table 5-3-2-1**. Results of the photocatalytic $H_2$ evolution experiments of **X'-DSPs** in 0.5 KI aqueous solution.

| X' | $\lambda_{ex}$ (nm) | $H_2{}^a$ (μmol) (0–6 h) | PS TON$^a$ (0–3 h) | PS TON$^a$ (0–6 h) | PS initial TOF$^a$ | AQY$^a$ (%) (0–6 h) | *i*AQY$^a$ (%) (0–1 h) |
|---|---|---|---|---|---|---|---|
| $H^+$ | 460 ± 15 | 8.80±0.7 | 23.2 | 35.2 | 8.47 | 0.302 | 0.436 |
| $Y^{3+}$ | 460 ± 15 | 17.9±1.3 | 49.6 | 71.5 | 21.5 | 0.614 | 1.11 |
| $Zr^{4+}$ | 460 ± 15 | 17.1±1.5 | 45.9 | 68.3 | 18.5 | 0.587 | 0.952 |
| $Hf^{4+}$ | 460 ± 15 | 16.4±1.0 | 45.2 | 65.5 | 21.1 | 0.562 | 1.09 |
| $Bi^{3+}$ | 460 ± 15 | 13.8±2.5 | 37.4 | 55.2 | 15.6 | 0.474 | 0.803 |
| $Fe^{2+}$ | 460 ± 15 | 13.7±1.9 | 37.4 | 54.9 | 15.5 | 0.470 | 0.798 |
| $H^+$ | 530 ± 15 | 1.95±0.47 | 5.06 | 7.80 | 2.01 | 0.102 | 0.157 |
| $Zr^{4+}$ | 530 ± 15 | 3.93±0.27 | 9.95 | 15.7 | 4.30 | 0.205 | 0.337 |
| $Hf^{4+}$ | 530 ± 15 | 4.61±0.08 | 11.8 | 18.4 | 4.41 | 0.241 | 0.345 |
| $Bi^{3+}$ | 530 ± 15 | 4.14±0.07 | 9.79 | 16.6 | 2.81 | 0.216 | 0.220 |

[a] Reaction conditions: [Ru-PS] = 100 μM in total, [KI] = 0.5 M, HCl aqueous solution (pH 2), $\lambda_{ex}$ = 460 ± 15 nm (70 mW in total) or 530 ± 15 nm (40 mW in total). The reaction solution was purged with bubbling Ar for 1 h before light irradiation. The numerical values represent the averages of more than three experiments. Definitions: PS, photosensitizer; TON, turnover number; TOF, turnover frequency; AQY, apparent quantum yield for total 6 h reaction; *i*AQY, AQY at the initial 1h of reaction.

**Table 5-3-2-2**. Control experiments of photocatalytic hydrogen evolution of **X'-DSP**

| Entry [a] | Photocatalyst | Electron Donor (ED) | Light irradiation | Evolved $H_2$ [b] |
|---|---|---|---|---|
| 1 | **$Zr^{4+}$-DSP** | 0.5 M KI | On | Yes |
| 2 | **$Zr^{4+}$-DSP** | 0.5 M KI | Off | - |
| 3 | **$Zr^{4+}$-DSP** | without KI | On | - |
| 4 | without photocatalyst | 0.5 M KI | On | - |

[a] Reaction conditions: [Ru] = 100 μM in HCl aqueous solution (pH = 2, 5 mL) under blue LED light irradiation (λ = 460 ± 15 nm) for 6 h. [b] Gas in the head space was analyzed qualitatively by Gas Chromatography (GC). "Yes" indicates that the evolved amount of $H_2$ was larger than the GC detection limit.

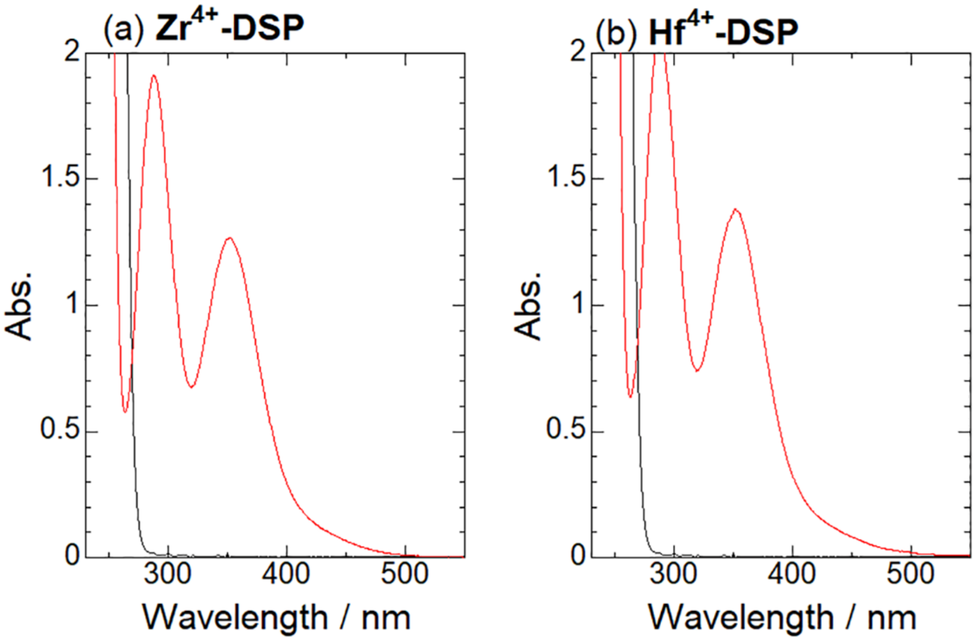

**Figure 5-3-2-2**. UV-vis absorption spectra of the supernatants obtained by centrifugation of the reaction solutions after 6 h irradiation of (a) **$Zr^{4+}$-DSP** and (b) **$Hf^{4+}$-DSP**. Each supernatant (1 mL) was diluted to 50 mL with deionized water prior to the measurement. Black line in each panel is the spectrum before irradiation.

**Table 5-3-2-3**. Redox potentials of chemical species used in this paper

| | E (V vs. NHE) |
|---|---|
| $Sr^{2+}/Sr$ | −2.90 [a] |
| $Y^{3+}/Y$ | −2.37 [a] |
| $Hf^{4+}/Hf$ | −1.70 [a] |
| $Zr^{4+}/Zr$ | −1.55 [a] |
| $Ru^{3+}/Ru^{2+}*$ of **RuCP$^6$** complex | −0.83 [b] |
| $Ru^{3+}/Ru^{2+}*$ of **RuP$^6$** complex | −0.50 [b] |
| $Fe^{2+}/Fe$ | −0.447 [a] |
| Conduction band minimum of $TiO_2$ at pH 2 | −0.29 |
| $Bi^{3+}/Bi^{+}$ | +0.2 [a] |
| $Bi^{3+}/Bi$ | +0.308 [a] |
| $I_3^-/ I^-$ | +0.54 [c] |
| $Fe^{3+}/Fe^{2+}$ | +0.771 [a] |
| $Ru^{3+}/Ru^{2+}$of **RuCP$^6$** complex | +1.12 [b] |
| $Ru^{3+}/Ru^{2+}$of **RuP$^6$** complex | +1.38 [b] |

[a] These values are interfered from literature[61]. [b] These values are interfered from literature[37]. [c] These values are interfered from literature[57].

To clarify the interaction between **X'-DSP** and iodide mediator, the zeta (ζ) potentials in HCl aqueous solution (pH 2) with/without KI were evaluated (Table 5-3-2-4). In the HCl aqueous solution without iodide, all metal-cation-immobilized **X'-DSPs** showed an almost neutral ζ potential (–3.5 to +3.8 mV). On the other hand, in the presence of KI, the ζ potential of each metal-cation-immobilized **X'-DSPs** was negatively shifted (–7.6 to –13 mV). Considering that the comparable zeta potential shift was also observed for the Pt-$TiO_2$ nanoparticle without Ru(II) dyes (+27 to +12 mV) and the **RuP$^{5-}$**sensitized Pt-$TiO_2$ nanoparticle (**RuP$^6$**@Pt-$TiO_2$, from –4.6 to –14 mV), the positively charged $TiO_2$ surface in the acidic pH condition may attract iodide anions electrostatically even after the loading of negatively charged Ru(II) dyes. This zeta potential shift by adding KI was negligible only for Zr-**RuP$^6$**@Pt-$TiO_2$, implying that not only the bare $TiO_2$ surface but also the 2nd-outer **RuCP$^6$** dye layer with the surface X' cations may act as the interaction sites for iodide attraction. The slight variation of zeta potential change among **X'-DSP** series may implies the contribution of surface metal cations for the iodide attraction. The photocatalytic activity of all the samples gradually decreased; for example, the AQY at the initial 1 h of reaction (*i*AQY) of **$Hf^{4+}$-**

**DSP** was 1.09%, whereas the average AQY after 6 h was approximately reduced by half (0.562%). The SEM image of **Hf$^{4+}$-DSP** was hardly changed after 6 h reaction, and the L and M radiations of Ru and Hf elements were clearly observed at 2.6 and 1.6 keV, respectively in the EDS spectra (Figure 5-3-2-3), suggesting that **Hf$^{4+}$-DSP** hardly decomposed during the reaction. Thus, the origin of gradual decrease of photocatalytic activity is because triiodide, generated as the oxidation product of $H_2$ evolution, exhibited moderate light absorptivity (1110 $M^{-1}$ $cm^{-1}$ at 460 nm) and disturbed the light absorption of the Ru(II) PSs (Figure 5-3-2-4).

**Table 5-3-2-4**. Estimated particle diameters and zeta(ζ)-potentials of Ru(II)-PS-immobilized nanoparticles in the HCl aqueous solution or 0.5 M KI aqueous solution. All measurements were done in pH = 2.0 aq.

| Photocatalyst | ζ potential (mV) | |
|---|---|---|
| | HCl aq. | 0.5 M KI aq. |
| Pt-$TiO_2$ | +27 | +12 |
| **RuP$^6$**@Pt-$TiO_2$ | −4.6 | −14 |
| Zr-**RuP$^6$**@Pt-$TiO_2$ | −0.37 | +4.7 |
| **RuCP$^{6-}$**Zr-**RuP$^6$**@Pt-$TiO_2$ **(H$^+$-DSP)** [a] | −1.7 | −11 |
| Zr-**RuCP$^{6-}$**Zr-**RuP$^6$**@Pt-$TiO_2$ **(Zr$^{4+}$-DSP)**[a] | −0.29 | −7.6 |
| Hf-**RuCP$^{6-}$**Zr-**RuP$^6$**@Pt-$TiO_2$**(Hf$^{4+}$-DSP)** | +3.8 | −15 |
| Bi-**RuCP$^{6-}$**Zr-**RuP$^6$**@Pt-$TiO_2$**(Bi$^{3+}$-DSP)** | +0.84 | −11 |
| Fe-**RuCP$^{6-}$**Zr-**RuP$^6$**@Pt-$TiO_2$**(Fe$^{2+}$-DSP)** | +1.7 | −13 |
| Y-**RuCP$^{6-}$**Zr-**RuP$^6$**@Pt-$TiO_2$**(Y$^{3+}$-DSP)** | −3.5 | −13 |

[a] These values of the samples are interfered from literature.[53]

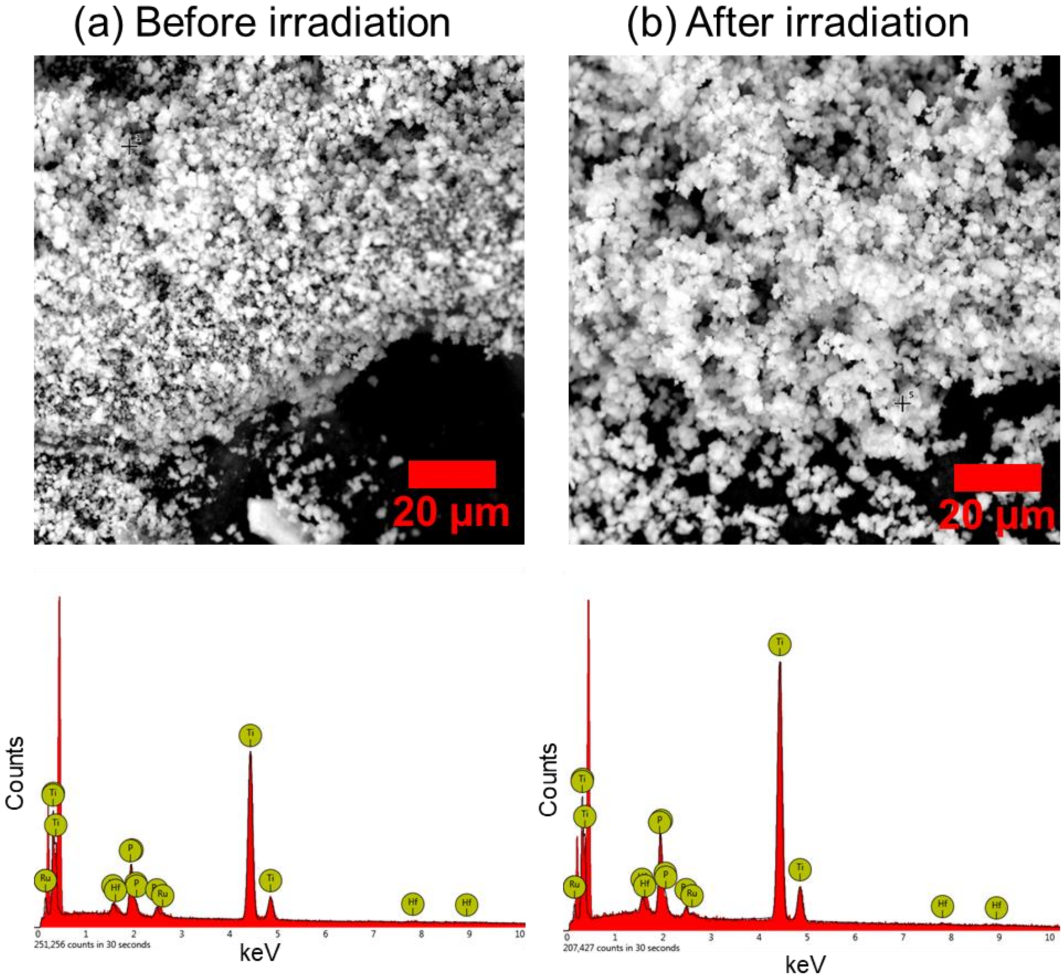

**Figure 5-3-2-3**. SEM images (upper) and EDS spectra (lower) of **$Hf^{4+}$-DSP** (a) before and (b) after photocatalytic $H_2$ evolution reaction for 6 h.

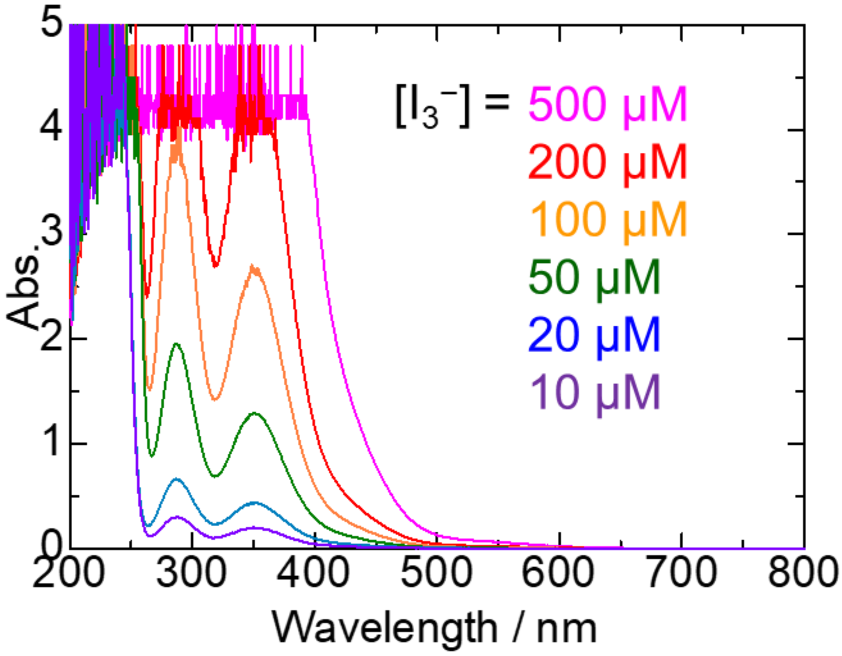

**Figure 5-3-2-4**. UV-vis absorption spectra of triiodide in 0.5 M KI and HCl aqueous solution (pH =2).

### 5-3-3 Excitation wavelength dependence for hydrogen evolution reaction

From the viewpoint of the effective utilization of solar light, the utilization of longer-wavelength light for photocatalytic $H_2$ evolution is crucial. The photocatalytic activities of **$Zr^{4+}$-DSP**, **$Hf^{4+}$-DSP**, and **$Bi^{3+}$-DSP** under green light excitation (λ = 530 ±15 nm) were next investigated. Although $[Ru(bpy)_3]$-type dyes are well-known PSs for blue light excitation because of their strong $^1$MLCT absorption character at approximately 460 nm, both **RuCP$^6$** and **RuP$^6$** exhibit weak MLCT absorption shoulders up to approximately 590 nm (molar absorption coefficient, $\varepsilon$ is 1540 and 1910 $M^{-1}$ $cm^{-1}$ at 530 nm, respectively, Figure 5-2-3 and Table 5-2-3-2.). Thus, it was expected that heavier surface X' cations, such as $Hf^{4+}$ and $Bi^{3+}$, might partially allow spin-forbidden $^3$MLCT excitation by the strong heavy-atom effect *via* the coordination bonds with the phosphonate group. In addition, light shielding by triiodide should be suppressed under green light irradiation because of its smaller $\varepsilon$ at 530 nm (152 $M^{-1}$ $cm^{-1}$) than at 460 nm (1110 $M^{-1}$ $cm^{-1}$; see Figure 5-3-2-4 and Table 5-3-3-1).

**Table 5-3-3-1**. Molar absorptivity of triiodide in aqueous solution estimated from **Figure 5-3-2-4**.

| | Molar absorptivity ($M^{-1}cm^{-1}$) | | | |
|---|---|---|---|---|
| | At 288 nm | At 350 nm | At 460 nm | At 530 nm |
| In this work | 39800 | 26700 | 1110 | 152 |
| Ref. A[62] | 38790 | 25750 | - | - |
| Ref. B[63] | 40000 | 26400 | - | - |

The results of the photocatalytic $H_2$ evolution reactions under green light irradiation are shown in Figure 5-3-3-2, while the estimated PS TON, TOF, and AQY values are listed in Table 5-3-2-1. Even under green light irradiation, the estimated TON for all cases exceeded one, indicating that $H_2$ evolution from iodide occurred photocatalytically. The amount of $H_2$ produced after 6 h of green light irradiation was smaller than that under blue light irradiation in all cases, because of the lower $\varepsilon$ of the Ru PSs for green light. The comparable TON value of **$Hf^{4+}$-DSP** to that under blue light irradiation (TON = 45.2 for 3 h) was achieved by long-term photocatalytic reaction for 20 h (TON ~ 40, Figure 5-3-3-3). A notable difference between the metal-cation-immobilized **X'-DSPs** and **$H^+$-DSP** was observed. Under blue light irradiation, the PS TON of metal-cation-immobilized **X'-DSPs** after 6 h irradiation was 1.6–1.94 times higher than that of **$H^+$-DSP**, while the difference under green light illumination was more pronounced (e.g., 1.9–2.4 times larger PS TON for metal-cation-immobilized **X'-DSPs**). The electron transfer from the redox-reversible iodide donor to the one-electron oxidized

Ru(III) dye should be the important step in these photocatalytic $H_2$ evolutions, because the back electron transfer to the iodide radical ($I^{\bullet}$, $E(I^{\bullet}/I^{-})$ = 1.33 V vs NHE) from the regenerated Ru(II) dye ($E(Ru^{III}/Ru^{II})$ = 1.12 V for **RuCP⁶**) possibly occurs just after the dye regeneration.[57-58] The photoexcitation frequency of Ru dyes under green light irradiation (λ = 530 nm, 40 mW) must be lower than that under blue light (λ = 460 nm, 70 mW) because of the lower $\varepsilon$ of the Ru dye and lower light intensity of the LED light source. Hence, the direct coupling between two iodine radicals to form a stable and weaker oxidant iodine molecule ($I_2$, $E(I_2/I^{-})$ = 0.54 V) should be negligible. The possible reaction in this case would be bond formation between the iodine radical $I^{\bullet}$ and iodide anion $I^{-}$ to form a diiodide radical anion ($I_2^{\bullet -}$, $E(I_2^{\bullet -}/I^{-})$ = 1.03 V), which should be favorable at high $I^{-}$ concentrations. Thus, the superior activity of metal-cation-immobilized **X'-DSPs** compared to that of **H⁺-DSP** was attributed to the more effective interaction between the iodide and positively charged outer surface of metal-cation-immobilized **X'-DSPs** than that with the negatively charged **H⁺-DSP**. This leads to more efficient dye regeneration by iodide, even at the lower photoexcitation frequency from green light irradiation.

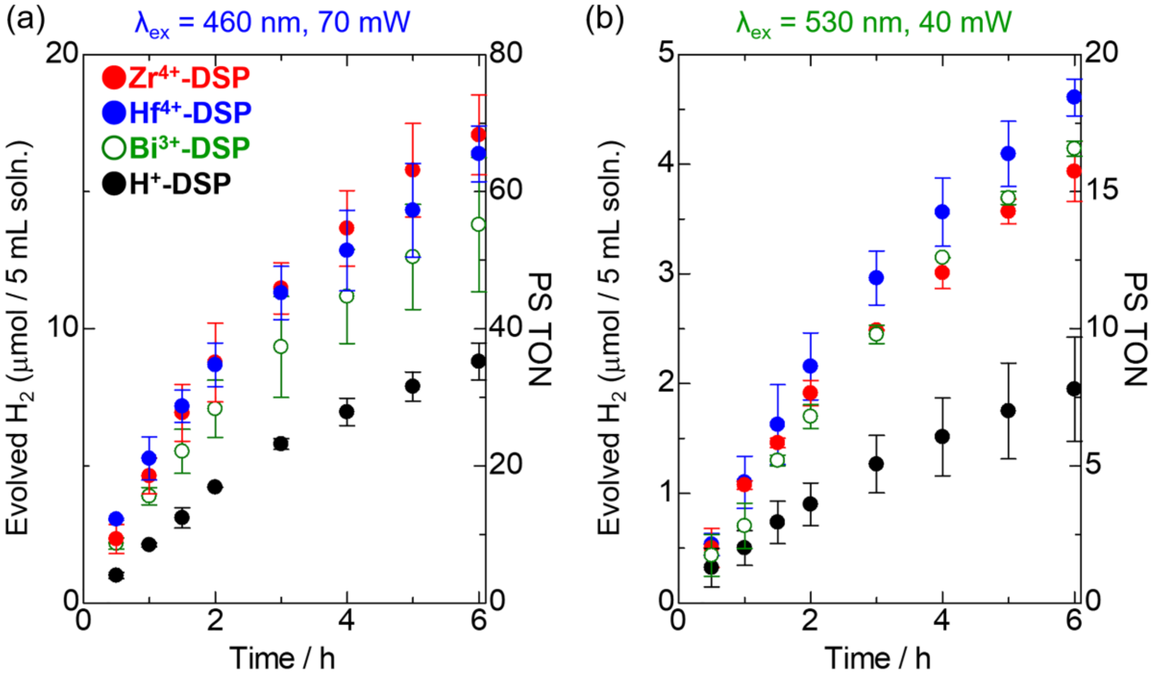

**Figure 5-3-3-2.** (a) Photocatalytic $H_2$ evolution reactions driven by **X'-DSPs** under blue light (460 ± 15 nm, 70 mW) or (b) green light (530 ± 15 nm, 40 mW in total) irradiation in the presence of 100 μM Ru(II) dye and 0.5 M KI as the electron donor (initial pH = 2.0).

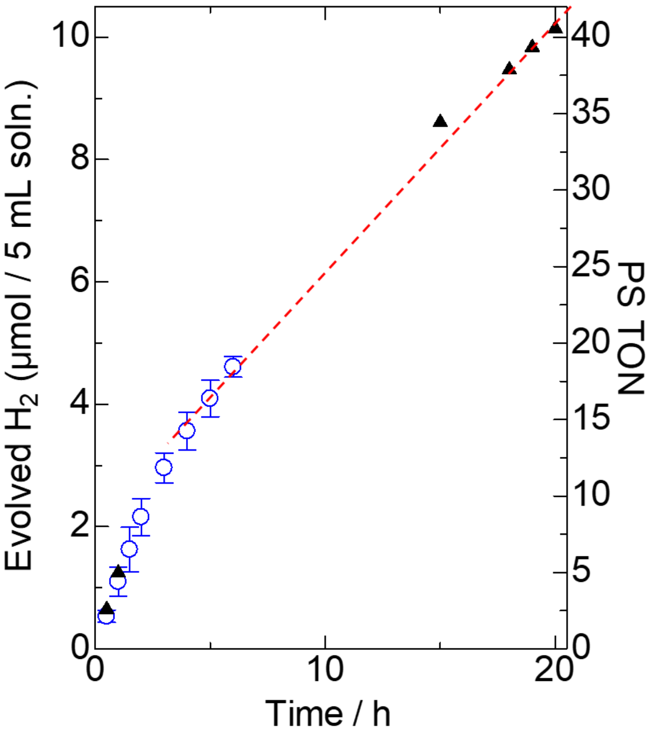

**Figure 5-3-3-3**. Photocatalytic $H_2$ evolution reactions driven by **$Hf^{4+}$-DSP** under green light irradiation ($\lambda$ = 530 ± 15 nm, 40 mW) in the presence of 100 µM Ru(II) dye and 0.5 M KI as the electron donor (initial pH = 2.0). Blue open circles and black closed triangles show the results of 6 and 20 h reactions driven by the same **$Hf^{4+}$-DSP**. Red dashed line is a guide to show the linear relationship between irradiation time and evolved amount of $H_2$.

The molar absorption coefficients of **$RuCP^6$** and **$RuP^6$** at 530 nm were estimated to be 1540 and 1950 $M^{-1}$ $cm^{-1}$, respectively, by UV-vis absorption spectroscopy in dilute HCl aqueous solution (pH 2, Figure 5-2-3-2 and Figure 5-3-3-4). The total amount of Ru(II) dye used in each photocatalytic $H_2$ evolution was 100 µM, so that the absorbance at 530 nm was estimated to be 0.17, based on the Lambert-Beer law in which the effects of dye immobilization on Pt-$TiO_2$, the crosslinking Zr ions, and surface metal ions were ignored. This value indicates that only 33% of irradiated green light was absorbed by the Ru(II) dyes. The absorbance of the reaction solution at 460 nm was similarly estimated to be approximately 1.6, suggesting that most of the irradiated blue light (~97%) was absorbed by the Ru(II) dyes. Thus, the decrease in AQY of **$Zr^{4+}$-DSP** at 530 nm irradiation to a third of that at 460 nm irradiation was primarily due to the smaller absorptivity. This implies that the irradiation wavelength dependence of the charge separation efficiency at the semiconductor–dye and dye–mediator interfaces of **$Zr^{4+}$-DSP** should be negligible.

Interestingly, the amounts of evolved $H_2$ for **$Bi^{3+}$-DSP** and **$Hf^{4+}$-DSP** after 6 h of green light irradiation were slightly larger than that of **$Zr^{4+}$-DSP**. The reverse trend was observed for blue light irradiation, wherein **$Bi^{3+}$-DSP** and **$Hf^{4+}$-DSP** respectively evolved slightly lower and comparable amounts of $H_2$ compared to that evolved by **$Zr^{4+}$-DSP**. The electrostatic interaction between the photocatalyst nanoparticle and iodide electron donor should be independent of the light source and was roughly estimated to be comparable among the three photocatalysts, as suggested by their zeta potentials (Table 5-3-2-4). One possible origin of the slightly higher activity of **$Bi^{3+}$-DSP** and **$Hf^{4+}$-DSP** than that of **$Zr^{4+}$-DSP** under green light illumination may be due to the different contributions of the spin-forbidden $^3$MLCT transition—this could be partially allowed by the stronger heavy atom effect of the surface-immobilized $Hf^{4+}$ and $Bi^{3+}$ cations compared to that of $Zr^{4+}$. Unfortunately, a negligible difference was observed in the UV-vis diffuse reflectance spectra in the solid state (Figure 5-3-3-4), probably because of the light scattering of the $TiO_2$ nanoparticles. Further investigations to clarify the role of the heavy-atom effect are now in progress, wherein not only the outer surface $Zr^{4+}$ but also the inner bridging $Zr^{4+}$ cations are replaced with heavier metal ions.

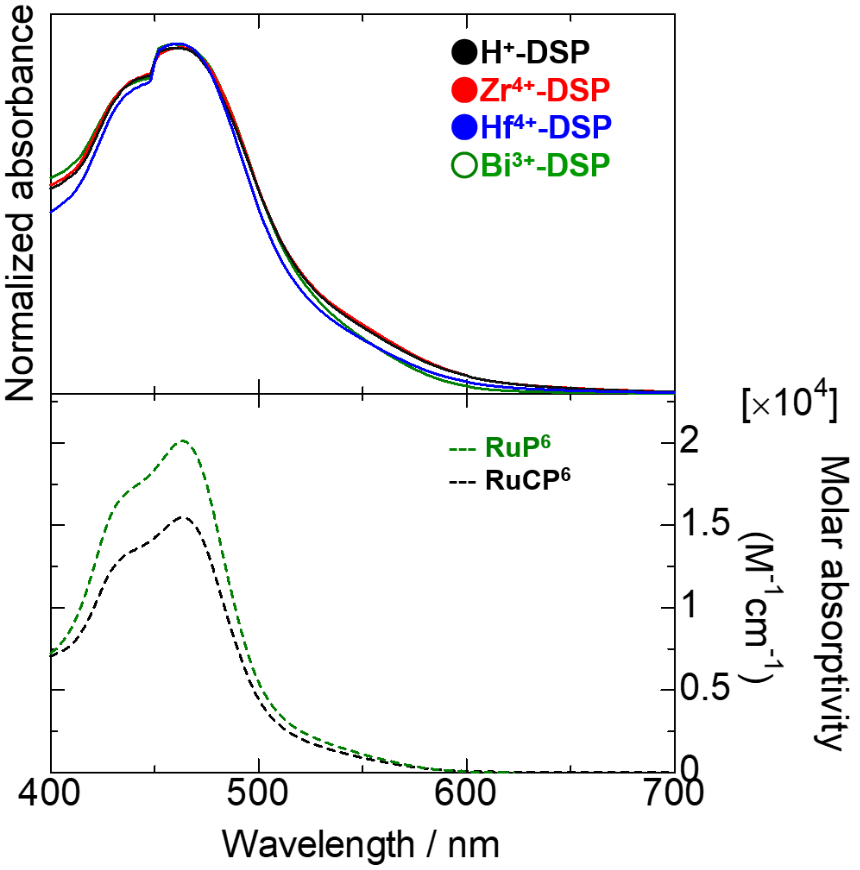

**Figure 5-3-3-4**. (Upper side) UV-vis diffuse reflectance spectra of **$H^+$-DSP** (black solid line), **$Zr^{4+}$-DSP** (red solid line), **$Hf^{4+}$-DSP** (blue solid line), and **$Bi^{3+}$-DSP** (green solid line) in solid. All samples were normalized at peak maximum of $^1$MLCT absorption band. (Lower side) UV-vis absorption spectra of 100 μM **$RuCP^6$** complex (black dashed line) and **$RuP^6$** complex (green dashed line) in aqueous solution (pH = 2). All samples were measured in 298 K.

## 5-4 Conclusion

To promote the dye regeneration by the redox-reversible electron donor, the outer metal ion dependence of the photocatalytic $H_2$ evolution activity of DSP nanoparticles were investigated, X'-**RuCP$^{6-}$**Zr-**RuP$^{6}$**@Pt-$TiO_2$ (**X'-DSPs**). It was found that not only the previously reported $Zr^{4+}$ but also the other metal cations ($Fe^{2+}$, $Y^{3+}$, $Hf^{4+}$, and $Bi^{3+}$) were successfully immobilized onto the outer surface of the **RuCP$^{6-}$**Zr-**RuP$^{6}$**@Pt-$TiO_2$nanoparticle (**$H^+$-DSP**), whereas the labile cation $Sr^{2+}$ was easily desorbed from the nanoparticle surface in the aqueous solution. These results suggest that metal cations with small hydration enthalpies are not suitable for the surface functionalization of the **$H^+$-DSP** nanoparticle photocatalyst. The AQY values of metal-cation-immobilized **X'-DSPs** at 460 nm in the presence of 0.5 M KI aqueous solution were in the range 0.47–0.61%, which are higher than that of **$H^+$-DSP** (AQY = 0.302%). This suggests that the surface metal cations act as the attracting site to promote the electron donation from iodide mediator. On the other hand, **$Bi^{3+}$-DSP** and **$Fe^{2+}$-DSP**, which comprise redox-active outer metal ions, showed slightly lower photocatalytic activity than the photocatalysts with redox-inactive outer metal cations (**X'-DSPs**, X' = $Zr^{4+}$, $Hf^{4+}$, and $Y^{3+}$), possibly because of the reverse electron transfer from the photoexcited Ru dye to the outer metal cations. It was also observed that **$Zr^{4+}$-DSP**, **$Hf^{4+}$-DSP**, and **$Bi^{3+}$-DSP** can drive the photocatalytic $H_2$ evolution reaction with 0.2–0.3% AQY under green light illumination at 530 nm, which is located in the absorption band edge of Ru PSs.

## 5-5 REFERENCES

1. S. Acharya, D.K. Padhi, K. M. Parida. *Catal. Today* **2020**, *353*, 220–231.
2. M. Graetzel. *Acc. Chem. Res.* **1981**, *14*, 376–384.
3. Y. Ma, X. Wang, X. Y. Jia, X. Chen, H. Han, C. Li. *Chem. Rev.* **2014**, *114*, 9987–10043.
4. A. Kudo, Y. Miseki. *Chem. Soc. Rev.* **2009**, *38*, 253–278.
5. X. Fang, S. Kalathil, E. Reisner. *Chem. Soc. Rev.* **2020**, *49* (14), 4926–4952.
6. A. Fujishima, K. Honda. *Nature* **1972**, *238*, 37–38.
7. G. Ma, S. Chen, Y. Kuang, S. Akiyama, T. Hisatomi, M. Nakabayashi, N. Shibata, M. Katayama, T. Minegishi, K. Domen, K. *J. Phys. Chem. Lett.* **2016**, *7*, 3892–3896.
8. A. Nakada, S. Nishioka, J. J. M. Vequizo, K. Muraoka, T. Kanazawa, A. Yamakata, S. Nozawa, H. Kumagai, S. Adachi, O. Ishitani, K. Maeda. *J. Mater. Chem. A* **2017**, *5*, 11710–11719.
9. Fang, M. J.; Tsao, C. W.; Hsu, Y. J. Semiconductor Nanoheterostructures for Photoconversion Applications. *J. Phys. D: Appl. Phys.* **2020**, *53*, 143001–143033.
10. H. Kumagai, R. Aoyagi, K. Kato, A. Yamakata, M. Kakihata, H. Kato. *ACS Appl. Energy Mater.* **2021**, 2056–2060.
11. Q. Wang, T. Hisatomi, Q. X. Jia, H. Tokudome, M. Zhong, C. Z. Wang, Z. H. Pan, T. Takata, M. Nakabayashi, N. Shibata, Y. B. Li, I. D. Sharp, A. Kudo, T. Yamada, K. Domen. *Nat. Mater.* **2016**, *15,* 611–615.
12. Y. Zhao, T. Liu, R. Chen, B. Zeng, X. Tao, J. Li, X. Jin, R. Li, C. Li. *ChemCatChem* **2020**, *12*, 1585–1590.
13. H. P. Duong, T. Mashiyama, M. Kobayashi, A. Iwase, A. Kudo, Y. Asakura, S. Yin, M. Kakihana, H. Kato. *Appl. Catal. B* **2019**, *252*, 222–229.
14. C. Zhou, S. Wang, Z. Zhao, Z. Shi, S. Yan, Z. Zou. *Adv. Funct. Mater.* **2018**, *28*, 1801214.
15. X. Li, J. Yu, J. Low, Y. Fang, J. Xiao, X. Chen. *J. Mater. Chem. A,* **2015**, *3*, 2485-2534.
16. J. K. Stolarczyk, S. Bhattacharyya, L. Polavarapu, J. Feldmann. *ACS Catal.*, **2018**, *8*, 3602-3635.
17. A. Nakada, T. Uchiyama, N. Kawakami, G. Sahara, S. Nishioka, R. Kamata, H. Kumagai, O. Ishitani, Y. Uchimoto, K. Maeda. *ChemPhotoChem* **2019**, *3*, 37–45.
18. M. V. Sheridan, Y. Wang, D. Wang, L. T. Troian-Gautier, C. J. Dares, B. D. Sherman, T. J. Meyer. *Angew. Chem. Int. Ed. Engl.* **2018**, *57*, 3449–3453.
19. J. Warnan, J. Willkomm, J. N. Ng, R. Godin, S. Prantl, J. R. Durrant, E. Reisner. *Chem. Sci.* **2017**, *8*, 3070–3079.
20. X. Wang, L. Chen, S. Y. Chong, M. A. Little, Y. Wu, W. H. Zhu, R. Clowes, Y. Yan, M. A. Zwijnenburg, R. S. Sprick, A. I. Cooper. *Nat. Chem.* **2018**, *10*, 1180–1189.
21. R. Gueret, L. Poulard, M. Oshinowo, J. Chauvin, M. Dahmane, G. Dupeyre, P. P. Lainé, J. Fortage, M. Collomb. *ACS Catal.* **2018**, *8*, 3792–3802.

22. S. Guo, K. Chen, R. Dong, Z. Zhang, J. Zhao, T. Lu. *ACS Catal.* **2018**, *8*, 8659–8670.

23. E. S. D. Da Silva, N. M. M. Moura, M. G. P. M. S. Neves, A. Coutinho, M. Prieto, C. G. Silva, J. L. Faria. *Appl. Catal. B* **2018**, *221*, 56–69.

24. T. Tsukamoto, K. Takada, R. Sakamoto, R. Matsuoka, R. Toyoda, H. Maeda, T. Yagi, M. Nishikawa, N, Shinjo, S. Amano, T. Iokawa, N. Ishibashi, T. Oi, K. Kanayama, R. Kinugawa, Y. Koda, T. Komura, S. Nakajima, R. Fukuyama, N. Fuse, M. Mizui, M. Miyasaki, Y. Yamashita, K. Yamada, W. Zhang, R. Han, W. Liu, T. Tsubomura, H. Nishihara. *J. Am. Chem. Soc.* **2017**, *139*, 5359–5366.

25. J. S. Lee, D. I. Won, W. J. Jung, H. J. Son, C. Pac, S. O. Kang. *Angew. Chem. Int. Ed. Engl.* **2017**, *56*, 976–980.

26. E.Aslan, M. K. Gonce, M. Z. Yigit, A. Sarilmaz, E. Stathatos, F. Ozel, M. Can, I. H. Patir. *Appl. Catal. B* **2017**, *220*, 320–327.

27. A. Tiwari, N. V. Krishna, L. Giribabu, U. Pal. *J. Phys. Chem. C* **2018**, *122*, 495–502.

28. F. Yu, S. Cui, X. Li, Y. Peng, Y. Yu, K. Yun, S. Zhang, J. Li, J. Liu, J. Hua. *Dyes Pigm*. **2017**, *139*, 7–18.

29. Y. Sun, Y. Sun, C. Dall'Agnese, X. Wang, G. Chen, O. Kitao, H. Tamiaki, K. Sakai, T. Ikeuchi, S. Sasaki. *ACS Appl. Energy Mater*. **2018**, *1*, 2813–2820..

30. R. Abe, K. Shinmei, N. Koumura, K. Hara, B. Ohtani. *J. Am. Chem. Soc.* **2013**, *135*, 16872–16884.

31. T. Oshima, S. Nishioka, Y. Kikuchi, S. Hirai, K. Yanagisawa, M. Eguchi, Y. Miseki, T. Yokoi, T. Yui, K. Kimoto, K. Sayama, O. Ishitani, T. E. Mallouk, K. Maeda. *J. Am. Chem. Soc.* **2020**, *142*, 8412–8420.

32. B. Tosco, B. P. V. Melo, D. H. Merino, J. F. Q. Rey, S. Brochsztain. *Langmuir,* **2011**, *37*, 2494–2502.

33. E. E. Beauvilliers, G. J. Meyer. *Inorg. Chem.,* **2016**, *55*, 7517–7526.

34. J. C. Wang, S. P. Hill, T. Dilbeck, O. O. Ogunsolu, T. Banerjee, K. Hanson. *Chem. Soc. Rev.*, **2018**, *47*, 104–148.

35. M. Freitag, E. Galoppini. *Energy Environ. Sci.*, **2011**, *4*, 2482–2494.

36. K. Hanson, D. A. Torelli, A. K. Vannucci, K. Brennaman, H. Luo, L. Alibabaei, W. Song, D. L. Ashford, M. R. Norris, C. R. K. Glasson, J. J. Concenpcion, T. J. Meyer. *Angew. Chem.,* **2012**, *124*, 12954–12957.

37. D. Ma, S. E. Bettis, K. Hanson, M. Minakova, L. Alibabaei, W. Fondrie, D. K. Ryan, G. A. Papoian, T. J. Meyer, M. L. Waters, J. M. Papanikolas. *J. Am. Chem. Soc*. **2013**, *135*, 5250–5253.

38. O. O. Ogunsolu, I. A. Murphy, J. C. Wang, A. Das, K. Hanson. *ACS Appl. Mater. Interfaces* **2016**, *8*, 28633–28640.

39. O. O. Ogunsolu, J. C. Wang, K. Hanson. *Inorg. Chem.* **2017**, *56*, 11168–11175.

40. O. O. Ogunsolu, A. J. Braun, A. J. Robb, S. R. Salpage, Y. Zhou, K. Hanson. *ACS Appl. Energy Mater*. **2019**, 29–36.
41. J. C. Wang, K. Violettem O. O. Ogunsolu, S. Cekli, E. Lambers, H. M. Fares, K. Hanson. *Langmuir* **2017**, *33*, 9609–9619.
42. J. C. Wang, K. Violette, O. O. Ogunsolu, K. Hanson. *Phys. Chem. Chem. Phys.* **2017**, *19*, 2679-2682.
43. J. C. Wang, O. O. Ogunsolu, M. Sykora, K. Hanson. *J. Phys. Chem. C* **2018**, *122*, 9835–9842.
44. Y. Zhou, C. Ruchlin, A. J. Robb, K. Hanson. *ACS Energy Lett.* **2019**, *4*, 1458–1463.
45. J. E. Kroeze, N. Hirata, S. Koops, Md. K. Nazeeruddin, L. Schmidt-Mende, M. Grätzel, J. R. Durrant. *J. Am. Chem. Soc.* **2006**, *128*, 16376–16383.
46. C. Pagba, G. Zordan, E. Galoppini, E. L. Piatnitski, S. Hore, K. Deshayes, P. Piotrowiak. *J. Am. Chem. Soc.* **2004**, *126*, 9888–9889.
47. H. Choi, S. O. Kang, J. Ko, G. Gao, H. S. Kang, M. Kang, Md. K. Nazeeruddin, M. Grätzel. *Angew. Chem., Int. Ed*., **2009**, *48*, 5938–5941.
48. M. Freitag, E. Galoppini. *Langmuir*, **2010**, *26*, 8262–8269.
49. H. Li, F. Li, Y. Wang, L. Bai, F. Yu, L. Sun. Visible-Light-Driven Water Oxidation on a Photoanode by Supramolecular Assembly of Photosensitizer and Catalyst. *ChemPlusChem*, **2016**, *81*, 1056–1059.
50. S. Furugori, A. Kobayashi, A. Watanabe, M. Yoshida, M. Kato. *ACS Omega*, **2017**, *2*, 3901–3912.
51. N. Yoshimura, A. Kobayashi, M. Yoshida, M. Kato, M. *Bull. Chem. Soc. Jpn.* **2019**, *92*, 1793–1800.
52. N. Yoshimura, A. Kobayashi, W. Genno, T. Okubo, M. Yoshida, M. Kato. *Sustain. Energy Fuels* **2020**, *4*, 3450–3457.
53. N. Yoshimura, A. Kobayashi, M. Yoshida, M. Kato. *Chem. Eur. J.* **2020**, *26*, 16939–16946.
54. N. Yoshimura, A. Kobayashi, T. Kondo, R. Abe, M. Yoshida, M. Kato. *ACS Appl. Energy Mater*., **2021**, *4*, 14352-14362.
55. H. Park, W. Choi, M. R. Hoffmann. *J. Mater. Chem.* **2008**, *18*, 2379-2385.
56. K. Hanson, M. K. Brennaman, A. Ito, H. Luo, W. Song, K. A. Parker, R. Ghosh, M. R. Norris, C. R. K. Glasson, J. J. Concepcion, R. Lopez, T. J. Meyer. *J. Phys. Chem. C* **2012**, *116*, 14837–14847.
57. L. Troian-Gautier, M. D. Turlington, S. A. M. Wehlin, A. B. Maurer, M. D. Brady, W. B. Swords, G. J. Meyer. *Chem. Rev.* **2019**, *119*, 4628–4683.
58. L. Troian-Gautier, W. B. Swords, G. J. Meyer. *Acc. Chem. Res.* **2019**, *52*, 170–179.
59. R. D. Shannon. *Acta. Cryst.* **1976**, *A32*, 751-767.
60. Y. Marcus. *Biophys. Chem.* **1994**, *51*, 111-127.
61. “CRC Handbook of Chemistry and Physics, 89th Edition,” ed. by D. R. Lide, CRC press, **2008**.
62. A. D. Awtrey, R. E. Connick. *J. Am. Chem. Soc.* **1951**, *73*, 1842-1843.

63. Palmer, D. A.; Ramette, R. W.; Mesmer, R. E. *J. Soln. Chem.* **1984**, *13*, 673-683.

# Chapter 6

# Interfacial Electron Flow Control by Double Nano-architectures for Efficient Ru-dye-sensitized Hydrogen Evolution from Water

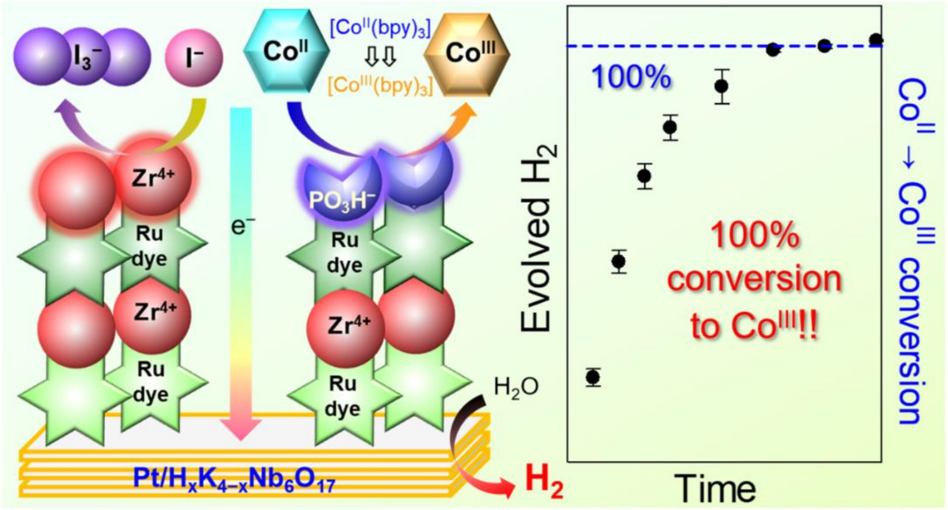

## 6-1 Introduction

The photocatalytic solar water-splitting reaction has recently attracted considerable attention as a promising approach to solve global warming and energy resource issues.[1–5] Since the discovery of the Honda–Fujishima effect,[6] many semiconductor photocatalysts have been developed.[1,7–15] Recently, K. Domen *et al.* achieved 96% apparent quantum yield (AQY) at 360 nm UV light excitation for Al-doped $SrTiO_3$, in which the two different cocatalysts were loaded on the different crystal facets.[16] This technique, which is based on the two different crystal facets, is remarkably effective for charge separation in a bulk semiconductor photocatalyst.[17,18] However, the achievement of 100% AQY for visible-light-driven water splitting remains challenging. Two-step photocatalytic water splitting (Z-scheme) systems coupled with a suitable electron mediator have been extensively studied to utilize visible light in the solar spectrum, because of the wide tunability of both their light absorption and redox potentials.[19–22] In such a Z-scheme photocatalysis process, one-way electron transfer from the oxygen- to the hydrogen-evolving photocatalyst is strongly required. In this context, various electron mediators ranging from soluble molecular mediators, such as $I_3^-/I^-$ and $[Co(bpy)_3]^{3+/2+}$ (bpy = 2,2′-bipyridine), to solid mediators like a photoreduced graphene oxide, have been developed.[23–25] However, back electron transfer at the photocatalyst–mediator interface remains a bottleneck issue.

Dye-sensitization based on photoinduced interfacial electron injection from a surface-immobilized photosensitizer (PS) to a semiconductor substrate is another promising method to utilize visible light for water splitting.[26–38] The typical n-type semiconductor $TiO_2$ has been widely used as a substrate to fabricate $H_2$ evolution dye-sensitized photocatalysts (DSPs). In addition, several noteworthy works have suggested that layered metal oxides are also promising candidates for the fabrication of highly active DSPs.[39–41] For example, Mallouk *et al.* reported a DSP composed of the Pt-cocatalyst-loaded layered niobate $Pt/K_{4-x}H_xNb_6O_{17}$ and a carboxy-functionalized Ru(II) PS.[42,43] This DSP is active for $H_2$ evolution reaction, even in an iodide aqueous solution that can act as an electron mediator. Abe *et al.* achieved overall water splitting using the coumarin- dye-sensitized internally platinated layered niobate $Pt/H_4Nb_6O_{17}$ as the $H_2$ evolution DSP and $IrO_2$-cocatalyst-loaded $WO_3$ as the $O_2$ evolution photocatalyst in the presence of an iodide mediator ($I_3^-/I^-$).[44] Further progress was recently reported by Maeda *et al.*, in that the surface deposition of $Al_2O_3$ clusters on an Ru(II)-dye-sensitized $Pt/HCa_2Nb_3O_{10}$ photocatalyst is effective for charge separation at the semiconductor– mediator interface (AQY = 2.4% at 420 nm).[45] These pioneering works indicate the importance of the surface structure of a DSP, but further investigation of the interfacial structure between the layered metal oxide semiconductor surface and solution mediator is strongly required.

In this work, a DSP system was newly fabricated by using two different nano-architectures, Ru-dye double layering and Pt cocatalyst intercalation, to overcome the back reactions at the solid–solution interface. The DSP reported herein is composed of the internally platinated layered niobate $Pt/K_xH_{4-}$

$_xNb_6O_{17}$ sensitized by double-layered Ru(II) dyes with different surface functional groups: **RuCP$^2$**-Zr-**RuP$^6$**@Pt/$K_xH_{4-x}Nb_6O_{17}$, **RuCP$^6$**-Zr-**RuP$^6$**@Pt/$K_xH_{4-x}Nb_6O_{17}$, and Zr-**RuCP$^6$**-Zr-**RuP$^6$**@Pt/$K_xH_{4-x}Nb_6O_{17}$ {Scheme 6-1; **RuCP$^2$** = $[Ru(bpy)_2$ $(mpbpy)]^{2-}$, **RuCP$^6$** = $[Ru(mpbpy)_3]^{10-}$, **RuP$^6$** = $[Ru(pbpy)_3]^{10-}$, bpy = 2,2′-bipyridine, $H_4$mpbpy = 2,2′-bipyridine-4,4′-bis(methane-phosphonic acid), and $H_4$pbpy = 2,2′-bipyridine-4,4′-bis(phosphonic acid)}. This strategy not only effectively suppresses the back reaction of the internally loaded Pt cocatalysts, as previously reported,[44] but also enabled us to control the reactivity with the electron mediators based on the surface structure and thus, the immobilized PS molecules.[46–48] This work clearly demonstrates that the double layering of Ru(II) PS remarkably improved the photocatalytic $H_2$ evolution activity (AQY ~0.4% at 470 nm) in redox-reversible electron donors (iodide or $[Co(bpy)_3]^{2+}$) and that the surface functional groups significantly affected the reactivity with these electron sources. Notably, **RuCP$^6$**-Zr-**RuP$^6$**@Pt/$K_xH_{4-x}Nb_6O_{17}$ continued to evolve $H_2$ until all the $[Co(bpy)_3]^{2+}$ donor species were consumed, even in the presence of an equimolar amount of the oxidized Co(III) mediator $[Co(bpy)_3]^{3+}$. These results indicate that dye assembly at the solid–solution interface coupled with the intercalation of cocatalyst to the layered semiconductor is a promising approach to achieve one-way electron transfer in Z-scheme water splitting photocatalysts.

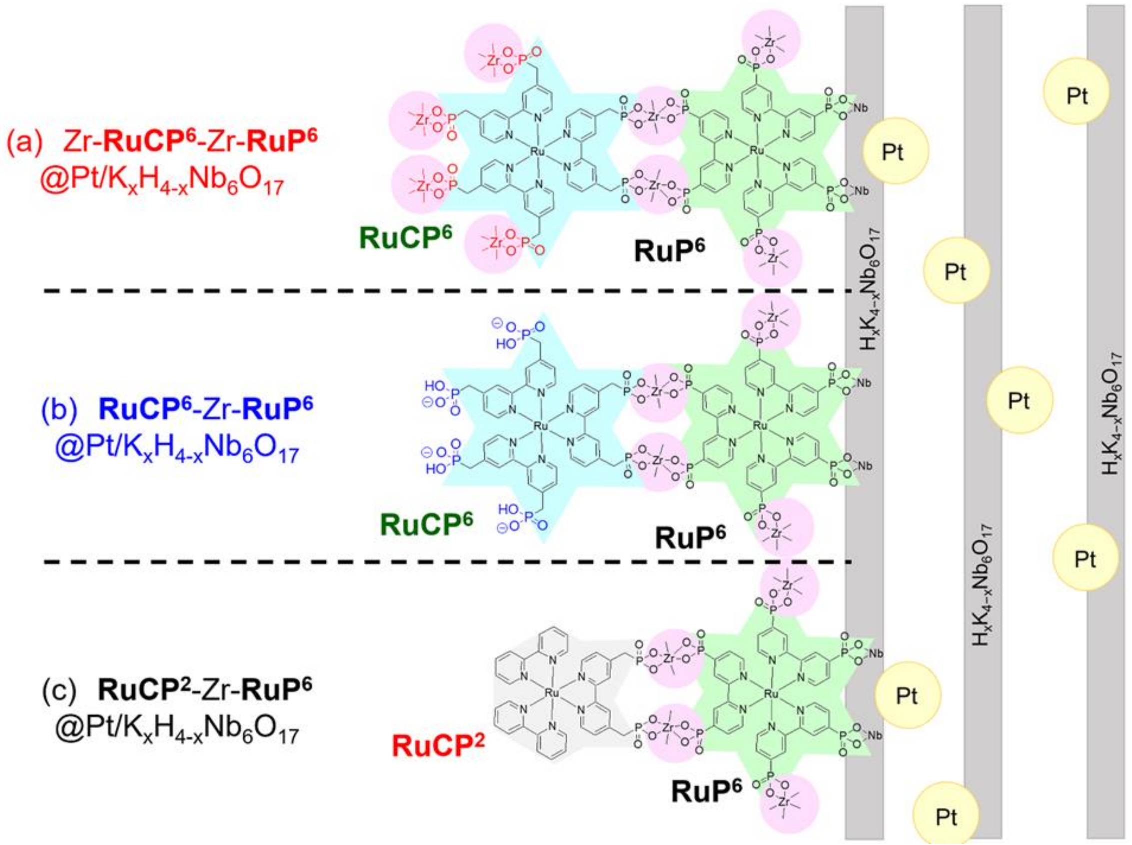

**Scheme 6-1.** Schematic surface structures of three types of PS-double-layered Pt/$K_xH_{4-x}Nb_6O_{17}$ photocatalysts: (a) Zr-**RuCP⁶**-Zr-**RuP⁶**@Pt/$K_xH_{4-x}Nb_6O_{17}$, (b) **RuCP⁶**-Zr-**RuP⁶**@Pt/$K_xH_{4-x}Nb_6O_{17}$, and (c) **RuCP²**-Zr-**RuP⁶**@Pt/$K_xH_{4-x}Nb_6O_{17}$.

## 6-2 Experimental

### 6-2-1 Preparation of the Ru(II)-dye-immobilized Pt/$K_xH_{4-x}Nb_6O_{17}$

Pt/$K_xH_{4-x}Nb_6O_{17}$ nanoparticle was synthesized by previous report.[43] Six types of Ru(II)-dye-immobilized Pt/$K_xH_{4-x}Nb_6O_{17}$ nanoparticles (**RuCP$^2$**@Pt/$K_xH_{4-x}Nb_6O_{17}$, **RuP$^6$**@Pt/$K_xH_{4-x}Nb_6O_{17}$, Zr-**RuP$^6$**@Pt/$K_xH_{4-x}Nb_6O_{17}$, **RuCP$^2$**-Zr-**RuP$^6$**@Pt/$K_xH_{4-x}Nb_6O_{17}$, **RuCP$^6$**-Zr-**RuP$^6$**@Pt/$K_xH_{4-x}Nb_6O_{17}$, and Zr-**RuCP$^6$**-Zr-**RuP$^6$**@Pt/$K_xH_{4-x}Nb_6O_{17}$) were synthesized according to previously reported procedure[48] for Ru(II)-dye-immobilized Pt-$TiO_2$ nanoparticles with several modifications as follows:

*I. Immobilization of the first Ru(II)-dye layer*. Exactly, 30 mg of Pt/$K_xH_{4-x}Nb_6O_{17}$ was dispersed in 2.5 mM Ru(II)-dye solution (**RuCP$^2$** or **RuP$^6$**, 6 mL). Next, 50 μL of 34% aqueous HCl solution was added to acidify the dispersion solution and stirred overnight at 293 K in the dark. The resultant Ru(II)-dye-immobilized Pt/$K_xH_{4-x}Nb_6O_{17}$ was isolated by ultracentrifugation (50,000 rpm, 15 min) and then washed twice with 0.4% aqueous HCl. The Ru(II)-dye-single-layered Pt/$K_xH_{4-x}Nb_6O_{17}$ (**RuCP$^2$**@Pt/$K_xH_{4-x}Nb_6O_{17}$ or **RuP$^6$**@Pt/$K_xH_{4-x}Nb_6O_{17}$) was finally obtained by drying under air at 293 K.

*II. Immobilization of $Zr^{4+}$ cations on the phosphonates of the Ru(II) dyes.* The well-dried **RuP$^6$**@Pt/$K_xH_{4-x}Nb_6O_{17}$ was dispersed in 6 mL of an MeOH solution of 50 mM $ZrCl_2O\cdot 8H_2O$ and stirred overnight at 293 K in the dark. The dispersed particles were collected by ultracentrifugation (50,000 rpm, 15 min), washed twice with MeOH, and then dried under air for several days to afford the orange Zr-**RuP$^6$**@Pt/$K_xH_{4-x}Nb_6O_{17}$.

*III. Immobilization of the second Ru(II)-dye layer*. The second immobilization of the Ru(II) dye was performed using an almost identical procedure to that used for the first dye layer immobilization, but using Zr-**RuP$^6$**@Pt/$K_xH_{4-x}Nb_6O_{17}$ instead of Pt/$K_xH_{4-x}Nb_6O_{17}$. Briefly, Zr-**RuP$^6$**@Pt/$K_xH_{4-x}Nb_6O_{17}$ was dispersed in 2.5 mM Ru(II)-dye solution (**RuCP$^2$** or **RuCP$^6$**, 6 mL) and then acidified with 50 μL of 34% aqueous HCl solution. After stirring overnight at 293 K in the dark, the dispersed particles were isolated by ultracentrifugation (50,000 rpm, 15 min) and then washed twice with 0.4% aqueous HCl. The Ru(II)-dye double-layered particles (**RuCP$^2$**-Zr-**RuP$^6$**@Pt/$K_xH_{4-x}Nb_6O_{17}$ or **RuCP$^6$**-Zr-**RuP$^6$**@Pt/$K_xH_{4-x}Nb_6O_{17}$) were obtained by drying under air for several days at 293 K. Subsequently, **RuCP$^6$**-Zr-**RuP$^6$**@Pt/$K_xH_{4-x}Nb_6O_{17}$ was treated with $ZrCl_2O\cdot 8H_2O$ MeOH solution (method II above) to form the $Zr^{4+}$-cation-modified Ru(II)-dye double-layered Zr-**RuCP$^6$**-Zr-**RuP$^6$**@Pt/$K_xH_{4-x}Nb_6O_{17}$ particles.

The immobilized amounts of Ru(II) dyes were estimated from the UV-vis absorption spectrum of each supernatant solution, isolated by ultracentrifugation of the Ru(II)-dye immobilization reaction (see "6-2-3 **Calculation of the surface coverage of Ru(II) complexes per unit area of $K_xH_{4-x}Nb_6O_{17}$**" section).

### 6-2-2 Photocatalytic water reduction reaction

This reaction was carried out in the dark. A KI (0.5 M, pH = 2 adjusted by adding aqueous HCl) or $[Co(bpy)_3]SO_4$ (16.4 mM or 1.64 mM, pH = 2 adjusted by adding aqueous HCl) solution containing Ru(II)-dye-immobilized particles (100 μM) was placed into an in-house Schlenk flask-equipped quartz cell (volume: 265 mL) with a small magnetic stirring bar. The other conditions were the same as described in chap. 2-2-4.

### 6-2-3 Calculation of the surface coverage of Ru(II) complexes per unit area of $K_xH_{4-X}Nb_6O_{17}$

Assuming that the $Pt/K_xH_{4-X}Nb_6O_{17}$ particles have parallelepiped shape, the surface area on the $Pt/K_xH_{4-X}Nb_6O_{17}$ particle ($S_m$) was simply calculated by using Equation (4). In these calculations, the effect of the loaded Pt co-catalyst was omitted.

$$S_m = 4 \times a \times b + 2 \times b^2 \text{ (cm}^2\text{ per one particle)} \quad (Eq. 4)$$

$a$ = Averaged particle thickness of $Pt/K_xH_{4-X}Nb_6O_{17}$ particle (13 nm)
$b$ = Averaged particle width and length of $Pt/K_xH_{4-X}Nb_6O_{17}$ particle (20~200 nm)

Since the calculated surface area ($S_m$) based on Equation (4) corresponds to only one $Pt/K_xH_{4-X}Nb_6O_{17}$ particle, it is necessary to determine the number of $Pt/K_xH_{4-X}Nb_6O_{17}$ particles ($P_t$) contained in 30 mg to estimate the total surface area of $Pt/K_xH_{4-X}Nb_6O_{17}$ ($S_t$) used in the immobilization reaction of the Ru(II) complexes. The total volume of 30 mg of $Pt/K_xH_{4-X}Nb_6O_{17}$ nanoparticles ($V_t$) can be calculated using Equation (5) based on the density of $Pt/K_xH_{4-X}Nb_6O_{17}$ ($K_4Nb_6O_{17}$ = 4.6 g/cm$^3$).

$$V_t = \frac{30 \times 10^{-3}\ \text{(g)}}{4.6\ \text{(g/cm}^3\text{)}} \text{ (cm}^3\text{)} \quad (Eq. 5)$$

The number of $Pt/K_xH_{4-X}Nb_6O_{17}$ particles ($P_t$) in 30 mg is also estimated using Equations (6) and (7) based on the volume of one $Pt/K_xH_{4-X}Nb_6O_{17}$ particle ($V_m$) and the total volume ($V_t$ ).

$$V_m = a \times b^2 \text{ (cm}^3\text{ per one particle)} \quad (Eq. 6)$$

$$P_t = \frac{V_t}{V_m} \quad (Eq. 7)$$

Then, the total surface area of 30 mg of $Pt/K_xH_{4-X}Nb_6O_{17}$ ($S_t$) can be estimated by Equation (8).

$$S_t = S_m \times P_t \text{ (cm}^2\text{)} \quad (Eq. 8)$$

The amount of immobilized Ru(II) complexes per unit area of $Pt/K_xH_{4-X}Nb_6O_{17}$ (Surface coverage: $N$) is estimated by Equation (9) based on the amount of immobilized Ru(II) complex ($M_i$) and the total surface area of 30 mg of $Pt/K_xH_{4-X}Nb_6O_{17}$ ($S_t$). The estimated $N$ and $M_i$ values are summarized in Table 6-3-1-1.

$$N = \frac{M_i}{S_t} \text{ (mol/cm}^2\text{)} \quad (Eq.\ 9)$$

## 6-3 Results and discussions.

### 6-3-1 Single-layered Ru(II)-dye-immobilized Pt/$K_xH_{4-x}Nb_6O_{17}$

Figure 6-3-1-1 summarizes the estimated amount of Ru(II)-dye molecules immobilized onto the surface of 1 mg particulate Pt/$K_xH_{4-x}Nb_6O_{17}$ sample. This was estimated from the decreased amount of dye molecules in the supernatant solutions, determined by comparing the UV-vis spectra before and after the immobilization process (Figure 6-3-1-2 and, Table 6-3-1-1). For the PS single layers (**RuCP$^2$** and **RuP$^6$**), the amount of **RuCP$^2$** dye immobilized on Pt/$K_xH_{4-x}Nb_6O_{17}$ was approximately double that of the **RuP$^6$** dye, probably owing to the difference in the occupied area of each dye molecule. **RuP$^6$** possesses more (six) phosphonate moieties than **RuCP$^2$** (two), and thus, compared to **RuCP$^2$**, it sterically and electrostatically occupies a larger area of the Pt/$K_xH_{4-x}Nb_6O_{17}$ surface. This results in a smaller amount of **RuP$^6$** being immobilized. A similar trend was previously reported for Pt-$TiO_2$ (48). The validity of the estimated values (e.g., 54 nmol/g for **RuP$^6$**) was assessed by considering the surface area of the Pt/$K_xH_{4-x}Nb_6O_{17}$ particles. The thickness of a Pt/$K_xH_{4-x}Nb_6O_{17}$ platelet particle was estimated to be 11±1 nm, based on the full width at half maximum of the (040) reflection of the PXRD pattern (Figure 6-3-1-3, while the average length and/or width, determined from the TEM images, was in the range 20–200 nm (Figure 6-3-1-4). Assuming the shape of a Pt/$K_xH_{4-x}Nb_6O_{17}$ particle as rectangular parallelepiped, the immobilization amount per unit area of Pt/$K_xH_{4-x}Nb_6O_{17}$ is 0.018–0.121 nmol/cm$^2$ (chapter 6-2-3, “Calculation of the surface coverage of Ru(II) complexes per unit area of $K_xH_{4-X}Nb_6O_{17}$”). This value approaches the calculated value (~0.083 nmol/cm$^2$) based on the occupied area of one **RuP$^6$** molecule (~2 nm$^2$ per one molecule), strongly suggesting that the surfaces of a Pt/$K_xH_{4-x}Nb_6O_{17}$ particle are almost fully covered by **RuP$^6$**. This hypothesis was supported by the fact that no significant adsorption occurred in the subsequent (second) **RuP$^6$** immobilization reaction without Zr(IV) cation linkers. Indeed, the UV-vis absorption spectra of the supernatant solution was near-identical to that recorded before the reaction (Figure 6-3-1-5). In addition, no characteristic **RuP$^6$** absorption band was observed for the supernatant solution obtained after subsequent reaction with the $Zr^{4+}$ cation to prepare the Zr-**RuP$^6$**@Pt/$K_xH_{4-x}Nb_6O_{17}$ precursor (Figures 6-3-1-2c and Figure 6-3-1-2f) for double layer formation.

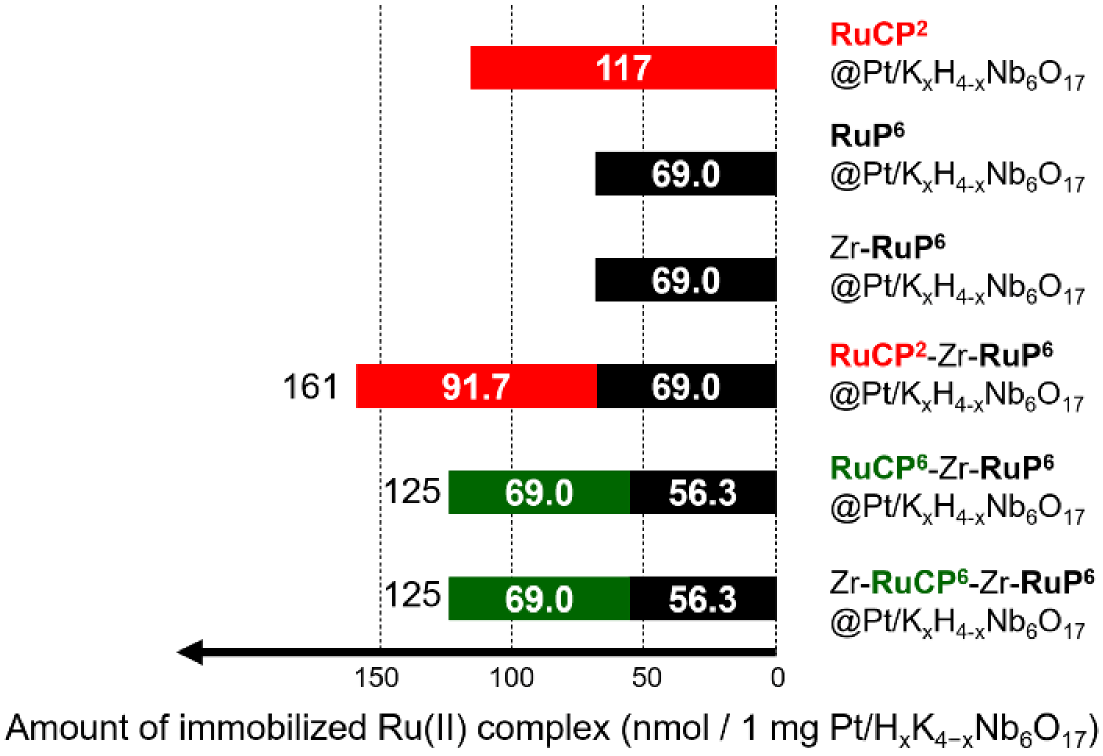

**Figure 6-3-1-1**. Amounts of immobilized Ru(II) complexes on Pt/$K_xH_{4-x}Nb_6O_{17}$. Two different batches of **RuP$^6$**@Pt/$K_xH_{4-x}Nb_6O_{17}$ were used for Zr-**RuP$^6$**@Pt/$K_xH_{4-x}Nb_6O_{17}$, **RuCP$^2$**-Zr-**RuP$^6$**@Pt/$K_xH_{4-x}Nb_6O_{17}$ and **RuCP$^6$**-Zr-**RuP$^6$**@Pt/$K_xH_{4-x}Nb_6O_{17}$, Zr-**RuCP$^6$**-Zr-**RuP$^6$**@Pt/$K_xH_{4-x}Nb_6O_{17}$, with immobilized **RuP$^6$** dye concentrations of 69.0 nmol/mg and 56.3 nmol/mg, respectively.

**Table 6-3-1-1.** Absorbance of each supernatant solution and the calculated $C_B$ and $M_i$ values.

| Photocatalyst | Immobilized Ru(II) PS | $A$ ($M^{-1}cm^{-1}$) | $C_B$ (mM) | $M_i$ (μmol) |
|---|---|---|---|---|
| **RuCP**$^{2}$ @Pt/$K_xH_{4-x}Nb_6O_{17}$ | **RuCP**$^{2}$ | 0.189 | 0.646 | 3.59 |
| **RuP**$^{6}$ @Pt/$K_xH_{4-x}Nb_6O_{17}$ | **RuP**$^{6}$ | 0.381 | 0.971 | 1.63 |
| Zr-**RuP**$^{6}$ @Pt/$K_xH_{4-x}Nb_6O_{17}$ | **RuP**$^{6}$ | 0.381 | 0.971 | 1.63 |
| **RuCP**$^{2}$-Zr-**RuP**$^{6}$ @Pt/$K_xH_{4-x}Nb_6O_{17}$ | 1st (inner) layer **RuP**$^{6}$ | 0.381 | 0.971 | 1.63 |
|  | 2nd (outer) layer **RuCP**$^{2}$ | 0.234 | 0.801 | 2.66 |
| **RuCP**$^{6}$-Zr-**RuP**$^{6}$ @Pt/$K_xH_{4-x}Nb_6O_{17}$ | 1st (inner) layer **RuP**$^{6}$ | 0.381 | 0.971 | 1.63 |
|  | 2nd (outer) layer **RuCP**$^{6}$ | 0.267 | 0.915 | 1.96 |
| Zr-**RuCP**$^{6}$-Zr-**RuP**$^{6}$ @Pt/$K_xH_{4-x}Nb_6O_{17}$ | 1st (inner) layer **RuP**$^{6}$ | 0.381 | 0.971 | 1.63 |
|  | 2nd (outer) layer **RuCP**$^{6}$ | 0.267 | 0.915 | 1.96 |

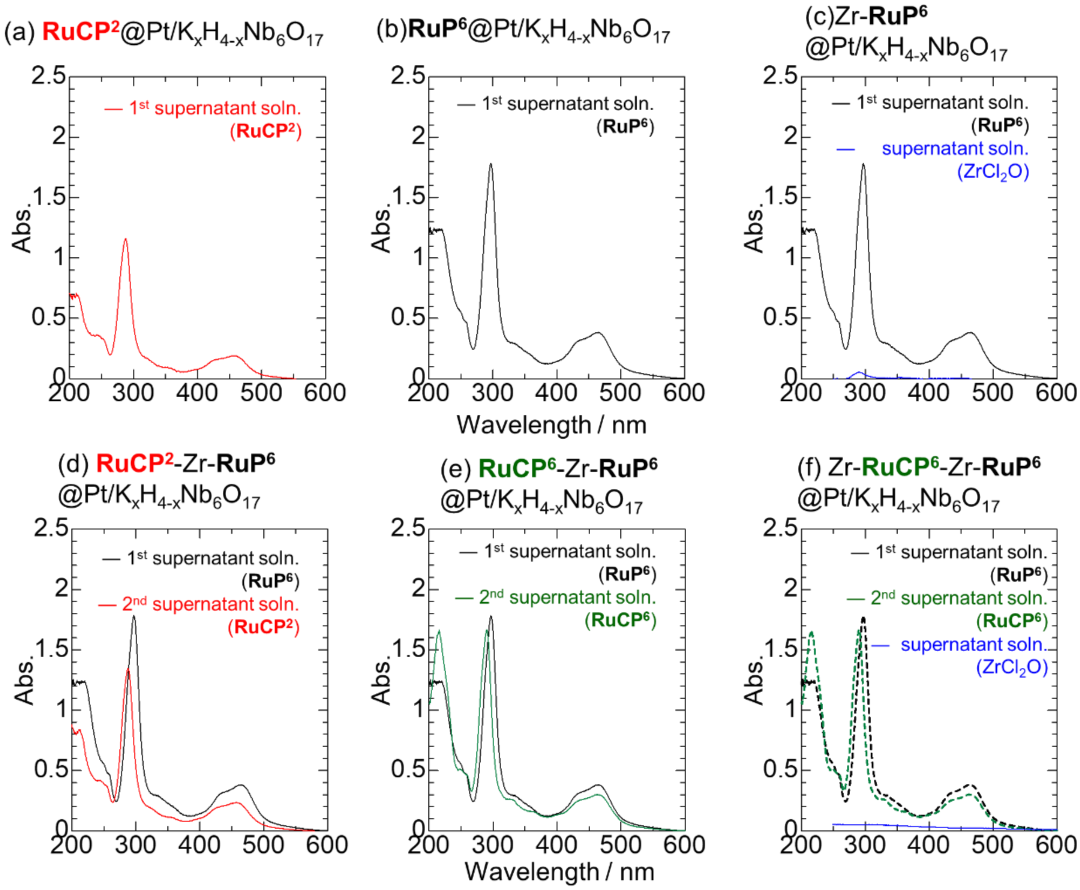

**Figure 6-3-1-2.** UV-Vis absorption spectra of the supernatant solutions at 298 K. (a) **RuCP²**@Pt/$K_xH_{4-x}Nb_6O_{17}$, (b) **RuP⁶**@Pt/$K_xH_{4-x}Nb_6O_{17}$, (c) Zr-**RuP⁶**@Pt/$K_xH_{4-x}Nb_6O_{17}$, (d) **RuCP²**-Zr-**RuP⁶**@Pt/$K_xH_{4-x}Nb_6O_{17}$, (e) **RuCP⁶**-Zr-**RuP⁶**@Pt/$K_xH_{4-x}Nb_6O_{17}$, (f) Zr-**RuCP⁶**-Zr-**RuP⁶**@Pt/$K_xH_{4-x}Nb_6O_{17}$, Note that each solution (1 mL) was diluted to 50 mL by the addition of deionized water before the spectral measurement

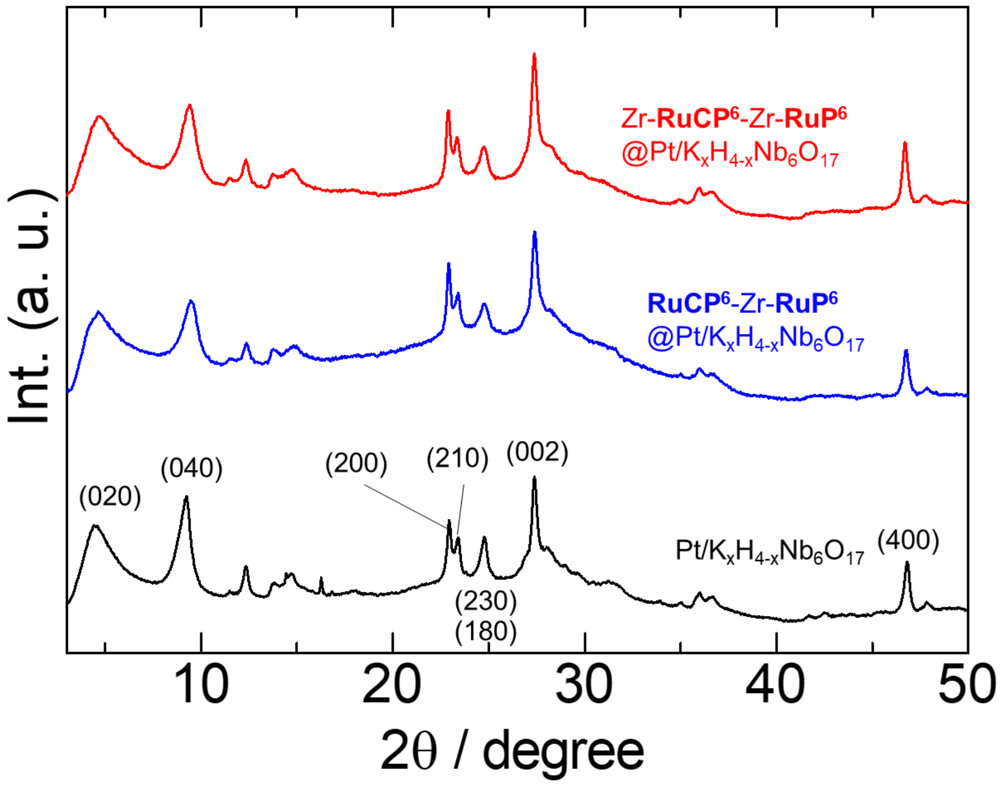

**Figure 6-3-1-3**. PXRD pattern of $Pt/K_xH_{4-x}Nb_6O_{17}$ nanoparticle in the solid, 298 K. Peak assignment was referred from previous report.[43] The particle thickness was estimated based on the full-width at half maximum of the (040) peak.

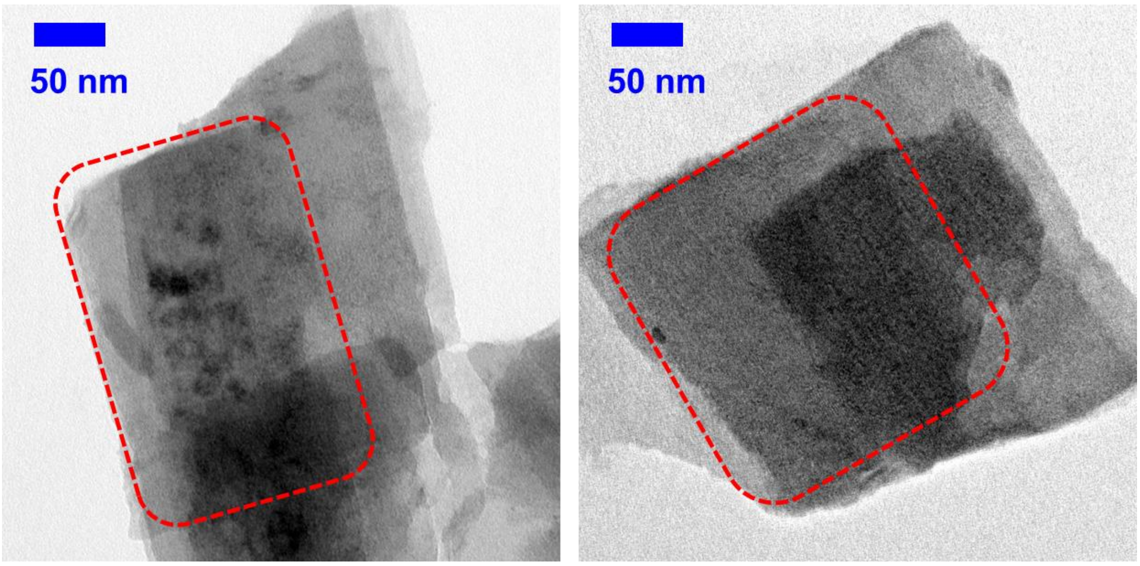

**Figure 6-3-1-4.** Transmission electron microscopy (TEM) images of $Pt/K_xH_{4-x}Nb_6O_{17}$ nanoparticles. The blue bar indicates 50 nm length. Red dashed squares show typical one particle.

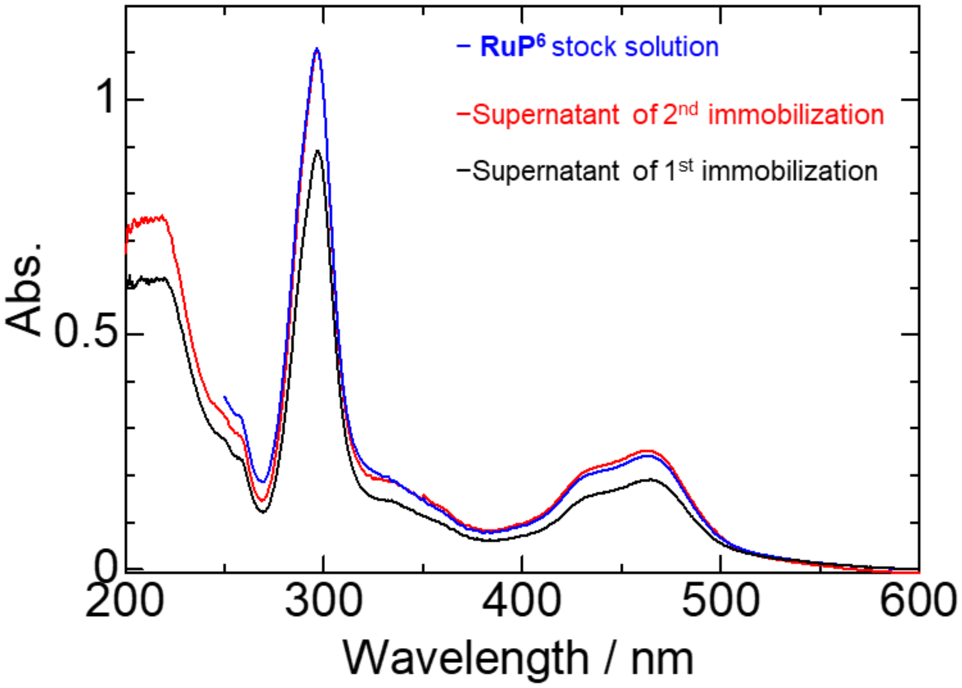

**Figure 6-3-1-5**. UV-Vis absorption spectra of the supernatant solutions obtained from the preparation of **RuP**$^6$@Pt/$K_xH_{4-x}Nb_6O_{17}$ (black line) at 298 K. Blue line shows the spectrum of the stock **RuP**$^6$ solution. Red line is the supernatant solution obtained from the 2nd immobilization reaction (by immersing **RuP**$^6$@Pt/$K_xH_{4-x}Nb_6O_{17}$ again in the 1.25 mM **RuP**$^6$ solution). Note that each supernatant solution (1 mL) was diluted to 100 mL by the addition of deionized water before the spectral measurement.

### 6-3-2 Double-layered Ru(II)-dye-immobilized Pt/$K_xH_{4-x}Nb_6O_{17}$

As shown in Figure 6-3-1-1, all three samples with PS-double-layered Ru dyes prepared using the Zr(IV) cation linkers were confirmed to contain at least double the amount of immobilized dye molecules than that of the single-layered sample (**RuP$^6$**@Pt/$K_xH_{4-x}Nb_6O_{17}$). Moreover, the negligible desorption of **RuP$^6$** during the subsequent reaction with the $Zr^{4+}$ cation indicates that the immobilized amount of **RuP$^6$** dye in Zr-**RuP**$^6$@Pt/$K_xH_{4-x}Nb_6O_{17}$ is near-identical to that of **RuP**$^6$@Pt/$K_xH_{4-x}Nb_6O_{17}$. Notably, neither desorption of **RuP$^6$** nor dye exchange from **RuP$^6$** to the dye used for the second layer (e.g., **RuCP$^2$** or **RuCP$^6$**) occurred, as confirmed by the emission and $^1$H NMR spectra and emission decay curve of the supernatant solution isolated from the second dye immobilization reaction (Figure 6-3-2-1). All three results were near-identical to that of the **RuCP$^6$** dye aqueous solution, and no signals assignable to **RuP$^6$** were detected. As was observed for the single-layered sample, the amount (~92 nmol) of immobilized **RuCP$^2$** in **RuCP$^2$**-Zr-**RuP$^6$**@Pt/$K_xH_{4-x}Nb_6O_{17}$ was 35% larger than that (~69 nmol) of **RuCP$^6$** in **RuCP$^6$**-Zr-**RuP$^6$**@Pt/$K_xH_{4-x}Nb_6O_{17}$. This was attributed to the smaller size and neutral nature of **RuCP$^2$**. In the **RuCP$^2$**-Zr-**RuP$^6$**@Pt/$K_xH_{4-x}Nb_6O_{17}$ sample, the amount of outer **RuCP$^2$** was approximately 1.3 times larger than that of the inner **RuP$^6$**. This seems quite reasonable on considering the number of phosphonic acid groups in each dye: The **RuP$^6$** dye in the inner layer is immobilized on the surface of $K_xH_{4-x}Nb_6O_{17}$ by three phosphonate linkers, leaving three free phosphonates for binding to the $Zr^{4+}$ cations. If the **RuCP$^2$**, with two phosphonates, occupies two of the three surface-bound $Zr^{4+}$ sites to form the second outer layer, the maximum amount of immobilized **RuCP$^2$** will be approximately one and a half times the amount of **RuP$^6$** in the inner layer, reasonably explaining the above result.

This is also a reasonable explanation for the comparable immobilization amounts of the two Ru(II) dyes in **RuCP$^6$**-Zr-**RuP$^6$**@Pt/$K_xH_{4-x}Nb_6O_{17}$. This is because **RuCP$^6$**, with six phosphonates, can occupy all the three surface-bound $Zr^{4+}$ sites, resulting in the 1:1 molar ratio of these two Ru(II) dyes. As discussed above, no $^1$MLCT absorption band derived from the Ru(II) dyes was detected in the UV-vis absorption spectrum of the supernatant solution obtained after the $Zr^{4+}$ immobilization reaction to form Zr-**RuCP$^6$**-Zr-**RuP$^6$**@Pt/$K_xH_{4-x}Nb_6O_{17}$ (Figure 6-3-1-2f). Thus, it was concluded that the immobilization amount of each Ru(II) dye in Zr-**RuCP$^6$-Zr-RuP$^6$**@Pt/$K_xH_{4-x}Nb_6O_{17}$ is near-identical to that in **RuCP$^6$**-Zr-**RuP$^6$**@Pt/$K_xH_{4-x}Nb_6O_{17}$.

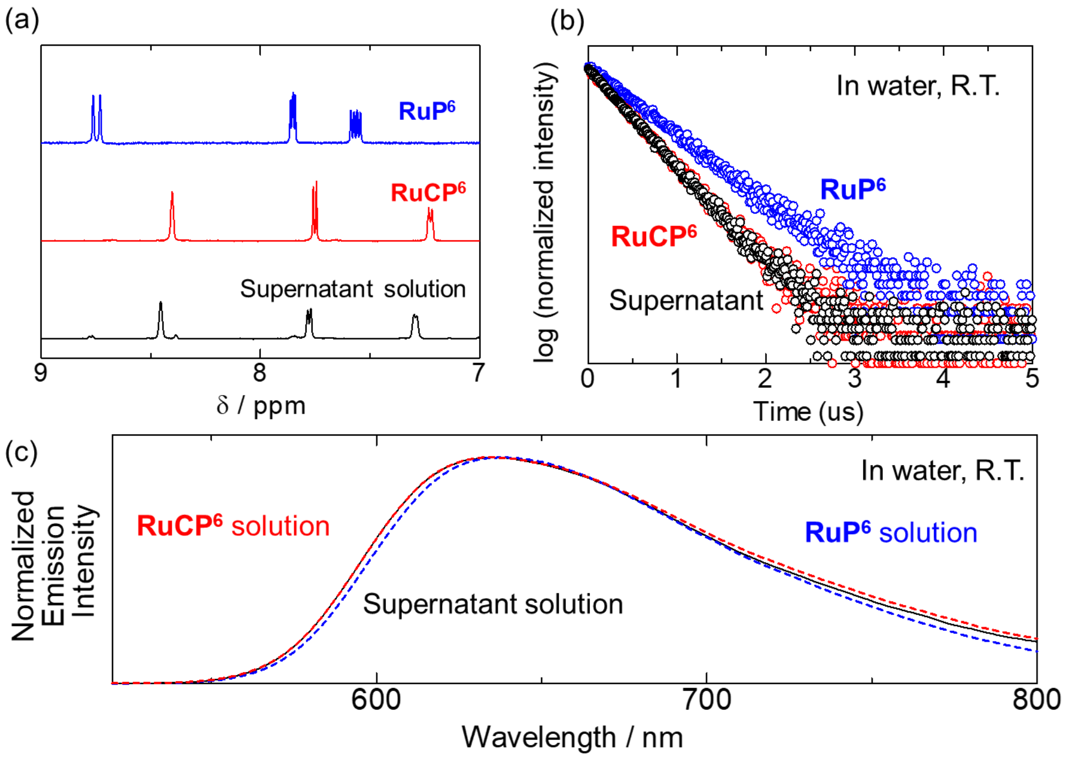

**Figure 6-3-2-1.** (a) $^{1}$H NMR, (b) emission decay, and (c) emission spectra of the supernatant solution (black lines and circles) obtained from the immobilization reaction of **RuCP$^6$** for the synthesis of **RuCP$^6$**-Zr-**RuP$^6$**@Pt-TiO$_2$ by ultracentrifugation. Blue and red plots are the spectra and decay of **RuP$^6$** and **RuCP$^6$** in the aqueous solution, respectively.

The chemical composition of each sample was estimated by XRF spectra (Figure 6-3-2-2). It was confirmed that the unmodified Pt/$K_xH_{4-X}Nb_6O_{17}$ sample only exhibited peaks derived from Pt and Nb. On the other hand, all the Ru(II)-dye-immobilized Pt/$K_xH_{4-X}Nb_6O_{17}$ particles exhibited Ru Kα radiation at 19.2 keV, confirming the presence of immobilized Ru(II) dyes on the surface. Although quantitative analysis on the amount of each Ru(II) dye was difficult, owing to the overlap between the Ru Kα and Nb Kβ radiations, the Ru Kα intensity of the PS-double-layered Pt/$K_xH_{4-X}Nb_6O_{17}$ was significantly stronger than that of the PS-single-layered counterpart. All the $Zr^{4+}$-treated samples, namely Zr-**RuP⁶**@Pt/$K_xH_{4-X}Nb_6O_{17}$, **RuCP²**-Zr-**RuP⁶**@Pt/$K_xH_{4-X}Nb_6O_{17}$, and **RuCP⁶**-Zr-**RuP⁶**@Pt/$K_xH_{4-X}Nb_6O_{17}$ presented a Zr Kα peak at 15.7 keV, confirming that the $Zr^{4+}$ cations were bound by the phosphonates of the Ru(II) dyes. As expected, the Zr Kα peak intensity of Zr-**RuCP⁶**-Zr-**RuP⁶**@Pt/$K_xH_{4-X}Nb_6O_{17}$ was larger than that of **RuCP⁶**-Zr-**RuP⁶**@Pt/$K_xH_{4-X}Nb_6O_{17}$, indicating an increased amount of $Zr^{4+}$ cations as a result of their immobilization to the phosphonate groups directed on the outside of the **RuCP⁶** layer. PXRD measurements revealed that the effect of Ru(II)-dye-immobilization on the crystal structure of the Pt/$K_xH_{4-X}Nb_6O_{17}$ particles was negligible (Figure 6-3-1-3).

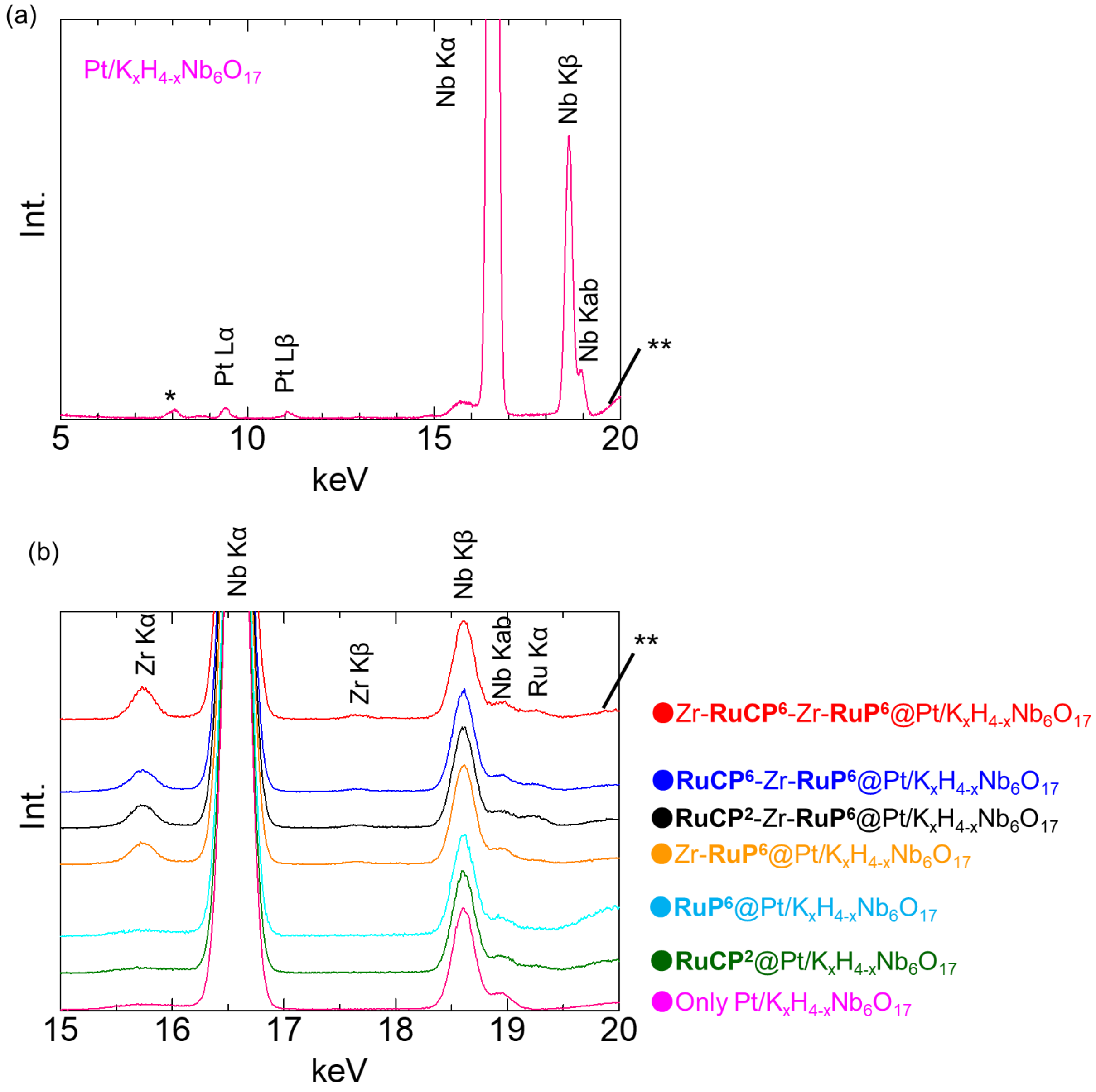

**Figure 6-3-2-2.** (a) XRF spectrum of Pt/$K_xH_{4-x}Nb_6O_{17}$ in the solid state. The excitation voltage was 50 kV. The marked peaks (* and **) are due to the background of Cu sample holder and Rh X-ray source, respectively. (b) Comparison of the XRF spectra of Pt/$K_xH_{4-x}Nb_6O_{17}$(pink), **RuCP$^2$**@Pt/$K_xH_{4-x}Nb_6O_{17}$(green), **RuP$^6$**@Pt/$K_xH_{4-x}Nb_6O_{17}$ (light-blue), Zr-**RuP$^6$**@Pt/$K_xH_{4-x}Nb_6O_{17}$ (orange), **RuCP$^2$**-Zr-**RuP$^6$**@Pt/$K_xH_{4-x}Nb_6O_{17}$ (black), **RuCP$^6$**-Zr-**RuP$^6$**@Pt/$K_xH_{4-x}Nb_6O_{17}$ (blue), Zr-**RuCP$^6$**-Zr-**RuP$^6$**@Pt/$K_xH_{4-x}Nb_6O_{17}$ (red) in Zr, Nb, and Ru Kα regions. All spectra of Ru(II)-PS-multilayered Pt/$K_xH_{4-x}Nb_6O_{17}$ nanoparticles were normalized based on the Nb Kα peak intensity.

### 6-3-3 Photocatalytic $H_2$ evolution reaction using KI as anionic electron donor

Figure 6-3-3-1 shows the time courses of photocatalytic hydrogen evolution on the Ru(II)-dye-immobilized Pt/$K_xH_{4-X}Nb_6O_{17}$ samples from aqueous KI solution (0.5 M, pH = 2), in which the iodide anions act as electron donors. In addition, the TON, TOF, and AQY values estimated for each reaction are summarized in Table 6-3-3-1. Note that the total amount of Ru(II) dye in each solution was constant (100 μM) and no hydrogen evolution was observed in the absence of Ru(II) PS, light, or electron donor (Table 6-3-3-2). As seen in Figure 6-3-3-1, all six samples, including the PS-single-layered samples, evolved $H_2$ with relatively steady rates. This is in stark contrast to previously reported results with Pt-$TiO_2$ nanoparticles, in which the PS-single-layered Pt-$TiO_2$ nanoparticles did not show any reliable $H_2$ production under the same conditions.[47] This implies the crucial role of the Pt cocatalyst loaded in the interlayer of $K_xH_{4-X}Nb_6O_{17}$, as discussed in various literature.[41–45] As seen in Table 6-3-3-1, all six samples exhibited TONs >1, confirming the occurrence of $H_2$ production via photocatalytic processes triggered by light absorption of a Ru(II) PS and subsequent electron donation from the iodide as the electron source. Clearly, the PS-double-layered particles evolved two- to fourfold the amount of $H_2$ than did the PS-single-layered particles with the same surface functional (Zr-$PO_3$-, $PO_3$-, or H-) group. This was attributed to the improved charge separation between the semiconductor and Ru(II) dyes, as previously mentioned in chapter 4. Briefly, the back electron transfer is suppressed by the introduction of PS-dye-double-layered particles. This suppression can be explained by the energy diagram shown in Scheme 6-3-3, which reveals that hole transfer from the inner to the outer PS is possible. These results suggest that PS-multilayering is a promising method to improve the charge-separation efficiency not only for the classical $TiO_2$ but also for the layered niobate $K_xH_{4-x}Nb_6O_{17}$. More interestingly, the activity of the PS-double-layered particles strongly depended on the surface functional group. After 6 h irradiation, the TONs of **RuCP$^{6}$**-Zr-**RuP$^{6}$**@Pt/$K_xH_{4-x}Nb_6O_{17}$ and Zr-**RuCP$^{6}$**-Zr-**RuP$^{6}$**@Pt/$K_xH_{4-x}Nb_6O_{17}$ were respectively approximately five and seven times higher than that of **RuCP$^{2}$**-Zr-**RuP$^{6}$**@Pt/$K_xH_{4-x}Nb_6O_{17}$.

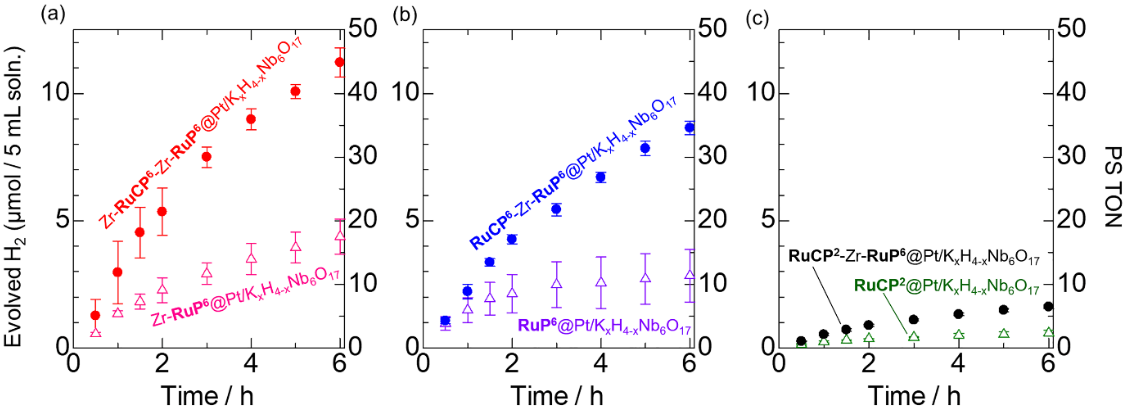

**Figure 6-3-3-1**. Photocatalytic $H_2$ evolution reactions driven by (a) Zr-**RuCP$^6$**-Zr-**RuP$^6$**@Pt/$K_xH_{4-x}Nb_6O_{17}$ (red closed circles) and Zr-**RuP$^6$**@Pt/$K_xH_{4-x}Nb_6O_{17}$ (pink open triangles), (b) **RuCP$^6$**-Zr-**RuP$^6$**@Pt/$K_xH_{4-x}Nb_6O_{17}$ (blue closed triangles) and **RuP$^6$**@Pt/$K_xH_{4-x}Nb_6O_{17}$ (purple open triangles), and (c) **RuCP$^2$**-Zr-**RuP$^6$**@Pt/$K_xH_{4-x}Nb_6O_{17}$ (black closed circles) and **RuCP$^2$**@Pt/$K_xH_{4-x}Nb_6O_{17}$ (green open circles) in the presence of 100 μM Ru(II) dye and 0.5 M KI as the electron donor (initial pH = 2.0, λ = 470 ± 10 nm).

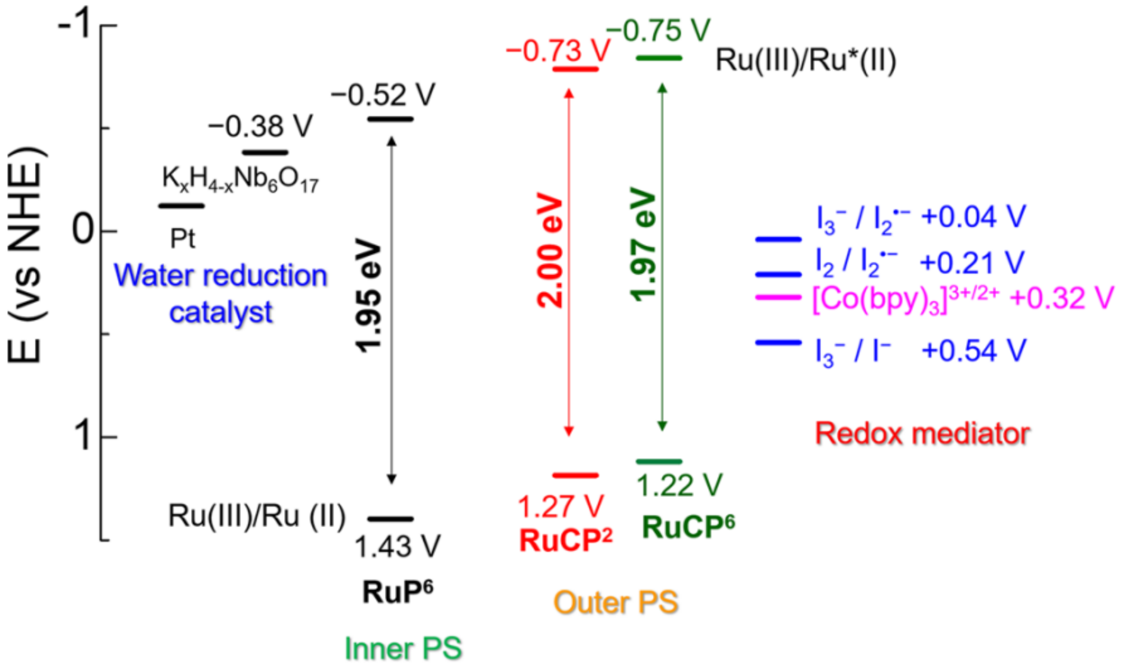

**Scheme 6-3-3.** Energy diagram of Ru(II)-PS double-layered Pt/$K_xH_{4-x}Nb_6O_{17}$ photocatalytic system in aqueous solution

**Table 6-3-3-1. Results of photocatalytic $H_2$ evolution experiments in 0.5 M KI aqueous solution.**

| Photocatalyst[a] | $H_2$ (μmol) (0–6 h) | Produced $I_3^-$ (μmol) | PS TON[a] (0–3 h) | PS TON[b] (0–6 h) | PS initial TOF[c] | AQY[a] (%) (0–6 h) | *i*AQY[a] (%) (0–1 h) |
|---|---|---|---|---|---|---|---|
| **RuCP$^2$**@ Pt/$K_xH_{4-x}Nb_6O_{17}$ | 0.589 | 0.33 | 1.58 | 2.36 | 1.0 | 0.020 | 0.049 |
| **RuP$^6$**@ Pt/$K_xH_{4-x}Nb_6O_{17}$ | 2.84 | 3.0 | 9.96 | 11.4 | 6.0 | 0.10 | 0.30 |
| Zr-**RuP$^6$**@ Pt/$K_xH_{4-x}Nb_6O_{17}$ | 4.38 | 3.7 | 11.6 | 17.5 | 5.4 | 0.15 | 0.27 |
| **RuCP$^2$**-Zr-**RuP$^6$**@ Pt/$K_xH_{4-x}Nb_6O_{17}$ | 1.62 | 1.5 | 4.40 | 6.48 | 2.1 | 0.054 | 0.11 |
| **RuCP$^6$**-Zr-**RuP$^6$**@ Pt/$K_xH_{4-x}Nb_6O_{17}$ | 8.64 | 7.7 | 21.8 | 34.6 | 8.9 | 0.29 | 0.45 |
| Zr-**RuCP$^6$**-Zr-**RuP$^6$**@Pt/$K_xH_{4-x}Nb_6O_{17}$ | 11.2 | 9.2 | 30.0 | 44.9 | 7.9 | 0.38 | 0.60 |

[a] Reaction conditions: [Ru-PS] = 100 μM in total, [KI] = 0.5 M, HCl aqueous solution (pH = 2), $\lambda_{ex}$ = 470 ± 10 nm, 70 mW. The reaction solution was purged by Ar bubbling for 1 h before light irradiation. The numerical values are averages of more than three experiments. Definitions: TON, turn-over number; TOF, turn-over frequency; AQY, apparent quantum yield.

**Table 6-3-3-2**. Control experiments of photocatalytic hydrogen evolution of Zr-**RuCP$^6$**-Zr-**RuP$^6$**@Pt/$K_xH_{4-x}Nb_6O_{17}$ and **RuCP$^6$**-Zr-**RuP$^6$**@Pt/$K_xH_{4-x}Nb_6O_{17}$.

| Entry [a] | Photocatalyst | Electron Donor (ED) | Light irradiation | Evolved $H_2$ [b] |
|---|---|---|---|---|
| 1 | Zr-**RuCP$^6$**-Zr-**RuP$^6$**@Pt/$K_xH_{4-x}Nb_6O_{17}$ | 0.5 M KI | Yes | Yes |
| 2 | Zr-**RuCP$^6$**-Zr-**RuP$^6$**@Pt/$K_xH_{4-x}Nb_6O_{17}$ | 16.4 mM $[Co(bpy)_3]SO_4$ | Yes | Yes |
| 3 | **RuCP$^6$**-Zr-**RuP$^6$**@Pt/$K_xH_{4-x}Nb_6O_{17}$ | 16.4 mM $[Co(bpy)_3]SO_4$ | Yes | Yes |
| 4 | Zr-**RuCP$^6$**-Zr-**RuP$^6$**@Pt/$K_xH_{4-x}Nb_6O_{17}$ | 0.5 M KI | No | - |
| 5 | Zr-**RuCP$^6$**-Zr-**RuP$^6$**@Pt/$K_xH_{4-x}Nb_6O_{17}$ | 16.4 mM $[Co(bpy)_3]SO_4$ | No | - |
| 6 | **RuCP$^6$**-Zr-**RuP$^6$**@Pt/$K_xH_{4-x}Nb_6O_{17}$ | 16.4 mM $[Co(bpy)_3]SO_4$ | No | - |
| 7 | Zr-**RuCP$^6$**-Zr-**RuP$^6$**@Pt/$K_xH_{4-x}Nb_6O_{17}$ | Nothing | Yes | - |
| 8 | Only Pt/$K_xH_{4-x}Nb_6O_{17}$ nanoparticle | 16.4 mM $[Co(bpy)_3]SO_4$ | Yes | - |
| 9[c] | - | 0.5 M KI | Yes | - |
| 10[c] | - | 16.4 mM $[Co(bpy)_3]SO_4$ | Yes | - |

[a] Reaction conditions: [Ru] = 100 μM in HCl aqueous solution (pH = 2, 5 mL) under blue LED light irradiation (λ = 470 ± 10 nm) for 6 h. [b] Gas in the head space was analyzed qualitatively by Gas Chromatography (GC). "Yes" indicates that the evolved amount of $H_2$ was larger than the GC detection limit. [c] No photocatalyst was used.

The Ru(III)/Ru(II) redox potentials of **RuCP$^2$** and **RuCP$^6$** immobilized in the second outer layer were reported to be near-identical by Meyer *et al.* [49] (Scheme 6-3-3). In addition, coordination to $Zr^{4+}$ had little effect on these values. Thus, the difference in activity was not thermodynamically (redox potential) induced but originated from the geometrical difference in the outer surface structure, as reported in the previously reported Pt-$TiO_2$ nanoparticle system. [48] Hence, iodide anions are attracted by the electrostatic and/or hydrogen bonding interactions with the surface functional groups of Zr-**RuCP$^6$**-Zr-**RuP$^6$**@Pt/$K_xH_{4-x}Nb_6O_{17}$ and **RuCP$^6$**-Zr-**RuP$^6$**@Pt/$K_xH_{4-x}Nb_6O_{17}$, enabling more efficient electron injection to the photo-oxidized Ru(III) dye. In the present Zr-**RuCP$^6$**-Zr-**RuP$^6$**@Pt/$K_xH_{4-x}Nb_6O_{17}$, the iodide anions are attracted by the $Zr^{4+}$-phosphonate groups at the outer surface, whereas they are electrostatically repelled by the surface phosphonate groups of **RuCP$^6$**-Zr-**RuP$^6$**@Pt/$K_xH_{4-x}Nb_6O_{17}$. The zeta potential of Zr-**RuCP$^6$**-Zr-**RuP$^6$**@Pt/$K_xH_{4-x}Nb_6O_{17}$ in the absence of iodide aqueous solution was positive, assumptions are supported by the zeta potential measurements while a large negative shift was observed following the addition of 0.5 M iodide (Table 6-3-3-3, +31 mV → +4.9 mV), suggesting the attraction of iodide anions to the particle surface. These results are consistent with those from the recent work on a dye-sensitized solar cell by Hanson *et al.*, whereby the surface $Zr^{4+}$-phosphonate moiety attached on a well-known Ru(II) dye (N3) suppressed back electron transfer from the redox mediator to improve the open circuit voltage ($V_{OC}$). [50] On the other hand, the change in the zeta potential of **RuCP$^6$**-Zr-**RuP$^6$**@Pt/$K_xH_{4-x}Nb_6O_{17}$ was negligible when iodide was added (+2.9 mV → +1.0 mV). Given that the pKa of phosphonic acid is ~1.5, [51] the particle surface of **RuCP$^6$**-Zr-**RuP$^6$**@Pt/$K_xH_{4-x}Nb_6O_{17}$ can be neutralized by the proton release from the surface phosphonic acid groups, resulting in weaker attraction with the iodide anion than is observed with Zr-**RuP$^6$**@Pt/$K_xH_{4-x}Nb_6O_{17}$. Although **RuCP$^2$**-Zr-**RuP$^6$**@Pt/$K_xH_{4-x}Nb_6O_{17}$ showed a large negative shift following the addition of the iodide (+32 mV → ±0.0 mV), implying attraction of the iodide anions, the photocatalytic activity was the lowest among the three PS-double-layered photocatalysts. Since the surface of **RuCP$^2$**-Zr-**RuP$^6$**@Pt/$K_xH_{4-x}Nb_6O_{17}$ has no interactive functional groups for iodide anions, [52,53] the electrostatic attraction between the surface-immobilized [$Ru^{2+}(bpy)_3$]-type molecules and iodide anions is less effective for electron donation from the iodide ions compared to that between the surface $Zr^{4+}$-phosphonates and iodides.

**Table 6-3-3-3**. Zeta(ζ)-potentials of Ru(II)-PS-immobilized nanoparticles in the HCl aqueous solution, 0.5 M KI aqueous solution, $H_2SO_4$ aqueous solution, and 16.4 mM $[Co(bpy)_3]SO_4$ aqueous solution. All measurements were done in pH = 2.0 aq.

| Photocatalyst | ζ potential (mV) | | | |
|---|---|---|---|---|
| | HCl aq. | 0.5 M KI aq. | pH = 2 $H_2SO_4$ aq. | 16.4 mM $[Co(bpy)_3]SO_4$ |
| $Pt/K_xH_{4-x}Nb_6O_{17}$ | +36 | +15 | −1.9 | +9.4 |
| **RuCP**$^2$ @$Pt/K_xH_{4-x}Nb_6O_{17}$ | +46 | +5.6 | +15 | +23 |
| **RuP**$^6$ @$Pt/K_xH_{4-x}Nb_6O_{17}$ | −16 | −11 | −11 | +1.8 |
| Zr-**RuP**$^6$ @$Pt/K_xH_{4-x}Nb_6O_{17}$ | +39 | +4.9 | −8.9 | −1.7 |
| **RuCP**$^2$-Zr-**RuP**$^6$ @$Pt/K_xH_{4-x}Nb_6O_{17}$ | +32 | ±0.0 | +11 | +17 |
| **RuCP**$^6$-Zr-**RuP**$^6$ @$Pt/K_xH_{4-x}Nb_6O_{17}$ | +2.9 | +1.0 | −0.83 | +6.7 |
| Zr-**RuCP**$^6$-Zr-**RuP**$^6$ @$Pt/K_xH_{4-x}Nb_6O_{17}$ | +31 | +4.9 | +2.1 | +5.6 |

The amount of oxidized iodide species was determined from the UV-vis absorption spectrum of the supernatant solution after each reaction (Figure 6-3-3-2). All solutions showed two characteristic triiodide anion ($I_3^-$) absorption bands at 290 and 350 nm.[52,55,56] Table 6-3-3-4 summarizes the amounts of $I_3^-$ produced for each reaction. Although their precise quantitative determination was difficult, owing to light scattering by the residual particles ever after ultracentrifugation, the produced $I_3^-$ amount approached the stoichiometric values of the evolved $H_2$. Thus, it was concluded that the iodide acted as the electron source for proton reduction to evolve $H_2$, as expressed in Eq. 10:

$$2H^+ + 3I^- \rightarrow H_2 + I_3^- \qquad (10)$$

Notably, $I_3^-$ production generally causes a gradual decrease in the $H_2$ production rate, as observed in each reaction during 6 h light irradiation (Figure 6-3-3-2), attributed to its light shielding effect. The absorbance values of the 20-fold diluted supernatant solutions of Zr-**RuCP$^6$**-Zr-**RuP$^6$**@Pt/$K_xH_{4-x}Nb_6O_{17}$ and **RuCP$^6$**-Zr-**RuP$^6$**@Pt/$K_xH_{4-x}Nb_6O_{17}$ at 470 nm were 0.07 and 0.06, respectively, indicating that the actual absorbance of the reaction solution is >1 (Table 6-3-3-4).

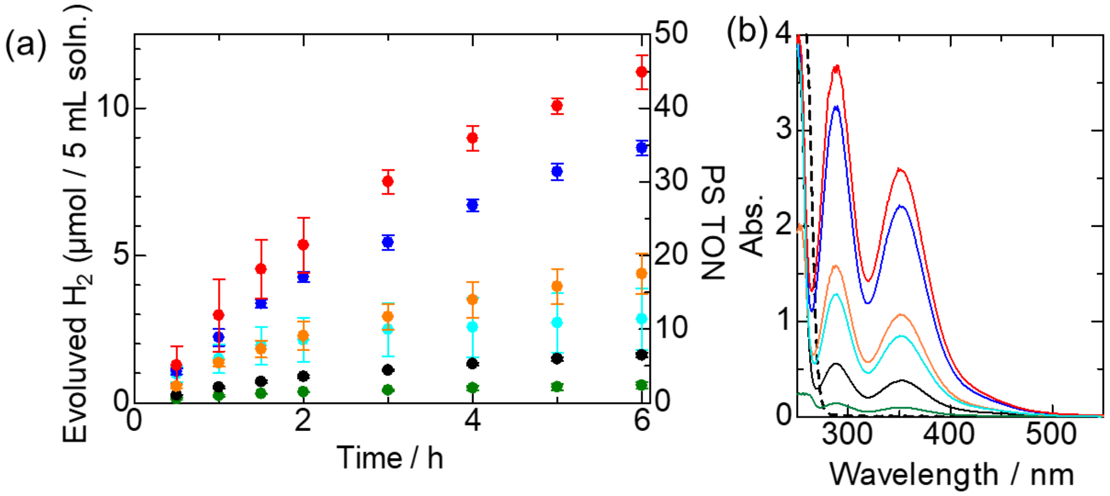

**Figure 6-3-3-2.** (a) Photocatalytic $H_2$ evolution reactions driven by Zr-**RuCP$^6$**-Zr-**RuP$^6$**@Pt/$K_xH_{4-x}Nb_6O_{17}$ (red closed circle), **RuCP$^6$**-Zr-**RuP$^6$**@Pt/$K_xH_{4-x}Nb_6O_{17}$ (blue closed triangle), Zr-**RuP$^6$**@Pt/$K_xH_{4-x}Nb_6O_{17}$ (orange closed circle), **RuP$^6$**@Pt/$K_xH_{4-x}Nb_6O_{17}$ (light-blue closed circle), **RuCP$^2$**-Zr-**RuP$^6$**@Pt/$K_xH_{4-x}Nb_6O_{17}$ (black closed circle), and **RuCP$^2$**@Pt/$K_xH_{4-x}Nb_6O_{17}$ (green closed circle) in the presence of 100 μM Ru(II) dye and 0.5 M KI as the electron donor (initial pH = 2.0, λ = 470 ± 10 nm). (b) UV-Vis absorption spectra of the supernatants obtained by centrifugation of the reaction solutions after 6 h irradiation of Zr-**RuCP$^6$**-Zr-**RuP$^6$**@Pt/$K_xH_{4-x}Nb_6O_{17}$ (red solid line), **RuCP$^6$**-Zr-**RuP$^6$**@Pt/$K_xH_{4-x}Nb_6O_{17}$ (blue solid line), **RuCP$^2$**-Zr-**RuP$^6$**@Pt/$K_xH_{4-x}Nb_6O_{17}$ (black solid line), Zr-**RuP$^6$**@Pt/$K_xH_{4-x}Nb_6O_{17}$ (orange solid line), **RuP$^6$**@Pt/$K_xH_{4-x}Nb_6O_{17}$ (light-blue solid line), and **RuCP$^2$**@Pt/$K_xH_{4-x}Nb_6O_{17}$ (green solid line). Each supernatant (1 mL) was diluted to 20 mL with deionized water prior to the measurement. The black dashed line is the spectrum before irradiation.

**Table 6-3-3-4**. The relationship between evolve $H_2$ and produced $I_3^-$ amounts after 6 h irradiation $^a$ In the condition of 0.5 M KI aqueous solution.

| Photocatalysts | Evolved $H_2$ amount after 6 h irradiation (μmol) $^a$ | Produced $I_3^-$ amount after 6 h irradiation (μmol) $^a$ | Absorbance at 470 nm of $I_3^-$ after 6 h irradiation ($M^{-1}$ $cm^{-1}$) |
|---|---|---|---|
| Zr-**RuCP**$^6$-Zr-**RuP**$^6$ @Pt/$K_xH_{4-x}Nb_6O_{17}$ | 11.2 | 9.2 | 1.4 |
| **RuCP**$^6$-Zr-**RuP**$^6$ @Pt/$K_xH_{4-x}Nb_6O_{17}$ | 8.64 | 7.7 | 1.2 |
| Zr-**RuP**$^6$ @Pt/$K_xH_{4-x}Nb_6O_{17}$ | 4.38 | 3.7 | 0.56 |
| **RuP**$^6$ @Pt/$K_xH_{4-x}Nb_6O_{17}$ | 2.84 | 3.0 | 0.45 |
| **RuCP**$^2$-Zr-**RuP**$^6$ @Pt/$K_xH_{4-x}Nb_6O_{17}$ | 1.62 | 1.5 | 0.23 |
| **RuCP**$^2$ @Pt/$K_xH_{4-x}Nb_6O_{17}$ | 0.59 | 0.33 | 0.050 |

### 6-3-4 Apparent quantum yields for $H_2$ evolution in the KI system

The AQYs after 6 h irradiation of Zr-**RuCP$^6$**-Zr-**RuP$^6$**@Pt/$K_xH_{4-x}Nb_6O_{17}$ and **RuCP$^6$**-Zr-**RuP$^6$**@Pt/$K_xH_{4-x}Nb_6O_{17}$ were estimated to be 0.38% and 0.29%, respectively. These values are slightly smaller but comparable to the values of previously reported Pt-$TiO_2$ nanoparticles with the same PS-double-layered structure (AQY = 0.54% for Zr-**RuCP$^6$**-Zr-**RuP$^6$**@1wt%Pt-$TiO_2$ and 0.30% for **RuCP$^6$**-Zr-**RuP$^6$**@1wt%Pt-$TiO_2$).[48] In contrast, the AQY of **RuCP$^2$**-Zr-**RuP$^6$**@Pt/$K_xH_{4-x}Nb_6O_{17}$ (0.054%), which does not comprise any surface phosphonate groups, was double that of the corresponding Pt-$TiO_2$ nanoparticle (0.028%, **RuCP$^2$**-Zr-**RuP$^6$**@1wt%Pt-$TiO_2$). Similarly, the PS-single-layered **RuCP$^2$**@Pt/$K_xH_{4-x}Nb_6O_{17}$ photocatalytically evolved $H_2$ (TON = 2.36, AQY= 0.020%), while the Pt-$TiO_2$ nanoparticle with the same **RuCP$^2$** dye was almost inactive (TON = 0.28, AQY = 0.0024%). These differences between Pt/$K_xH_{4-x}Nb_6O_{17}$ and Pt-$TiO_2$ are ascribable to the size relationship between the Pt cocatalyst and Ru(II)-dye layer. As discussed in various literature,[41,44] the Pt cocatalysts in Pt/$K_xH_{4-x}Nb_6O_{17}$ were incorporated into the $K_xH_{4-x}Nb_6O_{17}$ interlayer and the Pt surface was barely exposed to the solid–solution interface, while the Pt cocatalyst loaded on the $TiO_2$ nanoparticle was directly exposed to the interface. On the other hand, the thickness of the Ru(II)-dye double layer comprising surface phosphonate or $Zr^{4+}$-phosphonate groups, roughly estimated at 3–4 nm based on the molecular sizes of the immobilized Ru(II) dyes, was slightly larger than the size of the Pt cocatalyst (~2.9 nm) loaded on the $TiO_2$ nanoparticle.[48] These sizes indicate that the Pt cocatalysts loaded on $TiO_2$ were submerged in the Ru(II)-dye double layer and the Pt surface was barely exposed to the particle–solution interface, especially for the thickest layer Zr-**RuCP$^6$**-Zr-**RuP$^6$**@1wt%Pt-$TiO_2$. The photocatalytic activity is therefore comparable to that of the Pt/$K_xH_{4-x}Nb_6O_{17}$ particle with the same dye double layer structure. Thus, to suppress the back reaction on the Pt cocatalyst surface, double layering of Ru(II) dyes using $Zr^{4+}$ cations is comparably effective to the intercalation of a Pt cocatalyst into the interlayer of a semiconductor substrate. This technique shows great potential for application to other semiconductor photocatalysts. Further, the significant enhancement of the photocatalytic activity of a Pt/$K_xH_{4-x}Nb_6O_{17}$ particle by changing the surface structure of the Ru(II)-dye double layer from simple bpy to phosphonate or $Zr^{4+}$-phosphonate-functionalized bpy clearly indicates the importance of surface structure for photocatalytic $H_2$ evolution activity.

### 6-3-5 Photocatalytic $H_2$ evolution reaction using $[Co(bpy)_3]SO_4$ as cationic electron donor

To further investigate the impact of the surface structure on the $H_2$ evolution efficiency, the reaction was next carried out with $[Co(bpy)_3]SO_4$ aqueous solution instead of KI. In this case, it was predicted that the cationic $[Co(bpy)_3]^{2+}$ complex acts as a cationic one-electron donor, which completely differs from the process with the iodide anion. In addition, this complex molecule is too large to approach the Pt cocatalyst immobilized in the interlayer of $K_xH_{4-x}Nb_6O_{17}$. Thus, back electron transfer to the oxidized electron donor $[Co(bpy)_3]^{3+}$ is completely suppressed. Figure 6-3-6-1 shows the time courses of photocatalytic $H_2$ evolution from 16.4 mM $[Co(bpy)_3]SO_4$ aqueous solution (pH = 2, acidified by adding aqueous HCl); the results are also summarized in Table 6-3-6-1. No hydrogen evolution was observed in the absence of Ru(II) PS, light, or electron donor (Table 6-3-3-2). The absorption spectra after reaction suggested that similar shape as $[Co(bpy)_3]^{3+}$ from literature (57) (Figure 6-3-6-2). Unfortunately, the absorption band of $[Co(bpy)_3]^{3-}$ was overlapped with $[Co(bpy)_3]^{2+}$, **RuCP⁶** and **RuP⁶** dye, and $K_xH_{4-x}Nb_6O_{17}$, so the quantification of production amount of $[Co(bpy)_3]^{3+}$ was difficult. On the other hand, proton NMR spectrum after reaction clearly indicated that $[Co(bpy)_3]^{3-}$ was produced by reaction (Figure 6-3-6-3). These results imply that $[Co(bpy)_3]^{2+}$ donor was one-electron-oxidized by photocatalytic reaction and $[Co(bpy)_3]^{3+}$ was produced in these systems. The photocatalytic activity clearly depended on the surface structure. Indeed, the activity of the PS-double-layered particles increased in the order **RuCP²**-Zr-**RuP⁶**@Pt/$K_xH_{4-x}Nb_6O_{17}$ < Zr-**RuCP⁶**-Zr-**RuP⁶**@Pt/$K_xH_{4-x}Nb_6O_{17}$ < **RuCP⁶**-Zr-**RuP⁶**@Pt/$K_xH_{4-x}Nb_6O_{17}$. Notably, both Zr-**RuCP⁶**-Zr-**RuP⁶**@Pt/$K_xH_{4-x}Nb_6O_{17}$ and **RuCP⁶**-Zr-**RuP⁶**@ Pt/$K_xH_{4-x}Nb_6O_{17}$ evolved an amount of $H_2$ comparable to that evolved from the KI system, even though the donor concentration (16.4 mM $[Co(bpy)_3]SO_4$) was approximately 30-fold lower than that of the iodide (0.5 M). This is probably because the redox reaction of $[Co(bpy)_3]^{3+/2+}$ does not accompany any interatomic bond formation reactions, as is the case with $I_3^-$/ $I^-$. Interestingly, the TON for **RuCP⁶**-Zr-**RuP⁶**@Pt/$K_xH_{4-x}Nb_6O_{17}$ was 1.4 times higher than that for Zr-**RuCP⁶**-Zr-**RuP⁶**@Pt/$K_xH_{4-x}Nb_6O_{17}$, in contrast to the KI system (see Figure 6-3-3-1).

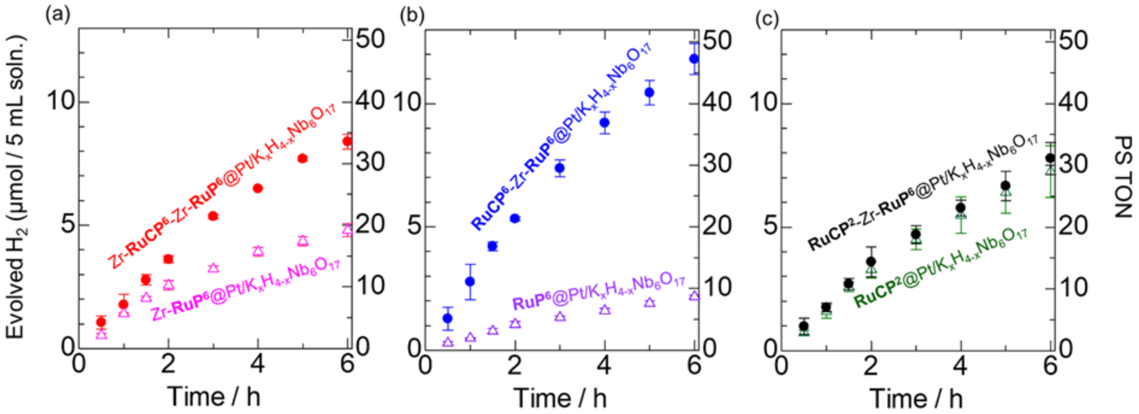

**Figure 6-3-6-1**. Photocatalytic $H_2$ evolution reactions driven by (a) Zr-**RuCP$^6$**-Zr-**RuP$^6$**@Pt/$K_xH_{4-x}Nb_6O_{17}$ (red closed circles) and Zr-**RuP$^6$**@Pt/$K_xH_{4-x}Nb_6O_{17}$ (pink open triangles), (b) **RuCP$^6$**-Zr-**RuP$^6$**@Pt/$K_xH_{4-x}Nb_6O_{17}$ (blue closed triangles) and **RuP$^6$**@Pt/$K_xH_{4-x}Nb_6O_{17}$ (purple open triangles), and (c) **RuCP$^2$**-Zr-**RuP$^6$**@Pt/$K_xH_{4-x}Nb_6O_{17}$ (black closed circles) and **RuCP$^2$**@Pt/$K_xH_{4-x}Nb_6O_{17}$ (green open circles) in the presence of 100 μM Ru(II) dye and 16.4 mM $[Co(bpy)_3]SO_4$ as the electron donor (initial pH = 2.0, λ = 470 ± 10 nm).

**Table 6-3-6-1.** Results of photocatalytic $H_2$ evolution experiments in $[Co(bpy)_3]SO_4$ aqueous solution.

| Photocatalyst | $[Co(bpy)_3]SO_4$ (mM) | $H_2$ (µmol) (0–6 h) | PS TON[a] (0–3 h) | PS TON[b] (0–6 h) | PS initial TOF[c] | AQY[a] (%) (0–6 h) | *i*AQY[a] (%) (0–1 h) |
|---|---|---|---|---|---|---|---|
| **RuCP$^2$**@$Pt/K_xH_{4-x}Nb_6O_{17}$ | 16.4 | 7.25 | 18.0 | 29.0 | 6.3 | 0.24 | 0.32 |
| **RuP$^6$**@$Pt/K_xH_{4-x}Nb_6O_{17}$ | 16.4 | 2.17 | 5.29 | 8.68 | 1.9 | 0.07 | 0.10 |
| Zr-**RuP$^6$**@$Pt/K_xH_{4-x}Nb_6O_{17}$ | 16.4 | 4.80 | 12.9 | 19.2 | 5.6 | 0.16 | 0.28 |
| **RuCP$^2$**-Zr-**RuP$^6$**@$Pt/K_xH_{4-x}Nb_6O_{17}$ | 16.4 | 7.79 | 18.8 | 31.1 | 7.0 | 0.26 | 0.35 |
| **RuCP$^6$**-Zr-**RuP$^6$**@$Pt/K_xH_{4-x}Nb_6O_{17}$ | 16.4 | 11.8 | 29.5 | 47.2 | 11 | 0.40 | 0.56 |
| **RuCP$^6$**-Zr-**RuP$^6$**@$Pt/K_xH_{4-x}Nb_6O_{17}$ | 1.64 | 4.15 | 14.8 | 16.6 | 7.9 | - | 0.40 |
| **RuCP$^6$**-Zr-**RuP$^6$**@$Pt/K_xH_{4-x}Nb_6O_{17}$ -2nd | 1.64 | 4.04 | 13.7 | 16.2 | 5.3 | - | 0.27 |
| Zr-**RuCP$^6$**-Zr-**RuP$^6$**@$Pt/K_xH_{4-x}Nb_6O_{17}$ | 16.4 | 8.39 | 21.4 | 33.6 | 7.1 | 0.28 | 0.36 |

[a] Measurement conditions: [Ru-PS] = 100 µM in total, HCl aqueous solution (pH = 2), $\lambda_{ex} = 470 \pm 10$ nm, 70 mW. The reaction solution was purged by Ar-bubbling for 1 h before light irradiation. The numerical values are averages of more than three experiments. Definitions: TON, turn-over number; TOF, turn-over frequency; AQY, apparent quantum yield.

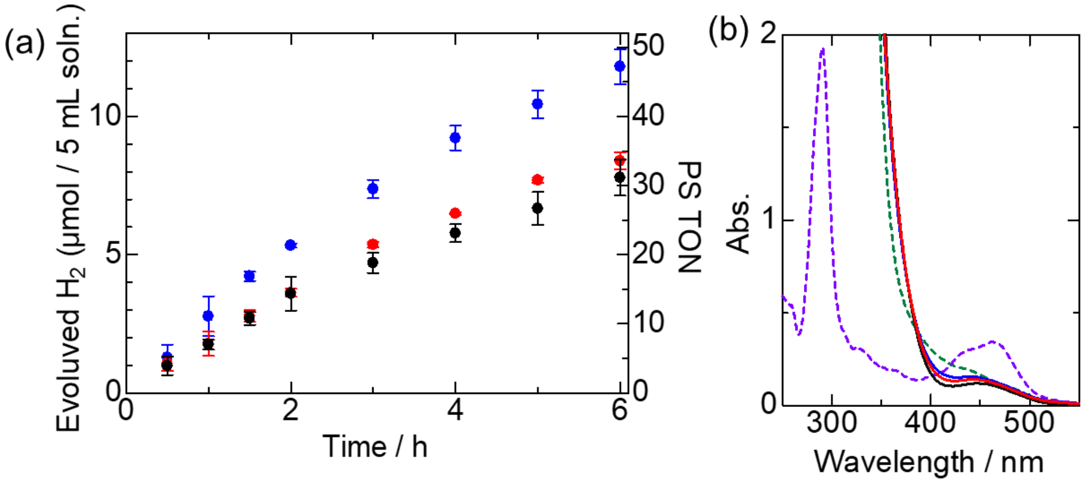

**Figure 6-3-6-2.** (a) Photocatalytic $H_2$ evolution reactions driven by Zr-**RuCP$^6$**-Zr-**RuP$^6$**@Pt/$K_xH_{4-x}Nb_6O_{17}$ (red closed circle), **RuCP$^6$**-Zr-**RuP$^6$**@Pt/$K_xH_{4-x}Nb_6O_{17}$ (blue closed triangle), and **RuCP$^2$**-Zr-**RuP$^6$**@Pt/$K_xH_{4-x}Nb_6O_{17}$ (black closed circle) in the presence of 100 μM Ru(II) dye and 16.4 mM $[Co(bpy)_3]SO_4$ as the electron donor (initial pH = 2.0, λ = 470 ± 10 nm). (b)UV-Vis absorption spectra of the supernatants obtained by centrifugation of the reaction solutions after 6 h irradiation of Zr-**RuCP$^6$**-Zr-**RuP$^6$**@Pt/$K_xH_{4-x}Nb_6O_{17}$ (red solid line), **RuCP$^6$**-Zr-**RuP$^6$**@Pt/$K_xH_{4-x}Nb_6O_{17}$ (blue solid line), and **RuCP$^2$**-Zr-**RuP$^6$**@Pt/$K_xH_{4-x}Nb_6O_{17}$ (black solid line). Each supernatant (1 mL) was diluted to 10 mL with deionized water prior to the measurement. The black dashed line is the spectrum before irradiation and the purple dashed line is the spectrum of 25 μM **RuCP$^6$** dye in aqueous solution (pH = 2).

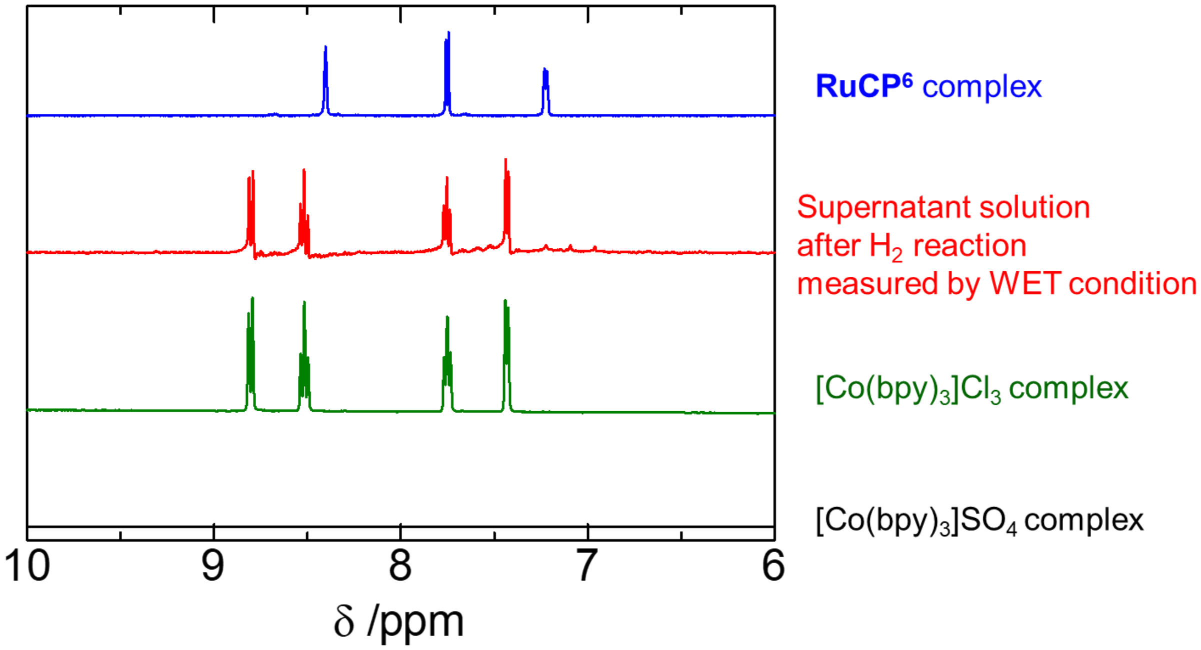

**Figure 6-3-6-3.** $^1$H NMR spectra of of the supernatant obtained by centrifugation of the reaction solution after 6 h irradiation of **RuCP$^6$**-Zr-**RuP$^6$**@Pt/$K_xH_{4-x}Nb_6O_{17}$ with 16.4 mM $[Co(bpy)_3]SO_4$aq (HClaq, pH = 2, 5 mL) in $H_2O$ (red solid line). The blue line is the spectrum of **RuCP$^6$** complex in $D_2O$, the green solid line is the spectrum of $[Co(bpy)_3]Cl_3$ complex in $D_2O$, and the black solid line is the $[Co(bpy)_3]SO_4$. complex in $D_2O$. All measurement were carried out in 293 K.

The zeta potential at pH 2 for **RuCP⁶**-Zr-**RuP⁶**@Pt/$K_xH_{4-x}Nb_6O_{17}$ was confirmed to be near-neutral both in the sulfuric acid (−0.83 mV) and aqueous HCl (+1.0 mV, Table 6-3-3-3) solutions. However, the potential positively shifted by up to +6.7 mV following the addition of $[Co(bpy)_3]^{2+}$, suggesting that cationic $[Co(bpy)_3]^{2+}$ molecules were attracted near the particle surface, probably through electrostatic attraction of the partially $H^+$-released surface phosphonates of **RuCP⁶**. In contrast, the zeta potential (+2.1 mV) of Zr-**RuCP⁶**-Zr-**RuP⁶**@Pt/$K_xH_{4-x}Nb_6O_{17}$ in the sulfuric acid solution shifted slightly to +5.6 mV. Considering that the potential of Zr-**RuCP⁶**-Zr-**RuP⁶**@Pt/$K_xH_{4-x}Nb_6O_{17}$ in aqueous HCl was highly positive (+31 mV), the $Zr^{4+}$ cations bound by the surface phosphonate of **RuCP⁶** may be surrounded by sulfate anions in $H_2SO_4$ aqueous solution, providing a near-neutral zeta potential. In this case, the electron donating $[Co(bpy)_3]^{2+}$ cations are indirectly attracted by the sulfate anions surrounding the surface $Zr^{4+}$ cations. The electron transfer kinetics is inversely proportional to the square of the distance between the electron donor and accepter. Thus, the plausible origin of the higher $H_2$ evolution activity in the $[Co(bpy)_3]^{2+}$ solution of **RuCP⁶**-Zr-**RuP⁶**@Pt/$K_xH_{4-x}Nb_6O_{17}$ over that in Zr-**RuCP⁶**-Zr-**RuP⁶**@Pt/$K_xH_{4-x}Nb_6O_{17}$ is due to the closer distance between the cationic $[Co(bpy)_3]^{2+}$ donor and **RuCP⁶** on the particle surface with direct electrostatic interaction with the anionic phosphonates. On the other hand, **RuCP²**-Zr-**RuP⁶**@Pt/$K_xH_{4-x}Nb_6O_{17}$, which exhibited the lowest $H_2$ evolution activity among the three PS-double-layered particles in aqueous KI, showed almost the same activity as Zr-**RuCP⁶**-Zr-**RuP⁶**@Pt/$K_xH_{4-x}Nb_6O_{17}$ when $[Co(bpy)_3]^{2+}$ was used instead. This possibly originates from the difference in the electron donating process: $[Co(bpy)_3]^{2+}$ donates one electron to form the stable Co(III) species, whereas electron donation from the iodide anion is accompanied by two I–I bond formations to form the stable $I_3^-$ anion. Thus, a high donor concentration is not required for $[Co(bpy)_3]^{2+}$ to donate one electron to the surface Ru(II)-PS, as mentioned above. The change in the zeta potential shift of **RuCP²**-Zr-**RuP⁶**@Pt/$K_xH_{4-x}Nb_6O_{17}$, following the addition of $[Co(bpy)_3]^{2+}$ (+11 mV → +17 mV) was similar to that of Zr-**RuCP⁶**-Zr-**RuP⁶**@Pt/$K_xH_{4-x}Nb_6O_{17}$, and is consistent with their comparable photocatalytic activities in the $[Co(bpy)_3]^{2+}$ donor solution. These results suggest that the appropriate surface modification of a photocatalyst particle to induce the desirable electrostatic attraction with redox mediators shows great potential as an effective strategy for boosting the electron donation from the mediators to the PS molecules. Although the dominant reason for the similar activity between the PS-single-layered **RuCP²**@Pt/$K_xH_{4-x}Nb_6O_{17}$ and PS-double-layered **RuCP²**-Zr-**RuP⁶**@Pt/$K_xH_{4-x}Nb_6O_{17}$ is unclear at present, it might be due to the difference in the amount of Ru(II) dyes immobilized directly on the surface of $K_xH_{4-x}Nb_6O_{17}$.

The photocatalytic hydrogen evolution reaction was also performed by using **RuCP⁶**-Zr-**RuP⁶**@Pt/$K_xH_{4-x}Nb_6O_{17}$ in a 10-fold lower concentration of $[Co(bpy)_3]SO_4$ (1.64 mM) solution to avoid light absorption by the $[Co(bpy)_3]^{3+/2+}$ mediators, which interferes with the light absorption of Ru(II) PSs (Figure 6-3-6-4). Even at this low donor concentration, the initial 1 h TOF approximated

70% in 16.4 mM donor solution, indicating the superior performance of this PS-double-layered photocatalyst. Notably, the evolved amount of $H_2$ after 4 h light irradiation reached approximately 4.1 μmol, which is nearly equal to the upper limit of evolved hydrogen from the total 8.2 μmol of the one-electron $[Co(bpy)_3]^{2+}$ donor. This finding strongly suggests that **$RuCP^6$**-Zr-**$RuP^6$**@Pt/$K_xH_{4-x}Nb_6O_{17}$ can drive the photocatalytic $H_2$ evolution reaction until all the $[Co(bpy)_3]^{2+}$ donors are oxidized to $[Co(bpy)_3]^{3+}$. To confirm this assumption, the photocatalytic reaction was next carried out by adding another 8.2 μmol $[Co(bpy)_3]SO_4$ followed by Ar-purging. Although the initial TOF in the second cycle was slightly lowered to ~70%, the amount of evolved $H_2$ still reached ~4 μmol, indicating the complete consumption of the $[Co(bpy)_3]^{2+}$ donor, even in the presence of 8.2 μmol of the one-electron oxidized $[Co(bpy)_3]^{3+}$ in the initial period. The lower activity in the second cycle compared to that in the first cycle was attributed to back electron transfer to the oxidized donor $[Co(bpy)_3]^{3+}$. Compared to the divalent species, the trivalent species is more effectively attracted near the particle surface by electrostatic interaction and thus, backward electron transfer occurs to some extent. Nevertheless, the $H_2$ evolution continued until another portion of $[Co(bpy)_3]^{2+}$ was completely oxidized. Therefore, the charge separation process triggered by the energy transfer process from the outer excited **$RuCP^{6*}$** to inner **$RuP^6$** followed by the electron injection process from the inner excited **$RuP^{6*}$** to Pt/$K_xH_{4-x}Nb_6O_{17}$ is relatively faster than the back electron transfer from the outer excited **$RuCP^{6*}$** to the oxidized $[Co(bpy)_3]^{3+}$, resulting in the complete consumption of the secondary added $[Co(bpy)_3]^{2+}$ donors.

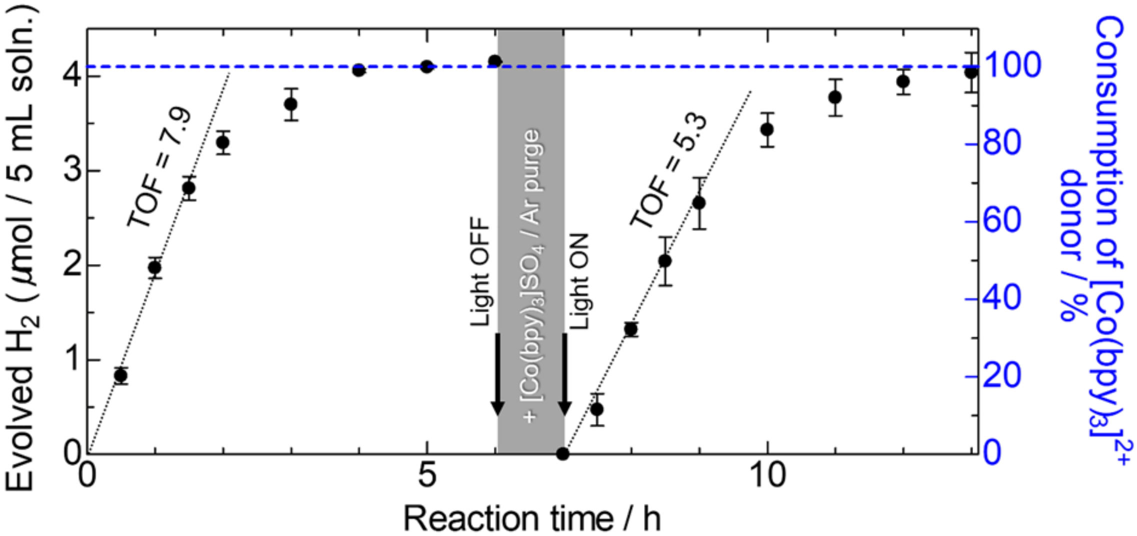

**Figure 6-3-6-4.** Two-cycle photocatalytic hydrogen production reactions using $RuCP^6$-Zr-$RuP^6$@Pt/$K_xH_{4-x}Nb_6O_{17}$ in the presence of 100 μM Ru(II) dye and 1.64 mM $[Co(bpy)_3]SO_4$ as the electron donor (initial pH = 2.0, λ = 470 ± 10 nm).

## 6-4 Conclusion

In this work, to suppress the back electron transfer processes that occur from a $H_2$ evolving photocatalyst to an oxidized redox mediator, new hybrid photocatalysts composed of the internally platinated layered niobate Pt/$K_xH_{4-x}Nb_6O_{17}$ and surface-immobilized double-layered Ru(II) photosensitizers with phosphonates coordinated to $Zr^{4+}$ cations were synthesized. As expected from the pioneering works on layered niobates,[41,43,44] the photocatalytic $H_2$ evolution activity (e.g., AQY) of the single-PS-layered photocatalyst **RuCP$^2$**@Pt/$K_xH_{4-x}Nb_6O_{17}$ in the presence of the KI redox-reversible electron donor was approximately 10 times higher than that of its $TiO_2$ analogue (**RuCP$^2$**@Pt/$TiO_2$).[48] This occurred because intercalation of the Pt-cocatalyst effectively suppressed back reaction with the oxidized mediators on the Pt cocatalyst surface. The double-layering of Ru(II) PS on the Pt/$K_xH_{4-x}Nb_6O_{17}$ surface significantly improved the photocatalytic $H_2$ evolution activity by enhancing the charge separation efficiency between the electron-injected semiconductor and photo-oxidized PS, as is the case with Pt-$TiO_2$ nanoparticles. The photocatalytic activity of the PS-double-layered Pt/$K_xH_{4-x}Nb_6O_{17}$ system strongly depended on the surface structure. Thus, Zr-**RuCP$^6$**-Zr-**RuP$^6$**@Pt/$K_xH_{4-x}Nb_6O_{17}$, with $Zr^{4+}$ cations on its surface, showed the highest AQY (0.38%) in the KI aqueous solution, while **RuCP$^6$**-Zr-**RuP$^6$**@Pt/$K_xH_{4-x}Nb_6O_{17}$, having phosphonate anions on its surface, exhibited the highest AQY (0.40%) in the $[Co(bpy)_3]SO_4$ aqueous solution. These results suggest that surface modification of dye-sensitized photocatalysts to modify the electrostatic interaction between the photocatalyst surface and redox mediator is a promising approach not only to enhance electron donation but also to suppress back electron transfer to the redox mediator. In fact, **RuCP$^6$**-Zr-**RuP$^6$**@Pt/$K_xH_{4-x}Nb_6O_{17}$ was photocatalytically active even in a 10-fold lower $[Co(bpy)_3]SO_4$ solution concentration, and almost all the $[Co(bpy)_3]^{2+}$ donors were consumed as an electron source for $H_2$ evolution. These results are important for the fabrication of Z-scheme water splitting photocatalysts, because back electron transfer to the oxidized redox mediator on a $H_2$ evolution photocatalyst is a bottleneck issue. In conclusion, the combination of two nano-architectures, the intercalation of a Pt cocatalyst and PS double layering, can suppress back electron transfer to the oxidized redox mediator and shows potential as an effective approach for the preparation of highly active Z-scheme water splitting photocatalysts.

## 6-5 Reference

1. S. Acharya, D.K. Padhi, K. M. Parida. *Catal. Today* **2020**, *353*, 220–231.
2. M. Graetzel. *Acc. Chem. Res.* **1981**, *14*, 376–384.
3. Y. Ma, X. Wang, X. Y. Jia, X. Chen, H. Han, C. Li. *Chem. Rev.* **2014**, *114*, 9987–10043.
4. A. Kudo, Y. Miseki. *Chem. Soc. Rev.* **2009**, *38*, 253–278.
5. X. Fang, S. Kalathil, E. Reisner. *Chem. Soc. Rev.* **2020**, *49*, 4926–4952.
6. A. Fujishima, K. Honda. *Nature* **1972**, *238*, 37–38.
7. H. Huang, B. Pradhan, J. Hofkens, M. B. J. Roeffaers, J. A. Steele. *ACS. Energy Lett.* **2020**, *5*, 1107–1123.
8. F. Niu, D. Wang, F. Li, Y. Liu, S. Shen, T. J. Meyer. *Adv. Energy Mater.* **2020**, *10*, 1900399.
9. L. Ju, J. Shang, X. Tang, L. Kou. *J. Am. Chem. Soc.* **2020**, *142*, 1492–1500.
10. H. Yu, L. Jiang, H. Wang, B. Huang, X. Yuan, J. Huang, J. Zhang, G. Zeng. *Small* **2019**, *15*, 1901008.
11. Q. Wang, M. Nakabayashi, T. Hisatomi, S. Sun, S. Akiyama, Z. Wang, Z. Pan, X. Xiao, T. Watanabe, T. Yamada, N. Shibata, T. Takata, K. Domen. *Nat. Mater.* **2019**, *18*, 827–832.
12. C. P. Xu, P. R. Ravi Anusuyadevi, C. Aymonier, R. Luque, S. Marre. *Chem. Soc. Rev.* **2019**, *48*, 3868–3902.
13. T. Hisatomi, K. Domen. *Nat. Catal.* **2019**, *2*, 387–399.
14. K. Iwashina, A. Kudo. *J. Am. Chem. Soc.* **2011**, *133*, 13272–13275.
15. Q. Wang, T. Hisatomi, Q. X. Jia, H. Tokudome, M. Zhong, C. Z. Wang, Z. H. Pan, T. Takata, M. Nakabayashi, N. Shibata, Y. B. Li, I. D. Sharp, A. Kudo, T. Yamada, K. Domen. *Nat. Mater.* **2016**, *15,* 611–615.
16. T. Takata, J. Z. Jiang, Y. Sakata, M. Nakabayashi, N. Shibata, V. Nandal, K. Seki, T. Hisatomi, K. Domen. *Nature* **2020**, *581*, 411–414.
17. L. Mu, Y. Zhao, A. Li, S. Wang, Z. Wang, J. Yang, Y. Wang, T. Liu, R. Chen, J. Zhu, F. Fan, R. Li, C. Li. *Energy Environ.* **2016**, *9*, 2463–2469.
18. R. Li, H. Han, F. Zhang, D. Wang, C. Li. *Energy Environ.* **2014**, *7*, 1369–1376.
19. G. Ma, S. Chen, Y. Kuang, S. Akiyama, T. Hisatomi, M. Nakabayashi, N. Shibata, M. Katayama, T. Minegishi, K. Domen. *J. Phys. Chem. Lett.* **2016**, *7*, 3892–3896.
20. A. Nakada, S. Nishioka, J. J. M. Vequizo, K. Muraoka, T. Kanazawa, A. Yamakata, S. Nozawa, H. Kumagai, S. Adachi, O. Ishitani, K. Maeda. *J. Mater. Chem. A* **2017**, *5*, 11710–11719.
21. M. J. Fang, C. W. Tsao, Y. J. Hsu. *J. Phys. D: Appl. Phys.* **2020**, *53*, 143001-1430033.
22. H. Kumagai, R. Aoyagi, K. Kato, A. Yamakata, M. Kakihata, H. Kato. *ACS Appl. Energy Mater.* **2021**, 2056–2060.
23. Y. Wang, H. Suzuki, J. Xie, O. Tomita, D. J. Martin, M. Higashi, D. Kong, R. Abe, J. Tang. *Chem.*

*Rev.* **2018**, *118*, 5201–5241.

24. Q. Wang, K. Domen. *Chem. Rev.* **2020**, *120*, 919–985.
25. B. J. Ng, L. K. Putri, X. Y. Kong, Y. W. Teh, P. Pasbakhsh, S. P. Chai. *Adv. Sci.* **2020**, *7*, 1903171.
26. A. Nakada, T. Uchiyama, N. Kawakami, G. Sahara, S. Nishioka, R. Kamata, H. Kumagai, O. Ishitani, Y. Uchimoto, K. Maeda. *ChemPhotoChem* **2019**, *3*, 37–45.
27. M. V. Sheridan, Y. Wang, D. Wang, L. T. Troian-Gautier, C. J. Dares, B. D. Sherman, T. J. Meyer. *Angew. Chem. Int. Ed. Engl.* **2018**, *57*, 3449–3453.
28. J. Warnan, J. Willkomm, J. N. Ng, R. Godin, S. Prantl, J. R. Durrant, E. Reisner. *Chem. Sci.* **2017**, *8*, 3070–3079.
29. X. Wang, L. Chen, S. Y. Chong, M. A. Little, Y. Wu, W. H. Zhu, R. Clowes, Y. Yan, M. A. Zwijnenburg, R. S. Sprick, A. I. Cooper. *Nat. Chem.* **2018**, *10*, 1180–1189.
30. R. Gueret, L. Poulard, M. Oshinowo, J. Chauvin, M. Dahmane, G. Dupeyre, P. P. Lainé, J. Fortage, M. Collomb. *ACS Catal.* **2018**, *8*, 3792–3802.
31. S. Guo, K. Chen, R. Dong, Z. Zhang, J. Zhao, T. Lu. *ACS Catal.* **2018**, *8*, 8659–8670.
32. E. S. D. Da Silva, N. M. M. Moura, M. G. P. M. S. Neves, A. Coutinho, M. Prieto, C. G. Silva, J. L. Faria. *Appl. Catal. B* **2018**, *221*, 56–69.
33. T. Tsukamoto, K. Takada, R. Sakamoto, R. Matsuoka, R. Toyoda, H. Maeda, T. Yagi, M. Nishikawa, N, Shinjo, S. Amano, T. Iokawa, N. Ishibashi, T. Oi, K. Kanayama, R. Kinugawa, Y. Koda, T. Komura, S. Nakajima, R. Fukuyama, N. Fuse, M. Mizui, M. Miyasaki, Y. Yamashita, K. Yamada, W. Zhang, R. Han, W. Liu, T. Tsubomura, H. Nishihara. *J. Am. Chem. Soc.* **2017**, *139*, 5359–5366.
34. J. S. Lee, D. I. Won, W. J. Jung, H. J. Son, C. Pac, S. O. Kang. *Angew. Chem. Int. Ed. Engl.* **2017**, *56*, 976–980.
35. E.Aslan, M. K. Gonce, M. Z. Yigit, A. Sarilmaz, E. Stathatos, F. Ozel, M. Can, I. H. Patir. *Appl. Catal. B* **2017**, *220*, 320–327.
36. A. Tiwari, N. V. Krishna, L. Giribabu, U. Pal. *J. Phys. Chem. C* **2018**, *122*, 495–502.
37. F. Yu, S. Cui, X. Li, Y. Peng, Y. Yu, K. Yun, S. Zhang, J. Li, J. Liu, J. Hua. *Dyes Pigm.* **2017**, *139*, 7–18.
38. Y. Sun, Y. Sun, C. Dall'Agnese, X. Wang, G. Chen, O. Kitao, H. Tamiaki, K. Sakai, T. Ikeuchi, S. Sasaki. *ACS Appl. Energy Mater.* **2018**, *1*, 2813–2820.
39. Y. H. Jung, H. K. Shim, H. W. Kim, Y. L. Kim. *Bull. Korean Chem. Soc.* **2007**, *28*, 921–928.
40. R. Abe, K. Sayama, H. Arakawa. *J. Photochem. Photobiol. A* **2004**, *166*, 115–122.
41. R. Abe, K. Shinmei, N. Koumura, K. Hara, B. Ohtani. *J. Am. Chem. Soc.* **2013**, *135*, 16872–16884.
42. Kim, Y. I.; Salim, S.; Huq, M. J.; Mallouk, T. E. *J. Am. Chem. Soc.* **1991**, *113*, 9561–9563.
43. Kim, Y. I.; Atherton, S. J.; Brigham, E. S.; Mallouk, T. E. *J. Phys. Chem.* **1993**, *97*, 11802–11810.

44. R. Abe, K. Shinmei, K. Hara, B Ohtani. *Chem. Commun.* **2009**, (24), 3577–3579.
45. T. Oshima, S. Nishioka, Y. Kikuchi, S. Hirai, K. Yanagisawa, M. Eguchi, Y. Miseki, T. Yokoi, T. Yui, K. Kimoto, K. Sayama, O. Ishitani, T. E. Mallouk, K. Maeda. *J. Am. Chem. Soc.* **2020**, *142*, 8412–8420.
46. N. Yoshimura, A. Kobayashi, M. Yoshida, M. Kato, M. *Bull. Chem. Soc. Jpn.* **2019**, *92*, 1793–1800.
47. N. Yoshimura, A. Kobayashi, W. Genno, T. Okubo, M. Yoshida, M. Kato. *Sustain. Energy Fuels* **2020**, *4*, 3450–3457.
48. N. Yoshimura, A. Kobayashi, M. Yoshida, M. Kato. *Chem. Eur. J.* **2020**, *26*, 16939–16946.
49. K. Hanson, M. K. Brennaman, A. Ito, H. Luo, W. Song, K. A. Parker, R. Ghosh, M. R. Norris, C. R. K. Glasson, J. J. Concepcion, R. Lopez, T. J. Meyer. *J. Phys. Chem. C* **2012**, *116*, 14837–14847.
50. O. O. Ogunsolu, J. C. Wang, K. Hanson. *Inorg. Chem.* **2017**, *56*, 11168–11175.
51. A. Kobayashi, K. Shimizu, A. Watanabe, Y. Nagao, N. Yoshimura, M. Yoshida, M. Kato. *Inorg. Chem.* **2019**, *58*, 2413–2421.
52. L. Troian-Gautier, M. D. Turlington, S. A. M. Wehlin, A. B. Maurer, M. D. Brady, W. B. Swords, G. J. Meyer. *Chem. Rev.* **2019**, *119*, 4628–4683.
53. L. Troian-Gautier, W. B. Swords, G. J. Meyer. *Acc. Chem. Res.* **2019**, *52*, 170–179.
54. Y. Sasaki, H. Kato, A. Kudo. *J. Am. Chem. Soc.* **2013**, *135*, 5441–5449.
55. A. D. Awtrey, R. W. E. Connick. *J. Am. Chem. Soc.* **1951**, *73*, 1842–1843.
56. D. A. Palmer, R. W. Ramette, R. E. Mesmer. *J. Solution Chem.* **1984**, *13*, 673–683.
57. J. Gao, W. Yang, A. M. El-zohry, G. K. Prajapati, Y. Fang, J. Dai, Y. Hao, V. Leandri, P. H. Svensson, I. Furó, G. Boschloo, T. Lund, L. Kloo. *J. Mater. Chem. A,* **2019**, *33*, 19496-19505
58. S. Furugori, A. Kobayashi, A. Watanabe, M. Yoshida, M. Kato. *ACS Omega* **2017**, *2*, 3901–3912.

# Chapter 7

# The Enhancement of Electron Donation Reaction with Redox Mediators by Surface Modification of Ru(II)-dye-multilayered Pt-cocatalyst-loaded Layered Niobate

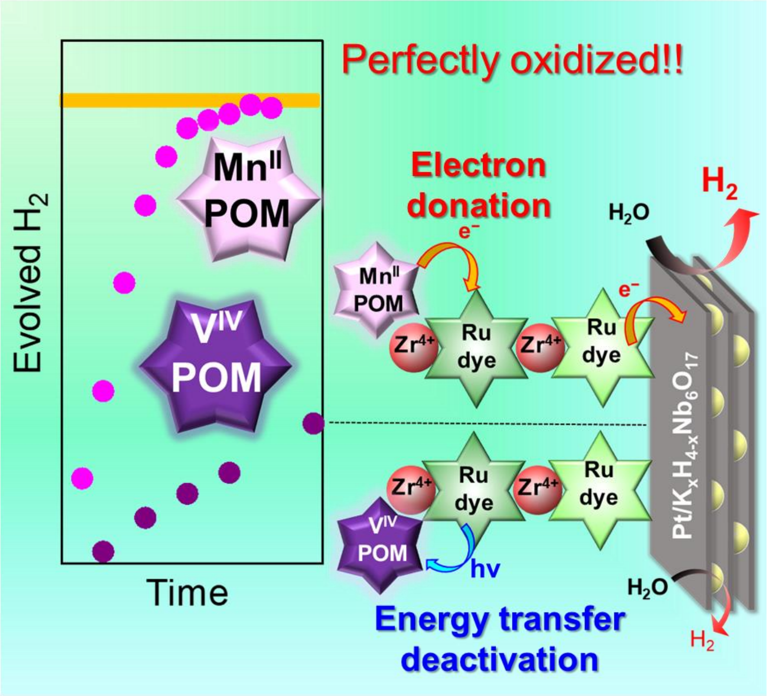

## 7-1 Introduction

Photocatalytic water splitting has attracted considerable attention as a promising reaction to resolve the global warming and energy crises.[1-5] The use of Z-scheme photocatalysts, composed of hydrogen ($H_2$) and oxygen ($O_2$) evolution photocatalysts with an appropriate redox-reversible electron mediator, is a promising approach to ensure enough driving force for both electron transfer and catalytic reactions.[6-9] For example, Domen et al. recently reported on a Z-scheme photocatalyst composed of Ir-$FeCoO_x$ and $BiVO_4$ as the $H_2$ and $O_2$ evolving photocatalysts, respectively, in the presence of $[Fe(CN)_6]^{3-/4-}$ as the electron mediator. This Z-scheme system exhibited 0.6% solar-to-hydrogen (STH) energy conversion efficiency and 12.3% apparent quantum efficiency (AQY) at 420 nm.[10] However, most Z-scheme systems developed to date still suffer from the thermodynamically favorable back electron transfer processes at the photocatalyst–mediator interface. Dye-sensitized photocatalysts (DSPs) consisting of a molecular photosensitizer (PS) and semiconductor catalyst have been extensively studied to utilize visible light in the solar spectrum, accounting for approximately half of the solar light energy for hydrogen production.[11-15] From the viewpoint of electron transfer in Z-scheme water-splitting photocatalysis, the surface modification of DSPs is an interesting and efficient method to control the electron transfer at the photocatalyst–mediator interface.[16-20] In fact, several state-of-the-art DSPs have been reported to produce $H_2$ effectively in the presence of a redox-reversible electron mediator (e.g., $I^-$ and $[Co(bpy)_3]^{2+}$) as the electron source for $H_2$ production.[21-33] Maeda et al. recently reported that the $H_2$ evolution activity of a DSP composed of a Pt-intercalated $HCa_2Nb_3O_{10}$ nanosheet and Ru(II) dye was significantly improved by surface modification with both amorphous $Al_2O_3$ and poly(styrenesulfonate) polymer, to achieve a remarkably high apparent quantum yield (AQY = 4.1% at 420 nm).[34] The origin of the high AQY was attributed to the suppression of back electron transfers from both the Pt co-catalyst and Ru(II) photosensitizer (PS) to the oxidized electron mediator, $I_3^-$, by covering the photocatalyst surface with poly(styrenesulfonate) polymer. As described in Chapter 6, the surface-modified Ru(II)-PS-double-layered photocatalyst Zr-**RuCP$^6$**-Zr-**RuP$^6$**@Pt/$K_xH_{4-x}Nb_6O_{17}$ (Scheme 7-1; **Zr$^{4+}$-DSP**, **RuCP$^6$** = $[Ru(mpbpy)_3]^{10-}$, where **RuP$^6$** = $[Ru(pbpy)_3]^{10-}$, $H_4$mpbpy = 2,2′-bipyridine-4,4′-bis(methane-phosphonic acid), and $H_4$pbpy = 2,2′-bipyridine-4,4′-bis(phosphonic acid))[35] was highly active for hydrogen production in the presence of redox-reversible electron donors (RREDs), such as iodide ($I^-$) anions and $[Co(bpy)_3]^{2+}$ (bpy = 2,2′-bipyridine) complex cations. Further, the surface modification drastically improved the activity owing to the electrostatic attraction of the RREDs induced by the photocatalyst surface. However, the number of active DSPs in the presence of RREDs remains limited. Thus, new strategies for DSPs to not only suppress the back reaction but also accelerate the forward reaction at the photocatalyst–mediator interface are strongly required.

In this work, to design an efficient way to accelerate the forward electron transfer from the RRED to the photocatalyst, two polyoxometalates were selected, namely $K_6[SiV^{IV}W_{11}O_{40}]$ and $K_6[SiW_{11}O_{39}Mn^{II}(H_2O)] \cdot nH_2O$ (**V$^{IV}$POM** and **Mn$^{II}$POM**, respectively), as the RREDs for photocatalytic $H_2$ production by the Ru(II)-PS-double-layered DSP, X-**RuCP$^6$**-Zr-**RuP$^6$**@Pt/$K_xH_{4-x}Nb_6O_{17}$, which is composed of Pt-intercalated layered-niobate and doubly-layered Ru(II) photosensitizers (Scheme 7-1; **X-DSP**, X = $H^+$ and $Zr^{4+}$)[35]. These POMs were used as the electron mediator in the Z-scheme water-splitting photocatalyst because of their suitable and comparable redox potentials and superior stabilities in aqueous solution.[36-43] The important feature for this work is that these POMs are hexavalent anionic molecules, suggesting a stronger electrostatic interaction with the photocatalyst surface than that observed with commonly used electron donors. In addition, these two POMs exhibit different light absorption behaviors that significantly affect the energy transfer process with the Ru(II) PS of **X-DSP** (Figure 7-1). This work demonstrates that the photocatalytic $H_2$ evolution reactions with **X-DSP** in the presence of **V$^{IV}$POM** and **Mn$^{II}$POM**. **H$^+$-DSP** successfully produced $H_2$ photocatalytically until it completely oxidized a very dilute 1 mM **V$^{IV}$POM** aqueous solution. Interestingly, the AQY in 1 mM **V$^{IV}$POM** was comparable to those observed in higher concentrations of the other less-charged electron donors (0.5 M KI and 16 mM $[Co(bpy)_3]^{2+}$ aq).[35] In contrast, **Zr$^{4+}$-DSP** exhibited almost the same activity as **H$^+$-DSP** under phosphate buffer conditions; however, its activity remarkably decreased in HCl aq. This drop in activity in the absence of phosphate buffer was attributed to the energy transfer quenching of the photo-excited Ru(II)-PS by the electrostatically immobilized **V$^{IV}$POM** on the **Zr$^{4+}$-DSP** surface $Zr^{4+}$ cations. This hypothesis was supported by the result that **Zr$^{4+}$-DSP** maintained its high activity in the presence of visible-light-transparent **Mn$^{II}$POM** electron donor solution.

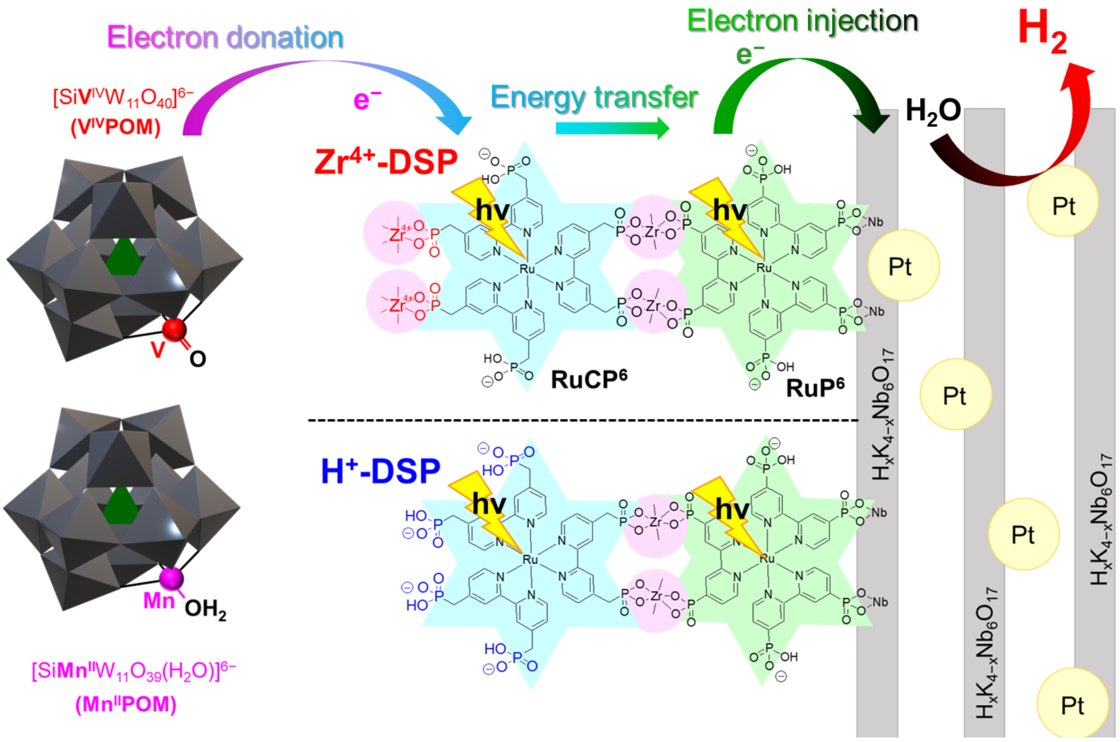

**Scheme 7-1**. Schematic illustration of **X-DSP**s and two redox-reversible POM anions.

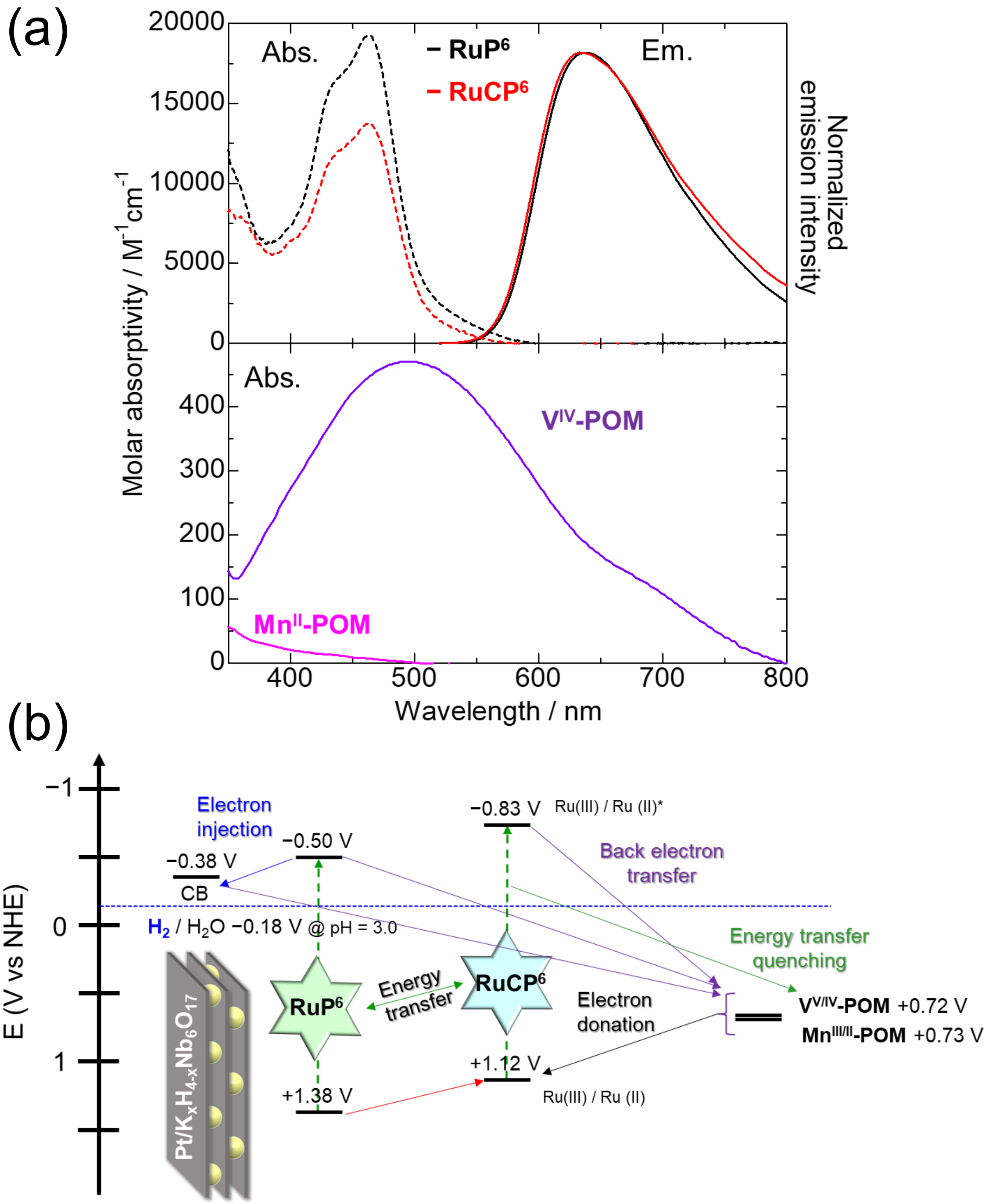

**Figure 7-1**. (a) (Upper) UV-vis absorption spectra of (black dashed line) **RuP$^6$** and (red dashed line) **RuCP$^6$**, and emission spectra of (black solid line) **RuP$^6$** and (red solid line) **RuCP$^6$** in HCl aqueous solution at 293 K. Excitation wavelength was 470 nm. (Bottom) UV-vis absorption spectra of (purple solid line) **V$^{IV}$-POM** and (pink solid line) **Mn$^{II}$-POM** in HCl aqueous solution at 293 K. (b) Plausible energy diagram of **H$^+$-DSP** and **Zr$^{4+}$-DSP** with **M-POM** (**M** = V$^{VI}$ and Mn$^{II}$). The values of redox potentials were interfered from literature[35,44,45].

## 7-2 Experimental

### 7-2-1 Synthesis and measurements

Two types of Ru(II)-dye-immobilized Pt/$K_xH_{4-x}Nb_6O_{17}$ nanoparticles, **$RuCP^6$**-Zr-**$RuP^6$**@Pt/$K_xH_{4-x}Nb_6O_{17}$ and Zr-**$RuCP^6$**-Zr-**$RuP^6$**@Pt/$K_xH_{4-x}Nb_6O_{17}$ were synthesized by the same procedure described in chapter 6-2. The results of dye immobilization reactions were summarized in Table 7-2 and Figure 7-2. All used measurement equipment were the same as described in chapter 6-2.

**Table 7-2.** Absorbance of each supernatant solution and the calculated $C_B$ and $M_i$ values about **$RuCP^6$**-Zr-**$RuP^6$**@ Pt/$K_xH_{4-x}Nb_6O_{17}$

| Photo-catalyst | Immobilized Ru(II) PS | *A* ($M^{-1}cm^{-1}$) | $C_B$ (mM) | $M_i$ (µmol) | Surface coverage *N* ($10^{-2}$ nmol / $cm^2$) |
|---|---|---|---|---|---|
| This work | 1st (inner) layer **$RuP^6$** | 0.380 | 0.969 | 1.64 | 7.11~14.5 |
| | 2nd (outer) layer **$RuCP^6$** | 0.236 | 0.808 | 2.61 | 11.3~23.0 |
| Previous work (chapter 6) | 1st (inner) layer **$RuP^6$** | 0.381 | 0.971 | 1.63 | 7.07~14.4 |
| | 2nd (outer) layer **$RuCP^6$** | 0.267 | 0.915 | 1.96 | 8.50~17.3 |

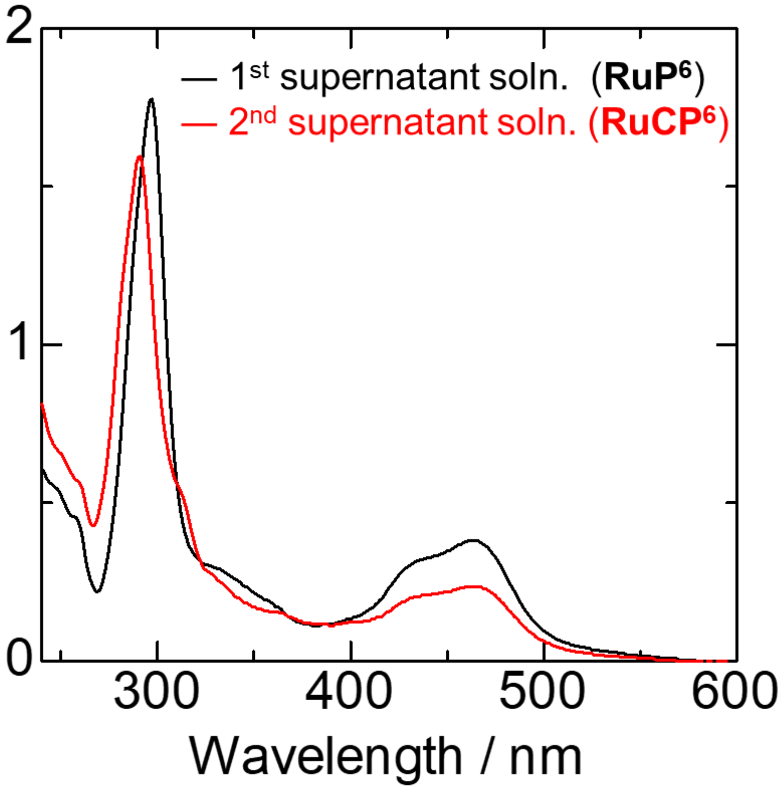

**Figure 7-2.** UV-vis absorption spectra of the supernatant solutions of Ru-PS immobilization experiment at 298 K. Note that each solution (1 mL) was diluted to 50 mL by the addition of deionized water before the spectral measurement

### 7-2-2 Photocatalytic hydrogen evolution reaction condition

A 1 mM $K_6[SiV^{IV}W_{11}O_{40}]$ (**$V^{IV}$POM**) or $K_6[SiW_{11}O_{39}Mn^{II}(H_2O)]\cdot nH_2O$ (**$Mn^{II}$POM**), as redox reversible electron donor, with HCl aqueous solution or 40 mM phosphonate buffer aqueous solution (pH = 3) was used to ensure the stable redox behavior of these POM species during the photocatalytic reaction.[36] The other conditions were the same as chapter 6-2.

## 7-3 Results and discussions

### 7-3-1 Photocatalytic hydrogen evolution reaction

Figures 7-3-1-1(a) and 7-3-1-1(b) show the results of the photocatalytic $H_2$ evolution reactions in 1 mM **$V^{IV}$-POM** aqueous solution using **$H^+$-DSP** and **$Zr^{4+}$-DSP** as the photocatalyst, respectively. The estimated turnover numbers and frequencies per one photosensitizing dye (PS TON and PS TOF, respectively) together with the apparent quantum yield (AQY) are listed in Table 7-3-1-1. Notably, the total amount of Ru(II) dye in each solution was constant (100 mM) and no hydrogen evolution was observed in the absence of Ru(II) dye, light, or electron donor (Table 7-3-1-2). Although **$H^+$-DSP** exhibited near-identical activities in the HCl and phosphate buffer aqueous solutions, in the early stage (<1 h), the activity in HCl aq was slightly higher than that in the phosphate buffer (Figure 7-3-1-1(a)). The produced amount of $H_2$ after 3 h reaction (~2.5 μmol) corresponded with the expected value when all **$V^{IV}$-POM** donors were one-electron oxidized to form **$V^{V}$-POM**. On the other hand, **$Zr^{4+}$-DSP** produced only 1.2 μmol of hydrogen after 6 h irradiation in the HCl aqueous solution, whereas it generated almost the same amount of hydrogen (~2.5 μmol) as did **$H^+$-DSP** after 3 h reaction in the phosphate buffer solution. The photocatalytic $H_2$ evolution was restarted by the addition of another 5 μmol of **$V^{IV}$-POM** (Figure 7-3-1-2, and Table 7-3-1-3), and the supernatant solutions after these reactions afforded UV-vis absorption spectra similar to that of the one-electron oxidized form, **$V^{V}$-POM** (Figure 7-3-1-3). These results indicate that **$V^{IV}$-POM** acted as the electron donor of the photocatalytic $H_2$ evolution reactions with **$H^+$-DSP** and **$Zr^{4+}$-DSP**. Notably, the absorption bands of the Ru dyes were hardly observed in the supernatant spectra (Figure 7-3-1-3), suggesting the negligible desorption of these dyes. The observed photocatalytic activity in the second cycle experiment of **$H^+$-DSP** was approximately 30% less (PS TOF = 5.16) than that of the first cycle (7.51) (Figure 7-3-1-2). This was attributed to the presence of some back reactions related to the one-electron oxidized **$V^{V}$-POM**. Considering that the $^3$MLCT emission of $[Ru(bpy)_3]^{2+}$ was strongly quenched by **$V^{V}$-POM** (Figure 7-3-1-4), the back electron transfer process from the photo-excited $Ru^{2+}$* PS to **$V^{V}$-POM** was suggested as the sole plausible back reaction. The AQY values for the initial hour of reaction (*i*AQY) of **$H^+$-DSP** and **$Zr^{4+}$-DSP** in phosphate buffer were estimated to be almost identical (0.39%), indicating no dependence on the surface structure of the photocatalytic nanoparticles in the phosphonate buffer. These *i*AQY values were also comparable to that in 0.5 M KI aq (pH = 2, *i*AQY = 0.60%) and 20 mM $[Co(bpy)_3]^{2-}$ aq (pH = 2, *i*AQY = 0.56%),[35] even though the reaction conditions—a slightly basic pH and lower donor concentration ([**$V^{IV}$-POM**] = 1 mM, pH = 3, *i*AQY = 0.39%)—were less favorable for the $H_2$ evolution reaction. Thus, it was supposed that redox-reversible POM species are potential materials as electron mediators for dye-sensitized Z-scheme water splitting systems. In contrast, the *i*AQY value of **$Zr^{4+}$-DSP** in HCl aq was approximately 87%

lower (*i*AQY = 0.050%) than that in the phosphate buffer. To reveal the origin of this lower activity, **H$^+$-DSP** and **Zr$^{4+}$-DSP** were analyzed by XRF analysis, in the solid state, after photocatalytic $H_2$ evolution reaction (Figure 7-3-1-5). The samples were collected by ultracentrifugation after the reaction was completely washed twice with HCl aqueous solution (pH = 3). The XRF spectra of **H$^+$-DSP** before and after photocatalytic $H_2$ evolution reaction were almost identical (Figure 7-3-1-5(a)). In contrast, for **Zr$^{4+}$-DSP**, the W Lα radiation derived from **V-POM** was clearly detected after the reaction in HCl aq (Figure 7-3-1-5(b)) but was hardly observed in the phosphate buffer solution reaction. These results suggest that the **V-POM** species were immobilized on the surface Zr$^{4+}$ ions of **Zr$^{4+}$-DSP** during photocatalytic $H_2$ evolution in HCl aq. In the phosphate buffer solution, however, immobilization of the **V-POM** species was suppressed because of the coordination of the phosphate anions to the surface Zr$^{4+}$ cations. In fact, the zeta potential of **Zr$^{4+}$-DSP** in the HCl aqueous solution significantly shifted negatively with the addition of **V$^{IV}$-POM** (Table 7-3-1-4; +31 mV → −34 mV). On the other hand, in the phosphate buffer solution, the zeta potential was largely negative even without **V$^{IV}$-POM** addition (−37 mV → −33 mV). These zeta potential changes also indicated the immobilization of **V-POM** on the **Zr$^{4+}$-DSP** surface in HCl aq.

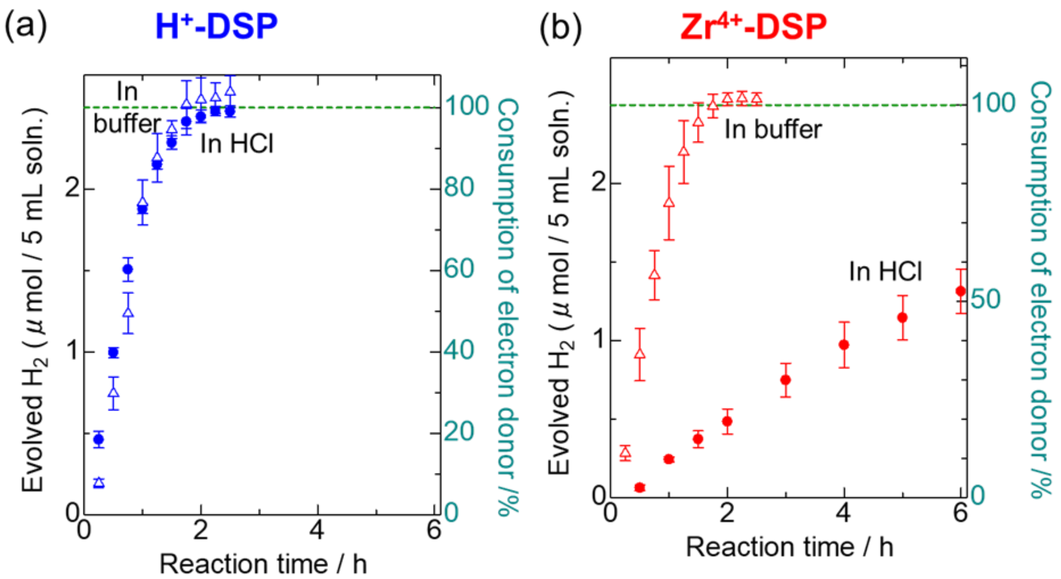

**Figure 7-3-1-1.** Photocatalytic $H_2$ evolution reactions driven by (a) **Zr$^{4+}$-DSP** and (b) **H$^+$-DSP** in the presence 1 mM **V$^{IV}$-POM** as the electron donor (closed circles) in HCl aqueous solution and (open triangles) in 40 mM phosphate buffer aqueous solution. Ru(II) dye concentration of all the reactions were adjusted to 100 μM. Initial pH of all the solutions was adjusted to 3.0 by adding HCl or phosphate buffer aqueous solution (λ = 460 ± 15 nm; 70 mW).

**Table 7-3-1-1**. Results of photocatalytic $H_2$ evolution experiments with POM electron donor in acidic aqueous solution.

| Photocatalyst[a] | Solution | Initial pH | Electron donor | $H_2$ (μmol) (0–2 h) | PS TON[a] (0–2 h) | PS initial TOF[a] (0–1 h) | *i*AQY[a] (%) (0–1 h) |
|---|---|---|---|---|---|---|---|
| **$H^+$-DSP** | Phosphate buffer | 3 | **$V^{IV}$-POM**, 1 mM | 2.55±0.18 | 10.2 | 7.67 | 0.39 |
| **$H^+$-DSP** | HCl aq | 3 | **$V^{IV}$POM**, 1 mM | 2.44 ± 0.04 | 9.78 | 7.51 | 0.39 |
| **$Zr^{4+}$-DSP** | Phosphate buffer | 3 | **$V^{IV}$-POM**, 1 mM | 2.54±0.06 | 10.1 | 7.50 | 0.39 |
| **$Zr^{4+}$-DSP** | HCl aq | 3 | **$V^{IV}$-POM**, 1 mM | 0.485 ± 0.079 | 1.94 | 0.976 | 0.050 |
| **$Zr^{4+}$-DSP** | HCl aq | 3 | **$Mn^{II}$-POM**, 1 mM | 2.41±0.26 | 9.62 | 7.86 | 0.40 |
| **$Zr^{4+}$-DSP***35* | HCl aq | 2 | KI, 0.5 M | 5.35±0.93 | 21.4 | 11.9 | 0.60 |
| **$H^+$-DSP***35* | HCl aq | 2 | $[Co(bpy)_3]SO_4$, 20 mM | 5.33±0.08 | 21.3 | 11.1 | 0.56 |

[a] Measurement conditions: [Ru-PS] = 100 μM in total, electron donor = 1 mM, volume = 5 mL aqueous solution, $\lambda_{ex} = 460 \pm 15$ nm, 70 mW in total. The reaction solution was purged by Ar bubbling for 1 h before light irradiation. Numeral values were an average of more than three repeated experiments. Definitions: PS = photosensitizer, PS TON = turnover number of PS, PS initial TOF = turnover frequency of PS during the initial hour of irradiation (from 0 to 1 h), *i*AQY = apparent quantum efficiency during the initial hour, **$V^{IV}$-POM** = $K_6[SiV^{IV}W_{11}O_{40}]$, **$Mn^{II}$-POM** = $K_6[SiW_{11}O_{39}Mn^{II}(H_2O)] \cdot nH_2O$

**Table 7-3-1-2**. Control experiments of photocatalytic hydrogen evolution of **Zr$^{4+}$-DSP** and **H$^{+}$-DSP**.

| Entry [a] | Photocatalyst | Electron Donor (ED) | Light irradiation | Evolved H$_2$ [b] |
|---|---|---|---|---|
| 1 | **Zr$^{4+}$-DSP** | **V$^{IV}$-POM** | Yes | Yes |
| 2 | **H$^{+}$-DSP** | **V$^{IV}$-POM** | Yes | Yes |
| 3 | **H$^{+}$-DSP** | **V$^{IV}$-POM** | No | - |
| 4 | **H$^{+}$-DSP** | Nothing | Yes | - |
| 5 | **H$^{+}$-DSP** | **V$^{V}$-POM** | Yes | - |
| 6 | **H$^{+}$-DSP** | **Mn$^{II}$-POM** | No | - |
| 7 [c] | - | **V$^{IV}$-POM** | Yes | - |

[a] Reaction conditions: [Ru] = 100 μM in HCl aqueous solution (pH = 3, 5 mL) under blue LED light irradiation (λ = 460 ± 15 nm) for 6 h. [b] Gas in the head space was analyzed qualitatively by Gas Chromatography (GC). "Yes" indicates that the evolved amount of H$_2$ was larger than the GC detection limit. [c] No photocatalyst was used.

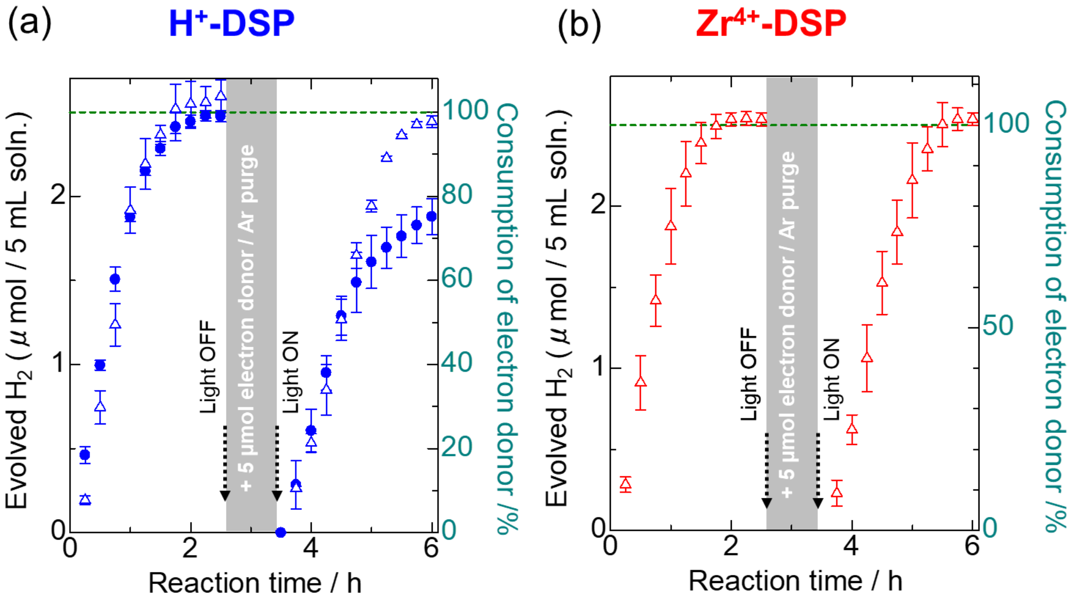

**Figure 7-3-1-2**. Two-cycle photocatalytic H$_2$ evolution reactions (λ = 460 ± 15 nm; 70 mW) driven by (a) **Zr$^{4+}$-DSP** and (b) **H$^{+}$-DSP** in the presence 1 mM **V$^{IV}$-POM** as the electron donor in HCl aqueous solution (closed circles) and in phosphate buffer aqueous solution (open triangles). The Ru(II) dye concentration of all DSPs were adjusted to 100 μM. Initial pH of all solutions were prepared to 3.0 by HCl aqueous solution or phosphate buffer.

**Table 7-3-1-3**. Results of two-cycle photocatalytic $H_2$ evolution experiments in HCl aqueous solution.

| Photocatalyst[b] | Solution | Reduced electron donor (**$V^{IV}$POM)** at initial state | Oxidized electron acceptor **($V^{V}$POM)** at initial state | $H_2$ (μmol) (0-2h) | PS TON[b] (0-2h) | PS initial TOF[b] (0-1h) | *i*AQY[b] (%) (0-1h) |
|---|---|---|---|---|---|---|---|
| **$H^+$-DSP** -1st | HCl aq. | 1 mM | - | 2.44 ±0.04 | 9.78 | 7.51 | 0.39 |
| **$H^+$-DSP** -2nd [a] | HCl aq. | 1 mM | 1 mM | 1.76 ±0.17 | 7.05 | 5.16 | 0.27 |
| **$H^+$-DSP** -1st | Phosphate buffer | 1 mM | - | 2.55±0.18 | 10.2 | 7.67 | 0.39 |
| **$H^+$-DSP** -2nd [a] | Phosphate buffer | 1 mM | 1 mM | 2.36±0.01 | 9.45 | 5.06 | 0.26 |
| **$Zr^{4+}$-DSP**-1st | Phosphate buffer | 1 mM | - | 2.54±0.06 | 10.1 | 7.50 | 0.39 |
| **$Zr^{4+}$-DSP**-2nd [a] | Phosphate buffer | 1 mM | 1 mM | 2.50±0.16 | 10.0 | 6.11 | 0.31 |

[a] Another 5 μmol of reduced electron donor was added and the reaction solution was re-purged by Ar bubbling for 1 h after 1st reaction experiment. [b] Measurement condition: [Ru-PS] = 100 μM in total, Electron donor = 1 mM, Initial pH = 3, Volume = 5 mL aqueous solution, $\lambda_{ex}$ = 460 ± 15 nm, 70 mW in total. The reaction solution was purged by Ar bubbling for 1 h before light irradiation. The numeral values were average of more than 3 times experiment. Definition: PS = photosensitizer, PS TON = turn over number of PS, PS initial TOF = turn over frequency of PS at initial 1 h irradiation (from 0 h to 1 h), *i*AQY = apparent quantum efficiency at initial 1 h, **$V^{IV}$-POM** = $K_6[SiV^{IV}W_{11}O_{40}]$, **$V^{V}$-POM** = $K_5[SiV^{V}W_{11}O_{40}]$.

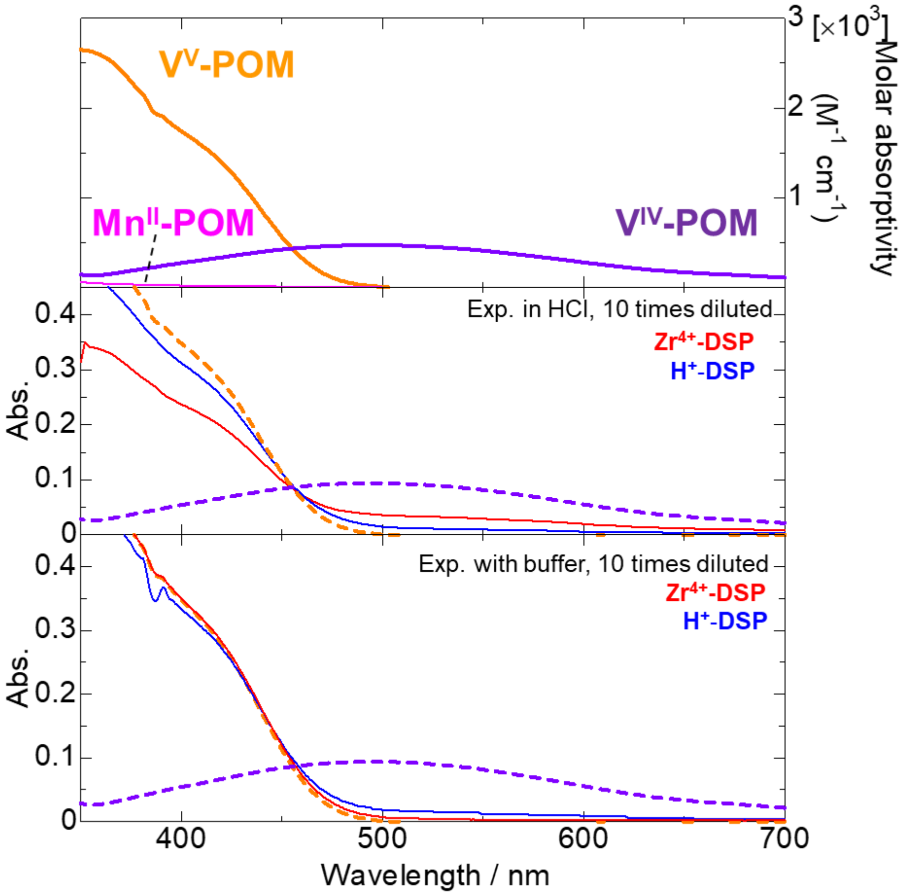

**Figure 7-3-1-3.** (Upper) UV-vis absorption spectra of (purple) **$V^{IV}$-POM** and (orange) **$V^{V}$-POM** in HCl aqueous solution (pH = 3.0). (Middle) UV-vis absorption spectra of the supernatants of (red) **$Zr^{4+}$-DSP** and (blue) **$H^{+}$-DSP** obtained by centrifugation of the reaction solutions after photocatalytic hydrogen evolution reaction in the condition of HCl aqueous solution (pH = 3.0) with **$V^{IV}$-POM** as an electron donor. (Bottom) UV-vis absorption spectra of the supernatants of (red) **$Zr^{4+}$-DSP** and (blue) **$H^{+}$-DSP** obtained by centrifugation of the reaction solutions after photocatalytic hydrogen evolution reaction in the condition of 50 mM phosphate buffer aqueous solution (pH = 3.0) with **$V^{IV}$-POM** as an electron donor. Each supernatant (1 mL) was diluted to 10 mL with deionized water prior to the measurement.

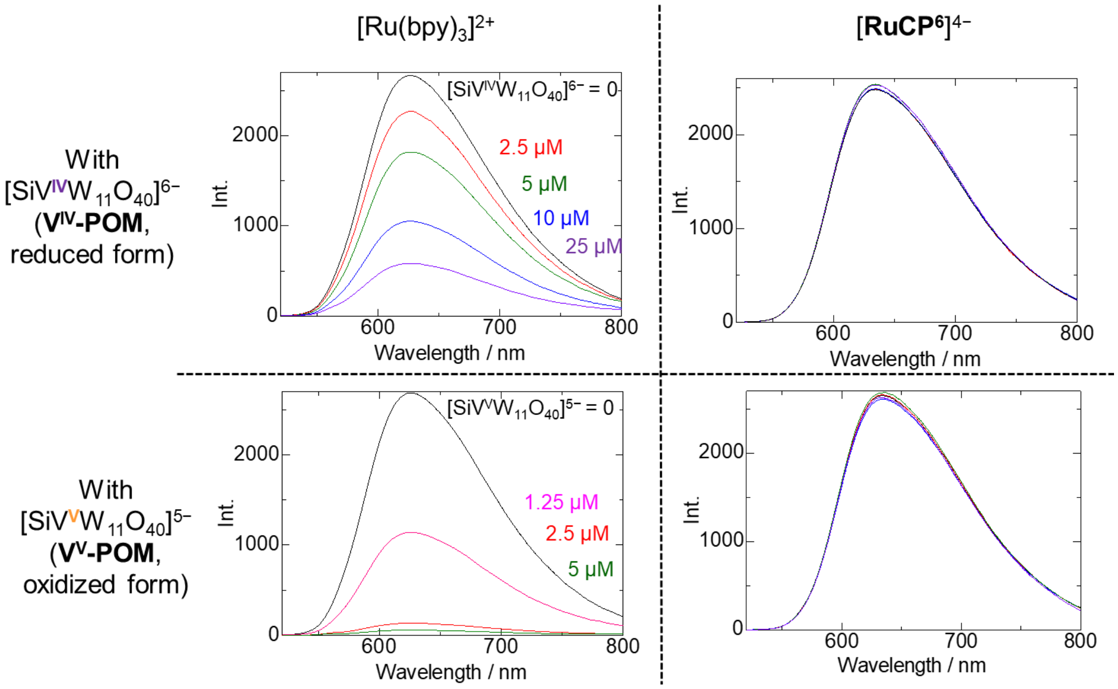

**Figure 7-3-1-4.** Photoluminescence spectra of $[Ru(bpy)_3]^{2+}$ and $[\mathbf{RuCP^6}]^{4-}$ complex with $[SiV^{IV}W_{11}O_{40}]^{6-}$ or $[SiV^{V}W_{11}O_{40}]^{5-}$ in HCl aqueous solution (pH = 3) at 298 K. All samples were purged and bubbled by $N_2$ gas for more than 30 minutes prior to the measurement. Excitation wavelength was 470 nm, and 490 nm of long pass filter was used.

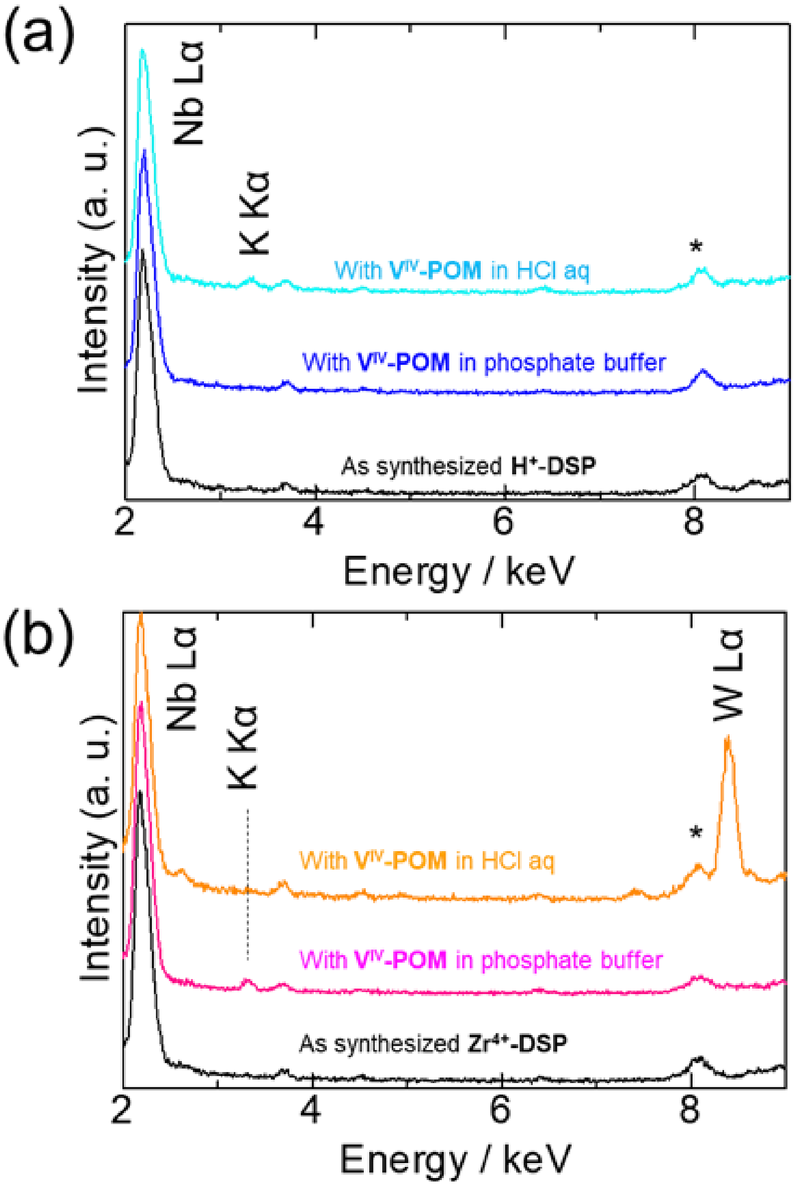

**Figure 7-3-1-5.** XRF spectra of (a) **$H^+$-DSP** and (b) **$Zr^{4+}$-DSP** obtained by centrifugation of the reaction solutions after photocatalytic hydrogen evolution reaction at 298 K under vacuum. All spectra were normalized with the intensity of the Nb Lα peak. The marked peak (*) is due to the background of the Cu sample holder.

**Table 7-3-1-4**. Zeta(ζ)-potentials of Ru(II)-PS-immobilized nanoparticles in the HCl aqueous solution, 6 mM KCl aqueous solution, 1 mM $K_6[SiV^{IV}W_{11}O_{40}]$ (**$V^{IV}$-POM**) aqueous solution, and 1 mM $K_6[SiMn^{II}W_{11}O_{39}(H_2O)]$ (**$Mn^{II}$-POM**) aqueous solution. All measurements were done in pH = 3.0 aq.

| Photocatalyst | Zeta potential / mV | | | | | |
|---|---|---|---|---|---|---|
| | HCl aq. | 6 mM KCl aq. | HCl aq. + **$V^{IV}$-POM** | HCl aq. + **$Mn^{II}$-POM** | Phosphate buffer | Phosphate buffer + **$V^{IV}$-POM** |
| **$Zr^{4+}$-DSP** | +31 | −4.2 | −34 | −36 | −37 | −33 |
| **$H^+$-DSP** | +2.9 | −29 | −28 | −35 | −29 | −23 |
| $Pt/K_xH_{4-x}Nb_6O_{17}$ | +36 | +5.9 | −33 | - | - | - |

As discussed above, the XRF spectra and zeta potential measurements revealed that the **V-POM** species were immobilized on the **$Zr^{4+}$-DSP** surface during the photocatalytic $H_2$ evolution reaction in HCl aq, resulting in the lower activity. As the reason why **$Zr^{4+}$-DSP** exhibited lower activity in the HCl aq condition, the energy transfer quenching of Ru dyes by **$V^{IV}$-POM** was presumed because the absorption band of **$V^{IV}$-POM** was effectively overlapped with the $^3$MLCT emission band of Ru(II) dyes (Scheme 7-3 and Figure 7-1). In fact, the $^3$MLCT emission of the simple cation $[Ru(bpy)_3]^{2+}$ was effectively quenched by **$V^{IV}$-POM**, while that of the negatively charged **$RuCP^6$**, which comprises six phosphonate groups, was hardly quenched (Figure 7-3-1-4). These contrasting results suggest that the electrostatic attraction between the $[Ru(bpy)_3]^{2+}$ cation and **$V^{IV}$-POM** anion effectively induce energy transfer quenching. The direct observation of the emission quenching of Ru(II) dyes in **$H^+$-DSP** and **$Zr^{4+}$-DSP** by **$V^{IV}$-POM** was difficult because of the strong light scattering of the $Pt/K_xH_{4-x}Nb_6O_{17}$ particles. However, it was supposed that the surface-immobilized **V-POM** species on **$Zr^{4+}$-DSP** should induce energy transfer quenching, resulting in a lower photocatalytic activity than those of the other reaction systems in which the **V-POM** species were hardly immobilized on the DSP surface.

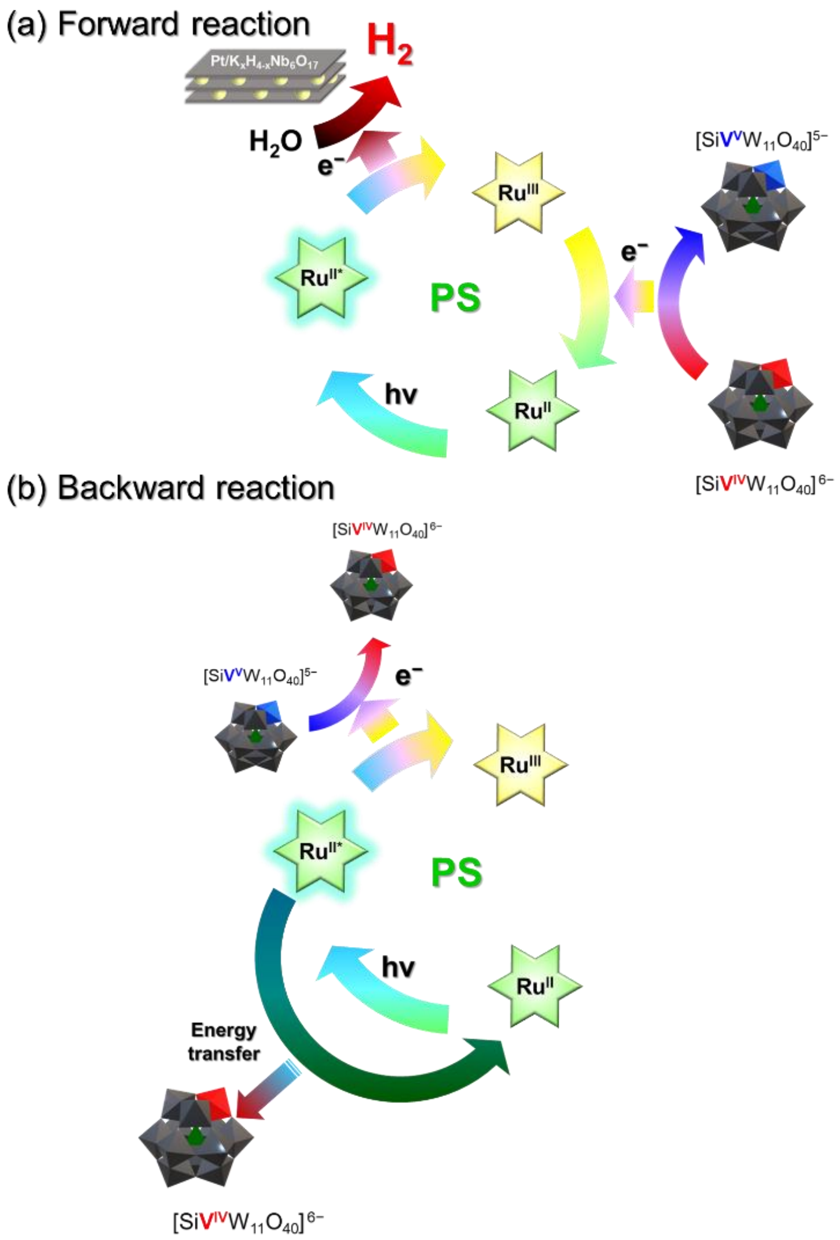

**Scheme 7-3.** Plausible mechanism of the (a) forward and (b) backward electron/energy transfer processes in the photocatalytic $H_2$ evolution reaction.

To overcome the energy transfer quenching by the **$V^{IV}$-POM** electron donor, next, a photocatalytic $H_2$ evolution experiment was performed in the presence of **$Mn^{II}$-POM**, which has almost the same redox potential (+0.73 V) as **$V^{IV}$-POM** without, however, the absorptivity in the $^3$MLCT region of Ru(II) dyes (Figure 7-1).[36] Figure 7-3-1-6(a) compares these results with those of **$V^{IV}$-POM**. Interestingly, in the HCl aqueous solution of **$Mn^{II}$-POM**, **$Zr^{4+}$-DSP** exhibited almost the same activity as that in the **$V^{IV}$-POM** solution with phosphate buffer. In the XRF spectrum of the sample obtained after the reaction (Figure 7-3-1-6 (b)), Mn Kα radiation at 5.9 keV, which was attributed to the **Mn-POM** species, was clearly observed in addition to W Lα radiation, indicating the immobilization of **Mn-POM** to the **$Zr^{4+}$-DSP** surface, as was the case with **V-POM**. These two results indicate that **Mn-POM** species were immobilized on the **$Zr^{4+}$-DSP** surface during the photocatalytic reaction, which, however, did not decrease the photocatalytic activity. This is because the energy transfer quenching by **$Mn^{II}$-POM** is negligible. It was expected that the photocatalytic activity of **$Zr^{4+}$-DSP** would be enhanced by the immobilization of **$Mn^{II}$-POM** because of the effective electron donation to the one-electron-oxidized Ru dye. However, the estimated PS TON and AQY values were almost comparable to those of **$Zr^{4+}$-DSP** in the phosphate buffer solution, thereby preventing the surface immobilization of POM species as discussed above (Table 7-3-1-1). This was attributed to the low immobilization amount of the sterically bulky **$Mn^{II}$-POM**, as suggested by the XRF spectrum, that is, only 6% of the $Zr^{4+}$ sites were occupied by the Mn-POM species.

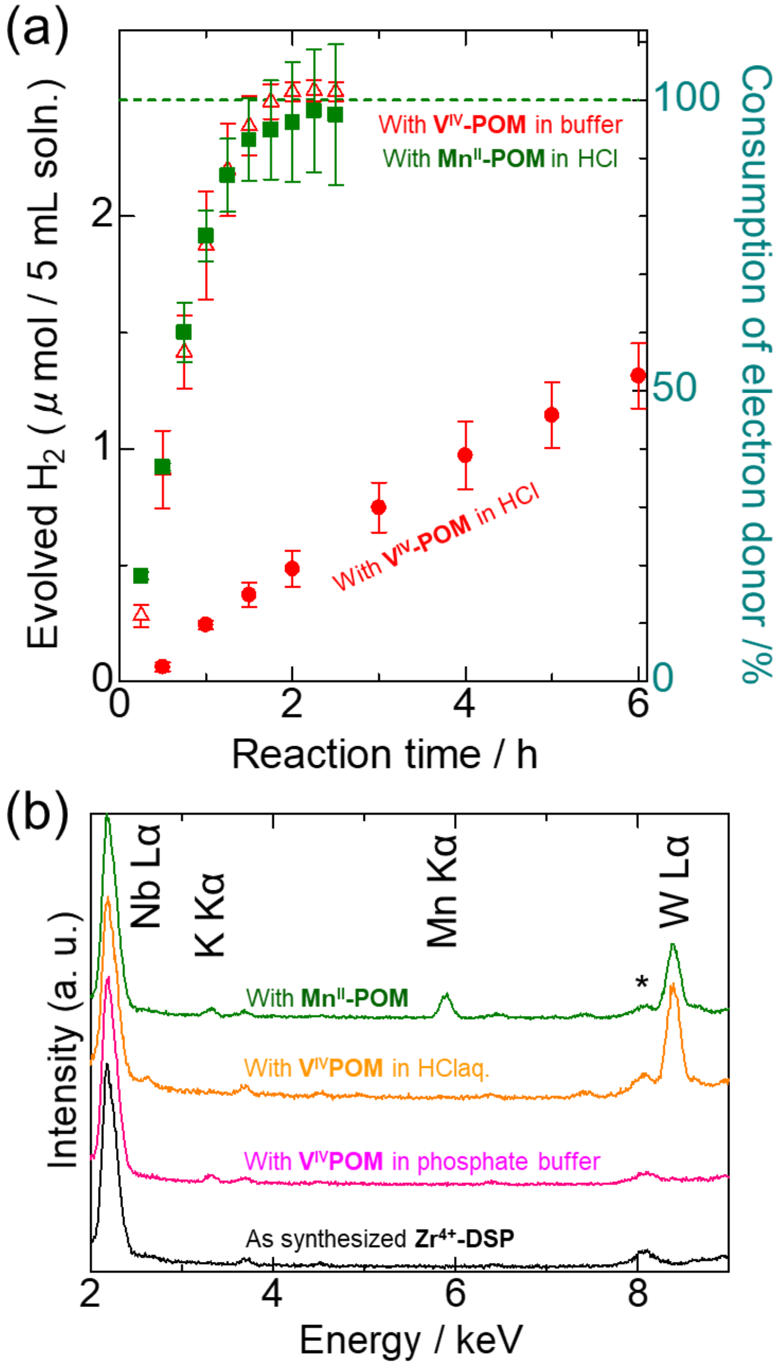

**Figure 7-3-1-6.** (a) Comparison of the photocatalytic $H_2$ evolution reaction driven by **$Zr^{4+}$-DSP** in the presence of 1 mM **$Mn^{II}$-POM** as the electron donor in HCl aqueous solution (initial pH = 3.0) under blue light irradiation (λ = 460 ± 15 nm; 70 mW) with that of **$Zr^{4+}$-DSP** in HCl or phosphonate buffer aqueous solutions with 1 mM **$V^{IV}$-POM** electron donor. (b) XRF spectra of **$Zr^{4+}$-DSP** obtained by centrifugation of the reaction solutions after photocatalytic hydrogen evolution reaction at 298 K under vacuum. All spectra were normalized with the intensity of the Nb Lα peak. The marked peak (*) is due to the background of the Cu sample holder.

## 7-4 Conclusion

In this work, the photocatalytic activity of two surface-modified dye-sensitized photocatalysts, **$H^+$-DSP** and **$Zr^{4+}$-DSP**, were evaluated in the presence of $[SiV^{IV}W_{11}O_{40}]^{6-}$ or $[SiMn^{II}W_{11}O_{39}(H_2O)]^{6-}$ (**$V^{IV}$-POM** or **$Mn^{II}$-POM**, respectively) as the RRED to find an effective interaction for one-way electron transfer from the electron mediator to the photocatalyst. **$H^+$-DSP**, comprising phosphonate groups on the photocatalyst surface, exhibited complete one-electron oxidation of **$V^{IV}$-POM** with 0.39% apparent quantum yield in the initial hour (*i*AQY) in both HCl and phosphate buffer aqueous solutions, even in the low concentration of 1 mM **$V^{IV}$-POM**. This *i*AQY value was comparable to that in higher concentrations of less charged RREDs (0.5 M $I^-$ and 16.4 mM $[Co(bpy)_3]^{2+}$), suggesting that stronger electrostatic interaction between the highly and negatively charged POM and photocatalyst surface can promote the forward electron transfer process. In contrast, the *i*AQY of **$Zr^{4+}$-DSP** in HCl aq was only 0.05%, owing to energy transfer deactivation by the surface-immobilized **$V^{IV}$-POM**, whereas almost the same activity (*i*AQY = 0.39%) was retained in the phosphate buffer solution. This deactivation process was further supported by the result that **$Zr^{4+}$-DSP** maintained almost the same activity in the HCl aq solution when **$V^{IV}$-POM** was replaced by the visible-light-transparent **$Mn^{II}$-POM**, which was also immobilized on the **$Zr^{4+}$-DSP** surface. These results suggest that to achieve efficient one-way electron transfer at the photocatalyst–mediator interface it is crucial to (1) ensure the driving force for the forward electron transfer and (2) eliminate non-favorable energy transfer quenching. Specifically, the accumulation of visible-light-transparent electron donors on the $H_2$ evolving photocatalyst surface should be a promising method for efficient one-directional electron transfer in the Z-scheme water splitting system.

## 7-5 References

1. S. Acharya, D.K. Padhi, K. M. Parida. *Catal. Today* **2020**, *353*, 220-231.
2. M. Graetzel. *Acc. Chem. Res*. **1981**, *14*, 376-384.
3. Y. Ma, X. Wang, Y. Jia, X. Chen, H. Han, C. Li. *Chem. Rev*. **2014**, *114*, 9987-10043.
4. A. Kudo, Y. Miseki.*Chem. Soc. Rev.* **2009**, *38*, 253-278.
5. X. Fang, S. Kalathil, E. Reisner.*Chem. Soc. Rev.* **2020**, *49*, 4926-4952.
6. A. Nakada, S. Nishioka, J. J. Vequizo, K. Muraoka, T. Kanazawa, A. Yamakata, S. Nozawa, H. Kumagai, S. Adachi, O. Ishitani, K. Maeda. *J. Mater. Chem. A* **2017**, *5*, 11710-11719.
7. M. J. Fang, C. Tsao, Y. J. Hsu. *J. Phys. D: Appl. Phys.* **2020**, *53*, 143001-143033.
8. H. Kumagai, R. Aoyagi, K. Kato, A. Yamakata, M. Kakihata, H. Kato. *ACS Appl. Energy Mater.* **2021**, 2056-2060.
9. Q. Wang, T. Hisatomi, Q. X. Jia, H. Tokudome, M. Zhong, C. Z. Wang, Z. H. Pan, T. Takata, M. Nakabayashi, N. Shibata, Y. B. Li, I. D. Sharp, A. Kudo, T. Yamada, K. Domen. *Nat. Mater.* **2016**, *15*, 611-615.
10. Y. Zhang, J. Qi, Y. Kong, Y. Zhao, S. Chen, D. Li, W. Liu, Y. Chen, T. Xie, J. Cui, K. Domen, F. Zhang. *Nat. Commun*. **2022**, *13*, 484.
11. R. Abe, K. Shinmei, N. Koumura, K. Hara, B. Ohtani. *J. Am. Chem. Soc*. **2013**, *135*, 16872-16884.
12. R. Abe, K. Shinmei, K. Hara, B. Ohtani. *Chem. Commun*. **2009**, *2009*, 3577-3579.
13. R. Abe, K. Sayama. *J. Photochem. Photobiol., A* **2004**, *166*, 115-122.
14. E. S. D. Silva, N. M. M. Moura, G. P. M. S. Neves, A. Coutinho, M. Prieto, C. G. Silva, J. Faria. *Appl. Catal., B* **2018**, *221*, 56-59.
15. J. Warnan, J. Willkomm, J. N. Ng, R. Godin, S. Prantl, J. R. Durrant, E. Reisner. *Chem. Sci.* **2017**, *8*, 3070-3079.
16. A. M. Deetz, G. J. Meyer. *JACS Au* **2022**, *2*, 985–995.
17. L. T. Gautier, M. D. Turlington, S. A. M. Wehlin, A. B. Maurer, M. D. Brady, W. B. Swords, G. J. Meyer. Chemistry *Chem. Rev*. **2019**, *119*, 4628-4683.
18. H. Kusama, T. Funaki, N. Koumura, K. Sayama. *Phys. Chem. Chem. Phys.* **2014**, *16*, 16166-16175.
19. H. Kusama. *J. Photochem. Photobiol., A* **2018**, *365*, 110-118.
20. L. Zhao, P. Wagner, H. Salm, K. C. Gordon, S. Mori, A. J. Mozer. *ACS Appl. Mater. Interfaces* **2015**, *7*, 22078–22083.
21. W. Wang, J. Chen, C. Li, W. Tian. *Nat. Commun.* **2014**, *5*, 4647-4654.
22. J. Lee, D. Won, W. Jung, H. Son, C. Pac, S. O. Kang. *Angew. Chem., Int. Ed.* **2017**, *56*, 976-980.
23. E. Aslan, M. K. Gonce, M. Z. Yigit, A. Sarilmaz, E. Stathatos, F. Ozel, M. Can, I. H. Patir. *Appl. Catal., B* **2017**, *220*, 320-327.

24. A. Tiwari, N. V. Krishna, L. Giribabu, U. Pal. *J. Phys. Chem. C* **2018**, *122*, 495-502.
25. F. Yu, S. Cui, X. Li, Y. Peng, Y. Yu, K. Yun, S. Zhang, J. Li, J. Liu, J. Hua. *Dyes Pigm.* **2017**, *139*, 7-18.
26. Y. Sun, Y. Sun, C. Dall'Agnese, X. Wang, G. Chen, O. Kitao, H. Tamiaki, K. Sakai, T. Ikeuchi, S. Sasaki. *ACS Appl. Energy Mater.* **2018**, *1*, 2813-2820.
27. T. Oshima, S. Nishioka, Y. Kikuchi, S. Hirai, K. Yanagisawa, M. Eguchi, Y. Miseki, T. Yokoi, T. Yui, K. Kimoto, K. Sayama, O. Ishitani, T. E. Mallouk, K. Maeda. *J. Am. Chem. Soc.* **2020**, *142*, 8412-8420.
28. A. Nakada, T. Uchiyama, N. Kawakami, S. Nishioka, R. Kamata, H. Kumagai, O. Ishitani, Y. Uchimoto, K. Maeda. *ChemPhotoChem* **2019**, *3*, 37-45.
29. M. V. Sheridan, Y. Wang, D. Wang, L. T. Gautier, C. J. Dares, B. D. Sherman, T. J. Meyer. *Angew. Chem. Int. Ed.* **2018**, *57*, 3449-3453.
30. N. Yoshimura, A. Kobayashi, M. Yoshida, M. Kato. *Bull. Chem. Soc. Jpn*. **2019**, *92*, 1793-1800.
31. N. Yoshimura, A. Kobayashi, W. Genno, T. Okubo, M. Yoshida, M. Kato. *Sustainable Energy Fuels* **2020**, *4*, 3450-3457.
32. N. Yoshimura, A. Kobayashi, M. Yoshida, M. Kato. *Chem. Eur. J*. **2020**, *26*, 16939-16946.
33. N. Yoshimura, M. Yoshida, M. Kato, A. Kobayashi. *Inorg. Chem*. **2022**, *61*, 11095-11102.
34. S. Nishioka, K. Hojo, L. Xiao, T. Gao, Y. Miseki, S. Yasuda, T. Yokoi, K. Sayama, T. E. Mallouk, K. Maeda. *Sci. Adv*. **2022**, *8*, 9115.
35. N. Yoshimura, A. Kobayashi, T. Kondo, R. Abe, M. Yoshida, M. Kato. *ACS Appl. Energy Mater.* **2021**, *4*, 14352-14362.
36. O. Tomita, H. Naito, A. Nakada, M. Higashi, R. Abe. *Sustainable Energy Fuels* **2022**, *6*, 664-673.
37. Y. Iwase, O. Tomita, H. Naito, M. Higashi, R. Abe. *J. Photochem. Photobiol., A* **2018**, *356*, 347-354.
38. K. Tsuji, O. Tomita, M. Higashi, R. Abe. *ChemSusChem* **2016**, *9*, 2201-2208.
39. J. Lei, J. Yang, T. Liu, T.; R. Yuan, D. Deng, M. Zheng, J. Chen, L. Cronin, Q. Dong. *Chem. Eur. J.* **2019**, *25*, 11432-11436.
40. Y. B. M'Barek, T. Rosser, J. Sum, S. Blanchard, F. Volatron, G. Izzet, R. Salles, J. Fize, M. Koepf, M. Chavarot-Kerlidou, V. Artero, A. Proust. *ACS Appl. Energy Mater.* **2020**, *3*, 163-169.
41. H. E. Moll, F. A. Black, C. J. Wood, A. Al-Yasari, A. Marri, I. V. Sazanovich, E. A. Gibson, J. Fielden. *Phys. Chem. Chem. Phys.* **2017**, *19*, 18831-18835.
42. H. Cruz, A. L. Pinto, J. C. Lima, L. C. Branco, S. Gago. *Mater. Lett.* **2020**, *6*, 100033-100038.
43. Y. Zhang, J. Liu, S. Li, Z. Su, Y. Lan. *Energy Chem.* **2019**, *1*, 100021-100078.

44. K. Hanson, M. K. Brennaman, A. Ito, H. Luo, W. Song, K. A. Parker, R. Ghosh, M. R. Norris, C. R. K. Glasson, J. J. Concepcion, R. Lopez, T. J. Meyer. *J. Phys. Chem. C* **2012**, *116*, 14837-14847.
45. S. Furugori, A. Kobayashi, A. Watanabe, M. Yoshida, M. Kato. *ACS Omega* **2017**, *2*, 3901-3912.

# Chapter 8

# Efficient Hydrogen Production by Photo-redox-cascade Catalyst Composing Dual Photosensitizers and Transparent Electron Mediator

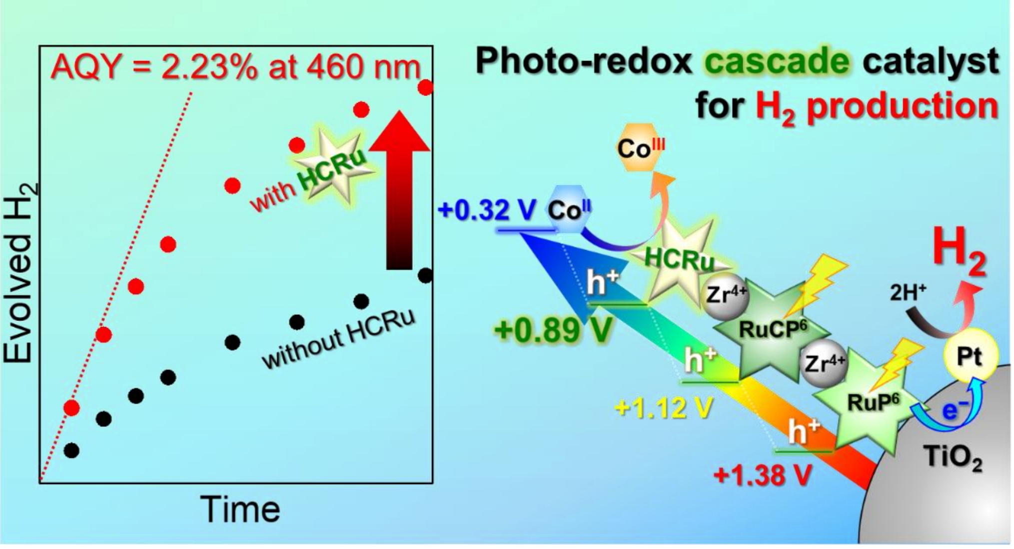

## 8-1 Introduction

A photocatalytic water splitting has attracted considerable attention as a promising reaction to solve the global warming and energy crises.[1-6] Two-step photoexcitation (Z-scheme) water-splitting photocatalysis composing water oxidation and reduction catalysts (WOC and WRC) with redox mediator (RM) is a powerful strategy not only to convert wide range of solar energy to the chemical energy stored in $H_2$ and $O_2$ but also to ensure the enough potentials for both water splitting and the electron transfer reactions.[7-13] For example, Domen *et. al.* recently reported that the visible-light-driven Z-scheme photocatalytic system consisting from the Ir-$FeCoO_x$, $BiVO_4$ and $[Fe(CN)_6]^{3-/4-}$ as WRC, WOC and RM, respectively, exhibited remarkably high solar-to-hydrogen energy conversion efficiency (STH = 0.6%) and apparent quantum efficiency (AQY = 12.3%) at 420 nm.[14] However, thermodynamically favorable back reactions at the WOC-RM-WRC interfaces are still bottle-neck issue to be overcome. Thus, a new strategy to regulate the electron transfer direction from WOC to WRC via RM is strongly required.[15-17]

In natural photosynthesis, such the back reactions are efficiently suppressed by the multistep photo-redox cascade structure in the electron transport chain constructed by precisely arraying of chlorophyl- and quinone-type RMs around the reaction center, the chlorophyl dimer (P680 and P700).[18]

In this work, with the aim of suppressing the back reactions at WRC-RM interface, a three-step photo-redox cascade structure on the surface of hydrogen evolution nanoparticle catalyst (Pt-$TiO_2$) was newly constructed by assembling two Ru(II) molecular photosensitizers (**RuP$^6$** and **RuCP$^6$**) and visible-light-transparent electron mediator (**HCRu**) to synthesize a photo-redox cascade catalyst,[19] **PRCC-1** (Figure 8-1; **PRCC-1 = HCRu**-Zr-**RuCP$^6$**-Zr-**RuP$^6$**@Pt-$TiO_2$; **HCRu** = $[Ru(CN)_6]^{4-}$, **RuCP$^6$** = $[Ru(mpbpy)_3]^{10-}$, **RuP$^6$** = $[Ru(pbpy)_3]^{10-}$, $H_4$mpbpy = 2,2′-bipyridine-4,4′-bis(methane-phosphonic acid), and $H_4$pbpy = 2,2′-bipyridine-4,4′-bis(phosphonic acid)).[20] Herein, it was reported that **PRCC-1** exhibited the highest apparent quantum yield in the initial 1 h irradiation (*i*AQY = 2.23%) among the dye-sensitized $TiO_2$ photocatalysts in the presence of $[Co(bpy)_3]^{2+}$ redox-reversible electron donor (RrED). Further, it was found that the photocatalytic hydrogen production from hydroquinone sulfonate as the hydrogen atom mediator was achieved by **PRCC-1**.

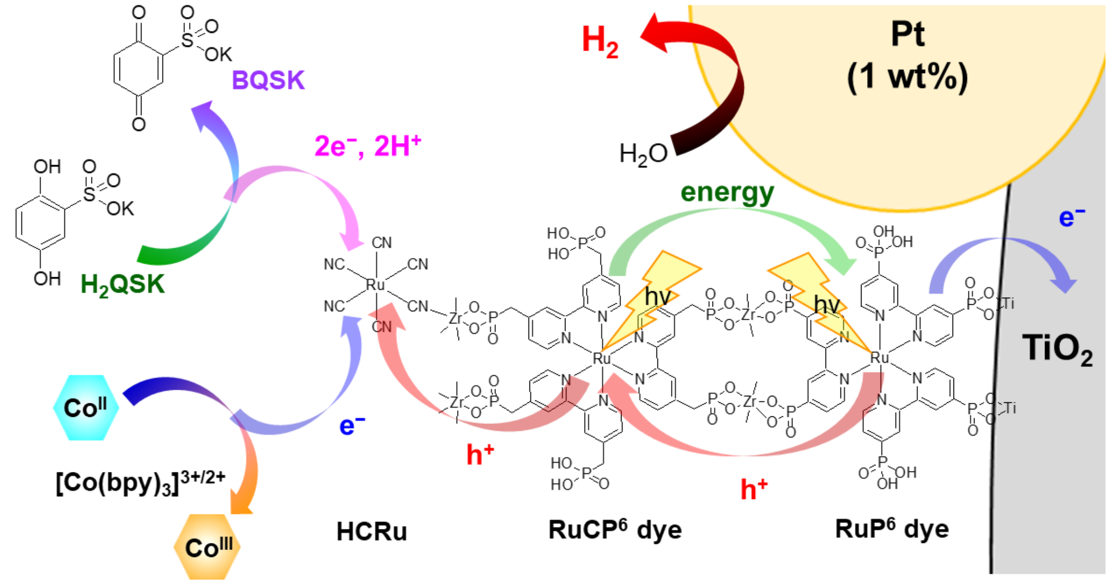

**Scheme 8-1**. Schematic illustration of **X-DSP**s and two redox-reversible POM anions.

## 8-2 Experimental

### 8-2-1 Synthesis and measurements

**Preparation of Ru(II)-dye-immobilized Pt-$TiO_2$ nanoparticles**

Three types of Ru(II)-dye-immobilized Pt-$TiO_2$ nanoparticles, Zr-**RuCP$^6$**-Zr-**RuP$^6$**@Pt-$TiO_2$ (**DDSP**), **HCRu**-Zr-**RuCP$^6$**-Zr-**RuP$^6$**@Pt-$TiO_2$ (**PRCC-1**), and **HCFe**-Zr-**RuCP$^6$**-Zr-**RuP$^6$**@Pt-$TiO_2$ (**PRCC-2**) were synthesized by previous procedure for Ru(II)-dye-immobilized Pt-$TiO_2$ nanoparticles with several modification as follows.

I. Immobilization of the first Ru(II) dye layer. 30 mg of Pt-$TiO_2$ nanoparticles were added and dispersed in 1.25 mM **RuP$^6$** solution (6 mL). A 50 μL of 60%$HClO_4$ aq. solution was added to the dispersion solution and stirred overnight at 293 K in dark condition. The Ru(II)-dye-immobilized Pt-$TiO_2$ nanoparticles were isolated by ultracentrifugation (50,000 rpm, 15-20 min) and then twice washed with 0.1 M $HClO_4$ aq. The **RuP$^6$**@Pt-$TiO_2$ were obtained by drying under air for several days at 293-343 K.

II. Immobilization of $Zr^{4+}$ cations to the phosphonates of Ru(II) dyes. The well dried **RuP$^6$**@Pt-$TiO_2$ nanoparticles were dispersed in 6 mL of MeOH solution of 50 mM $ZrCl_2O \cdot 8H_2O$ and stirred for 1 h at 293 K in dark condition. The dispersed nanoparticles were collected by ultracentrifugation (50,000 rpm, 20-25 min) washed twice with MeOH, and then dried under air for several days to afford the orange-colored Zr-**RuP$^6$**@Pt-$TiO_2$.

III. Immobilization of the second Ru(II)-dye layer. The second immobilization of Ru(II) dye was performed in the almost the same procedure to that used for the first layer immobilization as mentioned above by using Zr-**RuP$^6$**@Pt-$TiO_2$ nanoparticles instead of Pt-$TiO_2$. The Zr-**RuP$^6$**@Pt-$TiO_2$ nanoparticles were dispersed in 1.25 mM **RuCP$^6$** solution (6 mL) and then acidified by addition of a 50 μL of 60%$HClO_4$ aq. solution. After stirring overnight at 293 K in dark condition, the dispersed nanoparticles were isolated by ultracentrifugation (50,000 rpm, 15-20 min) and then twice washed with 0.1 M $HClO_4$ aq. The **RuCP$^6$**-Zr-**RuP$^6$**@Pt-$TiO_2$ nanoparticles were obtained by drying under air for several days at 293-343 K. Further treatment of **RuCP$^6$**-Zr-**RuP$^6$**@Pt-$TiO_2$ nanoparticles with $ZrCl_2O \cdot 8H_2O$ MeOH solution as mentioned above (see II. Immobilization of $Zr^{4+}$ cations to the phosphonates of Ru(II) dyes) was performed to form the $Zr^{4+}$-cation modified Ru(II)-dye-double-layered nanoparticle Zr- **RuCP$^6$**-Zr-**RuP$^6$**@Pt-$TiO_2$ (**DDSP**).

IV. Immobilization of $[M(CN)_6]^{4-}$ (**HCM**, M = $Ru^{2+}$ or $Fe^{2+}$). The well dried Zr-**RuCP**$^6$-Zr-**RuP**$^6$@Pt-$TiO_2$ (**DDSP**) nanoparticles were dispersed in 5 mL of aqueous solution of 30 μM $K_4[M(CN)_6]$ (M = $Ru^{2+}$ or $Fe^{2+}$). A 50 μL of 36% HClaq (12 M) were added and stirred for 1 h at 293 K in dark condition. The dispersed nanoparticles were collected by ultracentrifugation (50,000 rpm, 20-25 min) washed twice with 100 times diluted 34% HClaq (approximately 0.1 M), and then dried under air for several days to afford the orange-colored **HCM**-Zr-**RuCP**$^6$-Zr-**RuP**$^6$@Pt-$TiO_2$ (**PRCC-1** and **PRCC-2**).

The immobilized amounts of Ru(II) dyes were estimated by the UV-Vis absorption spectrum of each supernatant solution isolated by the ultracentrifugation of Ru(II) dye immobilization reaction (see **Figure 8-2-1** and **Table 8-2-1**). The immobilization amounts of **HCM** were estimated by the XRF spectrum of each sample (see **Figure 8-2-2** and **Table 8-2-2**). All used measurement equipment were the same as described in chapter 6-2.

**Table 8-2-1.** Absorbance of each supernatant solution and the calculated $C_B$ and $M_i$ values about **RuCP**$^6$-Zr-**RuP**$^6$@Pt-$TiO_2$.

| Photo-catalyst | Immobilized Ru(II) PS | $A$ ($M^{-1}cm^{-1}$) | $C_B$ (mM) | $M_i$ (μmol / 30 mg $TiO_2$) | Surface coverage $N$ (nmol / $cm^2$) |
|---|---|---|---|---|---|
| This work | 1st (inner) layer **RuP**$^6$ | 0.335 | 0.855 | 2.33 | 0.0755 |
| | 2nd (outer) layer **RuCP**$^6$ | 0.201 | 0.688 | 3.34 | 0.104 |
| Previous work[R1] | 1st (inner) layer **RuP**$^6$ | 0.324 | 0.826 | 2.50 | 0.0810 |
| | 2nd (outer) layer **RuCP**$^6$ | 0.206 | 0.705 | 3.23 | 0.101 |

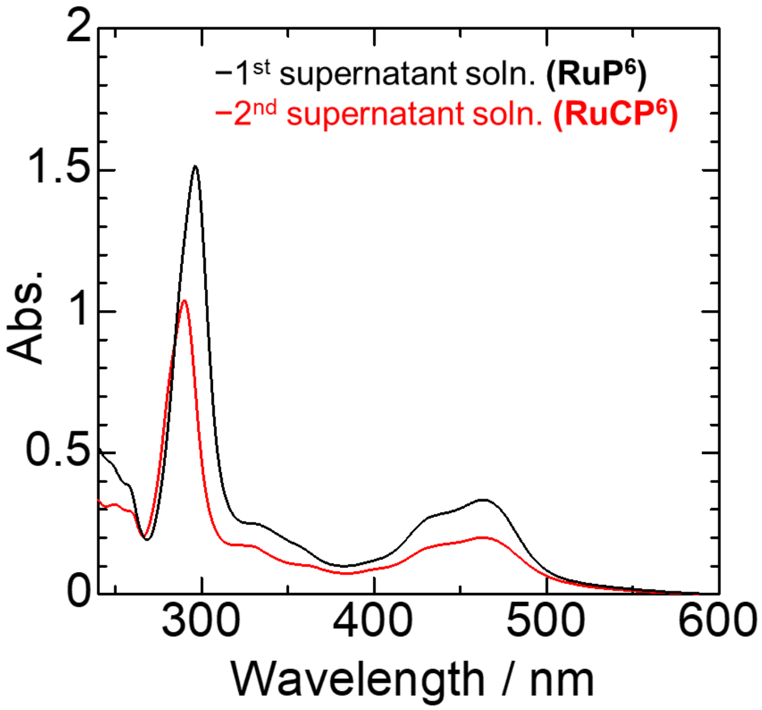

**Figure 8-2-1.** UV-Vis absorption spectra of the supernatant solutions at 298 K.

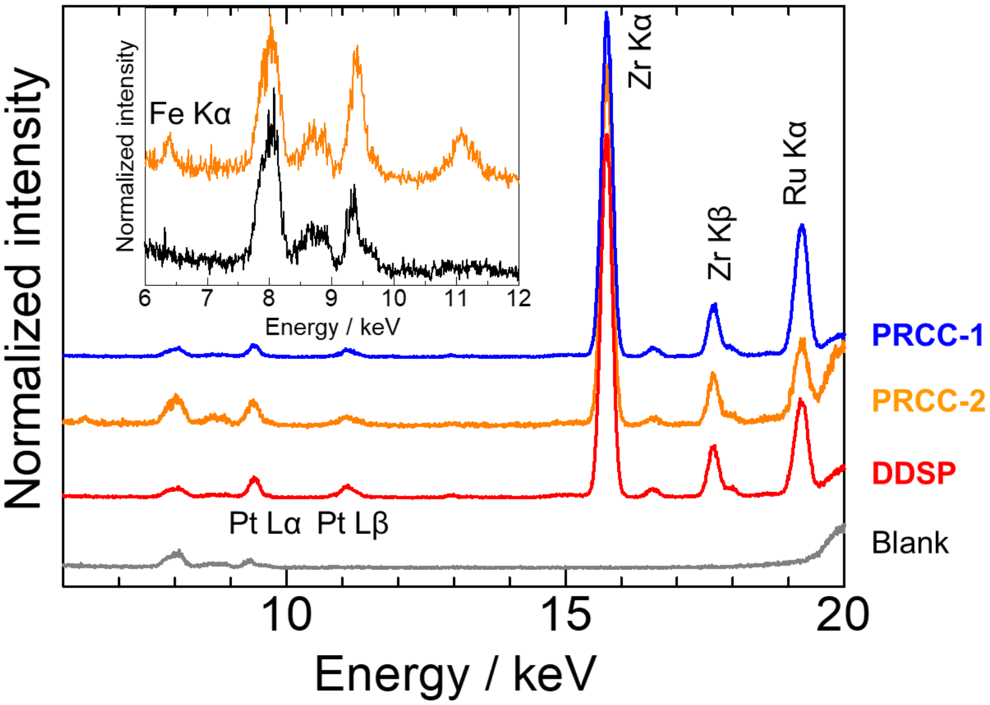

**Figure 8-2-2**. XRF spectra of (blue) **PRCC-1**, (orange) **PRCC-2**, and (red) **DDSP** in the solid state at 293 K, under vacuum. Black line describes the baseline.

**Table 8-2-2**. Estimated metal ion ratio of Ru(II)-PS-multilayered Pt-TiO$_2$ nanoparticles by XRF spectra shown in Figure 8-2-2.

| Photocatalyst<br>**X'-DSP** | Metal ion ratio (mol/mol) | | Molar ratio of HCM to RuCP$^6$ (mol/mol) |
|---|---|---|---|
| | Ru/Zr | Fe/Zr | HCM/**RuCP$^6$** |
| **DDSP** | 0.49(2) | - | - |
| **PRCC-2** | 0.45(2) | 0.37(3) | 1.34(8) |
| **PRCC-1** | 0.70(3) | - | 0.8(2) |

### 8-2-2 Photocatalytic hydrogen evolution reaction condition

A 0.5 M or 16.4 mM of [Co(bpy)$_3$]SO$_4$, or 0.5 M of hydroquinonesulfonate potassium salt (H$_2$QSK) as redox reversible electron donor with HCl aqueous solution (pH = 2). The other conditions were the same as chapter 6-2.

## 8-3 Results and discussions

**PRCC-1** was synthesized by immersion of the dual-dye-sensitized photocatalyst (**DDSP** = Zr-**RuCP**$^{6}$-Zr-**RuP**$^{6}$@Pt-$TiO_2$)[21] to the **HCRu** aqueous solution (see the supporting information for details). The observed stronger Ru Kα peak of **PRCC-1** in X-ray fluorescence (XRF) spectrum than that of **DDSP** suggests the successful immobilization of electron mediating **HCRu** to the surface $Zr^{4+}$ sites of **DDSP** (Figure 8-2-2 and Table 8-2-2). In 16.4 mM $[Co(bpy)_3]SO_4$ aqueous solution, **PRCC-1** produced approximately 1.9 times larger hydrogen and turn over number per one PS after 6 h irradiation (PS TON) than **DDSP** (Table 8-3-1, Figure 8-3-1).

**Table 8-2-2**. Results of photocatalytic $H_2$ evolution experiments in HCl aqueous solution (pH = 2).

| Photocatalyst | Electron donor | $H_2$ (μmol) (0-6h) | PS TON$^{b}$ (0-6h) | PS initial TOF$^{c}$ | AQY$^{a}$ (%) (0-6h) | *i*AQY$^{a}$ (%) (0-1h) |
|---|---|---|---|---|---|---|
| **DDSP** | $[Co(bpy)_3]SO_4$ = 16.4 mM | 15.2±1.6 | 60.7 | 18.7 | 0.523 | 0.963 |
| **PRCC-1** | $[Co(bpy)_3]SO_4$ = 16.4 mM | 28.9±2.4 | 116 | 43.3 | 0.994 | 2.23 |
| **PRCC-2** | $[Co(bpy)_3]SO_4$ = 16.4 mM | 11.9±0.4 | 47.8 | 11.9 | 0.409 | 0.613 |
| **PRCC-1** after washed with water | $[Co(bpy)_3]SO_4$ = 16.4 mM | 27.1 | 108 | 34.4 | 0.932 | 1.77 |
| **PRCC-1** after washed with water twice | $[Co(bpy)_3]SO_4$ = 16.4 mM | 24.3 | 97.1 | 27.5 | 0.836 | 1.42 |
| **DDSP** | $H_2QSK$ = 0.5 M | 8.33±0.95 | 33.3 | 10.1 | 0.280 | 0.519 |
| **PRCC-1** | $H_2QSK$ = 0.5 M | 12.6±1.6 | 50.5 | 21.3 | 0.433 | 1.10 |
| **PRCC-1** | $H_2QSK$ = 16.4 mM | 7.47±0.48 | 29.9 | 6.71 | 0.257 | 0.346 |

[a] Measurement condition: [Ru-PS] = 100 μM in total, Electron donor = 1 mM, Volume = 5 mL aqueous solution, $\lambda_{ex}$ = 460 ± 15 nm, 70 mW in total. The reaction solution was purged by Ar bubbling for 1 h before light irradiation. The numeral values were average of more than 3 times experiment. Definition: PS = photosensitizer, PS TON = turn over number of PS, PS initial TOF = turn over frequency of PS at initial 1 h irradiation (from 0 h to 1 h), *i*AQY = apparent quantum efficiency at initial 1 h, HQSK = hydroquinone sulfonate potassium.

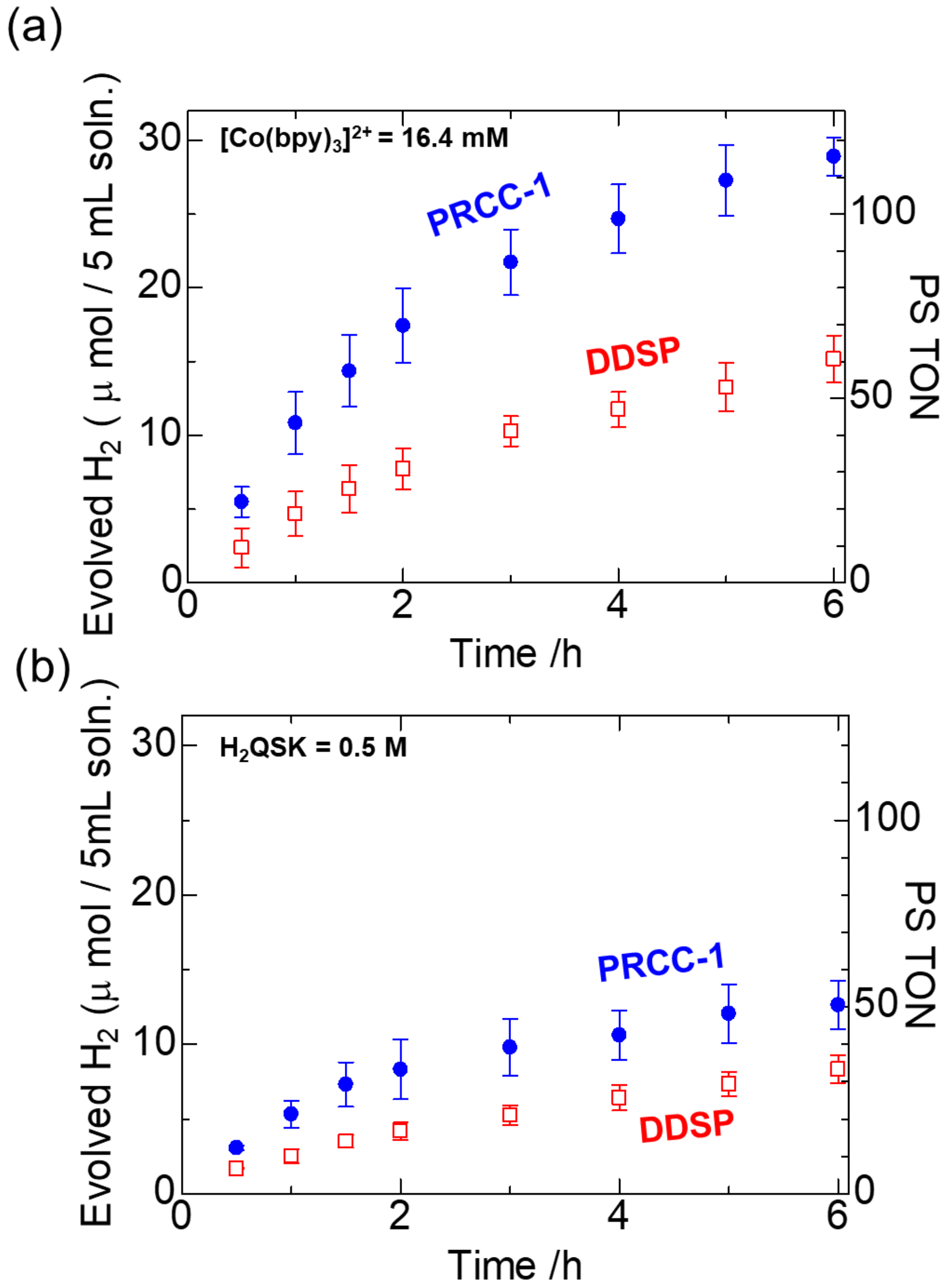

**Figure 8-3-1**. Photocatalytic $H_2$ evolution reactions driven by (blue closed circle) **PRCC-1** and (red open square) **DDSP** in the presence of (a) 16.4 mM $[Co(bpy)_3]SO_4$ and (b) 0.5 M $H_2QSK$ as the electron donor in HCl aqueous solution. Ru(II) dye concentration of all the reactions were adjusted to 100 μM. Initial pH of all the solutions was adjusted to 2.0 by adding HCl (λ = 460 ± 15 nm; 70 mW).

Surprisingly, the estimated *i*AQY value for **PRCC-1** reached 2.23% that is the highest record in the dye-sensitized $TiO_2$ photocatalysts with RrED so far. Note that the total amount of Ru(II) dye in each solution was constant (100 μM) and no hydrogen evolution was observed in the absence of Ru(II) dye, light (Table 8-3-2). On the other hand, **PRCC-1** exhibited hydrogen evolution without electron donor whereas **DDSP** did not. PS TON in this no electron donor condition was only approximately 0.3, suggesting that approximately 20~30% of **HCRu** was one-electron oxidized as electron source of hydrogen evolution.

**Table 8-3-2**. Control experiments of photocatalytic hydrogen evolution of **PRCC-1** and **DDSP**.

| Entry [a] | Photocatalyst | Electron Donor (ED) | Light irradiation | Evolved $H_2$ [b] |
|---|---|---|---|---|
| 1 | **PRCC-1** | $[Co(bpy)_3]SO_4$ | Yes | Yes |
| 2 | **DDSP** | $[Co(bpy)_3]SO_4$ | Yes | Yes |
| 3 | **PRCC-1** | $[Co(bpy)_3]SO_4$ | No | - |
| 4 | **PRCC-1** | None | Yes | Yes |
| 5 | **DDSP** | None | Yes | - |
| 6 | **PRCC-1** | HQSK | No | - |
| 7 [c] | - | $[Co(bpy)_3]SO_4$ | Yes | - |

[a] Reaction conditions: [Ru] = 100 μM in HCl aqueous solution (pH = 3, 5 mL) under blue LED light irradiation (λ = 460 ± 15 nm) for 6 h. [b] Gas in the head space was analyzed qualitatively by Gas Chromatography (GC). "Yes" indicates that the evolved amount of $H_2$ was larger than the GC detection limit. [c] No photocatalyst was used.

Considering that **HCRu** has more negative redox potential (Ru(III)/Ru(II) at +0.89 V vs. NHE)[19] than that of **RuCP⁶** PS (+1.12 V vs. NHE),[20] the improved *i*AQY of **PRCC-1** was probably due to the enhanced charge-separation between dual PS and RrED by electron mediating of **HCRu** from one-electron-oxidized **RuCP⁶**($h^+$) to $[Co(bpy)_3]^{2+}$ RrED (Scheme 8-1). In fact, photocatalytic $H_2$ evolution activity of **PRCC-1** gradually decreased by lowering the loading amount of **HCRu** (Figures 8-3-3, 8-3-4 and Table 8-3-3). Further, the analogue catalyst **PRCC-2** having $[Fe(CN)_6]^{4-}$ (**HCFe**) instead of **HCRu** of **PRCC-1** exhibited 36.3% lower hydrogen evolution activity than **DDSP** (Figure 8-3-5 and Table 8-3-1), probably because of the comparable the redox potential of **HCFe** (Fe(III)/Fe(II) at +0.36 V vs NHE)[22] and $[Co(bpy)_3]SO_4$ RrED (Co(III)/Co(II) at 0.32 V vs. NHE).[23] These results suggest that photo-redox cascade of **RuP⁶-RuCP⁶-HCRu** plays a key role of improving charge separation efficiency between PS and RM.

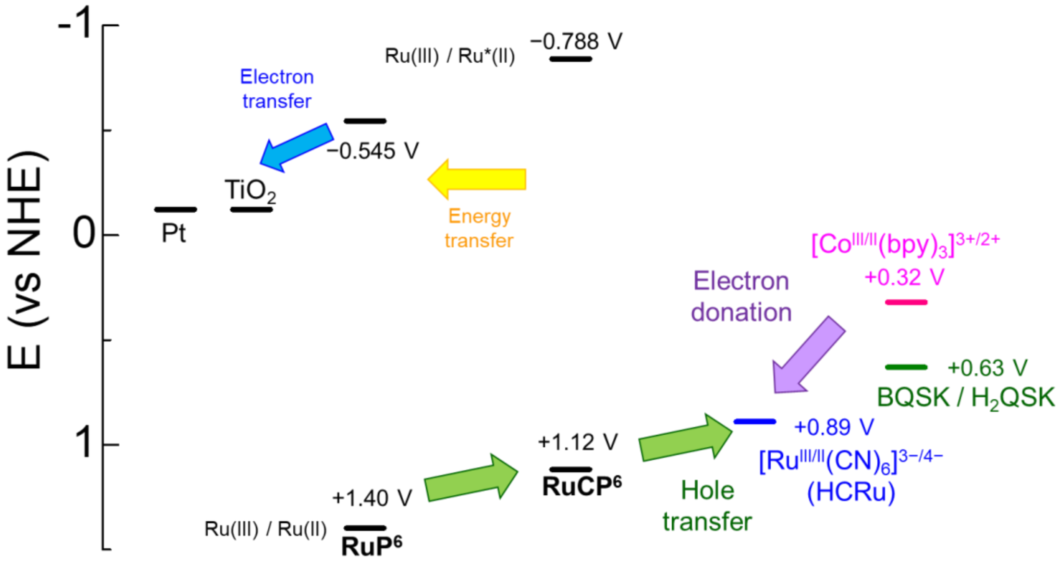

**Scheme 8-1**. Energy diagram of **PRCC-1** in HCl aqueous solution (pH = 2). The redox potential of BQSK / $H_2QSK$ was estimated by cyclic voltammograms measurement (Figure 8-3-2). The other redox potentials were interfered from the literature. [R2, R3, R4]

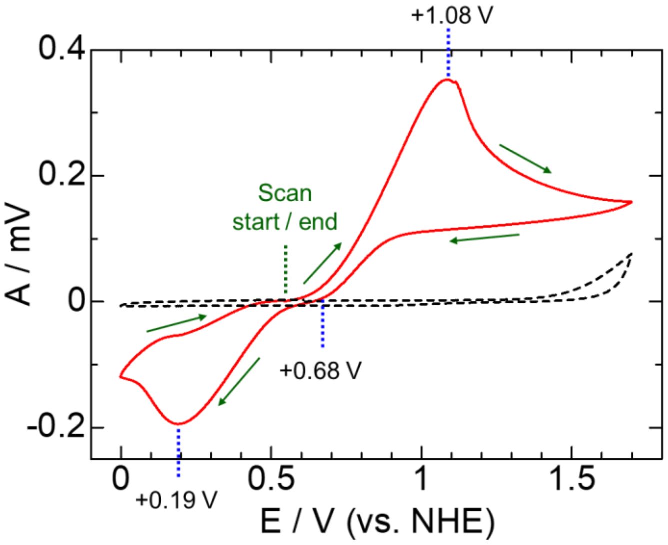

**Figure 8-3-2**. Cyclic voltammograms of 20 mM $H_2QSK$ (red solid line) in HCl aqueous solution (pH = 2). Glassy carbon, Pt wire and Ag/AgCl (in 3 M NaCl aq.) were used as the working, counter and reference electrodes, respectively. The black dashed line indicates the baseline. The scan rate was 50 mV/s.

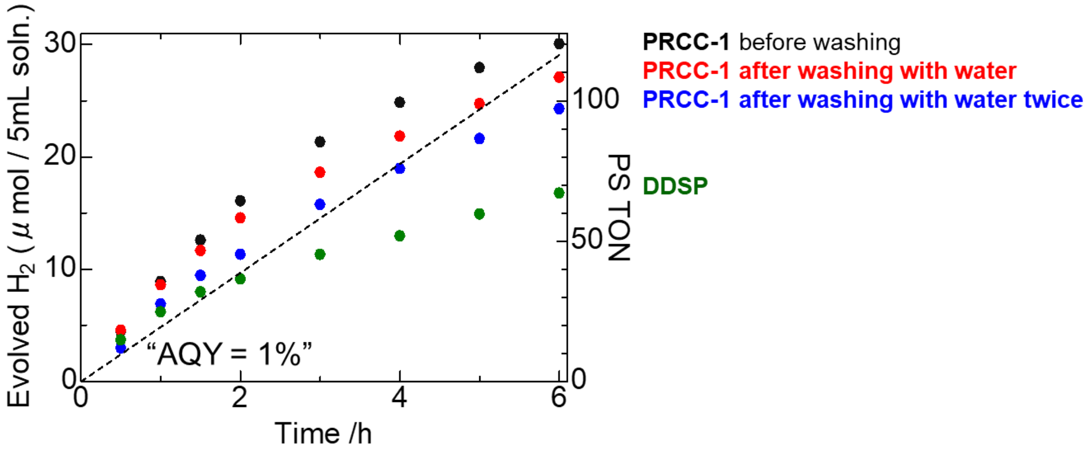

**Figure 8-3-3.** Photocatalytic $H_2$ evolution reactions driven by (black) **PRCC-1**, (red) **PRCC-1** after washing with water, (blue) **PRCC-1** after washing with water twice, and (green) **DDSP** in the presence of 16.4 mM $[Co(bpy)_3]SO_4$ as the electron donor in HCl aqueous solution (pH = 2). Ru(II) dye concentration of all reactions were adjusted to 100 μM. Initial pH of all solutions were adjusted to be 2.0 by adding HCl (λ = 460 ± 15 nm; 70 mW).

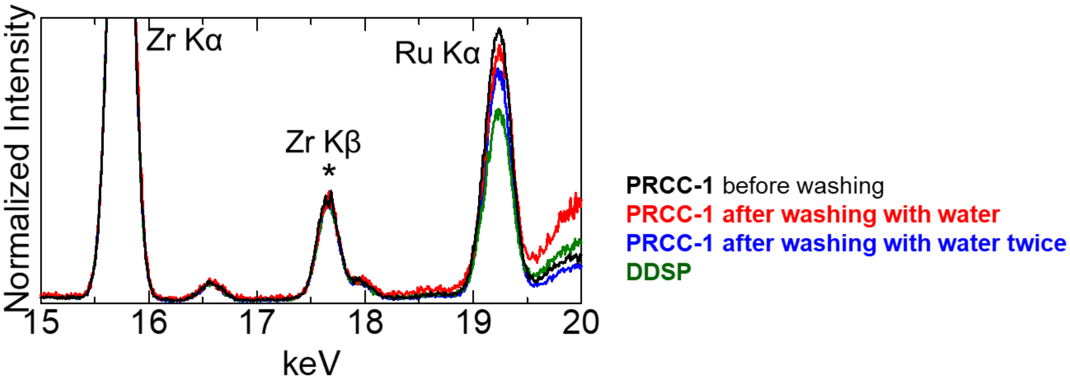

**Figure 8-3-4.** XRF spectra of (black) **PRCC-1**, (red) **PRCC-1** after washing with water, (blue) **PRCC-1** after washing with water twice, and (green) **DDSP** as synthesized in the solid state at 293 K under vacuum. The all spectra were normalized by Zr kβ line (* marked peak).

**Table 8-3-3** Results of analysis of XRF spectra described in Figure 8-3-4.

| Photocatalyst **X'-DSP** | Ru atom rate per Zr (mol/mol) | HCM rate per outer PS (mol/mol) |
|---|---|---|
| | Ru/Zr | HCM/**RuCP**$^6$ |
| **PRCC-1** before washing | 0.70(3) | 0.8(2) |
| **PRCC-1** after washing | 0.65(2) | 0.6(2) |
| **PRCC-1** after washing twice | 0.58(2) | 0.3(2) |
| **DDSP** | 0.49(2) | - |

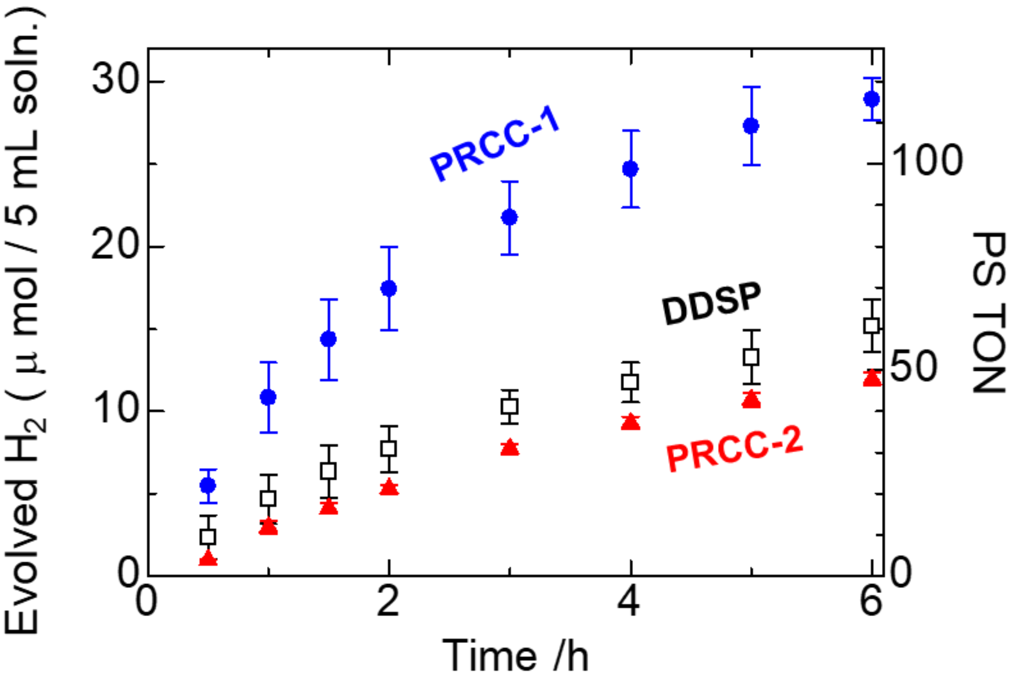

**Figure 8-3-5**. Photocatalytic $H_2$ evolution reactions driven by (blue) **PRCC-1**, (black) **DDSP**, and (red) **PRCC-2** in the presence of 16.4 mM $[Co(bpy)_3]SO_4$ as the electron donor in HCl aqueous solution (pH = 2). Ru(II) dye concentration of all reactions were adjusted to 100 μM. Initial pH of all solutions were adjusted to be 2.0 by adding HCl (λ = 460 ± 15 nm; 70 mW).

The photocatalytic activities of both photocatalysts during 6 h reaction decreased with time, probably because of the back electron transfer from photo-excited Ru*(II) PS to oxidized $[Co(bpy)_3]^{3+}$. However, it should be noteworthy that **PRCC-1** exhibited remarkably higher TON (1-2 h, PS TON = 26.4) than **DDSP** (3-4 h, PS TON = 5.9) when 5 mM one-electron oxidized $[Co(bpy)_3]^{2+}$ was produced. This result suggests that immobilization of **HCRu** EM is also effective for suppression of the back electron transfer from PS* to oxidized $[Co(bpy)_3]^{3+}$ RrED. **PRCC-1** produced about 40 μmol $H_2$ after 1d irradiation that suggests all $[Co(bpy)_3]^{2+}$ RrED (82 μmol) was one-electron oxidized (Figure 8-3-6). This is further supported by $^1H$ NMR spectroscopy in which the characteristic proton signals assignable to the diamagnetic one-electron oxidized $[Co(bpy)_3]^{3+}$ species were clearly observed (Figure 8-3-7). Notably, the molecular ratio of Ru/Zr estimated by XRF spectroscopy was hardly changed after the 1d irradiation, indicating that **HCRu** desorption from **PRCC-1** surface was negligible in the HCl aq. reaction condition (pH =2) (Figure 8-3-8 and Table 8-3-4).

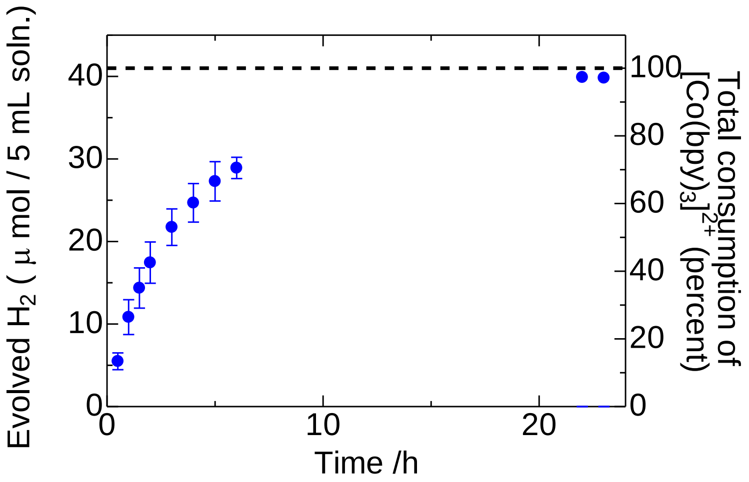

**Figure 8-3-6**. Long-term photocatalytic hydrogen evolution reaction driven by **PRCC-1** in the presence of 16.4 mM $[Co(bpy)_3]SO_4$ as the electron donor in HCl aqueous solution (pH = 2). Ru(II) dye concentration of all reactions were adjusted to 100 μM. Initial pH of all solutions were adjusted to be 2.0 by adding HCl (λ = 460 ± 15 nm; 70 mW).

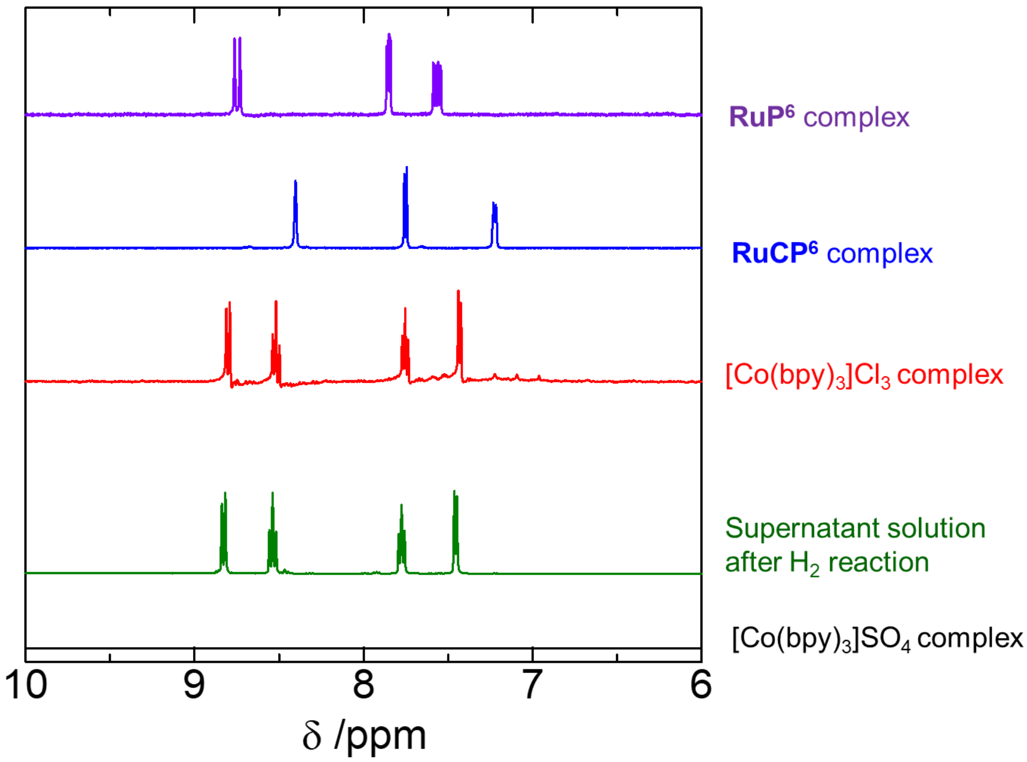

**Figure 8-3-7.** $^1$H NMR spectra of the supernatant obtained by centrifugation of the reaction solution after 23 h irradiation of **PRCC-1** with 16.4 mM $[Co(bpy)_3]SO_4$aq (HClaq, pH = 2, 5 mL) in $H_2O$ (green solid line). The purple line, blue line, red line, and black line is the spectrum of **RuP$^6$** complex in $D_2O$, **RuCP$^6$** complex in $D_2O$, $[Co(bpy)_3]Cl_3$ complex in $H_2O$, and $[Co(bpy)_3]SO_4$ complex in $D_2O$, respectively. All measurements were carried out at 293 K.

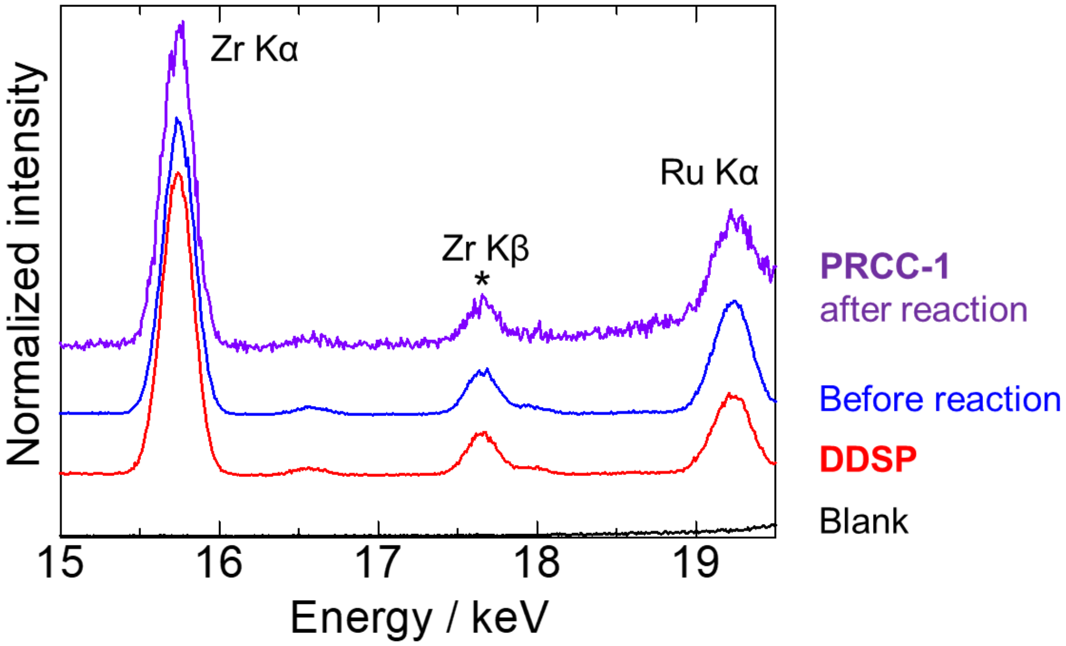

**Figure 8-3-8.** XRF spectra of (purple) **PRCC-1** washed with HClaq after hydrogen evolution experiment, (blue) **PRCC-1** before hydrogen evolution experiment, (red) **DDSP** as synthesized in the solid state at 293 K under vacuum. Black line indicates the baseline. The all spectra were normalized by Zr kβ line (* marked peak).

**Table 8-3-4** Results of analysis of XRF spectra described in Figure 8-3-8.

| Photocatalyst **X'-DSP** | Ru atom rate per Zr (mol/mol) | HCM rate per outer PS (mol/mol) |
|---|---|---|
| | Ru/Zr | HCM/**RuCP**$^6$ |
| **PRCC-1** after reaction | 0.8(2) | 1.1(7) |
| **PRCC-1** before reaction | 0.70(3) | 0.8(2) |
| **DDSP** | 0.49(2) | - |

To clarify the electron mediating effect of **HCRu**, photocatalytic $H_2$ production activity of **PRCC-1** in the presence of hydroquinone sulfonate ($H_2QS^-$) that is a redox mediator analogue used in the electron transport chain in natural photosynthesis.[24, 25] Both **PRCC-1** and **DDSP** produced $H_2$ photocatalytically, and the *i*AQY value of **PRCC-1** (1.10%) was approximately twice higher than **DDSP** (*i*AQY=0.519%). Although the *i*AQY value of **PRCC-1** decreased to be approximately one-third (*i*AQY=0.345%) by lowering the $H_2QS^-$ concentration to be 16.4 mM (Figure 8-3-9), the pH value of reaction solution after 6 h irradiation was almost unchanged (~2.0). These results suggest that $H_2QSK$ could function as not only the electron but also the proton source for $H_2$ production. Further characterization of the oxidation byproduct from $H_2QSK$ is necessary, but it is noteworthy that **PRCC-1** exhibited remarkably high *i*AQY value over 1% in the presence of hydrogen atom mediator, $H_2QS^-$. These results emphasize the importance of electron mediating effect for multi-electron transfer reaction (e.g. $H_2QS^- \rightarrow BQS^- + 2e^- + 2H^+$) at the photocatalyst-RM interface.

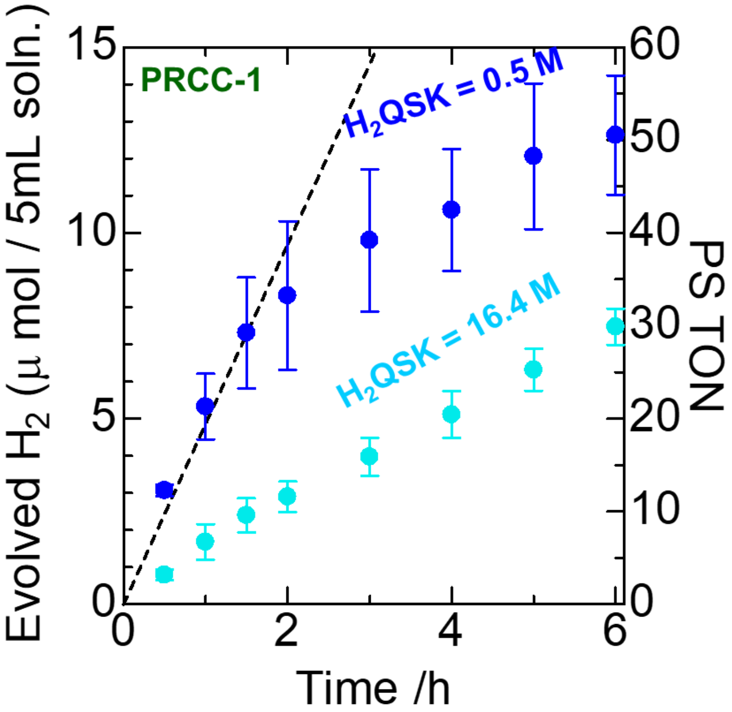

**Figure 8-3-9**. $H_2QSK$ concentration dependence driven by **PRCC-1** in HCl aqueous solution (pH = 2).

## 8-4 Conclusion

In this work, a novel photo-redox cascade catalyst **PRCC-1**, mimicking the electron transport chain of natural photosynthesis was newly synthesized by using two Ru(II) photosensitizers and visible-light-transparent electron mediator. The photocatalytic $H_2$ production reaction from the redox-reversible electron donating $[Co(bpy)_3]^{2+}$ and a hydrogen atom donor, $H_2$QSK were successfully achieved with the highest *i*AQY over 2 and 1%, respectively, among the dye-sensitized $TiO_2$ photocatalytic system. These findings indicate that the photo-redox cascade structure formed by molecular arraying of PS and RM should be an effective strategy for one-directional electron transfer at photocatalyst-RM interface as suggested by the electron transport chain in natural photosynthesis.

## 8-5 References

1. Fujishima, K. Honda. *Nature* **1972**, *238*, 37–38.
2. S. Acharya, D.K. Padhi, K. M. Parida. *Catal. Today* **2020**, *353*, 220-231.
3. M. Graetzel. *Acc. Chem. Res*. **1981**, *14*, 376-384.
4. Y. Ma, X. Wang, Y. Jia, X. Chen, H. Han, C. Li. *Chem. Rev*. **2014**, *114,* 9987-10043.
5. A. Kudo, Y. Miseki.*Chem. Soc. Rev*. **2009**, *38*, 253-278.
6. X. Fang, S. Kalathil, E. Reisner.*Chem. Soc. Rev*. **2020**, *49*, 4926-4952.
7. A. Nakada, S. Nishioka, J. J. Vequizo, K. Muraoka, T. Kanazawa, A. Yamakata, S. Nozawa, H. Kumagai, S. Adachi, O. Ishitani, K. Maeda. *J. Mater. Chem. A* **2017**, *5*, 11710-11719.
8. M. J. Fang, C. Tsao, Y. J. Hsu. *J. Phys. D: Appl. Phys.* **2020**, *53,* 143001-143033.
9. H. Kumagai, R. Aoyagi, K. Kato, A. Yamakata, M. Kakihata, H. Kato. *ACS Appl. Energy Mater.* **2021**, 2056–2060.
10. Q. Wang, T. Hisatomi, Q. X. Jia, H. Tokudome, M. Zhong, C. Z. Wang, Z. H. Pan, T. Takata, M. Nakabayashi, N. Shibata, Y. B. Li, I. D. Sharp, A. Kudo, T. Yamada, K. Domen. *Nat. Mater.* **2016**, *15,* 611-615.
11. R. Abe, K. Shinmei, N. Koumura, K. Hara, B. Ohtani. *J. Am. Chem. Soc*. **2013**, *135,* 16872-16884.
12. R. B. Chandran, S. Breen, Y. Shao, S. Ardo, A. Z. Weber. *Energy Environ. Sci.* **2018**, *11*, 115–135.
13. S. Nishioka, K. Hojo, L. Xiao, T. Gao, Y. Miseki, S. Yasuda, T. Yokoi, K. Sayama, T. E. Mallouk, K. Maeda. *Sci. Adv*. **2022**, *8*, 9115-9122.
14. Y. Zhang, J. Qi, Y. Kong, Y. Zhao, S. Chen, D. Li, W. Liu, Y. Chen, T. Xie, J. Cui, K. Domen, F. Zhang. *Nat. Commun*. **2022**, *13*, 484.
15. M. E. El-Khouly, Y. Chen, X. Zhuang, S. Fukuzumi. *J. Am. Chem. Soc*. **2009**, *131*, 6370–6371.
16. M. Borgström, N. Shaikh, O. Johansson, M. F. Anderlund, S. Styring, B. Åkermark, A. Magnuson, L. Hammarström. *J. Am. Chem. Soc*. **2005**, *127*, 17504–17515.
17. A. J. Cowana, J. R. Durrant. *Chem. Soc. Rev*., **2013**, *42*, 2281-2293.
18. Govindjee, D. Shevela, L. O. Björn. *Photosynth Res*., **2017**, *133*, 5–15.
19. H. Kitano, A. Kobayashi, M. Yoshida, M. Kato. *Sustainable Energy&Fuels* **2018**, *2*, 2609-2615.
20. K. Hanson, M. K. Brennaman, A. Ito, H. Luo, W. Song, K. A. Parker, R. Ghosh, M. R. Norris, C. R. K. Glasson, J. J. Concepcion, R. Lopez, T. J. Meyer. *J. Phys. Chem. C* **2012**, *116,* 14837-14847.
21. N. Yoshimura, A. Kobayashi, M. Yoshida, M. Kato. *Chem. Eur. J.* **2020**, *26,* 16939-16946.
22. H. Sato, M. Ide, R. Saito, T. Togashi, K. Kanaizuka, K. Kurihara, H. Nishihara, H. Ozawa, M. Haga. *J. Mater. Chem. C*, **2019**, *7*, 12491-12501.
23. Y. Sasaki, H. Kato, A. Kudo. *J. Am. Chem. Soc.* **2013**, *135*, 5441–5449.

24. C. M. Lewis,J. D. Flory, T. A. Moore, A. L. Moore, B. E. Rittmann, W. F. J. Vermaas, C.L. Torres, P. Fromme. *J. Am. Chem. Soc.* **2022**, *144*, 2933–2942.
25. M. Mure. Tyrosine-Derived Quinone Cofactors. *Acc. Chem. Res*. **2004**, *37*, 131–139.

# Chapter 9
# General Conclusion

In this thesis, the rational strategies not only to suppress the back reaction processes but also to accelerate forward reaction processes for highly active dye-sensitized water reduction photocatalyst were demonstrated.

Prior to this thesis, photocatalytic hydrogen evolution by dye-sensitized $TiO_2$ photocatalyst in the presence of redox reversible electron donor (=electron mediator in the Z-scheme water splitting photocatalysis) has been scarcely reported. This is because the charge-recombination and back reactions with redox reversible electron donor easily occurs at the semiconductor-PS-donor interfaces. To overcome these issues, various PS-multilayered structures were constructed on the surface of semiconductor photocatalyst in this thesis in anticipation of the suppression of back electron transfer from electron injected semiconductor, the blocking oxidized electron donor from approaching to the surface of co-catalyst, and the improved reactivity of PS with electron donor. This approach consisting of the PS-multi-layering and surface modification offered several advantages to systematically investigate and control the reaction scheme by replacing each component (semiconductor, PS, surface functional group, and electron donor). The apparent quantum yield for initial 1 h (*i*AQY) and total 6 h irradiation (AQY) of photocatalysts developed in this thesis are shown in Figure 9-1. The highest value, 2.23% of *i*AQY (apparent quantum yield of initial 1 h irradiation) at 460 nm irradiation was achieved by using HCRu-ZrP-2Ru@Pt-$TiO_2$ in the presence of 16.4 mM $[Co(bpy)_3]SO_4$ as discussed in chapter 8. This value is comparable to the highest record achieved by the dye-sensitized layered Pt/$HCa_2Nb_3O_{10}$ photocatalyst (AQY= 4.1% at 420 nm irradiation) reported recently by K. Maeda *et. al.*[1] The detail progresses obtained in this thesis are described below.

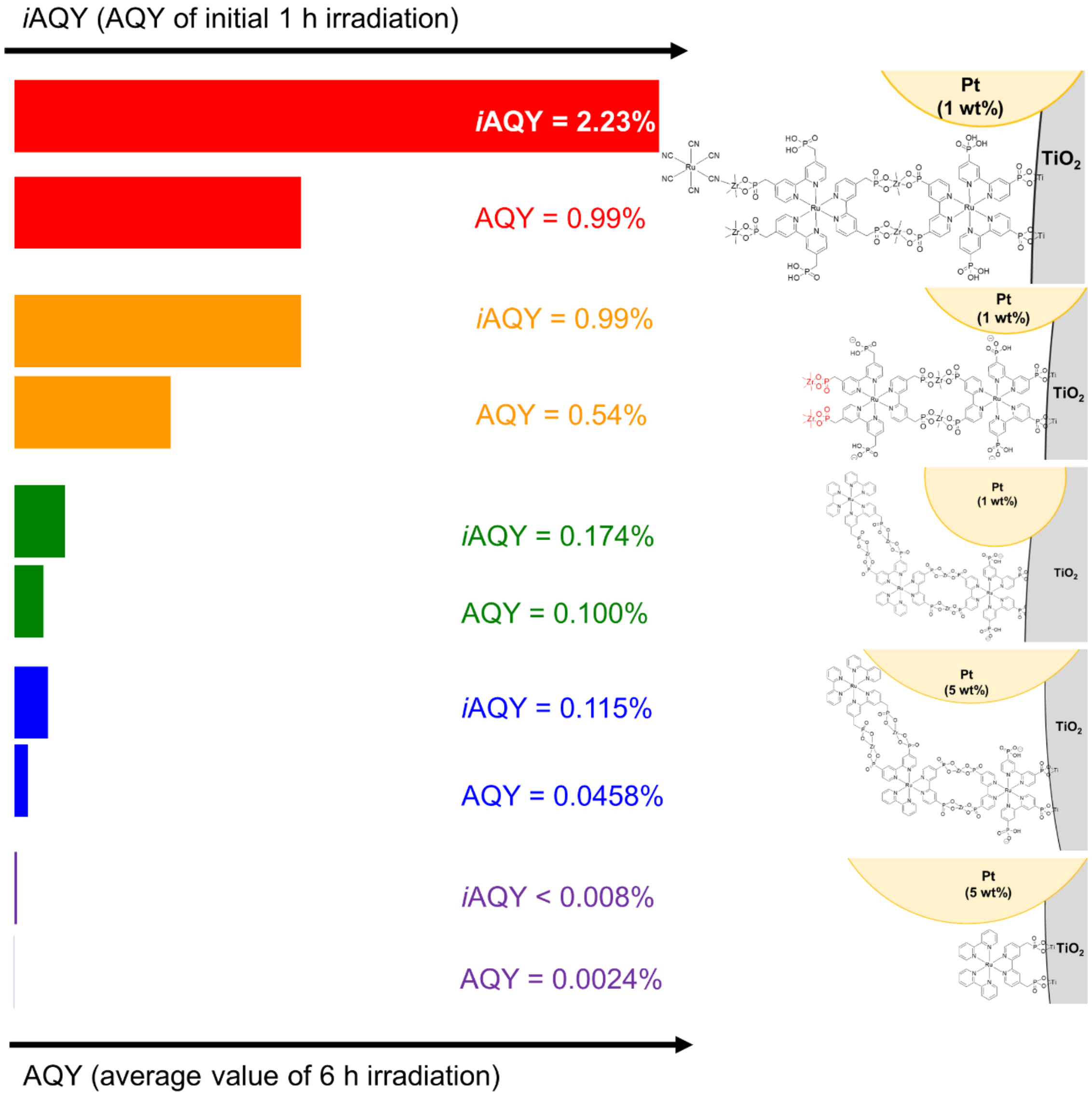

Figure 9-1. Improvement of photocatalytic hydrogen evolution activity in this thesis

In chapter 1, the background and purpose in this thesis were described. Honda-Fujishima effect about semiconductor photocatalysts, Z-scheme system, dye-sensitization, and outline of this thesis were summarized.

In chapter 2, the effect of energy transfer between the inner- and outer-PSs on water reduction photocatalyst was revealed by comparing outer Ru(II)-PS of PS-multilayered Pt-TiO$_2$ nanoparticle with different photoluminescent energy in the presence of ascorbic acid aqueous solution. The AQY was approximately 15% higher than **RuCP$^2$phen**-Zr-**RuP$^6$**@Pt-TiO$_2$, having forward gradient energy transfer from electron donor to PS, than **RuP$^2$**-Zr-**RuP$^6$**@Pt-TiO$_2$, having reverse gradient energy transfer system especially in low 20 mM of ascorbic acid concentration. This result indicates that photoexcitation energy transfer from the outer to inner Ru(II) PS plays a positive role on the photocatalytic activity especially in the low sacrificed electron donor concentration.

In chapter 3, PS-multilayer effect to photocatalytic hydrogen evolution reaction in the presence of redox reversible electron donor, iodide anion, was investigated by comparing PS-singly, doubly, and triply-layered Pt-TiO$_2$ nanoparticles. The PS-doubly-layered photocatalyst **RuCP$^2$**-Zr-**RuP$^6$**@5wt%Pt-TiO$_2$ exhibited photocatalytic hydrogen evolution activity with 0.018% of AQY, whereas PS-singly-layered photocatalyst **RuCP$^2$**@5wt%Pt-TiO$_2$ have almost no activity. Furthermore, the PS-triply-layered photocatalyst **RuCP$^2$**-Zr-**RuP$^4$**-Zr-**RuP$^6$**@5wt%Pt-TiO$_2$ exhibited higher activity with 0.0458% AQY than the others probably due to the following two improvements; one was the enhancement of the forward reaction on the electron donation process from iodide to Ru(II) PS by electrostatic interaction between iodide anion and Zr$^{4+}$ cation linkers as evidenced by Zeta potential measurements. Another was the suppression of back reaction from triiodide to iodide on Pt co-catalyst surface by bulkiness of PS-multilayered structure. Especially, **RuCP$^2$**-Zr-**RuP$^4$**-Zr-**RuP$^6$**@1wt%Pt-TiO$_2$ exhibited 0.100% AQY, and this value was comparable to singly-dye-sensitized layered niobate photocatalysts.[2,3] This result indicates that PS-multilayeted structure was effective to improve charge separation efficiency between photocatalysts and redox mediators.

In the electron donation from iodide, to attract several iodide anions near the one oxidized Ru-PS was important for the rapid formation of diiodide ($I_2^{\bullet-}$) and the suppression of back electron transfer from iodine radical ($I^{\bullet}$) to Ru-PS. In this context, in chapter 4, the effect of surface modification of PS-multilayered photocatalyst on photocatalytic hydrogen evolution activity with iodide was revealed by changing the outer Ru(II) PS from **RuCP$^2$** to **RuCP$^6$** and also immobilizing Zr$^{4+}$ cations to the outer-surface phosphonate group. Newly prepared Zr-**RuCP$^6$**-Zr-**RuP$^6$**@Pt-TiO$_2$ exhibited remarkably high AQY (0.54%) that was approximately five times higher than **RuCP$^2$**-Zr-**RuP$^4$**-Zr-**RuP$^6$**@1wt%Pt-TiO$_2$ (0.100%, chapter 3), indicating that surface Zr$^{4+}$ cations play a key role of attracting iodide electron donor.

In chapter 5, surface metal cation dependence for photocatalytic hydrogen evolution reaction with iodide was investigated by **X'-DSPs** (X' = H$^+$, Fe$^{2+}$, Y$^{3+}$, Zr$^{4+}$, Hf$^{4+}$, and Bi$^{3+}$, DSP = **RuCP$^6$**-Zr-

**RuP$^6$**@Pt-TiO$_2$) to reveal the electrostatic interaction effect between surface metal cation and iodide electron donor. The photocatalytic $H_2$ evolution activity under blue light irradiation ($\lambda$ = 460±15 nm) increased in the following order: non-metal-modified DSP, **H$^+$-DSP** (turn over number for 6 h irradiation = 35.2) < **Fe$^{2+}$-DSP** (54.9) ≅ **Bi$^{3+}$-DSP** (55.2) < **Hf$^{4+}$-DSP** (65.5) ≅ **Zr$^{4+}$-DSP** (68.3) ≅ **Y$^{3+}$-DSP** (71.5), suggesting that the redox-inactive and highly-charged metal cations tend to improve the electron donation from the iodide electron mediator. These results suggest that surface modification of dye-sensitized photocatalysts to modify the electrostatic interaction between the photocatalyst surface and redox mediator is a promising approach to enhance electron donation from the redox mediator.

In chapter 6, the extension of PS-multilayering strategy was achieved by developing Ru(II)-PS doubly-layered Pt/$K_xH_{4-x}Nb_6O_{17}$ semiconductor photocatalyst, Zr-**RuCP$^6$**-Zr-**RuP$^6$**@Pt/$K_xH_{4-x}Nb_6O_{17}$ and **RuCP$^6$**-Zr-**RuP$^6$**@Pt/$K_xH_{4-x}Nb_6O_{17}$ for photocatalytic hydrogen evolution reaction in the presence of iodide anion and $[Co(bpy)_3]^{2+}$ cation. Zr-**RuCP$^6$**-Zr-**RuP$^6$**@Pt/$K_xH_{4-x}Nb_6O_{17}$, having the surface $Zr^{4+}$-phosphonate groups, showed the highest AQY (0.38%) in the KI aqueous solution, while **RuCP$^6$**-Zr-**RuP$^6$**@Pt/$K_xH_{4-x}Nb_6O_{17}$, having phosphonate anions on its surface, exhibited the highest AQY (0.40%) in the $[Co(bpy)_3]SO_4$ aqueous solution. This is the similar trend to that observed for the Pt-TiO$_2$ analogues (as discussed in chapter 4), suggesting that PS-double layering and surface modification are useful strategies to improve the photocatalytic $H_2$ evolution activity in the presence of redox-reversible electron donor.

In chapter 7, the stronger interaction between photocatalyst surface and electron donor was formed to enhance the charge separation efficiency on the photocatalyst-donor interface by using highly charged polyoxometalates (POMs), $K_6[SiV^{IV}W_{11}O_{40}]$ (**V$^{IV}$POM**) and $K_6[SiMn^{II}W_{11}O_{39}(H_2O)]$ (**Mn$^{II}$POM**) as the redox reversible electron donor, and PS-double-layered photocatalyst (**X-DSP**, X-**RuCP$^6$**-Zr-**RuP$^6$**@Pt/$K_xH_{4-x}Nb_6O_{17}$, **X** = $Zr^{4+}$, $H^+$). **H$^+$-DSP** having surface phosphonate group completely one-electron oxidized **V$^{IV}$POM** with 0.39% of an apparent quantum yield in the initial 1 h (*i*AQY) in both HCl and phosphate buffer aqueous solutions, whereas *i*AQY of **Zr$^{4+}$-DSP** significantly decreased to be only 0.05% in the HCl aq. Considering that the higher activity (*i*AQY = 0.39%) was retained when replacing **V$^{IV}$POM** by **Mn$^{II}$POM** in the HCl aq., the energy transfer deactivation from photoexcited PS* to the surface-immobilized **V$^{IV}$-POM** should be the plausible origin of the lower *i*AQY because of the stronger visible light absorptivity of **V$^{IV}$-POM** than **Mn$^{II}$-POM**. These results suggest that the accumulation of visible-light-transparent electron donors to eliminate non-favorable energy transfer quenching on the photocatalyst surface should be a promising method for efficient one-directional electron transfer in the Z-scheme water splitting system.

Following the results of chapter 7, visible-light-transparent redox-active hexacyanoruthenate (**HCRu** = $[Ru(CN)_6]^{4-}$) was immobilized on the surface of Zr-**RuCP$^6$**-Zr-**RuP$^6$**@Pt-TiO$_2$ (**Zr$^{4+}$-DSP**) as the hole acceptor to further improve the photo-induced charge separation efficiency at the semiconductor-

PS interface in chapter 8. **HCRu**-immobilized photocatalyst (**HCRu-DSP**) exhibited approximately twice higher *i*AQY (2.23%) in the 16.4 mM $[Co(bpy)_3]SO_4$ donor condition than that without **HCRu** on the surface. This activity gradually decreased as surface **HCRu** amount decreased, suggesting that hole accepting **HCRu** could play a key role of improving reactivity with $[Co(bpy)_3]^{2+}$ electron donor. A plausible origin of the superior performance of **HCRu-DSP** is probably due to the hole migration to **HCRu** that generates the charge-separated state with longer separation distance between the electron and hole should suppress the charge-recombination effectively. Thus, the construction of photo-redox cascade structure should be important to achieve the one-directional electron transfer in Z-scheme water splitting photocatalysis.

The apparent quantum yield for initial 1 h (*i*AQY) and total 6 h irradiation (AQY) of photocatalysts developed in this thesis are shown in Figure 9-1. The several strategies to achieve one-directional electron transfer from redox mediator to hydrogen evolution catalyst were examined. Thus, PS-multilayering on the semiconductor surface should improve the charge separation efficiency between PS and semiconductor due to outer-to-inner PS energy transfer and hole migration after the electron injection to semiconductor substrate. This PS-multilayering was effective for $H_2$ evolution from the redox-reversible electron donor not only on classical Pt-$TiO_2$, but also on layered niobate Pt/$K_xH_{4-x}Nb_6O_{17}$. In addition, the electron donation reactivity from donor to PS could be improved by the surface modification of photocatalyst nanoparticle. Especially, the electrostatic interaction between electron donor and photocatalyst surface was found to be effective to attract donor near the surface of photocatalyst nanoparticle. To further improve the electron donation, immobilization of the hole accepter on the photocatalyst surface was found to greatly enhance the charge separation efficiency between PS and donor. This strategy should offer a new pathway to make a connection with electron mediating polymers such as PEDOT:PSS (poly(3,4-ethylenedioxythiophene) polystyrene sulfonate) and redox-active coordination polymer like Prussian white analogues (e.g. $Na_2Fe[Fe(CN)_6]$). Although photocatalytic water splitting activity of dye-sensitizing system was not sufficient for practical application, the findings in this thesis provide promising methods to design of highly active photocatalysts.

References

1. S. Nishioka, K. Hojo, L. Xiao, T. Gao, Y. Miseki, S. Yasuda, T. Yokoi, K. Sayama, T. E. Mallouk, K. Maeda. *Sci. Adv.*, **2022**, *8*, 9115.
2. G. B. Saupe, T. E. Mallouk, W. Kim, R. H. Schmehl. *J. Phys. Chem. B* **1997**, *101*, 2508–2513.
3. R. Abe, K. Shinmei, N. Koumura, K. Hara, B. Ohtani. *J. Am. Chem. Soc.*, **2013**, *135*, 16872-16884.

# Acknowledgements

The studies presented in this thesis were carried out at the Department of Chemistry, Faculty of Science, Hokkaido University during April 2017-March 2023.

The author would like to express greatest profound appreciation to Associate Professor Atsushi Kobayashi (Hokkaido University) for the best research environment and valuable discussions.

The author would like to express deepest gratitude to Professor Masako Kato (present affiliation Kwansei Gakuin University) for her valuable discussion, encouragements, and greatest financial support.

The author would like to express deepest gratitude to Professor Kazuki Sada (Hokkaido University) for his multifaceted discussion and encouragements.

Furthermore, the author would like to express deeply grateful to associate lecturer Masaki Yoshida (present affiliation Kwansei Gakuin University) for his helpful discussion and encouragements.

Moreover, the author would like to express his gratitude to Professor Kei Murakoshi, Kiyoharu Tadanaga, Kosei Ueno (all Hokkaido University) for reviewing this thesis.

The author also gratefully acknowledgements to Professor Takashi Okubo and Mr. Wataru Genno for their support with $TiO_2$-ITO preparation and DSSCs measurement (chapter 3). The author would like to acknowledge to Dr. Akiko Matsumoto for her support with SEM measurements. The author would like to acknowledge to Professor Yasuchika Hasegawa and Associate Professor Yuichi Kitagawa for their support with TEM measurements.

The author would like to acknowledge to Dr. Tomohiro Ogawa (Hokkaido university) and Assistant Professor Yasuhiro Shigeta (present affiliation Kanazawa University) for helpful advice and valuable comments as well as numerous words of encouragement.

The author is deeply grateful to Mr. Hirotsugu Kitano and Mr. Shuhei Watanabe for their kind supports for earnest guidance of water reduction measurements.

The author is also grateful to Dr. Daisuke Saito, Ms. Mari Kimura, Mr. Kenki Shimizu, Mr. Ryota Yano for helpful discussion, best friendship as well as dedicated supports.

The author would like to say thanks to Ms. Sae Kondo, Mr. Taku Shimamura, and Mr. Sääsk, Verner for their lenient treatment to author’s trivial contribution about their superior research articles.

This work was financially supported by the Hokkaido University DX Doctoral Fellowship Grant Number JPMJSP2119 from Hokkaido University.

Finally, I would like to special thanks to my family (Mr. Nobuhiko Yoshimura, Mrs. Kimiko Yoshimura, Ms. Towako Yoshimura, and Mr. Nobuhide Yoshimura) and friends for their supports and encouragements.

Nobutaka Yoshimura
Graduate School of Chemical Sciences and Engineering
Hokkaido University